UNIVERSITÀ DELLA CALABRIA

UNIVERSITY OF CALABRIA

Department of Physics

Research doctorate in

Science and Engineering of the Environment, Construction and Energy

CYCLE
XXXII

Synthesis and characterization of low-dimensional materials

Scientific Disciplinary Sector FIS/01

Coordinator: Prof. Salvatore Critelli

Firma oscurata in base alle linee guida del Garante della privacy
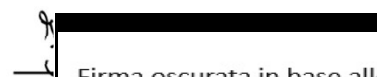
Supervisor: Prof. Lorenzo S. Caputi

Firma oscurata in base alle linee guida del Garante della privacy

Co-Supervisor   Dr. Anna Cupolillo

Firma oscurata in base alle linee guida del Garante della privacy

PhD Candidate: Dr. Francesca Alessandro

Firma oscurata in base alle linee guida del Garante della privacy

CONTENTS

PART II Carbon nano-onions and Activated carbon

Acknowledgment

Undertaking this PhD has been a truly important life-experience for me and it would not have been possible without the support that I received from many people.

So, firstly I would like to thank my supervisors Prof. Lorenzo Caputi and Dr. Anna Cupolillo for their valuable guidance, kindness and professionalism in the scientific matters which have allowed me to be more efficient throughout the period of my research. My thanks extend also to all my seniors and juniors colleagues of the Surface Nanoscience group: Diana, Salih, Marlon, Marilena and Andrea for the good teamwork and lovely friendship environment they have given me.

I wish to thank Prof. Diego Cazorla Amorós and Prof. Emilia Morallón Núñez, for the warm welcome I received in their laboratory at University of Alicante. To my labmates in Alicante (David, Miriam, Jhony, Mounya, Mohamed, Alex, Andres, Sandra, Samuel, Jessica, Ana, María José, Javi C., Javi Q., Verónica, Cristhian), for their nice welcome and kindness.

Thank you my family for always believing in me.

Thank you my friends Mara and Fabiola for sharing this journey with me.

Finally, a special thanks to Alessio for his unconditional support.

Abstract

(English Version)

The main aim of this thesis is to synthesize and study low-dimensional materials, with special focus on: silicene, $PtTe_2$, carbon nano-onions and activated carbon.

The first section of this work describes the study of the collective modes in silicene and $PtTe_2$.

Silicene, the silicon equivalent of graphene, is attracting increasing scientific and technological interest in view of the exploitation of its exotic electronic properties. This material has been theoretically predicted to exist as a free-standing layer in a low-buckled, stable form, and can be synthesized by the deposition of Si on appropriate crystalline substrates.
Using a combined experimental (High-Resolution Electron-Energy-Loss Spectroscopy, HR-EELS) and theoretical (Time Dependent Density Functional Theory, TDDFT) approach the electronic excitations of two phases of silicene growth on silver were studied showing that silicene grown in a mixed phase on Ag(111), preserves part of the semimetallic character of its freestanding form, exhibiting an interband π-like plasmon.

Recently, the $PtTe_2$ has emerged as one of the most promising among layered materials "beyond graphene". In this work, the electronic excitations of the bulk $PtTe_2$ were investigated by means of EELS and DFT detecting a sequence of modes at 3.9, 7.5 and 19.0 eV. The comparison of the excitation spectrum with the calculated density of states (DOS) allowed to ascribe spectral features to transitions between specific electronic states. Moreover, it has been observed that, in contrast to graphene, the high-energy plasmon in $PtTe_2$ gets red-shifted by 2.5 eV with increasing thickness.

The second section of this thesis reports the synthesis of polyhedral carbon nano-onions by arc discharge in water and the electrochemical performance of activated carbon in aqueous electrolytes.

CNOs, in their spherical or polyhedral forms, represent an important class of nanomaterials, due to their peculiar physical and chemical properties. In this work, polyhedral carbon nano-onions (CNOs) were obtained by underwater arc discharge of graphite electrodes using an innovative experimental arrangement. Dispersed nanomaterials and a black hard cathodic deposit were generated during the discharges and studied by scanning electron microscopy (SEM), transmission electron microscopy (TEM), Raman spectroscopy and thermogravimetric analysis (TGA). A model for the formation of the deposit was proposed, in which the crystallization is driven by an intense temperature gradient in the space very close to the cathode surface.

Electric double layer capacitors (EDLC) are gaining increasing popularity in high power energy storage applications. Novel carbon materials with high surface area, high electrical conductivity, as well as a range of shapes, sizes and pore size distributions are being constantly developed and tested as potential supercapacitor electrodes.
In this thesis, the electrochemical behavior of a highly microporous activated carbon was studied as electrode for symmetric and asymmetric capacitors in acid and neutral media. The highest capacity and energy density values were obtained in the case of the activated carbon in acid solution.

Abstract

(Italian Version)

Lo scopo di questa tesi risiede nella sintesi e nello studio di sistemi a bassa dimensionalità focalizzando, principalmente, l'attenzione sui seguenti materiali: silicene, $PtTe_2$, carbon nano-onions e carbone attivo.

Nella prima parte di questa tesi è descritto lo studio delle eccitazioni collettive del silicene e del $PtTe_2$.

A causa della sua particolare geometria, simile a quella del grafene, e della sua maggiore compatibilità nell'attuale elettronica, il silicene, ha suscitato una crescente attenzione sia in ambito teorico che sperimentale. Studi teorici e curve di dispersione fononiche hanno dimostrato che la sua stabilità nello stato libero bidimensionale è data da una struttura planare lievemente piegata che si origina quando l'ibridazione degli stati sp^2 si "mescola" con l' ibridazione degli stati sp^3. Sebbene il silicene sembri non esistere in natura sotto forma di singolo strato isolato, vari domini ordinati sono stati osservati per il silicene cresciuto su Ag(111), la cui formazione e coesistenza dipende dalla temperatura del substrato, durante la crescita di silicio, e dal tempo di deposizione. In questa tesi, usando la spettroscopia di perdita di energia di elettroni (High-Resolution Electron-Energy-Loss Spectroscopy, HREELS) supportata da calcoli teorici (Time Dependent Density Functional Theory, TDDFT) sono state esplorate le eccitazioni elettroniche di due fasi del silicene cresciuto su Ag(111), dimostrando che il silicene cresciuto su argento in una fase composta conserva parte del carattere semimetallico della sua forma freestanding, esibendo un plasmone π di interbanda.

Recentemente, anche il $PtTe_2$ è emerso tra i materiali più promettenti fra quelli "beyond graphene". L'idea di questo lavoro è stata quella di studiare gli spettri di eccitazione di

bulk e degli strati sottili del PtTe$_2$ mediante spettroscopia di perdita di energia degli elettroni combinata a dettagliati calcoli *ab initio*. L'analisi EELS ha evidenziato l'esistenza di una serie di chiari e distinti picchi aventi le seguenti energie: ~ 3.9, ~ 7.5 e ~ 19.0 eV. Un confronto fra la densità degli stati (DOS) e i picchi osservati nello spettro EELS ha permesso di identificare gli stati coinvolti nelle transizioni. Inoltre, è stato osservato che il picco del plasmone ad alta energia del PtTe$_2$ mostra un red-shift pari a 2.5 V all'aumentare dello spessore, in contrasto con il grafene.

La seconda parte di questa tesi presenta la sintesi selettiva di carbon nano-onions poliedrici mediante scarica ad arco in acqua e la caratterizzazione elettrochimica di un carbone attivo in soluzioni acquose.

I carbon nano-onions (CNO), nella loro forma sferica o poliedrica, rappresentano un' importante classe di nanomateriali a causa delle loro peculiari proprietà fisiche e chimiche. In questo lavoro, carbon nano-onions di tipo poliedrico sono stati ottenuti mediante scarica elettrica in acqua tra due elettrodi di grafite utilizzando un apparato sperimentale innovativo. Nello specifico, sono stati prodotti materiali in sospensione ed un deposito sulla superficie del catodo. I campioni ottenuti sono stati studiati mediante microscopia elettronica a scansione (SEM), microscopia elettronica a trasmissione (TEM), spettroscopia Raman e analisi termogravimetrica (TGA). È stato proposto un possibile meccanismo di sintesi per il deposito in cui si ipotizza che la cristallizzazione non sia dovuta al gradiente di temperatura esistente tra il plasma e l' acqua, ma al gradiente localizzato nelle immediate vicinanze della superficie del catodo, che durante la scarica si mantiene ad una temperatura sensibilmente inferiore rispetto a quella dell'anodo.

I supercapacitori a doppio strato elettrico (EDLC) sono, attualmente, al centro di un grande interesse scientifico e tecnologico, e si prevede che avranno nei prossimi decenni un forte impatto sul mercato dei sistemi di accumulo di energia, soprattutto nei casi in cui le sorgenti di energia sono discontinue, casi che sono anche tra quelli più importanti ai fini dello sviluppo sostenibile. Le caratteristiche dei supercapacitori dipendono in maniera cruciale sia dal tipo di materiale utilizzato come rivestimento degli elettrodi, sia dal tipo di elettrolita impiegato. In questa tesi, il comportamento elettrochimico di un

carbone attivo, altamente microporoso, è stato investigato mediante voltammetria ciclica e cicli di carica/scarica galvanostatica, in due diverse soluzioni acquose. I risultati ottenuti evidenziano elevati valori di capacità per il campione in soluzione acida. Da un punto di vista applicativo, le prestazioni elettrochimiche del materiale carbonioso sono state studiate mediante la realizzazione di supercapacitori simmetrici ed asimmetrici. In entrambi i casi, elevati valori di capacità e densità di energia, sono stati osservati per il materiale in mezzo acido.

LIST OF FIGURES

surface.

LIST OF TABLES

Introduction

Nanotechnology is part of a natural progression in many different areas of science coupled with development of new tools that enable researchers to see, model, and control structures at the nanometer scale. Although, in many ways, nanotechnology is not new, experimental and computational tool development enables research to be done that was not previously possible. New approaches can be taken to address previously intractable problems. Therefore, nanoscience and nanotechnology do not represent a new discipline, but rather advancements within several disciplines and a convergence of concepts and ideas across disciplines. As such, nanotechnology introduces important new ideas and cross-fertilization that enables scientific breakthroughs and development of various new technologies.

After the groundbreaking impact of graphene, the scientific community is actively exploring two-dimensional (2D) semiconductors "beyond graphene" for their promising application capabilities, often complementary to those of graphene. Different classes of 2D semiconductors have emerged in recent years: transition-metal dichalcogenides (TMDs); monolayer black phosphorus; silicene/germanene; and IV-VI semiconductors. Many innovative applications, widely used in our daily lives, are based on the exploitation of collective properties of matter (ferromagnetism, superconductivity, the quantum Hall effect and plasmonic excitations). Therefore, the comprehension of collective electronic excitations is crucial in order to develop new disruptive technologies for health, telecommunications, energy etc. In particular, the novel field of plasmonics has recently emerged, in consideration of the progress of nanotechnology and nanofabrication. Plasmonics deals with the generation, propagation and detection of plasmonic excitations, which are collective electronic excitations produced by an electromagnetic field. The field confinement and enhancement resulting from the interaction between matter and radiation can be technologically used for

devising plasmonic devices for diverse applications, ranging from optics, biology, nanoelectronics and nanophotonics.

At the same time, due to growing concerns about the environmental impacts of fossil fuels and the capacitance and resilience of energy grids around the world, scientists, engineers and policymakers are increasingly turning their attention to energy storage solutions. Indeed, energy storage systems are the key to deal with the intermittent nature of renewable energy sources and increase the power transmitted into the grid from systems such as wind and solar power. In addition, an increase in the efficiency of a vehicle requires kinetic energy to be stored somewhere whenever the vehicle slows down or stops. Although these operations have been successfully performed with batteries on a low-power scale, new methods for efficiency enhancement will require large amounts of power that can only be provided by other energy storage technologies such as supercapacitors. These have attracted significant attention due to their high power capabilities and long cycle-life, giving a very good chance to build more advanced hybrid energy storage systems, for both on-board and stationary applications. In this field, microporous carbons are the primary materials used to make supercapacitor electrodes. They have relatively high electrical conductivity, essential for power applications, and large specific surface area (SSA), necessary for enhancing the capacitance. However, research and industrial developments for supercapacitors are oriented to improving the device's energy density through the design of new electrode materials.

For these reasons, on the one hand, this thesis will focus on understanding the electronic properties of Silicene and $PtTe_2$ crucial to devise broadband photodetectors, ultraviolet-imaging applications, and plasmon devices. On the other hand, in this work will be studied porous carbon materials such as CNOs and an activated carbon which due to their high specific surface area, high electric conductivity, high thermal stability and appropriate microstructure, have been evaluated as a potential candidates in many different fields: tribology, lithium-ion batteries, fuel cells, supercapacitors and catalysis.

This thesis was carried out at the laboratory of the Surface Nanoscience in the Department of Physics of University of Calabria. The development of the work was supplemented by a research stay at the University of Alicante under the supervision of Professor Diego Cazorla Amorós.

This thesis is divided into two main sections: in the Section I, the collective electronic properties of two surface reconstructions of silicene on Ag(111) and the broadband excitation spectrum of bulk crystals and thin layers of $PtTe_2$ will be studied by electron-energy-loss spectroscopy (EELS); in the Section II, first, the properties of polyhedral CNOs obtained by underwater arc discharge will be explored using scanning electron microscopy (SEM), transmission electron microscopy (TEM), Raman spectrocopy and thermogravimetric analysis (TGA), and subsequently, the electrochemical performance of an activated carbon will be studied in aqueous electrolytes.

Part I

1 Silicene

1.1 Introduction

Following the isolation of graphene sheets by mechanical exfoliation of its parent crystal graphite [1], enormous effort has been directed towards two-dimensional (2D) crystals made of group-IV elements other than carbon. A particularly noteworthy example is silicene, the silicon equivalent of graphene with a natural compatibility with current semiconductor technology [2-4]. First-principles calculations of the structural properties report an intrinsic stability of a honeycomb arrangement of Si atoms in slightly buckled form, with mixed sp^2-sp^3 hybridization. This system, referred to as freestanding or (1×1) silicene, presents a graphenelike, semimetallic electronic structure characterized by linearly dispersing π and π^* bands around the Fermi energy E_F, thus effectively allowing the charge carriers to mimic massless relativistic particles. Unlike graphene, freestanding silicene has a large spin-orbit coupling, which would make it suitable for valley-spintronic applications [5,6], and an electrically, magnetically, or chemically tunable band gap [7-12], which would be crucial for engineering on-off current ratios and charge-carrier mobility in silicene field-effect transistors.

1.2 Freestanding Silicene

1.2.1 Structure and electronic properties

Free-standing silicene consists in a single layer of Si atoms with a hexagonal arrangement. But contrary to graphene, silicene is predicted to be slightly buckled in its lowest energy configuration [13-15], consisting of top and bottom Si atoms, separated

by a vertical distance ΔZ of about 0.44 Å, as shown in Fig 1.1. The origin of the buckling of silicene arises from the larger Si–Si bond length, as compared to the C–C bond-length, which prevents the Si atoms to be 'purely' sp^2 hybridized and to form π-bonds [16]. The buckling of the Si atoms enables a larger overlapping of its orbitals and results in a mixed sp^2–sp^3 hybridization. The computed lattice parameters of free-standing silicene, obtained from Density Functional Theory (DFT) [Appendix A.1] simulations, are about a = b = 3.87 Å, $\alpha = \beta = 90°$ and $\gamma = 120°$ and the Si–Si bond length is about 2.28Å [17].
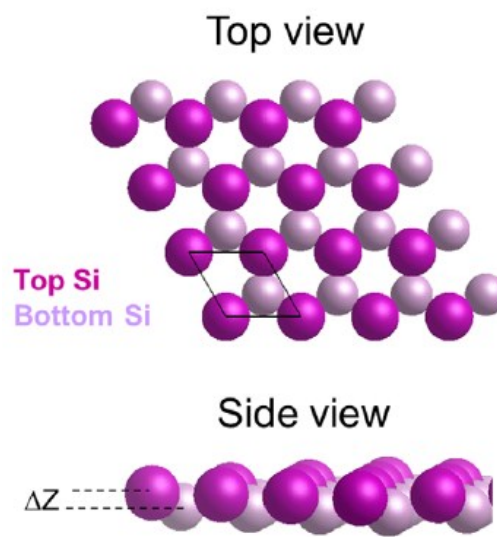
Figure 1.1. Top and side views of the atomic configuration of free-standing silicene [3].

Slightly buckled silicene is predicted to be a gapless semiconductor, like graphene, with Dirac cones at the K-points of the hexagonal Brillouin zone (BZ) [7,18,19], as shown in Figure 1.2. As a result, the electrons near these points behave as massless Dirac fermions obeying the relativistic Dirac equation. Applying an electric field perpendicular to its plane is predicted to open an energy gap at the K-points [7,20-22], as illustrated in Figure 1.3; the opening of the energy gap results from the charge transfer between the top and bottom Si atoms, breaking the inversion-symmetry in the system. The electric field induced gap opening in silicene is potentially very interesting for logic applications. In addition, the effect of electron and hole doping on the stability, electronic and vibrational properties of silicene was reported in [23], and it was found that doping changes the occupation of its π and $\pi*$ bands and therefore affects the

strength and length of the Si–Si bonds, as well as the frequency of the silicene active Raman modes.
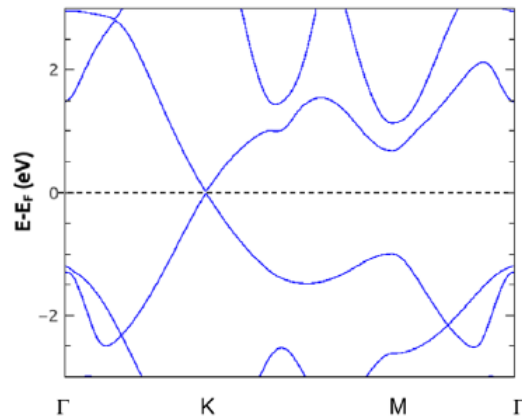
Figure 1.2. Calculated electronic energy band structure of free-standing silicene. The Fermi level corresponds to the reference (zero) energy [3].

When spin–orbit coupling is included in the DFT calculations, silicene is predicted to present a topological phase transition from a quantum spin Hall state to a trivial insulator when the out-of-plane electric field is increased, silicene thus potentially being a topological insulator [24].

The chemical functionalization of silicene with different ad-atoms and molecules has also been reported recently [25-30]. The adsorption of various atoms on silicene usually results in the opening of an energy gap, due to the sp^3-hybridization of the Si atoms. Very interestingly, the decoration of silicene with e.g. Co atoms is predicted to result in the observation of the quantum anomalous Hall effect in the system [30].
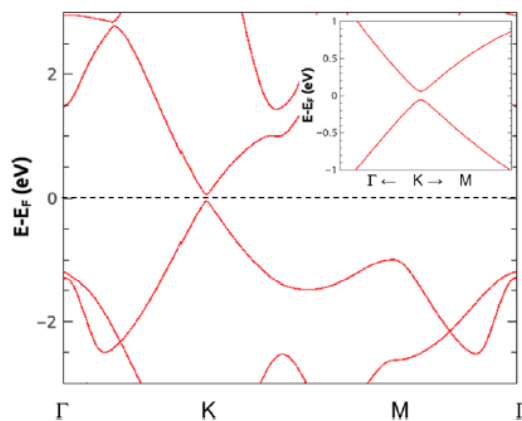
Figure 1.3. Calculated energy band structure of silicene in presenceof an out-of-plane electric field of $E_z = 1$ V/Å. The Fermi level corresponds to the reference (zero) energy. The inset shows a magnification of the band structure near the K-point [3].

1.3   Silicene growth on Ag(111)

1.3.1   Atomic structure

While evidence for freestanding silicene has not yet been experimentally obtained, silicene syntheses by Si deposition on surfaces have been pursued as an alternative method to examine its properties.

On the practical side, silicene-like nanostructures are synthesized by the epitaxial growth [31,32] of silicon on silver [33–39] and a few other metal substrates [40,41], very recently including gold [42]. In particular, a number of well-ordered domains have been observed on Ag(111), the formation and coexistence of which depend on the substrate temperature, during silicon growth, and the silicon deposition rate [43–49]. Most of these domains have a crystalline morphology that is closely commensurate with the (4×4), $\left(2\sqrt{3} \times 2\sqrt{3}\right)R30°$ and $\left(\sqrt{13} \times \sqrt{13}\right)R13.9°$ phases [47–59]. The different orientation, out-of-plane atomic buckling, and lattice constant of the Si atoms in these superstructures, denoted as (3×3), $\left(\sqrt{7} \times \sqrt{7}\right)_{\text{I}}$, $\left(\sqrt{7} \times \sqrt{7}\right)_{\text{II}}$, are reflected in markedly distinct electronic properties of the silicene overlayers that, even without the supporting Ag substrate below, may or may not preserve the Dirac cones of (1×1) silicene [46,47,60,61].

A continuous two dimensional (2D) sheet of silicene with a large area of an almost defect free honeycomb structure presenting a $\left(2\sqrt{3} \times 2\sqrt{3}\right)R30°$ superstructure on the Ag(111) surface, was observed for the first time by Scanning Tunneling Microscopy (STM) [31]. In a subsequent study, Le Lay et al. [62] claimed that the STM image of $\left(2\sqrt{3} \times 2\sqrt{3}\right)R30°$ did not correspond to a silicene layer but to a bare Ag(111) surface due to a contrast inversion [62] (a graphically inverted image or to a tip effect). These results were refuted by Enriquez et al. [55]. Figures 1.4(a) and (b) show the STM images obtained by Enriquez et al. [55], respectively, on the bare Ag(111) substrate, and on the $\left(2\sqrt{3} \times 2\sqrt{3}\right)R30°$ superstructure. The STM investigation revealed a highly ordered silicon honeycomb lattice structure [Figure 1.4(b)]. The authors observed that the basal chains of the honeycomb silicene sheet were rotated by an angle of $(30 - 19.1)° = 10.9°$ with respect to the axes of the Ag(111), exactly matching the

expected rotation for a $(2\sqrt{3} \times 2\sqrt{3})R30°$ superstructure. In the case of an inversion of contrast of the STM image of bare silver, the angle between the observed honeycomb structure, and that of the bare Ag(111) would be 0° and not 10.9°. Also, the same authors reported that the line profile along line (A) gives a lateral Si–Si distance of 0.2 nm, and a height difference between neighboring Si atoms (buckling) of 0.02 nm [Figures 1.4(b) and (c)]. The (111) surface of silver has a smooth density of states which gives a small corrugation of 0.02 nm and a perceived buckling of 0.002 nm. This is 10 times smaller than the corrugation and buckling observed in the STM images of the honeycomb $(2\sqrt{3} \times 2\sqrt{3})R30°$ superstructure [31].
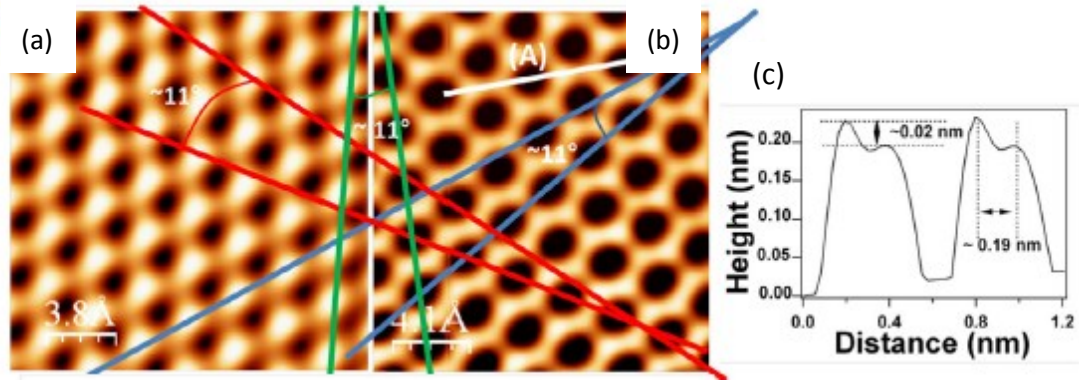
Figure 1.4. (a) Filled-state atomically resolved STM image of the clean Ag(111) surface. (b) Filled-state atomically resolved STM image of the same sample after deposition of one silicon monolayer.(c) Line-profile joining neighbouring Si atoms along the direction (A) indicated in (a) [55].

The (4×4) silicene structure on Ag(111) has attracted considerable attention because it is the silicene phase with the simplest and best characterized atomic structure.

The (4×4) superstructure is obtained with a substrate temperature around 200 °C. Majzik et al. [45] studied this structure by combining non-contact atomic force microscopy (nc-AFM) and scanning tunneling microscopy. The resulting STM topography and nc-AFM image of the same area are shown in Figure 1.5(a) and (b), respectively. The nc-AFM image [Figure 1.5(a)] was taken with a z-height where the repulsive force over the imaged Si atoms prevails. Therefore, the bright protrusions in the image correspond to sites that had a greater repulsive action on the tip apex. The STM and nc-AFM images are remarkably similar, showing protrusions at identical

locations in the unit cell. Each triangle represents one half of the elementary surface unit cell. The atomic contrast acquired by nc-AFM and STM consists of 6 characteristic protrusions arranged in 2 triangles within the unit cell. The observation coincides very well with the (4×4) model structure proposed in literature [44,55] which show that the Si atoms are relaxed out of the surface plane forming pyramids, whose apices are located at the positions where both the STM and AFM show bright protrusions.
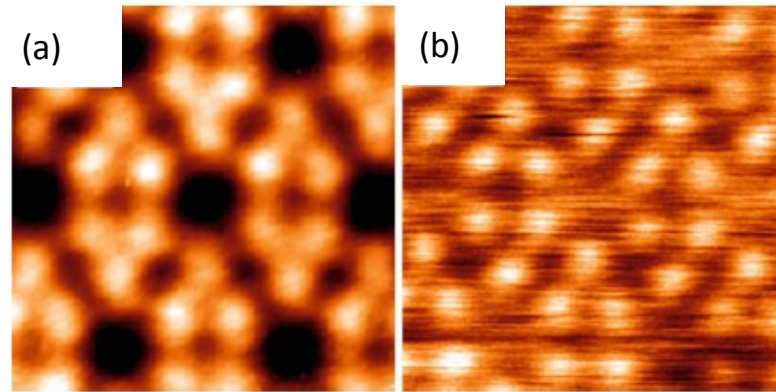
Figure 1.5. (a) Atomically resolved STM image of the (4×4) superstructure; (b) The same area was mapped in constant height nc-AFM operation [45].

The $\left(\sqrt{13} \times \sqrt{13}\right)R13.9°$ phase is obtained after deposition at a substrate temperature around 250 °C. The atomically resolved STM images of the $\left(\sqrt{13} \times \sqrt{13}\right)R13.9°$ system show two types of structures. The $\left(\sqrt{13} \times \sqrt{13}\right)R13.9°$ type I and type II superstructures are shown in Figures 1.6(a) and (b), respectively. Under similar tunneling conditions, the unit cell of the $\left(\sqrt{13} \times \sqrt{13}\right)R13.9°$ type II is composed of four protrusions per unit cell, whereas that of the $\left(\sqrt{13} \times \sqrt{13}\right)R13.9°$ type I superstructure is composed of only one protrusion. Within the unit cell, the relative positions of the Si and Ag atoms are very different between the type I and type II superstructures leading to very different out-of-plane coordinates.

Three-dimensional models for the type I and type II superstructures were investigated by DFT calculations in [45,55]. The type I and type II structures correspond to orientations of 5.2° and 33° relative to the (111) surface, respectively. These results indicate that two different configurations co-exist with different atomic positions. In

other words, small changes in the buckling of the silicene modify the observed structure.
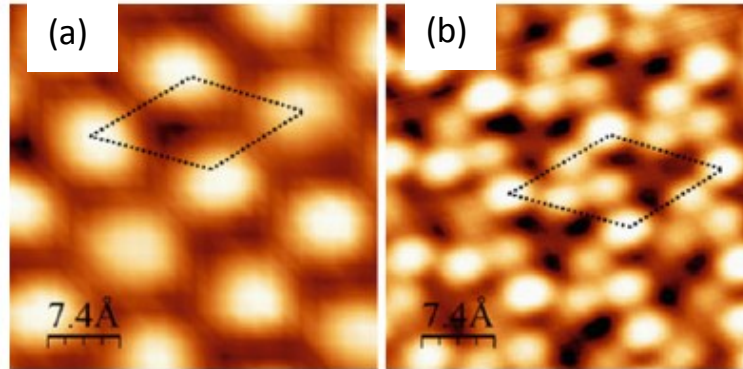
Figure 1.6. Atomically resolved STM images corresponding to the $\left(\sqrt{13} \times \sqrt{13}\right)R13.9°$ for (a) type I and (b) type II. The corresponding unit cells are shown with dotted lines [52].

1.3.2 Electronic structure of Silicene on Ag(111)

Since free-standing silicene is expected to present a Dirac cone [2,14,15,18], it is possible to ask whether silicene preserves the Dirac cone on a supporting substrate or not. The (4×4) silicene structure on Ag(111) has attracted considerable attention in this respect because its atomic structure is well known.

Two groups have claimed the existence of Dirac fermions in silicene on the Ag (111) surface [38,59]. Vogt et al. [38] have studied the electronic structure of the (4×4) silicene reconstruction by angular-resolved photoemission spectroscopy (ARPES). The authors found a linear dispersion near the K point of the Brillouin zone of silicene. They attributed the linear dispersion to silicene with the Dirac point 0.3 eV below the Fermi level. In addition, the Fermi velocity was estimated to be 1.3×10^6 ms^{-1}; higher than the value reported for graphene.

The second claim of the existence of Dirac fermions in silicene on the Ag(111) surface was reported by Chen et al. [59]. They studied the silicene structure using scanning tunneling spectroscopy (STS). A quasiparticle interference pattern (QPI) at the surface

of the silicene was observed, and the Dirac cone was deduced from the linear dispersion curve obtained from the STS curves [59].

However, STM measurements recorded under high magnetic field by Lin et al. [53] pointed to the absence of discrete Landau levels expected in the case of massless carriers. Hence, the authors concluded that the carriers in the (4×4) silicene do not show a Dirac cone.

The interpretation of the single-layer silicene photoemission data [38] has also been questioned on the basis of band structure calculations [63]. Indeed, these theoretical analyses propose that the experimentally reported bands should be attributed to the Ag states. The calculation revealed that the Dirac cone in the (4×4) silicene phase is destroyed as a result of the strong band hybridization between silicene and the Ag surface.

Mahatha et al. [64] repeated the same experiment as Vogt et al. [38] in order to confirm, or not confirm, the presence of the Dirac cone. They performed a detailed ARPES study coupled with DFT calculations of the (4×4) silicene structure. They found that silicene on Ag(111) does not preserve the Dirac cone at all due to the hybridization of silicene and silver states. Their result contradicts completely the interpretation of the observed linear dispersion by Vogt et al. [38] and Chen et al. [59]. The sp branch of the bare Ag(111) was observed as a linear trend near the K point of (4×4) silicene. The sp states were still observable even after the growth of the (4×4) silicene sheet indicating that the previous observations of the linear dispersion corresponded only to the sp branch of silver. This would suggest that there is no Dirac cone for the (4×4) structure of silicene on Ag(111).

The effect of the electronic interaction with the substrate for the $\left(\sqrt{13} \times \sqrt{13}\right)R13.9°$ and $\left(2\sqrt{3} \times 2\sqrt{3}\right)R30°$ structures is almost unexplored.

Sheverdyaeva et al. [65] compared the electronic structure of (4×4), $\left(\sqrt{13} \times \sqrt{13}R\right)$ 13.9°, and $\left(2\sqrt{3} \times 2\sqrt{3}\right)R30°$ phases by ARPES and first-principles calculations. They found that the systems displayed very similar silicene bands of σ character and the formation of Ag derived interface states with saddle-like band dispersion. Nevertheless, the identification of umklapp replicas in the ARPES data of the $\left(2\sqrt{3} \times 2\sqrt{3}\right)R30°$ phase allowed the authors a reinterpretation of the features

previously ascribed to silicene σ bands. All the examined silicene allotropic structures did not show Dirac cones at E_F, characteristic of free-standing silicene. The absence of π-like Dirac cones found explanation in the strength of the hybridization between silicene and Ag states, which also overwhelms the electronic effects of specific structural details of the different silicene allotropes.

1.4 Experimental apparatus: Ultra-High Vacuum Chamber (UHV)

Ultra-High Vacuum (UHV) is a necessary condition to impede chimico-physical processes caused by the action of atmospheric gases (melting of reactive gases as Mo, W, Ta, maintainment controlled conditions in gas surface interaction experiments) and to increase the mean free path of probe particles (molecules, electrons, ions) up to macroscopic distances (cathodic ray tubes, thermoionic tubes, electron based spectroscopies, particle accelerators).

In order to achieve good ultrahigh vacua, special attention must be paid to the choice of the materials exposed to the inside of the chamber. Furthermore, once exposed to air, all surfaces inside the vacuum chamber may adsorb constituents from the atmosphere, in particular, water vapor.

The vapor pressure of materials as well as the desorption rate of adsorbates increase with rising temperature. Therefore, once closed, UHV chambers are subjected to a bake-out procedure, in which the whole vacuum system is heated to 150-250 °C for many hours while pumping. Likewise, filaments and the samples themselves have to be preheated to temperatures higher that in the following experiments in order to aoutgas unwanted contaminants. Obviously, bake-out and outgassing temperatures put constraints on the materials that can be used for and in a UHV system. The most commonly used material for vacuum chambers is stainless steel. Aluminum alloys, copper, titanium, tungsten, tantalum and molybdenum are the widely used metals inside vacuum systems. Copper is the typical material for gaskets, while tungsten, tantalum and molybdenum are often used for high-temperature-resistant sample holders.

The easiest way to lower the pressure in the vessel is to expand the volume. However, this principle would require tremendous expansion in order to achieve UHV starting from atmospheric pressure. Therfore, the use of UHV requires high pumping speed, possibly multiple vacuum pumps in series and/or parallel.

The experimental measurements presented in the first part of this thesis were carried out at room temperature in an UHV chamber (Figure 1.7), in which the ordinary pressure is about 2×10^{-10} Torr.
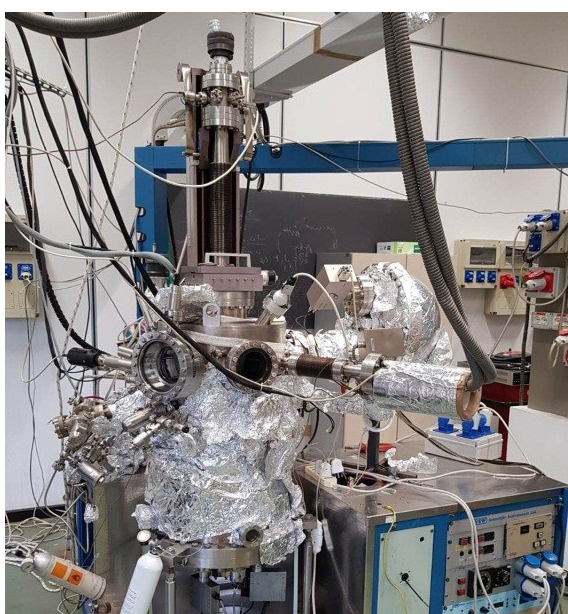
Figure 1.7. Ultra-high vacuum chamber.

The vacuum system used in this chamber consists of three main pumps: rotary pump, turbomolecular pump and ion pump.

The first pumping stage, a rough vacuum of 10^{-1}-10^{-3} Pa is produced by rotary vane pumps. It belongs to the category of the so-called wet pumps, which use oil as lubricant, coolant and sealant. As a consequence, such pumps contain oil vapor so that a cold trap between pump and vacuum chamber is needed to prevent this vapor from contaminating the chamber. The operation of a turbomolecular pump is based on a high-speed rotating stack of rotors that have multiple, angled blades. Turbomolecular pumps producing vacua down to 10^{-10} Pa. Finally the ion pumps are the main ingredient of UHV systems,

capable of reaching pressures as low as 10^{-11} Pa. Ion pumps capture and store molecules of gas. In a diode ion pump, a gas molecule collides with high energy electrons, loses one or more of its own electrons, and is left with a positive charge. The resulting ion is under the influence of a strong electric field, and is therefore accelerated into a titanium cathode. The force of the collision is great enough that the ions and some titanium ions are ejected from the cathode and collide with the adjacent walls of the pump, where they accumulate.

This UHV chamber can be ideally divided into two communicating sections.

In the upper section is located an electron gun that provides focused and accelerated electron beams. The electrons emitted from the sample are detected by the hemispherical analyzer. The presence of the electron gun and the hemispherical analyzer make it possible to perform a multi-spectroscopy investigation with electron energy loss spectroscopy (EELS) [Appendix A.2] and x-ray photoemission spectroscopy (XPS) [Appendix A.7]. Furthermore, the presence of a low-energy electron diffraction (LEED) [Appendix A.4] spectrometer makes it possible to determine the surface structure of single-crystalline materials. Conversely, a high-resolution EELS spectrometer with two 50 mm hemispherical deflectors for both monochromator and analyzer is mounted in the lower part of the chamber.

1.5 Results and discussions

1.5.1 Substrate preparation and Silicene growth

The silver substrate (a disk of about 8 mm diameter) was cleaned through several cycles of sputtering with 1 keV Ar^+ ions, at an operating pressure of 5×10^{-5} Torr, followed by annealing at 500 °C until a sharp LEED pattern showed the achievement of a clean and well-ordered Ag(111) surface. Silicon was deposited on Ag(111) by thermal evaporation from a pure source, which was *slab cut* from a silicon wafer, clamped between two electrodes, and heated up, by passing a direct current thorough it, to obtain a stable vapor flux. During deposition, the silicon source was placed in front of the silver substrate, which was maintained at a constant temperature, controlled by a

thermocouple placed close to the sample. The pressure during growth was less than 2×10^{-9} Torr. The uptake of Si was monitored by XPS and LEED. XPS spectrum [Figure 1.8(a)] acquired on the clean silver surface shows the high quality of the substrate. The silicon deposition on the clean silver was confirmed by the presence of the 2s Si line as shown in the Figure1.8(b). Figure 1.9(a) shows the diffraction pattern acquired with the Ag substrate kept at 300°C, during Si deposition. The LEED spots from this first sample are consistent with the reciprocal space points of Figure 1.9(c). Accordingly, they are readily interpreted as originating from a sufficiently *pure* $\left(2\sqrt{3} \times 2\sqrt{3}\right)R30°$ phase, in agreement with several previous studies [44,45,55-57]. On the other hand, the LEED image of Figure 1.9(b) was acquired with the Ag substrate kept at 270°C, during Si deposition. This second sample is characterized by a mixture of the (4×4), $\left(2\sqrt{3} \times 2\sqrt{3}\right)R30°$ and $\left(\sqrt{13} \times \sqrt{13}\right)R30°$ phases. The possible formation of recently isolated multilayer silicene can be ruled out, because it would provide a different LEED pattern [66]. Real and reciprocal spaces of (4×4), $\left(2\sqrt{3} \times 2\sqrt{3}\right)R30°$ and one of the two equivalent $\left(\sqrt{13} \times \sqrt{13}\right)R30°$ phases of silicene on Ag(111) are show also in Figure 1.10. The LEED spots from the second sample are in line with the reciprocal space points of the three phases, reported in Figure 1.10(e), where the silicene superstructures are assumed to be perfectly matched with the silver substrate. Interestingly, a visual inspection of Figures 1.9(b) and 1.9(c) suggests a lattice mismatch of the $\left(\sqrt{7} \times \sqrt{7}\right)_{\mathrm{I}}$ and $\left(\sqrt{7} \times \sqrt{7}\right)_{\mathrm{II}}$ overlayers of ~1% and ~5%, respectively. Similar patterns, mostly concerning the (4×4) and $\left(\sqrt{13} \times \sqrt{13}\right)R30°$ phases, have been discussed elsewhere [32,44,57-59], nonetheless, the composite structure observed in this work, presenting a dominant $\left(2\sqrt{3} \times 2\sqrt{3}\right)R30°$ which coexists with the (4×4) and $\left(\sqrt{13} \times \sqrt{13}\right)R30°$ phases has yet to be reported.
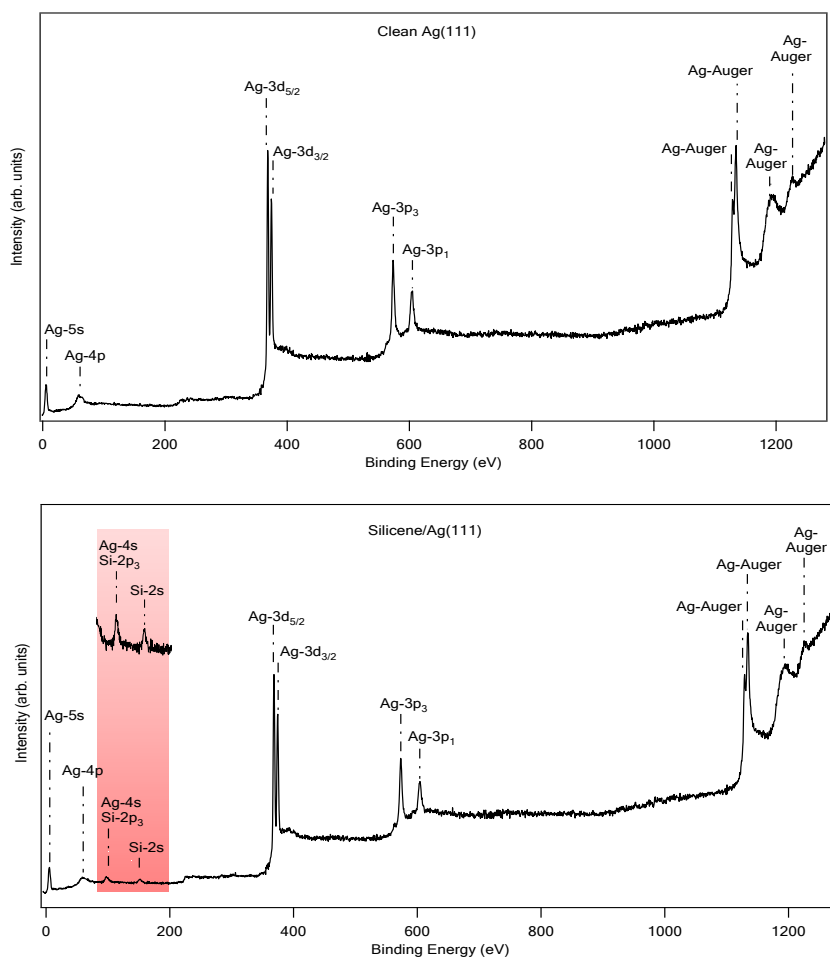
Figure 1.8. XPS spectra for (a) clean silver surface and (b) silicene/Ag(111) system.
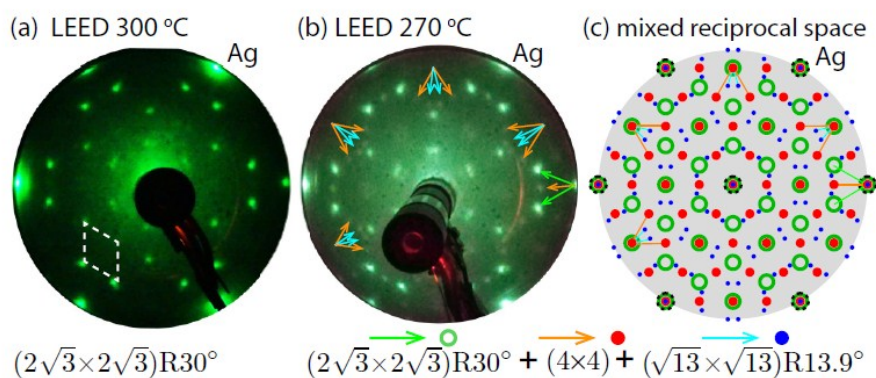
Figure 1.9. LEED patterns of (a) the $(2\sqrt{3} \times 2\sqrt{3})R30°$ phase and (b) the $(4 \times 4) + (2\sqrt{3} \times 2\sqrt{3})R30° + (\sqrt{13} \times \sqrt{13})R30°$ phase of silicene on Ag(111). The coexistence of multiple domains in (b) is attested by spots of different intensity, being consistent with the mixed reciprocal space representation in (c).

Figure 1.10. Real and reciprocal spaces of the (4×4), $(2\sqrt{3} \times 2\sqrt{3})R30°$ and one of the two inequivalent $(\sqrt{13} \times \sqrt{13})R30°$ phases of silicene on silver. The unit cells of the superstructures are delimited by orange lines. The main geometric parameters of the silicene overlayers (commensurate supercell, average in-plane bond length d_{Si-Si}, minimum Si-Ag distance d_{Si-Ag}, and out-of-plane atomic buckling Δ_i) are derived from Refs. [60,61].

The table (Silicene overlayer):

		Silicene overlayer	
Si/Ag phase	(4×4)	$(2\sqrt{3} \times 2\sqrt{3})R30°$	$(\sqrt{13} \times \sqrt{13})R30°$
Si supercell	(3×3)	$(\sqrt{7} \times \sqrt{7})_{\text{I}}$	$(\sqrt{7} \times \sqrt{7})_{\text{II}}$
d_{Si-Si},	2.17	2.18	2.25
d_{Si-Ag}	2.17	2.16	2.13
• $\Delta_1(\text{Å})$	0.78	0.36	0.36
• $\Delta_2(\text{Å})$		1.19	0.59
• $\Delta_3(\text{Å})$			0.79

1.5.2 Collective-plasmon mode in Silicene mixed and pure phases

The EELS measurements were performed with the samples directly transferred in the ELL spectrometer, without breaking the vacuum, and kept at room temperature with a pressure below 2×10^{-10} Torr. The EL spectra were acquired with an incident electron beam, about 0.2 mm wide, positioned at a fixed angle of 45° from the surface normal. The kinetic energy of the incident electrons was 40 eV. Scattered electrons were collected at an angle of 46° from the surface normal, with an overall energy resolution of 20 meV and an angular acceptance of 2°. Figure 1.11 shows the EL spectra, in the range of 0–6 eV, obtained from (i) clean Ag(111), (ii) the pure $(2\sqrt{3} \times 2\sqrt{3})R30°$ phase with the LEED pattern of Figure 1.9(a), and (iii) the mixed phase with the LEED pattern of Figure 1.9(b). A prominent feature at $\sim$ 3.8 eV, which corresponds to the surface plasmon of Ag(111), dominates all spectra. Besides, the Si/Ag(111) spectrum shows an additional loss at $\sim$ 0.7 eV in the pure phase and 1.75 eV in the mixed phase. The excitation energy of the former mode suggests the presence of a hybridized Si-Ag plasmon, whereas the latter mode resembles the π-like plasmon of (1×1) silicene [67].
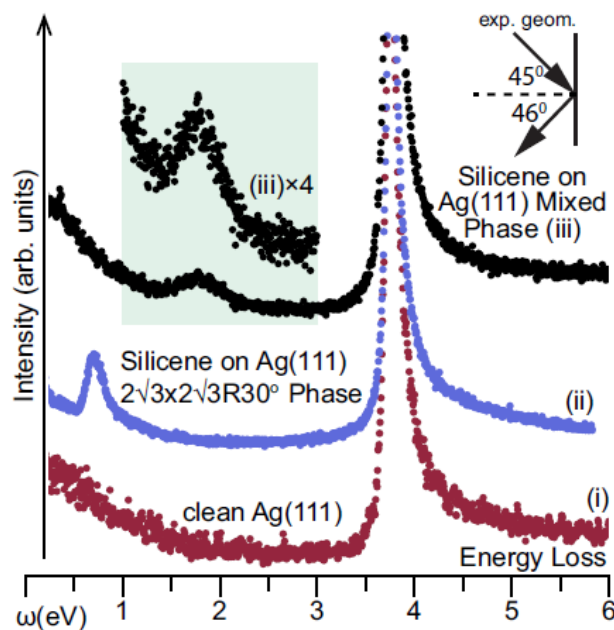
Figure 1.11. EL spectra acquired, with a primary electron energy of 40 eV and the experimental geometry shown in the inset, from (i) clean Ag(111), (ii) silicene on Ag(111) in the pure $(2\sqrt{3} \times 2\sqrt{3})R30°$ phase, and (iii) silicene on Ag(111) in the mixed $(4 \times 4) + (2\sqrt{3} \times 2\sqrt{3})R30° + (\sqrt{13} \times \sqrt{13})R30°$ phase.

To support this observation, TDDFT in the random phase approximation (RPA) has been used and have been computed the dielectric properties of (1×1) silicene [67] in comparison with the (3×3), $\left(\sqrt{7} \times \sqrt{7}\right)_{\text{I}}$, $\left(\sqrt{7} \times \sqrt{7}\right)_{\text{II}}$, and overlayers of silicene, peeled from the silver substrate, in the (4×4), $\left(2\sqrt{3} \times 2\sqrt{3}\right)R30°$, $\left(\sqrt{13} \times \sqrt{13}\right)R30°$ phases of Figure 1.10. These superstructures represent instructive examples of monolayer silicene, which, without the Ag substrate below, would not and would preserve the Dirac cones [46,47,65,66]. The electronic structure and density of states (DOS) of DFT+LDA computations are reported in Figure 1.12, with the band energies represented along the $\Gamma K M \Gamma$ paths of the corresponding reciprocal spaces (Figure 1.10).
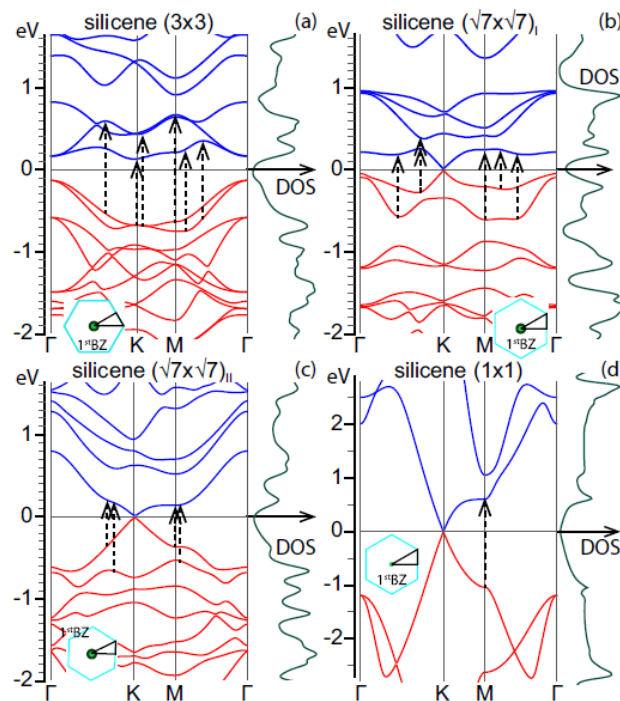
Figure 1.12. Band structure (relative to $E_F = 0$) and DOS for (3×3), $\left(\sqrt{7} \times \sqrt{7}\right)_{\text{I}}$, $\left(\sqrt{7} \times \sqrt{7}\right)_{\text{II}}$, and (1×1) silicene. The leading transitions concurring to the lower-energy loss peaks of Figure 1.13 are represented by dashed arrow lines. The $\Gamma K M \Gamma$ paths of the superstructures are defined in the reciprocal spaces of Figures 1.10(d)–1(f).

(3×3) silicene has no Dirac cones at K and presents a direct gap at $\Gamma \sim 0.3$ eV between two couples of nearly degenerate states of leading σ and π symmetries, respectively [Figure 1.12(a)]. $\left(\sqrt{7} \times \sqrt{7}\right)_{\text{I}}$, $\left(\sqrt{7} \times \sqrt{7}\right)_{\text{II}}$ silicene exhibit a quasilinear π-like dispersion in the first valence band (VB) and first (conduction band) CB at K,

i.e., a Dirac-cone structure with a tiny band gap below ~0.02 eV [Figures 1.12(b) and 1.12(c)]. The second VB and CB of these superstructures are of dominant σ symmetry. (1×1) silicene has two quasimetallic bands of dominant π character [Figure 1.12(d)], whose dispersions resemble the π bands of graphene [68] on a reduced energy scale and with a smaller Fermi velocity [67]. All these silicene systems have specific high-intensity peaks in their DOS that support electron excitations between the first or second VB and CB near E_F, in a region of the first BZ where the bands are quasiflat, and may assist π-like and π-σ plasmon oscillations. The corresponding low-energy vertical transitions, leading to small-momentum EL peaks, are indicated by dashed arrow lines in Figures 1.12 and 1.13.

In Figure 1.13, the theoretical loss spectra of silicene systems have been compared, at fixed small momentum transfers parallel to ΓK in an energy loss range below 2.5 eV. The superstructures present a sequence of low-energy peaks associated with quasivertical electron excitations between the first or second VB and CB, of dominant π or σ character [Figures 1.12(a)–1.12(c)]. Accordingly, the momentum-dependent investigation of Figures 1.14(a)–1.14(c) allowed to identifiy two dispersive modes, which can be respectively attribute to a π-like plasmon, assisted by first-VB to- first-CB transitions, and a π-σ plasmon, assisted by second-VB-to-first-CB and first-VB-to-second-CB transitions.
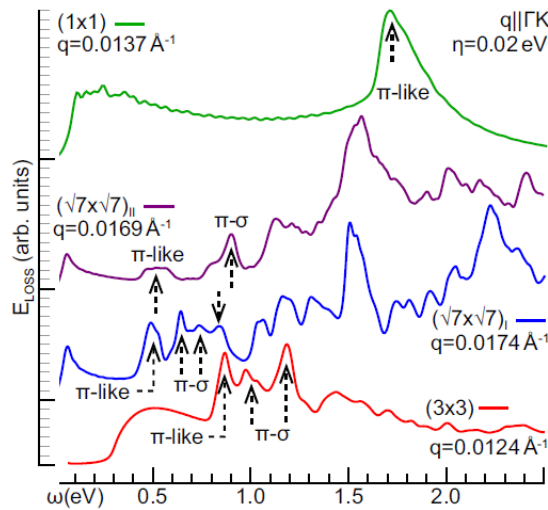
Figure 1.13 EL function of (3×3), $\left(\sqrt{7} \times \sqrt{7}\right)_{I}$, $\left(\sqrt{7} \times \sqrt{7}\right)_{II}$ and (1×1) silicene for $q < 0.02 \text{Å}^{-1}$ and $\omega < 2.5$ eV with the lower energy peaks, associated with transitions close to E_F, being represented by dashed arrow lines.

More importantly, it is possible to notice that there is no way that the EL functions of the silicene superstructures can be combined to reproduce the experimental loss spectrum of the mixed phase [curve (iii) in Figure 1.11]. Conversely, (1×1) silicene exhibits a broad primary π-like plasmon peak [Figures 1.13 and 1.14(d)], consistent with the EELS spectrum of the mixed phase, which is assisted by first-VB-to-first-CB transitions around the M point and superimposed to secondary one-electron excitation structures.
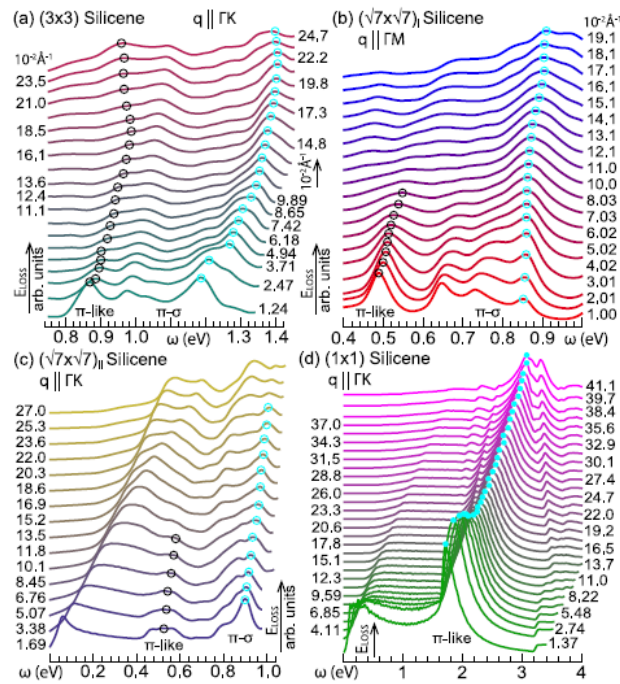
Figure 1.14. EL functions of (a) (3×3), (b) $\left(\sqrt{7} \times \sqrt{7}\right)_{\mathrm{I}}$, (c) $\left(\sqrt{7} \times \sqrt{7}\right)_{\mathrm{II}}$ and (d) (1×1) silicene along ΓK [(a), (b), (d)] and ΓM [(c)] directions of the first BZs.

Of particular significance are then the low-energy features at $\omega = 0.8 - 1.3$ eV, for (3×3) silicene, and $\omega = 0.4 - 0.9$ eV for $\left(\sqrt{7} \times \sqrt{7}\right)_{\mathrm{I}}$, $\left(\sqrt{7} \times \sqrt{7}\right)_{\mathrm{II}}$ silicene, because they appear not to be completely erased by the interaction with Ag(111). Indeed, the experimental loss of the pure $\left(2\sqrt{3} \times 2\sqrt{3}\right)R30°$ phase shows a peak, which has some match with the low-energy end of the theoretical loss function of $\left(\sqrt{7} \times \sqrt{7}\right)_{\mathrm{I}}$ silicene, lying within the energy window of vertical transitions associated with the π-σ plasmon (Figures 1.12 and 1.13). The interaction with silver destroys the high-energy loss properties of the peeled phase and distorts the low-energy peak, which can be ascribe to

a hybridized Si-Ag plasmon. This interpretation is confirmed by existing DFT calculations [63] and validated by analysis on the $(2\sqrt{3} \times 2\sqrt{3})R30°$. Figure 1.15 display the anisotropic dispersions of this mode along the ΓK and ΓM paths of the reciprocal space [Figure 1.10(e) and inset in Figure 1.12(b)]. When the Ag substrate, and its interaction with the $(\sqrt{7} \times \sqrt{7})_I$ silicene layer, is included in the calculations, the mode is expected to survive, though being strongly contaminated by the aforementioned Si-Ag hybridization.
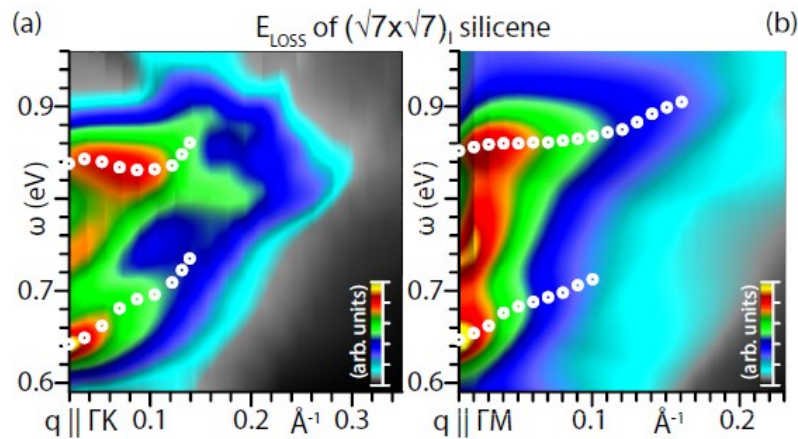
Figure 1.15. Theoretical EL functions of $(\sqrt{7} \times \sqrt{7})_I$ silicene in response to an energy transfer ω in the range of 0.59 to 0.96 eV, and a momentum transfer below 0.33 Å^{-1}, along the ΓK [(a)] and ΓM [(b)] directions of the first BZ. The loss-peaks are spotted as white circles.

In support of this idea, the EELS data, labelled (ii) in Figure 1.11, are juxtaposed in Figure 1.16 to the theoretical EL curve of the $(\sqrt{7} \times \sqrt{7})_I$ superstructure. The experimental low-energy peak at 0.75 eV falls within the same energy-window of vertical transitions from the second VB to the first CB of $(\sqrt{7} \times \sqrt{7})_I$ silicene [Figure 1.12(b)]. When Ag is included in the calculations, the electronic properties of the silicene layer change dramatically with respect to the peeled case, destroying the loss features at absorbed energies above ~ 1 eV.

On the other hand, a comparison of the DOS of the $(\sqrt{7} \times \sqrt{7})_I$ superstructure alone [Figure 1.12(b)] with the different projected DOS curves of the $(2\sqrt{3} \times 2\sqrt{3})R30°$ phase (Figure 1.16) indicates that the low energy features associated to the band levels, at energies below ~1 eV from E_F, are distorted but not completely erased.

On the contrary, no signature of an interband plasmon at ω = 1.7–2 eV appears in the theoretical loss spectrum of the silicene superstructures. A more suggestive result is shown in Figure 1.17, where (1×1) silicene calculations are compared with the EL measurements on the coexisting silicene/Ag(111) phases [loss-curve (iii) in Figure 1.11].
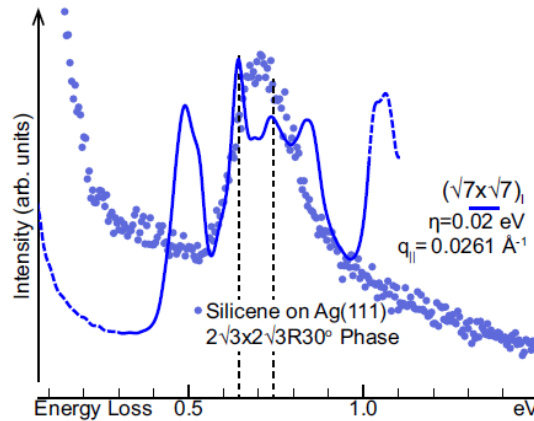
Figure 1.16. Theoretical EL function of $\left(\sqrt{7} \times \sqrt{7} \right)_{I}$ silicene and experimental loss spectrum (ii) of Figure 1.11.

The excellent agreement, at energy losses below 3 eV, allowed to conclude that this morphology indeed presents a dielectric response that matches what is expected for the π-like plasmon of ideal silicene.
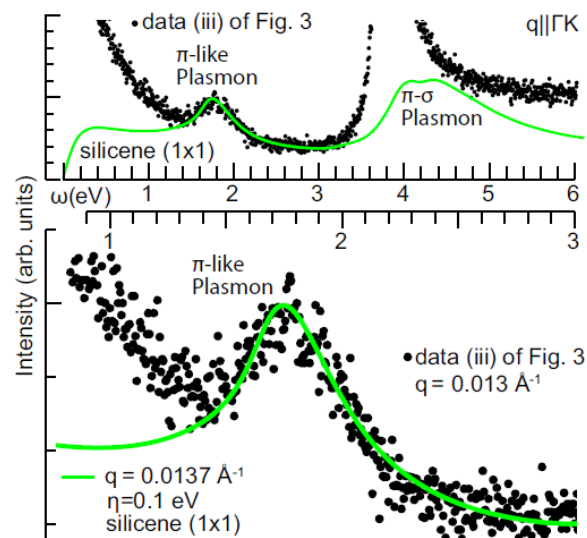
Figure 1.17. Experimental loss spectrum (iii) of Figure 1.11 and theoretical loss function of (1×1) silicene, where the lowest sampled q value along ΓK is considered with an overall broadening of 0.1 eV to match the experimental resolution.

Also interesting to notice is that the π-σ plasmon of (1×1) silicene may be present as well, though it is hidden by the Ag plasmon of the interface, as verified by comparing the loss spectrum of the mixed phase with that of clean Ag(111) [(i) in Figure 1.11]. Hence, the interaction between the pure phases not only weakens the hybridization of Si and Ag states, but also appears to *merge* the different buckling levels of supported silicene into a configuration that resembles that of freestanding silicene. Indeed, the different silicene superstructures are expected to arrange into buckling conformations that mimic that of (1×1) silicene, when their distances, relative to the Ag substrate, are increased above the 2.13–2.16 Å values, predicted for the pure phases.

1.6   Conclusions

To summarize the results obtained, it was presented a combined experimental (EELS) and theoretical (TDDFT) approach to show that silicene grown in a mixed phase on Ag(111) preserves at least part of the semimetallic character of its freestanding form, exhibiting an interband π-like plasmon assisted by excitation processes at the *M* point of the first BZ. Such a mode parallels the π plasmon of freestanding graphene [67]. The presence of a π-like plasmon by itself does not allow to conclude that the silicene overlayer maintains its natural Dirac-cone structure. For example, the interfaces of graphene on the (111) faces of copper and nickel have a well-characterized π plasmon, with the Dirac cone being preserved and destroyed, respectively, by hybridization with the *d* bands of the supporting metal [69,70]. Nonetheless, in the latter case, the shape, position, and dispersion of the plasmon peak is substantially different from that of freestanding graphene [71], which encourages performing further investigations on mixed-phase morphologies of silicene on silver. A similar approach would help to characterize the first VB and CB of silicene on Au(111) [43], and corroborate the expected Dirac-cone properties of the system. On the other hand, recent progress on the epitaxial synthesis of pure, single phases of silicene on Ag(111), supported by DFT computations of their electronic properties, indicate that strong hybridization effects make it impractical to separate a silicene structure with a well-defined quasimetallic character. An experimental fingerprint of this phenomenon is the hybridized Si-Ag

plasmon, discovered at low energy. This study then suggests to shift the efforts of making silicene a feasible two-dimensional nanomaterial beyond graphene on the epitaxial growth of silicene in mixed domains.

References

[1] K. S.Novoselov, A.K. Geim, S.V. Morozov, D. Jiang,Y. Zhang, S. V. Dubonos, I. V. Grigorieva, and A. A. Firsov, Electric field effect in atomically thin carbon films, Science **306**, 666 (2004).

[2] A. Kara, H. Enriquez, A. P. Seitsonen, L. C. Lew Y. Voon, S. Vizzini, B. Aufray, and H. Oughaddou, A review on silicene–New candidate for electronics, Surf. Sci. Rep. **67**, 1 (2012).

[3] M. Houssa, A. Dimoulas, and A. Molle, Silicene: A review of recent experimental and theoretical investigations, J. Phys.: Condens. Matter **27**, 253002 (2015).

[4] S. Cahangirov, H. Sahin, G. Le Lay, and A. Rubio, *Introduction to the Physics of Silicene and other 2DMaterials*, Lecture Notes in Physics No. 930 (Springer, Berlin, 2017).

[5] C.-C. Liu, W. Feng, and Y. Yao, Quantum Spin Hall Effect in Silicene and Two-Dimensional Germanium, Phys. Rev. Lett. **107**, 076802 (2011).

[6] H. Pan, Z. Li, C.-C. Liu, G. Zhu, Z. Qiao, and Y. Yao, Valley-Polarized Quantum Anomalous Hall Effect in Silicene, Phys. Rev. Lett. **112**, 106802 (2014).

[7] Z. Ni, Q. Liu, K. Tang, J. Zheng, J. Zhou, R. Qin, Z. Gao, D. Yu, and J. Lu, Tunable bandgap in silicene and germanene, Nano Lett. **12**, 113 (2011).

[8] T. H. Osborn, A. A. Farajian, O. V. Pupysheva, R. S. Aga, and L. L. Y. Voon, *Ab initio* simulations of silicene hydrogenation, Chem. Phys. Lett. **511**, 101 (2011).

[9] N. D. Drummond, V. Zólyomi, and V. I. Fal'ko, Electrically tunable band gap in silicene, Phys. Rev. B **85**, 075423 (2012).

[10] H.-R. Chang, J. Zhou, H. Zhang, and Y. Yao, Probing the topological phase transition via density oscillations in silicene and germanene, Phys. Rev. B **89**, 201411 (2014).

[11] C. J. Tabert and E. J. Nicol, Dynamical polarization function, plasmons, and screening in silicene and other buckled honeycomb lattices, Phys. Rev. B **89**, 195410 (2014).

[12] S. Trivedi, A. Srivastava, and R. Kurchania, Silicene and germanene: A first principle study of electronic structure and effect of hydrogenation-passivation, J. Comput. Theor. Nanosci. **11**, 781 (2014).

[13] K. Takeda and K. Shiraishi, Theoretical possibility of stage corrugation in Si and Ge analogs of graphite, Phys. Rev. B **50**, 14916 (1994).

[14] G. G. Guzman-Verri and L. C. Lew Yan Voon, Electronic structure of silicon-based nanostructures, Phys. Rev. B **76**, 075131 (2007).

[15] S. Cahangirov, M. Topsakal, E. Akturk, H. Sahin, and S. Ciraci, Two- and One-Dimensional Honeycomb Structures of Silicon and Germanium, Phys. Rev. Lett. **102**, 236804 (2009).

[16] D. Jose and A. Datta, Structures and chemical properties of silicene: unlike graphene, Acc. Chem. Res. **47,** 593 (2014).

[17] M. Houssa, G. Pourtois, V. V. Afanas'ev and A. Stesmans, Can silicon behave like graphene? A first-principles study Appl. Phys. Lett. **97,** 112106 (2010).

[18] S. Lebègue and O. Eriksson, Electronic structure of twodimensional crystals from *ab initio* theory, Phys. Rev. B **79**, 115409 (2009).

[19] L. C. Lew Yan Voon, E. Sandberg, R. S. Aga, and A. A. Farajian, Hydrogen compounds of group-IV nanosheets, Appl. Phys. Lett. **97**, 163114 (2010).

[20] H. H. Gurel, V. O. Ozcelik and S. Ciraci, Effects of charging and perpendicular electric field on the properties of silicene and germanene, J. Phys.: Condens. Matter **25**, 305007 (2013).

[21] W. F. Tsai, C. Y. Huang, T. R. Chang, H. Lin, H. T. Jeng and A. Bansil, Gated silicene as a tunable source of nearly 100% spin-polarized electrons, Nat. Commun. **4,** 1500 (2013).

[22] V. Vargiamidis, P. Vasilopoulos and G. Q. Hai, Dc and ac transport in silicene J. Phys.: Condens. Matter **26,** 345303 (2014).

[23] Y. C. Cheng, Z. Y. Zhu and U. Schwingenschlögl, Doped silicene: Evidence of a wide stability range, Eur. Phys. Lett. **95,** 17005 (2011).

[24] M. Ezawa, Valley-polarized metals and quantum anomalous Hall effect in silicene, Phys. Rev. Lett. **109,** 055502 (2012).

[25] L. C. Lew Yan Voon, E. Sandberg, R. S. Aga and A. A. Farajian, Hydrogen compounds of group-IV nanosheets Appl. Phys. Lett. **97,** 163114 (2010).

[26] M. Houssa, E. Scalise, K. Sankaran, G. Pourtois, V. V. Afanas'ev and A. Stesmans, Electronic properties of hydrogenated silicene and germanene Appl. Phys. Lett. **98,** 223107 (2011).

[27] R. Quhe, R. Fei, Q. Liu, J. Zheng H., Li, C. Xu, Z. Ni, Y. Wang, D. Yu, Z. Gao and J. Lu, Tunable and sizable band gap in silicene by surface adsorption, Sci. Rep. **2,** 853 (2012).

[28] Y. Ding and Y. Wang, Electronic structures of silicene fluoride and hydride, Appl. Phys. Lett. **100,** 083102 (2012).

[29] B. van den Broek, M. Houssa, E Scalise, G. Pourtois, V. V. Afanas'ev and A. Stesmans, Two-dimensional hexagonal tin: ab initio geometry, stability, electronic structure and functionalization Appl. Surf. Sci. **291,** 104 (2014).

[30] T. P. Kaloni, N. Singh and U. Schwingenschlögl, Prediction of a quantum anomalous Hall state in Co-decorated silicene, Phys. Rev. B **89,** 035409 (2014).

[31] B. Lalmi, H. Oughaddou, H. Enriquez, A. Kara, S. Vizzini, B. Ealet, and B. Aufray, Epitaxial growth of a silicene sheet, Appl. Phys. Lett. **97**, 223109 (2010).

[32] A. Bhattacharya, S. Bhattacharya, and G. P. Das, Exploring semiconductor substrates for silicene epitaxy, Appl. Phys. Lett. **103**, 123113 (2013).

[33] C. Léandri, H. Oughaddou, B. Aufray, J. M. Gay, G. Le Lay, A. Ranguis, and Y. Garreau, Growth of Si nanostructures on Ag(001), Surf. Sci. **601**, 262 (2007).

[34] A. Kara, C. Léandri, M. E. Dévila, P. De Padova, B. Ealet, H. Oughaddou, B. Aufray, and G. Le Lay, Physics of silicene stripes, J. Supercond. Novel Magn. **22**, 259 (2009).

[35] B. Aufray, A. Kara, S. Vizzini, H. Oughaddou, C. Léandri, B. Ealet, and G. Le Lay, Graphene-like silicon nanoribbons on Ag(110): A possible formation of silicene, Appl. Phys. Lett. **96**, 183102 (2010).

[36] P. De Padova, C. Quaresima, C. Ottaviani, P. M. Sheverdyaeva, P. Moras, C. Carbone, D. Topwal, B. Olivieri, A. Kara, H. Oughaddou, B. Aufray, and G. Le Lay, Evidence of graphenelike electronic signature in silicene nanoribbons, Appl. Phys. Lett. **96**, 261905 (2010).

[37] P. De Padova, P. Perfetti, B. Olivieri, C. Quaresima, C. Ottaviani, and G. Le Lay, 1D graphene-like silicon systems: Silicene nano-ribbons, J. Phys.: Condens. Matter **24**, 223001 (2012).

[38] P. Vogt, P. De Padova, C. Quaresima, J. Avila, E. Frantzeskakis, M. C. Asensio, A. Resta, B. Ealet, and G. Le Lay, Silicene: Compelling Experimental Evidence for Graphenelike Two-Dimensional Silicon, Phys. Rev. Lett. **108**, 155501 (2012).

[39] B. Feng, Z. Ding, S. Meng, Y. Yao, X. He, P. Cheng, L. Chen, and K. Wu, Evidence of silicene in honeycomb structures of silicon on Ag(111), Nano Lett. **12**, 3507 (2012).

[40] A. Fleurence, R. Friedlein, T. Ozaki, H. Kawai, Y. Wang, and Y. Yamada-Takamura, Experimental Evidence for Epitaxial Silicene on Diboride Thin Films, Phys. Rev. Lett. **108**, 245501 (2012).

[41] L. Meng, Y. Wang, L. Zhang, S. Du, R. Wu, L. Li, Y. Zhang, G. Li, H. Zhou, W. A. Hofer, and M. J. Gao, Buckled silicene formation on Ir(111), Nano Lett. **13**, 685 (2013).

[42] S. Sadeddine, H. Enriquez, A. Bendounan, P. K. Das, I. Vobornik, A. Kara, A. J. Mayne, F. Sirotti, G. Dujardin, and H. Oughaddou, Compelling experimental evidence of a Dirac cone in the electronic structure of a 2D silicon layer, Sci. Rep. **7**, 44400 (2017).

[43] C.-L. Lin, R. Arafune, K. Kawahara, N. Tsukahara, E. Minamitani, Y. Kim, N. Takagi, and M. Kawai, Structure of silicene grown on Ag(111), Appl. Phys. Express **5**, 45802 (2012).

[44] H. Jamgotchian, Y. Colignon, N. Hamzaoui, B. Ealet, J. Y. Hoarau, B. Aufray, and J. P. Biberian, Growth of silicene layers on Ag(111): Unexpected effect of the substrate temperature, J. Phys.: Condens. Matter **24**, 172001 (2012).

[45] Z. Majzik, M. R. Tchalala, M. Svec, P. Hapala, H. Enriquez, A. Kara, A. J. Mayne, G. Dujardin, P. Jelinek, and H. Oughaddou, Combined AFM and STM measurements of a silicene sheet grown on the Ag(111) surface, J. Phys.: Condens. Matter **25**, 225301 (2013).

[46] C. Grazianettia, D. Chiappe, E. Cinquanta, G. Tallarida, M. Fanciullia, and A. Molle, Exploring the morphological and electronic properties of silicene superstructures, Appl. Surf. Sci. **291**, 109 (2014); Z. L. Liu, M. X. Wang, J. P. Xu, J. F. Ge, G. Le Lay, P. Vogt, D. Qian, C. L. Gao, C. H. Liu, and J. F. Jia, Various atomic structures of monolayer silicene fabricated on Ag(111), New J. Phys. **16**, 075006 (2014).

[47] E. Scalise, E. Cinquanta, M. Houssa, B. van den Broek, D. Chiappe, C. Grazianetti, G. Pourtoisc, B. Ealet, A. Molle, M. Fanciulli, V. V. Afanas'ev, and A. Stesmans, Vibrational properties of epitaxial silicene layers on (111) Ag, Appl. Surf. Sci. **291**, 113 (2014).

[48] P. Moras, T. O. Mentes, P. M. Sheverdyaeva, A. Locatelli, and C. Carbone, Coexistence of multiple silicene phases in silicon grown on Ag(111), J. Phys.: Condens. Matter **26**, 185001 (2014).

[49] H. Enriquez, S. Vizzini, A. Kara, B. Lalmi, and H. Oughaddou, Silicene structures on silver surfaces, J. Phys.: Condens. Matter **24**, 314211 (2012).

[50] R. Arafune, C.-L. Lin, K. Kawahara, M. Kanno, N. Tsukahara, E. Minamitani, Y. Kim, N. Takagi, and M. Kawai, Structural transition of silicene on Ag(111), Surf. Sci. **608**, 297 (2013).

[51] K. Kawahara, T. Shirasawa, R. Arafune, C.-L. Lin, T. Takahashi, M. Kawai, and N. Takagi, Determination of atomic positions in silicene on Ag(111) by low-energy electron diffraction, Surf. Sci. **623**, 25 (2014).

[52] M. R. Tchalala, H. Enriquez, H. Yildirim, A. Kara, A. J. Mayne, G. Dujardin, M. Ait Ali, and H. Oughaddou, Atomic and electronic structures of the, $\left(\sqrt{13} \times \sqrt{13}\right)R30°$ of silicene sheet on Ag(111), Appl. Surf. Sci. **303**, 61 (2014).

[53] C.-L. Lin, R. Arafune, K. Kawahara, M. Kanno, N. Tsukahara, E. Minamitani, Y. Kim, M. Kawai, and N. Takagi, Substrate- Induced Symmetry Breaking in Silicene, Phys. Rev. Lett. **110**, 076801 (2013).

[54] Z.-L. Liu, M.-X. Wang, C. Liu, J.-F. Jia, P. Vogt, C. Quaresima, C. Ottaviani, B. Olivieri, P.De Padova, and G. Le Lay, The fate of the $\left(2\sqrt{3} \times 2\sqrt{3}\right)R30°$, silicene phase on Ag(111), APL Mater. **2**, 092513 (2014).

[55] H. Enriquez, A. Kara, A. J. Mayne, G. Dujardin, H. Jamgotchian, B. Aufray, and H. Oughaddou, Atomic structure of $\left(2\sqrt{3} \times 2\sqrt{3}\right)R30°$, the of silicene on Ag(111) surface, J. Phys.: Conf. Ser. **491**, 012004 (2014).

[56] J. Avila, P. De Padova, S. Cho, I. Colambo, S. Lorcy, C. Quaresima, P. Vogt, A. Resta, G. Le Lay, and M. C. Asensio, Presence of gapped silicene-derived band in the prototypical (3 × 3) silicene phase on silver (111) surfaces, J. Phys.: Condens. Matter **25**, 262001 (2013).

[57] A. Resta, T. Leoni, C. Barth, A. Ranguis, C. Becker, T. Bruhn, P. Vogt, and G. Le Lay, Atomic structures of silicene layers grown on Ag(111): Scanning tunneling microscopy and noncontact atomic force microscopy observations, Sci. Rep. **3**, 2399 (2013).

[58] H. Jamgotchian, Y. Colignon, B. Ealet, B. Parditka, J.-Y. Hoarau,C. Girardeaux, B. Aufray, and J.-P. Bibérian, Silicene on Ag(111): Domains and local defects of the observed superstructures, J. Phys.: Conf. Ser. **491**, 012001 (2014).

[59] L. Chen, C.-C. Liu, B. Feng, X. He, P. Cheng, Z. Ding, S. Meng, Y.Yao, and K.Wu, Evidence for Dirac Fermions in aHoneycomb Lattice Based on Silicon, Phys. Rev. Lett. **109**, 056804 (2012).

[60] Z.-X. Guo, S. Furuya, J. I. Iwata, and A. Oshiyama, Absence and presence of Dirac electrons in silicene on substrates, Phys. Rev. B **87**, 235435 (2013).

[61] Z.-X. Guo, S. Furuya, J. Iwata, and A. Oshiyama, Absence of Dirac Electrons in Silicene on Ag(111) Surfaces, J. Phys. Soc. Jpn. **82**, 063714 (2013).

[62] G. Le Lay, P. De Padova, A. Resta, T. Bruhn, and P. Vogt, Epitaxial silicene: can it be strongly strained?, J. Phys. D Appl. Phys. **45**, 392001 (2012).

[63] Wang Y.-P., and Cheng H.-P., Absence of a Dirac cone in silicene on Ag (111): First-principles density functional calculations with a modified effective band structure technique, Phys. Rev. B. **87**, 245430 (2013).

[64] S. K. Mahatha, P. Moras, V. Bellini, P. M. Sheverdyaeva, C. Struzzi, L. Petaccia, and C. Carbone, Silicene on Ag(111): A honeycomb latticewithout Dirac bands,Phys. Rev. B **89**, 201416 (2014).

[65] P. M. Sheverdyaeva, S. K. Mahatha, P. Moras, L. Petaccia, G. Fratesi, G. Onida, and C. Carbone, Electronic states of silicene allotropes on Ag(111), ACS Nano **11**, 975 (2017).

[66] P. De Padova, A. Generosi, B. Paci, C. Ottaviani, C. Quaresima, B. Olivieri, E. Salomon, T. Angot, and G. Le Lay, Multilayer silicene: clear evidence, 2D

Mater. **3**, 031011 (2016).

[67] C. Vacacela Gomez, M. Pisarra, M. Gravina, P. Riccardi, and A. Sindona, Plasmon properties and hybridization effects in silicene, Phys. Rev. B **95**, 085419 (2017).

[68] A. Sindona, M. Pisarra, C. Vacacela Gomez, P. Riccardi, G. Falcone, and S. Bellucci, Calibration of the fine-structure constant of graphene by time-dependent density-functional theory, Phys. Rev. B **96**, 201408(R) (2017).

[69] A. V. Generalov and Y. S. Dedkov, EELS study of the epitaxial graphene/Ni(111) and graphene/Au/Ni(111) systems, Carbon **50**, 183 (2012).

[70] A. Cupolillo, N. Ligato, and L. S. Caputi, Two-dimensional character of the interface π plasmon in epitaxial graphene on Ni(111), Carbon **50**, 2588 (2012); M. Pisarra, P. Riccardi, A. Cupolillo, A. Sindona, and L. S. Caputi, Studies of electron emission in the interaction of electrons with graphene on Ni(111) surface, Nanosci. Nanotechnol. Lett. **4**, 1100 (2012);
M. Pisarra, P. Riccardi, A. Sindona, A. Cupolillo, N. Ligato, C. Giallombardo, and L. Caputi, Probing graphene interfaces with secondary electrons, Carbon **77**, 796 (2014); A. Cupolillo, M. Pisarra, A. Sindona, M. Commisso, and P. Riccardi, Electron excitation in the interaction of slow ions and electrons with metals and monolayer graphite on Ni(111) surfaces, Vacuum **84**, 1029 (2010); M. Commisso, A. Bonanno, A. Oliva, M. Camarca, F. Xu, P. Riccardi, and R. A. Baragiola, Plasmon excitation and electron promotion in the interaction of slow Na$^+$ ions with Al surfaces, Nucl. Instrum. Methods Phys. Res., Sect. B **230**, 438 (2005).

[71] T. Eberlein, U. Bangert, R. R. Nair, R. Jones, M. Gass, A. L. Bleloch, K. S. Novoselov, A. Geim, and P. R. Briddon, Plasmon spectroscopy of free-standing graphene films, Phys. Rev. B **77**, 233406 (2008).

2 PtTe$_2$

2.1 Introduction

Recently, the PtX$_2$ (X = Se, Te, S) class of transitionmetal dichalcogenides (TMDCs) has attracted a huge interest from the scientific community. This class of TMDCs combines promising application capabilities along with the fundamental physics interest arising from the existence of topological type-II Dirac fermions [1-9]. As opposed to type-I Dirac materials, which have a closed Fermi surface with either an electron or a hole pocket, type-II Dirac materials have an unbounded Fermi surface with both electron and hole pockets [3]. The presence of a bulk topological Dirac node leads to the existence of surface states as well. These surface states are robust against perturbations and have interesting physical properties [10,11].

Thin layers of the PtX$_2$ class of materials are equally interesting due to their relatively higher mobility, and superior gas sensing properties, among others [2, 12-16]. The quantum confinement effect dramatically changes the properties of the thin layers of PtTe$_2$ which undergo a metal-semiconductor transition with decreasing thickness [17,18]. Apart from this, the monolayer exhibits a unique property: because of the local dipole-induced Rashba effect, opposite spins with the same energy get spatially separated on opposite sides of the monolayer [19]. This is known as spin layer locking and it can have potential applications in electrically tunable spintronic devices.

Preceding discussions made it clear that the PtX$_2$ class of materials has emerged as promising for future electronics. While the band structure of PtTe$_2$ has been explored comprehensively [5], along with the Dirac plasmons in the infrared range of the electromagnetic spectrum, the high-energy excitations in PtTe$_2$ still remain unexplored. The comprehension of the excitation spectrum of collective modes in the visible-ultraviolet range is crucial to devise broadband photodetectors [21,22], ultraviolet-imaging applications [23], and broadband plasmonic devices [24,25]. Monolayer PtTe$_2$ has the smallest energy band gap in the PtX$_2$ class of materials [26], offering it an advantage over the other members for applications in nanoelectronics.

2.2 Stucture of Bulk TMDCs

Layered TMDCs have the generic formula MX$_2$, where M stands for a metal and X represents a chalcogen. The interatomic interaction within layers is covalent in nature, while the layers are held together by weak van der Waals (vdW) forces. The presence of the latter allows the crystals to cleave easily similar to graphene.

The structure of a typical layered TMDC is shown in Figure 2.1. In this structure, each layer consists of three atomic planes with a typical thickness of 6–7Å with a hexagonally packed plane of metal atoms sandwiched between two planes of chalcogen atoms. In some cases, the hexagonal in-plane geometry of metal ions is distorted and the layers are not planar. In TMDCs, the metal atoms provide four electrons to fill the bonding states and the transition metal and chalcogens can be ascribed a formal charge of +4 and −2, respectively [27]. As a result, the coordination around chalcogenides is lopsided, which leads to the marked cleavage properties perpendicular to the hexagonal/trigonal symmetry axis [28].
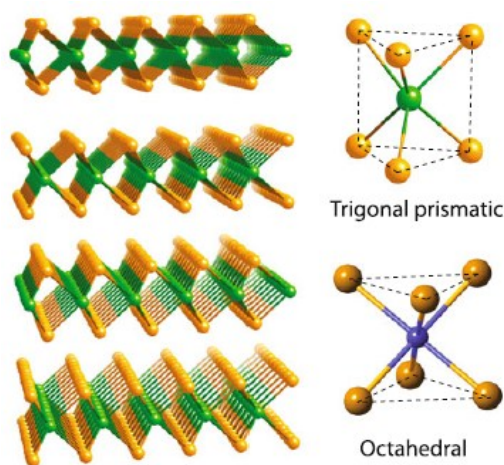
Figure 2.1. Three-dimensional representation of a typical layered MX$_2$ structure, with the metal atoms shown in green and the chalcogen atoms shown in orange (left panel) [29]. The local coordination of the metal species can be of the two types shown in the right panel, viz., trigonal prismatic (top) and octahedral (bottom).

The absence of dangling bonds makes the surfaces very stable and non-reactive. Metal atoms within a triple layer are six-fold coordinated and their bonding geometry can be either trigonal prismatic or octahedral (Figure 2.1). Note that in the trigonal prismatic arrangement the two chalcogenide planes forming a slab are stacked directly above each

other, while in the octahedral arrangement they stagger. The preferred phase adopted by TMDCs depends predominantly on the *d*-electron count of the transition metals, although a certain dependence on the relative size of the atoms plays a role. Group IV metals all have octahedral structures. Most of group V metals also have octahedral structures, while some have trigonalprismatic structures; the reverse is true for the group VI metals. In group VII one finds again octahedral structures, although in this case they are distorted.

TMDCs are usually found in three polymorphs called 1*T*, 2*H* and 3*R* where the numbers stand for the number of layers in the unit cell and the letters indicate symmetry (T: trigonal, H: hexagonal, and R: rhombohedral).

The 1*T* polytype is constructed by piling up single layers, where each subsequent layer is exactly the same as the previous one, with one transition metal atom (or chalcogen atom) located on top of another transitionmetal atom (or chalcogen atom), in an octahedral coordination. In bulk TMDC, the stacking of the 1*T* polytype is /AbC/AbC and it belongs to the $P\bar{3}m1$ symmorphic space group. The unit cell comprises three atoms.

The 2*H* bulk polytype can assume two major forms with different stacking symmetries: 2*Ha* (or /AbA CbC/ stacking), and 2*Hc* (/CaC AcA/ stacking). Both polytypes belong to the nonsymmorphic hexagonal space group $P6_3/mmc$ [28] (or D_{6h}^4 in Schönflies notation). The primitive unit cell for the bulk has six atoms.

The reciprocal space high-symmetry points and directions for the 2*H* and 1*T* polytypes are shown in Figure 2.2.
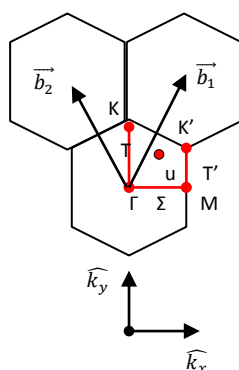
Figure 2.2. The Brillouin zone symmetries: *Γ*, *K*, *K'*, and *M* are high-symmetry points; *T*, *T'*, and *Σ* are high-symmetry lines, and *u* denotes the symmetry for a generic point [30]. $\vec{b_1}$ and $\vec{b_2}$ denote the in-plane reciprocal lattice vectors.

Considering that $\vec{a_1}$ and $\vec{a_2}$ are the primitive vectors of the real 2D lattice described by 2.1, the reciprocal vectors $\vec{b_1}$ and $\vec{b_2}$ are described by 2.2 and shown in Figure 2.2.

$$\vec{a_1} = \frac{a}{2}\left(\sqrt{3}\hat{x} + \hat{y}\right) \quad \vec{a_2} = \frac{a}{2}\left(-\sqrt{3}\hat{x} + \hat{y}\right) \tag{2.1}$$

$$\vec{b_1} = \frac{2\pi}{a}\left(\frac{\sqrt{3}}{3}\hat{k}_x + \hat{k}_y\right) \quad \vec{b_2} = \frac{2\pi}{a}\left(-\frac{\sqrt{3}}{3}\hat{k}_x + \hat{k}_y\right) \tag{2.2}$$

2.3 Electronic properties

Dirac and Weyl fermions were originally introduced in high-energy physics [31]. Their counterparts in condensed matter physics have been realized in three-dimensional (3D) Dirac and Weyl semimetals. Such topological semimetals exhibit a rich variety of novel phenomena, such as negative magnetoresistance (MR) [32–34], chiral magnetic effects [35], and the quantum anomalous Hall effect [36]. Dirac and Weyl semimetals can be classified into type I and type II, depending on whether the Lorentz invariance is preserved or not. For type-I Dirac [37,38] and Weyl semimetals [39–41], massless Dirac fermions with linear dispersions are expected at the Dirac or Weyl points. However, type-II Dirac and Weyl fermions [3] emerge at the topologically protected touching points of electron and hole pockets, and they show highly tilted Dirac cones along certain momentum directions (Figure 2.3), thus breaking the Lorentz invariance [42–44].
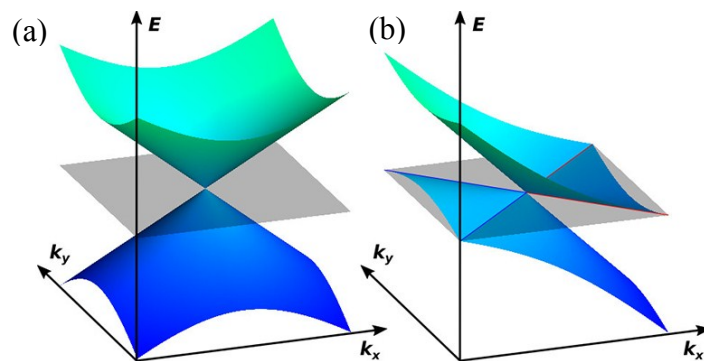
Figure 2.3. Possible types of Dirac semimetals [3]. (a**)** Type-I with a point-like Fermi surface. (b**)** A type-II Dirac point appears as the contact point between electron and hole pockets. The *grey plane* corresponds to the position of the Fermi level, and the *blue* (*red*) *lines* mark the boundaries of the hole (electron) pockets.

While type-I Dirac and Weyl semimetals exhibit negative magnetoresistance along all directions, the magnetoresistance properties of type-II semimetals are expected to be extremely anisotropic due to the anisotropic electronic structure, and negative magnetoresistance is expected only along certain momentum directions where the cones are not tilted enough to break the Lorentz invariance [3,45,46]. A Dirac semimetal can be tuned to a Weyl semimetal or topological crystalline insulator when the crystal symmetry or time-reversal symmetry is broken [47,48], and therefore they are ideal candidates for investigating topological phase transitions and potential device applications.

Experimentally, type-II Dirac fermions have been found in PtTe$_2$ [3,5], PtSe$_2$ [6], and PdTe$_2$ [5,7] by angle-resolved photoemission spectroscopy (ARPES) experiments reporting anisotropic and tilted Dirac cones.

ARPES spectrum of bulk PtTe$_2$ taken along the high-simmetry direction M-Γ-K of the BZ is shown in Figure 2.4(a) [3]. The main focus of the authors was to study the evolution of the conical dispersion centered at the Γ point with the out-of-plane momentum k$_z$. A conical dispersion is observed when the phonon energy was $\hbar\omega = 22eV$ (k$_z$ = 3.5c* (c*=2π/c)). The dispersion shows a pair of strongly tilted Dirac cones along the Γ-A direction confirming PtTe$_2$ as a type-II Dirac [Figure 2.4(b)].
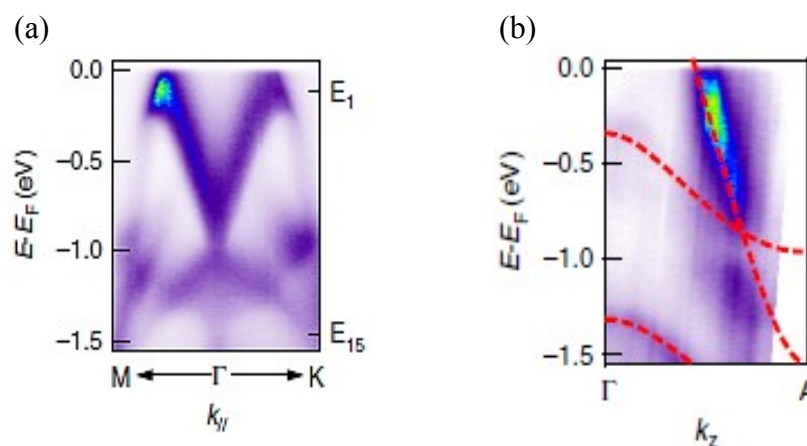
Figure 2.4. ARPES spectra of bulk PtTe$_2$ [3]. (a) In-plane Dirac cone along the M-Γ-K direction. (b) Measured dispersion at k$_\parallel$ = 0; red broken lines are calculated dispersions for comparison.

Another interesting ARPES study was performed on PtSe$_2$ [6]. To reveal the 3D Dirac cone, the dispersions around k$_\parallel$ = 0 at different k$_z$ were measured using different photon energies. A conical dispersion is observed along the in-plane directions parallel to the Γ-K [Figure 2.5(a)] and Γ-M [Figure 2.5(b)] at k$_z$ = 0.37c* ($\hbar\omega$ = 23.5 eV) of the reduced BZ. Along the out-of-plane direction [Figure 2.5(c)] the dispersion shows highly tilted Dirac cone. The band dispersions of PtSe$_2$ are similar to those of PtTe$_2$, except that the Dirac points are slightly different energies and at different k$_z$ values that are attributed to the different lattice constants. This observations were also supported by first-principles calculations.
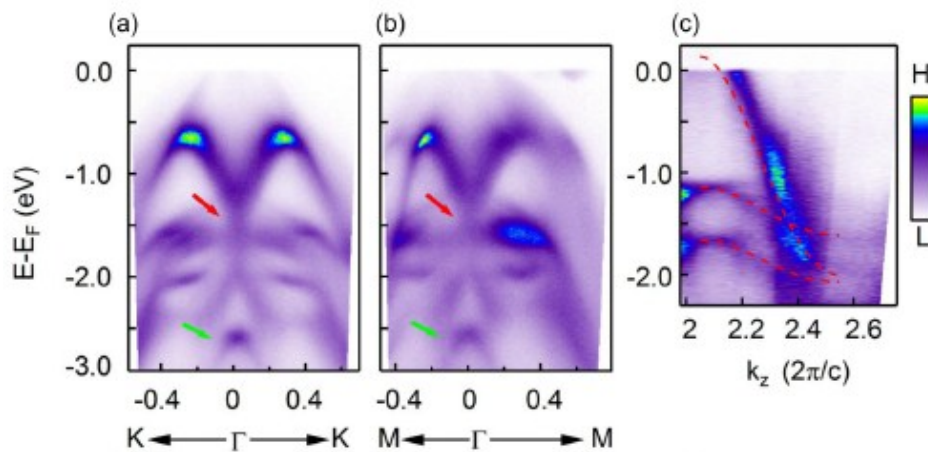
Figure 2.5. PtSe$_2$ band dispersions along the (a) Γ-K and (b) Γ-M directions at k$_z$ = 0.37c*. (c) k$_z$ dispersions of PtSe$_2$ measured at k$_\parallel$= 0 [6].

ARPES measurements on PdTe$_2$ were carried out by Noh et al. [7]. In this study by combining angle-resolved photoemission spectroscopy and ab initio band calculations the authors reported the experimental discovery of type-II Dirac fermions in PdTe$_2$. The k$_z$ scan suggests that the type-II Dirac point can be caught when $\hbar\omega$ = 61 eV photons (k$_z$ = 3.6c*) are used as shown in Figure 2.6.

In the prospect of plasmonic devices based on 3D Dirac fermions, the possibility of using a few layers exfoliated from a parental layered bulk crystal as active channels in nanodevices [49] is crucial. Unfortunately, PtSe$_2$ fails to fulfil this prerequisite. By

contrast, PtTe$_2$ can be grown as bulk crystals with superb crystalline quality and it can be easily exfoliated.
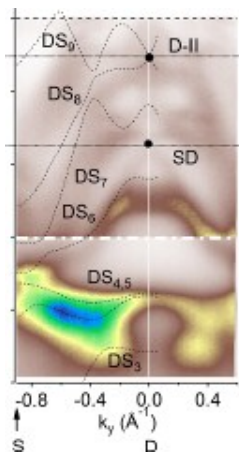
Figure 2.6. ARPES image along the D-S line (k$_z$ = 3.6c*) obtained by summing two ARPES images [7]. The dotted curves are calculated bulk bands along the same line.

Recently, Politano et al. [50] identified the collective excitations of type-II Dirac fermions (3D Dirac plasmons) in PtTe$_2$ single crystals by means of high-resolution electron energy loss spectroscopy and density functional theory. The observed plasmon energy in the long-wavelength limit is ~0.5 eV [Figure 2.7 (a)], which makes PtTe$_2$ suitable for near-infrared optoelectronic applications. The authors, also demonstrated that interband transitions between the two Dirac bands in PtTe$_2$ give rise to additional excitations at ~1 and ~ 1.4 eV [Figure 2.7 (b)]. This results offer useful insights regarding the dielectric properties of type-II DSMs. The comprehension of their excitation spectrum is crucial for the promising prospect of plasmonic devices based on PtTe$_2$ single crystals, which are also cleavable, due to the weak van der Waals interlayer bonds, with subsequent ease for the nanofabrication process.
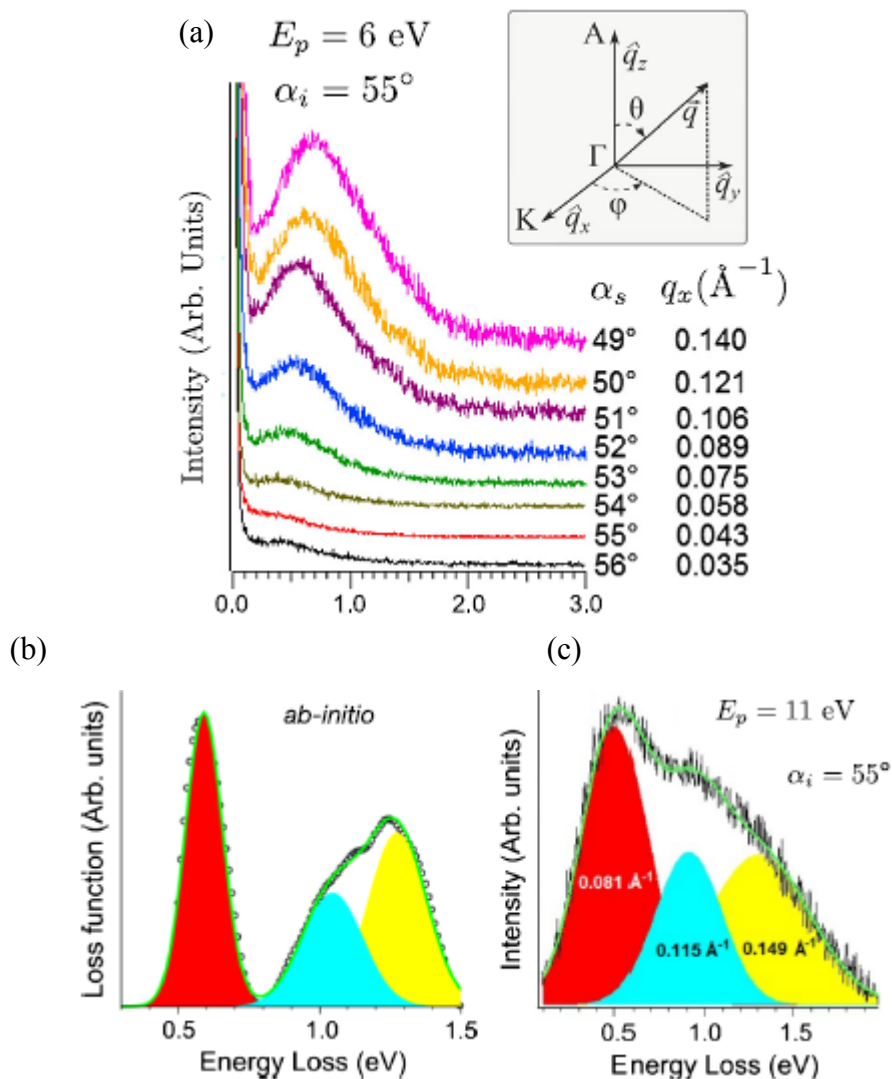
Figure 2.7. (a) HREELS spectra, acquired for E$_p$ =6 eV as a function of the scattering angle [50]. (b) Ab initio loss function for the selected case of q = 0.026 Å−1 along the Γ − K direction. (c) HREELS spectrum recorded for a higher value of impinging energy (Ep = 11 eV), enabling the observation of three well separated spectral components.

2.4 Synthesis: from 3D to 2D

Two-dimensional TMDCs can be fabricated using two types of approaches: the top-down approach, where the bulk forms are exfoliated into a few-layer structures and monolayers (MLs), and the bottom-up approach using growth methods such as chemical vapour deposition (CVD) or molecular epitaxy.

2.4.1 Top-down method

Mechanical exfoliation is the most efficient way to produce the cleanest, highly crystalline and atomically thin nanosheets of layered materials. In a typical mechanical exfoliation process, appropriate thin TMDC crystals are first peeled off from the bulk crystal by using an adhesive Scotch-tape. These freshly cleaved thin crystals on the Scotch-tape are brought into contact with a target substrate and rubbed to further cleave them. After the Scotch-tape is removed, single layer and multilayer TMDC nanosheets are left on the substrate. While this method produces single-crystal flakes of high purity and cleanliness that are suitable for fundamental characterization and even for fabrication of individual devices, it is not scalable and does not allow systematic control of flake thickness and size. Therefore, this technique is not feasible for large-scale production of TMDCs monolayers for technological applications.

As a way to exfoliate large-area monolayers, it was proposed to make use of chemically enhanced adhesion. The use of chemical affinity of sulphur atoms that can bind to a gold surface more strongly that to neighbouring layers, single layers of various vdW bonded chalcogenides, such as MoS$_2$, WSe$_2$ and Bi$_2$Te$_3$ with lateral sizes of several hundreds of microns were successfully exfoliated [51].

Liquid exfoliation by direct ultrasonication was also employed to fabricate single-layer and multilayer nanosheets of a number of layered TMDCs, such as MoS$_2$, WS$_2$, MoSe$_2$, NbSe$_2$, TaSe$_2$, MoTe$_2$, MoTe$_2$ and others [52, 53], where the authors initially sonicated commercial powders in a number of solvents with varying surface tensions; the resultant dispersions were centrifuged. Successful solvents were those with dispersive, polar, and H-bonding components of the cohesive energy density within certain well-defined ranges. Some of the more promising solvents were N-methylpyrrolidone and isopropanol. Using this method, the exfoliated nanosheets have to be stabilized against re-aggregation either by solvation or by steric or electrostatic repulsion due to the adsorption of molecules from solution. This method allowed the authors to prepare films of BN, MoS$_2$, and WS$_2$ by vacuum filtration or spraying, with thicknesses ranging from a few nanometers to hundreds of micrometers.

Ion intercalation, such as lithium-intercalation or ultrasound-promoted hydration, is another approach, allowing fabrication of single-layer materials. The intercalation of

TMDCs by ionic species [54, 55] allows the layers to be exfoliated in liquid. The typical procedure involves submerging bulk TMDC powder in a solution of a lithium-containing compound such as *n*-butyllithium for a relatively long time (days) to allow lithium ions to intercalate, which is followed by exposure of the intercalated material to water. The water reacts with the lithium between the layers; the process results in the formation of H$_2$ gas, which serves to separate the layers [54, 55]. Such chemical exfoliation methods allows one to produce significant quantities of submicrometre-sized monolayers [56], but the resulting material differs structurally and electronically from the source bulk. Lithium-based chemical exfoliation has been demonstrated for various TMDCs, in particular MoS$_2$, WS$_2$, MoSe$_2$ and SnS$_2$ [57, 58]. This method was also used to exfoliate topological insulators such as Bi$_2$S$_3$ and Bi$_2$Te$_3$ [59]. An effective method for mass production of exfoliated TMD nanosheets is the ultrasound-promoted hydration of lithium-intercalated compounds. An alternative method of lithiation that uses an electrochemical cell with a lithium foil anode and TMDC-containing cathode was demonstrated for MoS$_2$, WS$_2$, TiS$_2$, TaS$_2$, ZrS$_2$ and graphene [60], and then extended for BN, NbSe$_2$, WSe$_2$, Sb$_2$Se$_3$ and Bi$_2$Te$_3$ [61]. Because the intercalation occurs while a galvanic discharge is occurring in the electrochemical cell, the degree of lithiation can be monitored and controlled. The resulting Li-intercalated material is exfoliated by ultrasonication in water as before, yielding monolayer TMDC nanosheets.

2.4.2 Bottom-up method

Developing methods for synthesizing large-area and uniform layers is an important step for applications such as wafer-scale fabrication of electronic devices and flexible, transparent optoelectronics. As previously demonstrated for graphene, the development of wafer-scale synthesis methods via chemical vapour deposition (CVD) on metal substrates [62] and epitaxial growth on SiC substrates [63] has enabled large-scale device fabrication [64–66].

Some CVD methods for growing atomically thin films of MoS$_2$ on insulating substrates have recently been reported [67–69]. These methods use different solid precursors

heated to high temperatures: sulphur powder and MoO$_3$ powder vaporized and co-deposited onto a nearby substrate [67,70]; a thin layer of Mo metal deposited onto a wafer heated with solid sulphur [68]; and substrates dip-coated in a solution of (NH$_4$)$_2$MoS$_4$ and heated in the presence of sulphur gas [69]. In many of these methods, the final MoS$_2$ film thickness is dependent on the concentration or thickness of the initial precursor, although precise control of the number of layers over a large area has not yet been achieved. CVD growth of MoS$_2$ has also been demonstrated using previously CVD-grown graphene on Cu foil as a surface template, resulting in single-crystal flakes of MoS$_2$ several micrometres in lateral size [71].

Chemical preparation of MoS$_2$ [71] and MoSe$_2$ [73] have also been demonstrated using hydrothermal synthesis (that is, growth of single crystals from an aqueous solution in an autoclave at high temperature and pressure). Matte et al. [74,75] have described a number of methods to synthesize WS$_2$, MoS$_2$, WSe$_2$ and MoSe$_2$, including the reaction of molybdic or tungstic acid with either thiourea or selenourea at elevated temperatures to give the corresponding layered TMDC material [74,75]. Such methods give reasonably good-quality material with typical flake sizes of hundreds of nanometres to a few micrometres, although the flake thickness is not conclusively shown to be monolayers.

2.5   Structure of single layers

Monolayers of TMDCs have only two polymorphs, trigonal prismatic and octahedral phases (Figure 2.8). The former belongs to the D$_{3d}$ point group and the latter belongs to the D$_{3d}$ point group. Another important change upon 3D to 2D transition is the disappearance of inversion symmetry (present in films with an even number of layers). It is explicitly broken in films with an odd number of layers, with concomitant effects on the material's properties such as second harmonic generation and polarised photoluminescence. It should also be noted that, similar to graphene, monolayer TMDCs are not flat but possess ripples that may reach 6–10Å in height [76]. When prepared by dry methods such as Scotch-tape exfoliation or ultrasonication of the bulk material in an appropriate organic solvent, which has also been reported as a simple

approach to exfoliation for a number of layered compounds [77], the yield of single layers is typically low, but the crystal structure of the bulk-2*H* exfoliated layers remains essentially undisturbed during the process.
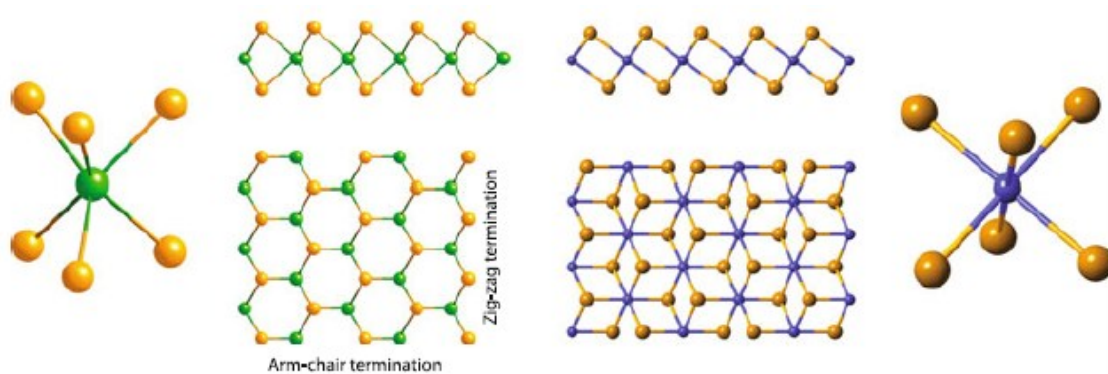
Figure 2.8. Side and top views of the two polymorphs of monolayer TMDCs [29]. Left panel trigonal prismatic (2H); right panel octahedral (1T). Chalcogen atoms are shown in orange and metal atoms are shown in green (blue).

Layered transition metal dichalcogenides can also be efficiently exfoliated via alkali metal, e.g. lithium, intercalation and subsequent addition of excess water which leads to hydrogen formation and forced separation of the layers [78, 79]. This process results in exfoliated layers being in a metastable phase [80]. It is believed that the electron transfer from Li during intercalation causes a change in the electron count from d_2 to d_3, leading to destabilization of the original crystal structure resulting in a change in the metal coordination from trigonal prismatic (2*H*) to octahedral geometry (1*T*) [81, 82].

2.6 Broadband excitation spectrum of bulk crystals and thin layers of PtTe$_2$

2.6.1 Sample preparation

The single crystals of PtTe$_2$ used in this work were prepared at the National Cheng Kung University, (Taiwan) by the self-flux method. High-purity Pt (99.99%) foil and Te ingot (99.9999%) were mixed in the ratio of 1:17 and wrapped in a quartz tube under vacuum. The quartz tube was heated to 1000 °C, dwelled there for 8 h, and slowly

cooled at a rate of 3–5 °C/h to 500 °C. Successively, the excess Te flux was separated by centrifugation. The resulting crystals have typical dimensions of $8 \times 8 \times 1$ mm [13] with the c axis perpendicular to the plates and can be easily cleaved. The structure of the grown crystals was examined by x-ray diffraction (XRD) [Appendix A.6] using Cu $K\alpha$ radiation and Laue diffraction at room temperature.

Bulk PtTe$_2$ belongs to the large family of $1T$–metal dichalcogenides with CdI$_2$-type crystal structure [space group $P\bar{3}m1$].
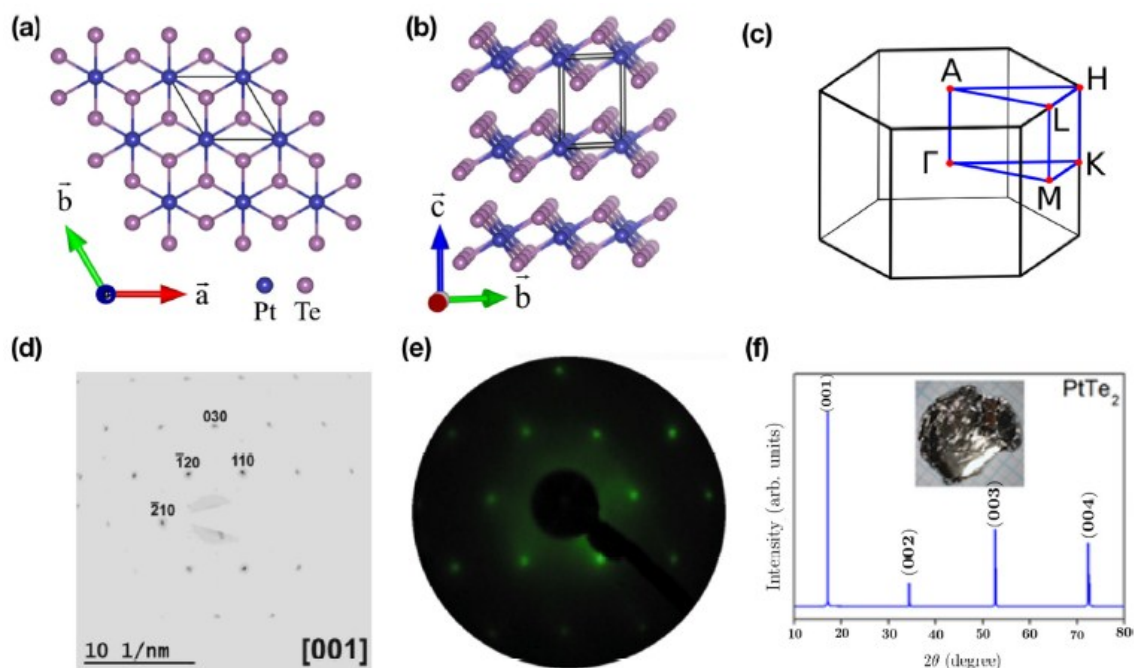
Figure 2.9. Panels (a) and (b) show the top and side views of the atomic crystal structure of PtTe$_2$. The corresponding bulk Brillouin zone of the hexagonal PtTe$_2$ crystal, along with various high-symmetry points is shown in (c). (d) SAED patterns acquired on PtTe$_2$ flakes match with [0001]-oriented single-crystal trigonal PtTe$_2$. (e) LEED pattern of bulk PtTe$_2$ single crystal oriented along the (0001) direction. (f) XRD pattern of (0001)-oriented planes of PtTe$_2$.

The bulk structure can be viewed as a collection of isolated monolayers stacked in the out-of-plane direction [Figures 2.9(a), (b)].

In each of these monolayers there are three sublayers, Te-Pt-Te, where the central Pt atom is strongly bonded with six neighboring Te atoms forming a hexagonal honeycomb structure. Both selected-area electron diffraction (SAED) and LEED patterns shown in Figures 2.9(d) and 2.9(e) match with [0001]-oriented flakes and bulk PtTe$_2$, respectively. This orientation is the one characterizing most of the regions probed

by transmission electron microscopy (TEM) and used to extract information for the current work. Correspondingly, the XRD pattern only exhibits (00n) peaks as shown in Figure 2.9(f).

To demonstrate cleanliness, the surface of the single crystal has been characterized by means of vibrational spectroscopy and x-ray photoelectron spectroscopy, without finding any contamination (Figure 2.10). Once prepared in ultrahigh vacuum, the surface remains uncontaminated for a timescale of several weeks, thus ensuring sample stability. The LEED pattern shows sharp spots against a low background [Figure 2.9(e)].
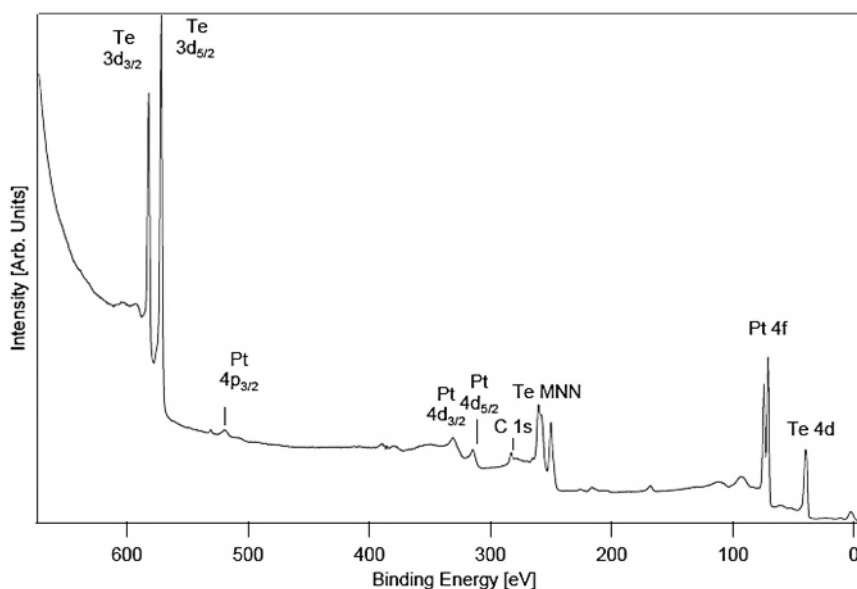
Figure 2.10. XPS spectrum of PtTe$_2$.

2.6.2 Broadband spectrum of bulk PtTe$_2$

The reflection EELS experiments were performed at room temperature by means of an EELS apparatus with two 50-mm hemispherical deflectors for both monochromator and analyzers, mounted in an ultrahigh-vacuum chamber (described in the 1.4 section). The primary electron beam was used with an incident angle θ_i of 43° with respect to the surface normal, along the Γ-K direction of the surface Brillouin zone. The primary

electron beam energy was Ep = 100 eV. The experimental broadband EELS spectra of the PtTe$_2$ bulk sample is shown in Figures 2.11(a)–2(c). The broadband EELS spectrum shows distinctly resolved peaks at energies ~0.5, ~1.4, ~3.9, ~7.5, and ~19.0 eV, among others.
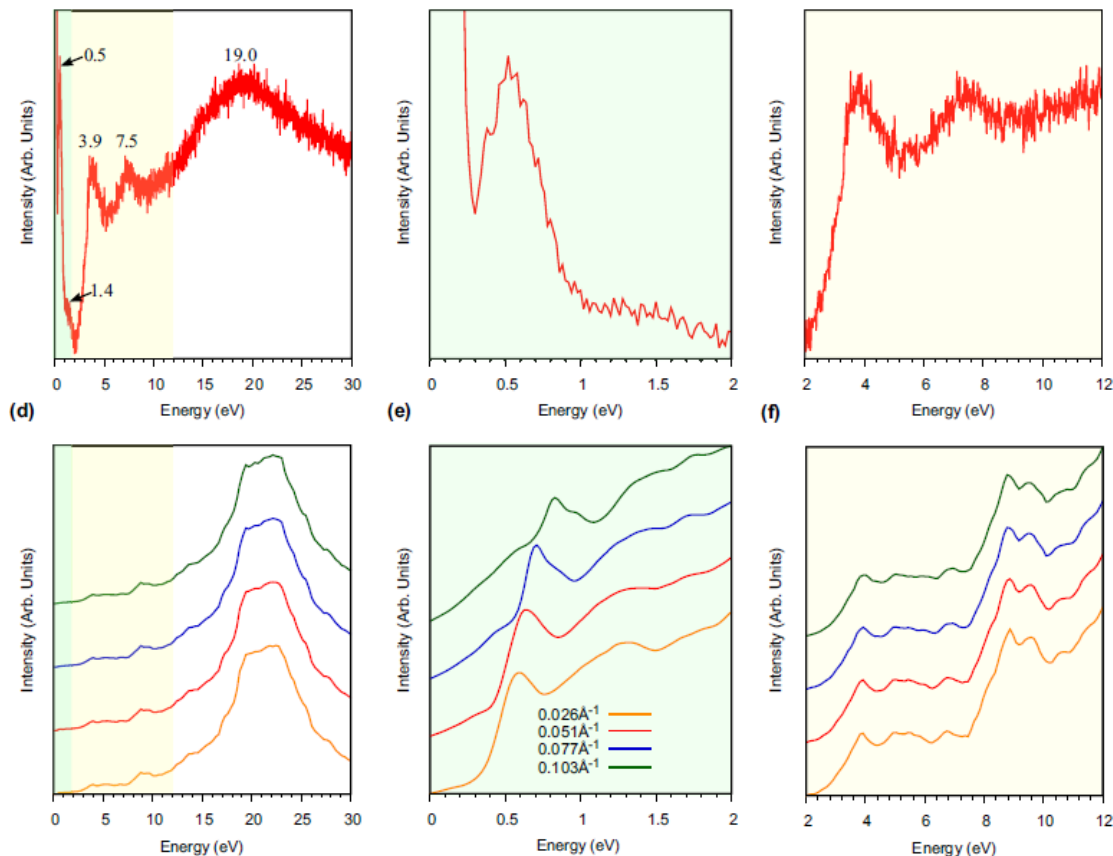
Figure 2.11. (a) Broadband EELS spectrum for bulk PtTe$_2$ measured in reflection mode with a primary electron beam energy of 100 eV. The EELS spectrum shows several distinct peaks at energies 0.5, 1.4, 3.9, 7.5, and 19.0 eV, which are highlighted in (b) and (c). The experimental broadband EELS spectrum is also reasonably captured by the loss function obtained from *ab initio* calculations, as shown in (d)–(f) for different momentum values, reported in the legend of panel (e). The 19.0 eV peak in (d) has the highest intensity in experiment as well as the *ab initio* calculations. The other dominant intraband peaks at 3.9 and 7.5 eV are resolved in panel (f).

The lowest-energy peak at 0.5 eV is the intraband gapped three dimensional (3D) Dirac plasmon excitation in bulk PtTe$_2$, which disperses with momentum [Figure 2.11(e)] [50]. In this thesis, the focus was on the remaining interband excitations, which are relatively less dispersive compared to the intraband 3D Dirac plasmon peak. It was

found that their peak location and relative intensity are nearly independent of the scattering geometry and, consequently, of the momentum in the range of k~0.0–0.2 Å^{-1}.

The theoretical loss function in Figures 2.11(d)–(f) captures the qualitative features of the experimental excitation spectrum reasonably well. Note that the spectral amplitudes of the theoretical and experimental peaks cannot be directly compared, as the experimental features in the reflection mode EELS depend on the energy of the primary electron beam. This was shown explicitly for the case of Sb$_2$Te$_3$ recently, for which the calculated intensities were found to match with the EELS spectrum acquired in the transmission mode, and only for very high value of the impinging electron energies (~500 eV) in the reflection mode [83–85].

In order to identify the interband transitions corresponding to the observed peaks in the EELS spectrum, the orbital-resolved density of states (DOS) are showed in Figures 2.12(a) and 2.12(b).

(a)   (b)
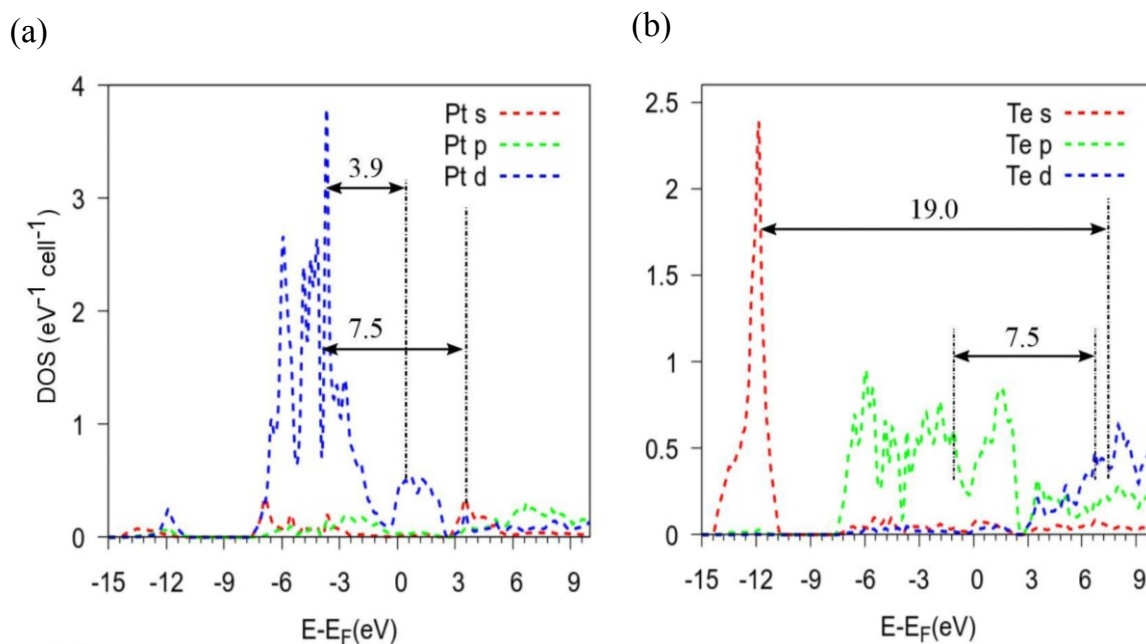
Figure 2.12. Orbital-resolved density of states corresponding to (a) Pt orbitals and (b) Te orbitals. The dominant transitions, corresponding to the observed EELS peaks, are marked by arrows.

The corresponding orbital-resolved band-structure plot is shown in Figure 2.13. The energetically lower valence band is situated approximately between −15 and −10 eV and it is mostly dominated by Te$_{5s}$ states. The upper valence band extends from

−7 eV up to the Fermi level and mostly comprises Pt$_{5d}$ and Te$_{5p}$ orbitals. The lower conduction-band states until ∼3 eV are also primarily formed by Pt$_{5d}$ and Te$_{5p}$ orbitals. The conduction-band states at higher energy have contributions mainly from the Pt$_{6p}$ and Te$_{5d}$ orbitals. A comparison of the orbital-resolved DOS with the observed spectral features in the broadband EELS spectrum allowed to identify the prominent states involved in the transitions. It was found that the peaks at 3.9, 7.5, and 19.0 eV are predominantly connected to Pt$_{5d}$ → Pt$_{5d}$, Te$_{5p}$ → Te$_{5d}$, and Te$_{5s}$ → Te$_{5d}$ transitions, respectively, as marked by arrows in Figures 2.12(a) and 2.12(b).
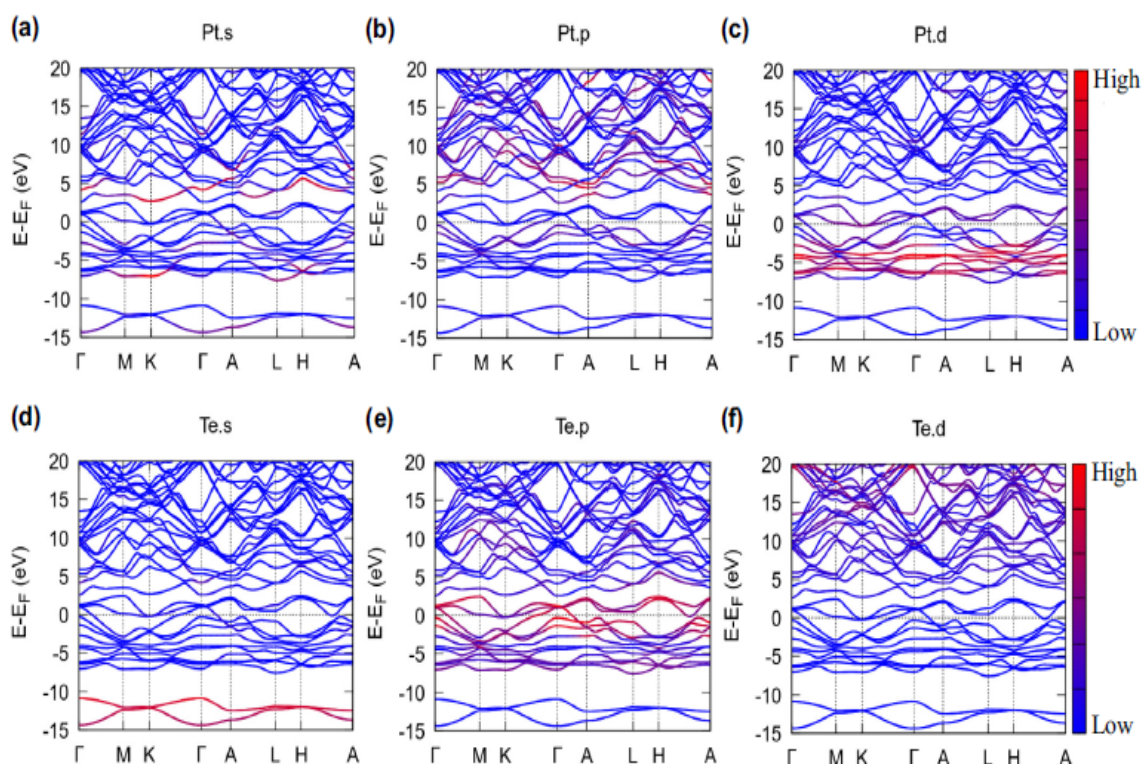
Figure 2.13. Orbital-projected band structure of PtTe$_2$. The lowest energy states are dominated by the Te$_{5s}$ orbital. Near the Fermi energy the states have major contributions from the Pt$_{5d}$ and Te$_{5p}$ orbitals. The higher energy states are mostly Pt$_{6p}$ and Te$_{5d}$ states.

2.6.3 Broadband spectrum of thin PtTe$_2$ layers

Having discussed the EELS spectrum of the bulk PtTe$_2$ crystal, now it is possible to proceed to discuss the EELS spectrum of thin PtTe$_2$ layers employing the STEM-EELS technique, which affords the spatial resolution necessary to identify regions with

different thickness within the flakes. High-angle annular dark-field-scanning transmission electron microscopy (HAADF-STEM) [Appendix A.3] and scanning transmission electron microscopy EELS (STEM-EELS) analyses were carried out at the Italian Institute of Technology (IIT).

Samples for TEM analyses were prepared by drop casting of the flakes dispersion onto a holey carbon-coated Cu grid. The EELS spectra were collected from flakes regions suspended on holes in the carbon support film. From the same spectra, the local thickness was evaluated using the log-ratio method [86]. The estimated inelastic free path through PtTe$_2$ in these conditions is $\lambda \approx 78$ nm. For these experiments a primary electron beam energy Ep = 200 keV and a collection angle of 13 mrad were used. As shown in Figure 2.14(a), the liquid phase exfoliation of PtTe$_2$ has produced flakes with inhomogeneous thickness. Therefore, for STEM-EELS experiments, different thicknesses [Figure 2.14(b)] were probed on different areas of the same fragments.
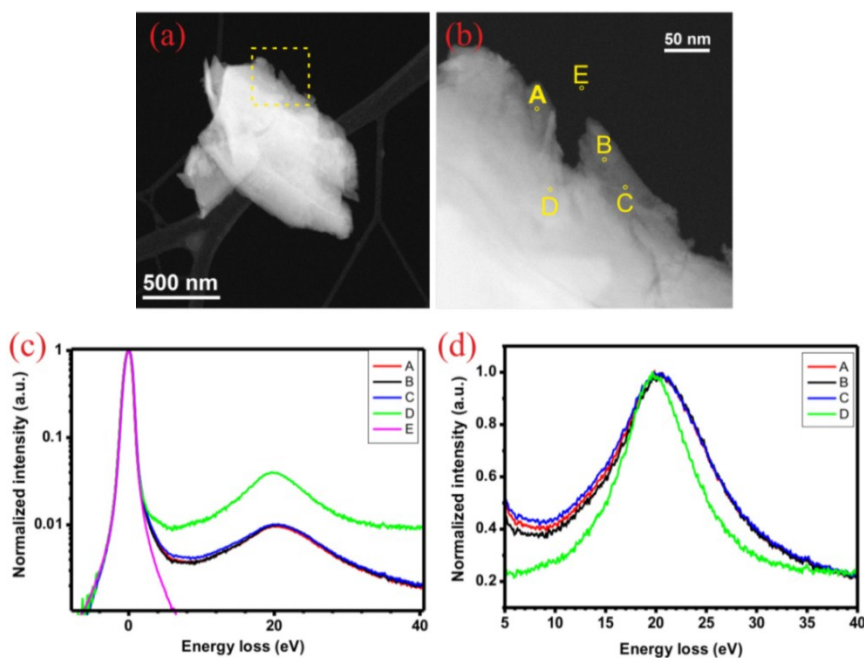
Figure 2.14. (a) HAADF-STEM image of a PtTe$_2$ flake, partially suspended on a hole in the amorphous carbon support film. The portion magnified in (b) was used for STEM-EELS analysis. The points A, B, and C exhibit a lower thickness (lower brightness in HAADF-STEM mode, corresponding to ~0.2λ) than point D (corresponding to ~0.8λ). (c) Only the zero-loss peak appears in the spectrum recorded at point E, i.e., 35 nm far from the PtTe$_2$ flake. (d) The broadband STEM-EELS spectra acquired for points A, B, C, and D. In panel (c) the intensity is normalized to the zero-loss peak maximum, while in panel (d) it is normalized to that of the peak at at ~20 eV, in order to highlight the dissimilarities in the line shape of the peaks corresponding to different thickness.

STEM-EELS investigation suggests that in PtTe$_2$ the momentum-integrated (over the collection angle) high-energy EELS peak changes in both line shape and energy position as a function of thickness. Specifically, an asymmetrical line shape, centered at about 23 eV [Figure 2.14(c)], is recorded for thinner regions (about 30 PtTe$_2$ unit cells along the *c* axis), whereas a symmetrical line shape, with a corresponding centroid around 20.5 eV, is revealed for thicker regions (about 120 PtTe$_2$ unit cells along the *c* axis). This is in contrast to other layered materials such as graphene [87,88] and phosphorene [89]. The high-energy EELS peak in PtTe$_2$ is redshifted with increasing thickness. The change in the line shape, with an asymmetrical shape characterizing the thinner regions, is ascribable to the multiple contributions (i.e., due to regions with different thickness) to the spectra acquired in the thinner regions of the flakes. The presence of contributions from regions a few nanometers away from the position of the electron beam is due to the delocalization of inelastic scattering, prominent in the low-energy-loss range [90,91].

2.7 Conclusions

The broadband excitation spectrum of bulk crystals and thin layers of PtTe$_2$, has been studied, using EELS in reflection mode for bulk and STEM-EELS for thin layers. In the case of bulk PtTe$_2$, different modes in the ultraviolet regime at 3.9, 7.5, and 19.0 eV were observed in addition to the excitations associated to the 3D Dirac cones observed in the infrared range at 0.5 and 1.4 eV. These observations are well explained by the DFT- based orbital-resolved band-structure and DOS calculations.

Specifically, it was found that in bulk PtTe$_2$ the observed peaks at 3.9, 7.5, and 19.0 eV are predominantly connected to Pt$_{5d}$ → Pt$_{5d}$, Te$_{5p}$ → Te$_{5d}$, and Te$_{5s}$ → Te$_{5d}$ transitions, respectively. In thin layers, with decreasing thickness, the high-energy EELS peak gets shifted from 20.5 to 23.0 eV. This redshift with increasing thickness is in contrast to the blueshift observed in the case of graphene. Moreover, with an increasing number of layers a decrease in the asymmetry of the line shape of the high-energy plasmon peak is observed. This peculiarity can be exploited for characterizing the thickness of PtTe$_2$ thin films.

References

[1]   A. Castellanos-Gomez, Why all the fuss about 2D semiconductors?, Nat. Photonics **10**, 202 (2016).

[2]   L. Li, W. Wang, Y. Chai, H. Li, M. Tian, and T. Zhai, Few-Layered PtS2 Phototransistor on h-BN with High Gain, Adv. Funct. Mater. **27**, 1701011 (2017).

[3]   A. A. Soluyanov, D. Gresch, Z. Wang, QuanSheng Wu, M. Troyer, X. Dai, and B. A. Bernevig, Type-ii weyl semimetals, Nature (London) **527**, 495 (2015).

[4]   M. Yan, H. Huang, K. Zhang, E. Wang, W. Yao, K. Deng, G. Wan, H. Zhang, M. Arita, H. Yang, Z. Sun, H. Yao, Y. Wu, S. Fan, W. Duan, and S. Zhou, Lorentz-violating type-II Dirac fermions in transition metal dichalcogenide $PtTe_2$, Nat. Commun. **8**, 257 (2017).

[5]   M. S. Bahramy, O. J. Clark, B.-J. Yang, J. Feng, L. Bawden, J. M. Riley, I. Markovic, F. Mazzola, V. Sunko, D. Biswas, S. P. Cooil, M. Jorge, J. W. Wells, M. Leandersson, T. Balasubramanian, J. Fujii, I. Vobornik, J. E. Rault, T. K. Kim, M. Hoesch, K. Okawa, M. Asakawa, T. Sasagawa, T. Eknapakul, W. Meevasana, and P. D. C. King, Ubiquitous formation of bulk Dirac cones and topological surface states from a single orbital manifold in transition-metal dichalcogenides, Nat. Mater. **17**, 21 (2018).

[6]   K. Zhang, M. Yan, H. Zhang, H. Huang, M. Arita, Z. Sun, W. Duan, Y. Wu, and S. Zhou, Experimental evidence for type-II Dirac semimetal in $PtSe_2$, Phys. Rev. B **96**, 125102 (2017).

[7]   H.-J. Noh, J. Jeong, E.-J. Cho, K. Kim, B. I. Min, and B.-G. Park, Experimental Realization of Type-II Dirac Fermions in a $PdTe_2$ Superconductor, Phys. Rev. Lett. **119**, 016401 (2017).

[8]   H. Huang, S. Zhou, and W. Duan, Type-II Dirac fermions in the $PtSe_2$ class of transition metal dichalcogenides, Phys. Rev. B **94**, 121117 (2016).

[9]   T.-R. Chang, S.-Y. Xu, D. S. Sanchez, W.-F. Tsai, S.-M. Huang, G. Chang, C.-H. Hsu, G. Bian, I. Belopolski, Z.-M. Yu, S. A. Yang, T. Neupert, H.-T. Jeng, H. Lin, and M. Z. Hasan, Type-II symmetry-protected topological Dirac semimetals, Phys. Rev. Lett. **119**, 026404 (2017).

[10]   M. Kargarian, M. Randeria, and Y.-M. Lu, Are the surface Fermi arcs in Dirac semimetals topologically protected?, Proc. Natl. Acad. Sci. USA **113**, 8648 (2016).

[11]   M. Kargarian, Y.-M. Lu, and M. Randeria, Deformation and stability of surface states in Dirac semimetals, Phys. Rev. B **97**, 165129 (2018).

[12]   X. Lin, J. C. Lu, Y. Shao, Y. Y. Zhang, X. Wu, J. B. Pan, L. Gao, S. Y. Zhu, K. Qian, Y. F. Zhang , D. L. Bao, L. F. Li, Y. Q. Wang, Z. L. Liu, J. T. Sun, T.

Lei, C. Liu, J. O. Wang, K. Ibrahim, D. N. Leonard, W. Zhou, H. M. Guo, Y. L. Wang, S. X. Du, S. T. Pantelides, and H.-J. Gao., Intrinsically patterned two-dimensional materials for selective adsorption of molecules and nanoclusters, Nat. Mater. **16**, 717 (2017).

[13] Y. Zhao, J. Qiao, Z. Yu, P. Yu, K. Xu, S. P. Lau, W. Zhou, Z. Liu, X. Wang, W. Ji, and Y. Chai, High-Electron-Mobility and Air-Stable 2D Layered PtSe2 FETs, Adv. Mater. **29**, 1604230 (2017).

[14] X. Chia, A. Adriano, P. Lazar, Z. Sofer, J. Luxa, and M. Pumera, Layered Platinum Dichalcogenides (PtS$_2$, PtSe$_2$, and PtTe$_2$) Electrocatalysis: Monotonic Dependence on the Chalcogen Size, Adv. Funct. Mater. **26**, 4306 (2016).

[15] Y. Wang, L. Li, W. Yao, S. Song, J. T. Sun, J. Pan, X. Ren, C. Li, E. Okunishi, Y.-Q. Wang, E. Wang, Y. Shao, Y. Y. Z. H.-t. Yang, E. F. Schwier, H. Iwasawa, K. Shimada, M. Taniguchi, Z. Cheng, S. Zhou, S. Du, S.J. Pennycook, S. T. Pantelides, and H.-J. Gao, Monolayer PtSe$_2$, a New Semiconducting Transition-Metal-Dichalcogenide, Epitaxially Grown by Direct Selenization of PtNano Lett. **15**, 4013 (2015).

[16] Z. Wang, Q. Li, F. Besenbacher, and M. Dong, Facile Synthesis of Single Crystal PtSe2 Nanosheets for Nanoscale Electronics, Adv. Mater. **28**, 10224 (2016).

[17] H. Ma, P. Chen, B. Li, J. Li, R. Ai, Z. Zhang, G. Sun, K. Yao, Z. Lin, B. Zhao, R. Wu, X. Tang, X. Duan, and X. Duan, Thickness-Tunable Synthesis of Ultrathin Type-II Dirac Semimetal PtTe$_2$ Single Crystals and Their Thickness-Dependent Electronic Properties, Nano Lett. **18**, 3523 (2018).

[18] A. Ciarrocchi, A. Avsar, D. Ovchinnikov, and A. Kis, Thickness-modulated metal-to-semiconductor transformation in a transition metal dichalcogenide, Nat. Commun. **9**, 919 (2018).

[19] W. Yao, E. Wang, H. Huang, K. Deng, M. Yan, K. Zhang, K. Miyamoto, T. Okuda, L. Li, Y.Wang, H. Gao, C. Liu,W. Duan, and S. Zhou, Direct observation of spin-layer locking by local Rashba effect in monolayer semiconducting PtSe$_2$ film, Nat.Commun. **8**, 14216 (2017).

[20] A. Politano, G. Chiarello, B. Ghosh, K. Sadhukhan, C.-N. Kuo, C. S. Lue, V. Pellegrini, and A. Agarwal, 3D Dirac Plasmons in the Type-II Dirac Semimetal PtTe$_2$, Phys. Rev. Lett. **121**, 086804 (2018).

[21] F. H. L. Koppens, T. Mueller, P. Avouris, A. C. Ferrari, M. S. Vitiello, and M. Polini, Photodetectors based on graphene, other two-dimensional materials and hybrid systems, Nat. Nanotechnol **9**, 780 (2014).

[22] X. Yu, P. Yu, D. Wu, B. Singh, Q. Zeng, H. Lin, W. Zhou, J. Lin, K. Suenaga, Z. Liu, and Q. J. Wang, Atomically thin noble metal dichalcogenide: a broadband mid-infrared semiconductor, Nat. Commun. **9**, 1545 (2018).

[23] X. Zhang, K. Wang, J. Ma, Q. Zhang, P. Yan, and X. Tian, Ultraviolet Imaging Based on Surface Plasmon Resonance With Azo-Polymer Sensing

Layer, IEEE Photonics Technol. Lett. **27**, 1297 (2015).

[24] J.-Y. Ou, J.-K. So, G. Adamo, A. Sulaev, L. Wang, and N. I. Zheludev, Ultraviolet and visible range plasmonics in the topological insulator $Bi_{1.5}Sb_{0.5}Te_{1.8}Se_{1.2}$, Nat. Commun. **5**, 5139 (2014).

[25] F. Bisio, R. Proietti Zaccaria, R. Moroni, G. Maidecchi, A. Alabastri, G. Gonella, A. Giglia, L. Andolfi, S. Nannarone, L. Mattera, and M. Canepa, Pushing the high-energy limit of plasmonics, ACS Nano **8**, 9239 (2014).

[26] S.-D. Guo and J.-L. Wang, Semicond. Spin–orbital coupling effect on the power factor in semiconducting transition-metal dichalcogenide monolayers, Sci. Technol. **31**, 095011 (2016).

[27] M. Chhowalla, H.S. Shin, G. Eda, L.J. Li, K.P. Loh, and H. Zhang, The chemistry of two-dimensional layered transition metal dichalcogenide nanosheets, Nat. Chem. **5**, 263 (2013).

[28] J.Wilson, and A. Yoffe, The transition metal dichalcogenides discussion and interpretation of the observed optical, electrical and structural properties, Adv. Phys. **18**, 193 (1969).

[29] A. V. Kolobov, and J. Tominaga, Two-Dimensional Transition-Metal Dichalcogenides, Springer Series in Materials Science, Vol. 239, Springer, Switzerland (2016).

[30] J. Ribeiro-Soares, R. Almeida, E. Barros, P. Araujo, M. Dresselhaus, L. Cançado, and A. Jorio, Group theory analysis of phonons in two-dimensional transition metal dichalcogenides, Phys. Rev. B **90**, 115438 (2014).

[31] H. Weyl, Gravitation and the electron, Proc. Natl. Acad. Sci. USA **15**, 323 (1929).

[32] J. Xiong, S. K. Kushwaha, T. Liang, J. W. Krizan, M. Hirschberger, W. Wang, R. J. Cava, and N. P. Ong, Evidence for the chiral anomaly in the Dirac semimetal Na_3Bi, Science **350**, 413 (2015).

[33] T. Liang, Q. Gibson, M. N. Ali, M. Liu, R. J. Cava, and N. P. Ong, Ultrahigh mobility and giant magnetoresistance in the Dirac semimetal Cd_3As_2, Nat. Mater. **14**, 280 (2014).

[34] X. Huang, L. Zhao, Y. Long, P. Wang, D. Chen, Z. Yang, H. Liang, M. Xue, H.Weng, Z. Fang, X. Dai, and G. Chen, Observation of the chiral-anomaly-induced negative magnetoresistance in 3D Weyl semimetal TaAs, Phys. Rev. X **5**, 031023 (2015).

[35] A. A. Zyuzin and A. A. Burkov, Topological response in Weyl semimetals and the chiral anomaly, Phys. Rev. B **86**, 115133 (2012).

[36] C. X. Liu, P. Ye, and X. L. Qi, Phys. Rev. B **87**, 235306 (2013); Erratum: Chiral gauge field and axial anomaly in a Weyl semimetal, **92**, 119904(E) (2015).

[37] Z. K. Liu, B. Zhou, Y. Zhang, Z. J. Wang, H. M. Weng, D. Prabhakaran, S.-K.Mo, Z. X. Shen, Z. Fang, X. Dai, Z. Hussain, and Y. L. Chen, Discovery of a three-dimensional topological Dirac semimetal, Na_3Bi, Science **343**, 864

(2014).

[38]   M. Neupane, S.-Y. Xu, R. Sankar, N. Alidoust, G. Bian, C. Liu, I. Belopolski, T.-R. Chang, H.-T. Jeng, H. Lin, A. Bansil, F. Chou, and M. Z. Hasan, Observation of a three-dimensional topological Dirac semimetal phase in high-mobility Cd_3As_2, Nat. Commun. **5**, 3786 (2014).

[39]   H. M. Weng, C. Fang, Z. Fang, B. A. Bernevig, and X. Dai, Weyl semimetal phase in noncentrosymmetric transition-metal monophosphides, Phys. Rev. X **5**, 011029 (2015).

[40]   B.Q. Lv, H. M. Weng, B. B. Fu, X. P. Wang, H.Miao, J. Ma, P. Richard, X. C. Huang, L. X. Zhao, G. F. Chen, Z. Fang, X. Dai, T. Qian, and H. Ding, Experimental discovery of Weyl semimetal TaAs, Phys. Rev. X **5**, 031013 (2015).

[41]   S.-Y. Xu, I. Belopolski, N. Alidoust, M. Neupane, G. Bian, C. Zhang, R. Sankar, G. Chang, Z. Yuan, C.-C. Lee, S.-M. Huang, H. Zheng, J. Ma, D. S. Sanchez, B. Wang, A. Bansil, F. Chou, P. P. Shibayev, H. Lin, S. Jia, and M. Z. Hasan, Discovery of a Weyl fermion semimetal and topological Fermi arcs, Science **349**, 613 (2015).

[42]   K. Deng, G. Wan, P. Deng, K. Zhang, S. Ding, E. Wang, M. Yan, H. Huang, H. Zhang, and Z. Xu, Experimental observation of topological Fermi arcs in type-II Weyl semimetal $MoTe_2$, Nat. Phys. **12**, 1105 (2016).

[43]   T.-R. Chang, S.-Y. Xu, G. Chang, C.-C. Lee, S.-M. Huang, B. Wang, G. Bian, H. Zheng, D. S. Sanchez, I. Belopolski, N. Alidoust, M. Neupane, A. Bansil, H.-T. Jeng, H. Lin, and M. Z. Hasan, Prediction of an arc-tunable Weyl Fermion metallic state in $Mo_xW_{1-x}Te_2$, Nat. Commun. **7**, 10639 (2016).

[44]   L. Huang, T. M. McCormick, M. Ochi, Z. Zhao, M.-t. Suzuki, R. Arita, Y. Wu, D. Mou, H. Cao, J. Yan, N. Trivedi and A. Kaminsk, Spectroscopic evidence for a type II Weyl semimetallic state in $MoTe_2$, Nat. Mater. **15**, 1155 (2016).

[45]   A. A. Zyuzin and R. P. Tiwari, Intrinsic anomalous Hall effect in type-II Weyl semimetals, JETP Lett. **103**, 717 (2016).

[46]   F. Fei, X. Bo, R. Wang, B. Wu, J. Jiang, D. Fu, M. Gao, H. Zheng, Y. Chen, X. Wang, H. Bu, F. Song, X. Wan, B. Wang, and G. Wang, Nontrivial Berry phase and type-II Dirac transport in the layered material $PdTe_2$, Phys. Rev. B **96**, 041201 (2017).

[47]   A. A. Burkov and L. Balents, Weyl semimetal in a topological insulator multilayer, Phys. Rev. Lett. **107**, 127205 (2011).

[48]   G. B. Halász and L. Balents, Time-reversal invariant realization of the Weyl semimetal phase, Phys. Rev. B **85**, 035103 (2012).

[49]   G. Fiori, F. Bonaccorso, G. Iannaccone, T. Palacios, D. Neumaier, A. Seabaugh, S. K. Banerjee, and L. Colombo, Electronics based on two-dimensional materials, Nat. Nanotechnol. **9**, 768 (2014).

[50]   A. Politano, G. Chiarello, B. Ghosh, K. Sadhukhan, C.-N. Kuo, C. Shan Lue,

V. Pellegrini and A. Agarwal, 3D Dirac Plasmons in the Type-II Dirac Semimetal $PtTe_2$, Phys. Rev. Lett. **121**, 086804 (2018).

[51] T. Sekine, C. Julien, I. Samaras, M. Jouanne, and M. Balkanski, Vibrational modifications on lithium intercalation in MoS_2, Mater. Sci. Eng. B **3**, 153 (1989).

[52] G. Lucovsky, R.White, J. Benda, and J. Revelli, Infrared-reflectance spectra of layered group-IV and group-VI transition-metal dichalcogenides, Phys. Rev. B **7**, 3859 (1973).

[53] T. Egami, S.J.L. Billinge, Underneath the Bragg Peaks: Structural Analysis of ComplexMaterials (Pergamon, Kiddington, 2003).

[54] P. Fons, A.V. Kolobov, M. Krbal, J. Tominaga, K. Andrikopoulos, S. Yannopoulos, G. Voyiatzis, and T. Uruga, Phase transition in crystalline GeTe: Pitfalls of averaging effects, Phys. Rev. B **82**, 155209 (2010).

[55] A. Schumacher, L. Scandella, N. Kruse, R. Prins, Single-layer MoS_2 on mica: studies by means of scanning force microscopy, Surf. Sci. **289**, L595 (1993).

[56] V. Petkov, S.J.L. Billinge, P. Larson, S.D. Mahanti, T. Vogt, K.K. Rangan, and M.G. Kanatzidis, Phys. Rev. B **65**, 092105 (2002).

[57] X. Rocquefelte, F. Boucher, P. Gressier, G. Ouvrard, P. Blaha, and K. Schwarz, Structure of nanocrystalline materials using atomic pair distribution function analysis: Study of $LiMoS_2$, Phys. Rev. B **62**, 2397 (2000).

[58] H.L. Tsai, J. Heising, J.L. Schindler, C.R. Kannewurf, and M.G. Kanatzidis, Exfoliated−Restacked Phase of WS_2, Chem. Mater. **9**, 879 (1997).

[59] J. Heising, and M.G. Kanatzidis, Exfoliated and Restacked MoS_2 and WS_2: Ionic or Neutral Species? Encapsulation and Ordering of Hard Electropositive Cations, J. Am. Chem. Soc.**121**, 11720 (1999).

[60] M. Kan, J.Wang, X.W. Li, S. Zhang, Y. Li, Y. Kawazoe, Q. Sun, and P. Jena, Structures and Phase Transition of a MoS_2 Monolayer, J. Phys. Chem. C **118**, 1515 (2014).

[61] L. Mattheiss, Band structures of transition-metal-dichalcogenide layer compounds, Phys. Rev. B **8**, 3719 (1973).

[62] X. Li, W. Cai, J. An, S. Kim, J. Nah, D. Yang, R. Piner, A. Velamakanni, I. Jung, E. Tutuc, S. K. Banerjee, L. Colombo, and R. S. Ruoff, Large-area synthesis of high-quality and uniform graphene films on copper foils, Science **324**, 5932 (2009).

[63] J. Hass, W. A. de Heer, and E. H. Conrad, The growth and morphology of epitaxial multilayer graphene, J. Phys. Condens. Matter **20**, 32 (2008).

[64] Y. Wu, K. A. Jenkins, A. Valdes-Garcia, D. B. Farmer, Y. Zhu, A. A. Bol, C. Dimitrakopoulos, W. Zhu, F. Xia, and P. Avouris, and Yu-Ming Lin, State-of-the-art graphene high-frequency electronics, Nano Lett. **12,** 6, 3062 (2012).

[65] Y. Wu, Y.-M. Lin, A. A. Bol, K. A. Jenkins, F. Xia, D. B. Farmer, Y. Zhu, and P. Avouris, High-frequency, scaled graphene transistors on diamond-like carbon, Nature **472**, 74 (2011).

[66] Y-M. Lin, A. Valdes-Garcia, S.-J. Han, D. B. Farmer, I. Meric, Y. Sun, Y. Wu, C. Dimitrakopoulos, A. Grill, P. Avouris, and K. A. Jenkins, Wafer-scale graphene integrated circuit, Science **332**, 6035 (2011).

[67] Y-H. Lee, X-Q Zhang, W. Zhang, M-T. Chang, C.-T Lin, K.-D. Chang, Y-C. Yu, J. T.-W. Wang, C.-S. Chang, L.-J. Li, and T.-W. Lin, Synthesis of Large-Area MoS_2 Atomic Layers with Chemical Vapor Deposition, Adv. Mater. **24,** 17, 2320 (2012).

[68] Y. Zhan, Z Liu, S. Najmaei, P. M. Ajayan, and J. Lou, Large-Area Vapor-Phase Growth and Characterization of MoS_2 Atomic Layers on a SiO_2 Substrate, Small **8**, 966 (2012).

[69] K.-K. Liu, W. Zhang, Y.-H. Lee, Y.-C. Lin, M.-T. Chang, C.-Y. Su, C.-S. Chang, H. Li, Y. Shi, H. Zhang, C.-S. Lai, and L.-J. Li, Growth of Large-Area and Highly Crystalline MoS2 Thin Layers on Insulating Substrates, Nano Lett. **12**, 3, 1538 (2012).

[70] S. Balendhran, J. Z. Ou, M. Bhaskaran, S. Sriram, S. Ippolito, Z. Vasic, E. Kats, S. Bhargava, S. Zhuiykovd and K. Kalantar-zadeh, Atomically thin layers of MoS 2 via a two step thermal evaporation–exfoliation method, Nanoscale **4**, 461 (2012).

[71] Y. Shi, W. Zhou, A.-Y. Lu, W. Fang, Y.-H. Lee, A. L. Hsu, S. M. Kim, K. K. Kim, H. Y. Yang, L.-J. Li, J.-C. Idrobo, and J. Kong, van der Waals Epitaxy of MoS_2 Layers Using Graphene As Growth Templates, Nano Lett. **12,** 6, 2784 (2012).

[72] Y. Peng, Z. Meng, C. Zhong, J. Lu, W. Yu, Z. Yang, and Y. Qian, Hydrothermal synthesis of MoS_2 and its pressure-related crystallization, J. Solid State Chem. **159,** 170 (2001).

[73] Y. Peng, Z. Meng, C. Zhong, J. Lu, W. Yu, Y. Jia, and Y. Qian, Hydrothermal Synthesis and Characterization of Single-Molecular-Layer MoS_2 and $MoSe_2$, Chem. Lett. **30,** 772 (2001).

[74] H. S. S. R. Matte, A. Gomathi, A. K. Manna, D. J. Late, R. Datta, S. K. Pati, and C. N. R. Rao, Angew. Chem. Int. Ed. **49,** 4059 (2010).

[75] H. S. S. R. Matte, B. Plowman, R. Datta, and C. N. R. Rao, MoS_2 and WS_2 Analogues of Graphene, Dalton Trans. **40,** 10322 (2011).

[76] J. Brivio, D.T. Alexander, and A. Kis, Ripples and Layers in Ultrathin MoS2 Membranes, Nano Lett. **11**, 5148 (2011).

[77] J.N. Coleman, M. Lotya, A. O'Neill, S.D. Bergin, P.J. King, U. Khan, K. Young, A. Gaucher, S. De, and R.J. Smith, Two-dimensional nanosheets produced by liquid exfoliation of layered materials, Science **331**, 568 (2011).

[78] D. Yang, and R. Frindt, Li-intercalation and exfoliation of WS_2, J. Phys. Chem. Solids **57,**1113 (1996).

[79] P. Joensen, R. Frindt, and S.R. Morrison, Single-layer MoS_2, Mat. Res. Bull. **21**, 457 (1986).

[80] S.J. Sandoval, D. Yang, R. Frindt, and J. Irwin, Raman study and lattice

dynamics of single molecular layers of MoS_2, Phys. Rev. B **44**, 3955 (1991).

[81] M. Py, and R. Haering, Structural destabilization induced by lithium intercalation in MoS_2 and related compounds, Can. J. Phys. **61**, 76 (1983).

[82] M. Kertesz, and R. Hoffmann, Octahedral vs. trigonal-prismatic coordination and clustering in transition-metal dichalcogenides, J. Am. Chem. Soc. **106**, 3453 (1984).

[83] I. A. Nechaev, I. Aguilera, V. De Renzi, A. di Bona, A. Lodi Rizzini, A. M. Mio, G. Nicotra, A. Politano, S. Scalese, Z. S. Aliev, M. B. Babanly, C. Friedrich, S. Blügel, and E. V.Chulkov, Quasiparticle spectrum and plasmonic excitations in the topological insulator Sb_2Te_3,Phys. Rev. B **91**, 245123 (2015).

[84] A. Politano, V. Formoso, and G. Chiarello, Interplay between single-particle and plasmonic excitations in the electronic response of thin Ag films, J. Phys.: Condens.Matter **25**, 305001 (2013).

[85] V. U. Nazarov, Multipole surface-plasmon-excitation enhancement in metals, Phys. Rev. B **59**, 9866 (1999).

[86] T. Malis, S. C. Cheng, and R. F. Egerton, Microsc. Res. Tech. **8**, 193 (1988).

[87] T. Eberlein, U. Bangert, R. R. Nair, R. Jones, M. Gass, A. L. Bleloch, K. S. Novoselov, A. Geim, and P. R. Briddon, EELS log-ratio technique for specimen-thickness measurement in the TEM, Phys. Rev. B **77**, 33406 (2008).

[88] P. Wachsmuth, R. Hambach, G. Benner, and U. Kaiser, Plasmon bands in multilayer graphene, Phys. Rev. B **90**, 235434 (2014).

[89] R. J. Wu, M. Topsakal, T. Low, M. C. Robbins, N. Haratipour J. S. Jeong, R. M. Wentzcovitch, S. J. Koester, and K. A. Mkhoyan, Atomic and electronic structure of exfoliated black phosphorus, J. Vacuum Sci. Technol. A **33**, 060604 (2015).

[90] C. C. Ahn, Transmission Electron Energy Loss Spectrometry in Materials Science and the EELS Atlas (Wiley-VCH,Weinheim, 2004).

[91] R. F. Egerton, Electron Energy-Loss Spectroscopy in the Electron Microscope, Language of science (Plenum, New York, 1996).

Appendix A

A.1 Density Functional Theory (DFT)

Density functional theory (DFT) constitutes a family of methodologies for quantum mechanical electronic structure calculations. These methods are of particular value for transition metal complexes where electron correlation effects can be large [1,2], and for systems of similar complexity like metals, solid-state compounds, and surfaces [3]. The problems that can be studied effectively include electronic structure, charge and spin distributions, molecular geometries, and reaction pathway energetics [2,4]. There are now a variety of applications both to ground state and to excited state energies, properties, and pathways [5–8]. DFT methods for medium and large sized systems combine high computational efficiency with very good physical accuracy.

From a fundamental viewpoint, the goal of DFT is to obtain the "best", ultimately "universal" forms for the "exact" exchange and correlation energy, E_{xc}, and the corresponding exchange-correlation potential v_{xc}. These in combination with the Coulomb potential of the electron density V_{Coul} and the nuclear electron attraction potential V_{Ne} can then be used to construct the Kohn–Sham (KS) potential, v_s:

$$v_s = V_{Ne} + V_{Coul} + v_{xc} \, . \tag{A.1}$$

This local density dependent one-electron potential operates on the KS orbitals, and gives accurate one-electron orbitals, electron densities, and energies.

It is useful to distinguish "exact KS" theory from practical approximate KS-DFT methods. In the "exact KS" theory, it is assumed that the exact correct electron density is obtained (or known from preceding work). There is then no remaining "correlation contribution" to the nuclear-electron attraction energy V. However, because the one-electron KS orbitals are solutions to a local one-electron potential v_s, the kinetic energy (T_s) of the KS wave function $\Psi_s[\rho]$ is the sum of the orbital kinetic energies. The KS potential acts like a local external potential, and the KS total kinetic energy T_s is not the "true" total kinetic energy of the interacting system T, with the difference being the correlation contribution to the kinetic energy $T_c = T - T_s$ within KS-DFT theory. This will enter into some important equations below.

Defining the "true" electronic total energy of the system as $E_{elect} = T - V_{Ne} + W$ and the total system as $E_{tot} = E_{elect} + V_{NN}$, where V_{NN} is the nuclear-nuclear electrostatic repulsion energy, with the total kinetic energy of the system as T, the total nuclear-electron attraction as V_{Ne}, and the total electron-electron repulsion energy as W, the last can be decomposed into

$$W = W_{Coul} + W_{xc} \tag{A.2}$$

where $W_{Coul} = (1/2) \int \rho(1)\rho(2)/r_{12} d1 d2$ is the classical Coulomb repulsion of the electronic density with $\rho(1)$ the electron density at position r_1 with spin index $S_1 = \alpha$ or β and W_{sc} is the exchange-correlation term in the total $e^- - e^-$ repulsion. This result occurs because the correlated joint probability density $\Gamma(1,2)$ is not just equal to the product of the one electron probability densities.

Instead

$$\Gamma(1,2) = \rho(1)\rho(2) + \Gamma_{xc}(1,2) \tag{A.3}$$

$\Gamma(1,2)$ can be separated into four terms for $\alpha\alpha, \beta\beta, \alpha\beta$ and $\beta\alpha$. In a related way, the conditional probability density for finding an electron at position 2 when another electron is known to be a position 1 is given by

$$\rho_{cond}(2|1) = g(1,2)\rho(2) = \Gamma(1,2) / (\rho(1) = \rho(2) + \Gamma_{xc}(1,2)/\rho(1)$$
$$= \rho(2) + \rho_{xc}^{hole}(2|1). \tag{A.4}$$

This defines the important exchange-correlation hole density $\rho_{sc}^{hole}(2|1)$ as the difference between the conditional probability density and the ordinary electron density. The following total charge integral rules hold for parallel $\alpha\alpha$ and $\alpha\beta$ antiparallel electron spins:

$$\int \rho_{xc}^{hole}{}_{\alpha\alpha} dr_2 = -1 \tag{A.5}$$

$$\int \rho_{xc}^{hole}{}_{\alpha\beta} dr_2 = 0. \tag{A.6}$$

Eq. (A.5) represents the Fermi hole, which is a consequence of the Pauli exclusion principle, and represents the combined exchange and correlation of parallel spin electrons. (It applies also for the $\beta\beta$ integral). Note that exchange alone will also satisfy this integral. Eq. (A.6) represents the behavior of the Coulomb type hole for opposite

spin electrons; while electron correlation allows these electrons to avoid one another, this is less effective than for parallel spin electrons, and is not a consequence of the Pauli antisymmetry principle. Correspondingly, the Pauli principle requires that no two parallel spin electrons can be at the same position simultaneously, or equivalently

$$\rho_{xc}^{hole}{}_{\alpha\alpha}(1|1) = -\rho_\alpha(1) \tag{A.7}$$

(with an analogous equation for β), while there is no such guarantee for opposite spin electrons. These and other limits are used to determine reasonable forms for the exchange-correlation hole functions, and to find v_{xc}.

The exchange-correlation term in the total $e^- - e^-$ can be defined in terms of these densities by

$$W_{xc} = (1/2)\int \rho(1)\,\rho_{xc}^{hole}\,(2|1)/r_{12}d1d2 = (1/2)\int \rho(1)\,v_{xc}^{hole}(1)d1 \tag{A.8}$$

so that

$$v_{xc}^{hole}(1) = \int \rho_{xc}^{hole}\,(2|1)/r_{12}d2 \,. \tag{A.9}$$

The exact total energy equation is

$$E_{tot} = T + V_{Ne} + V_{NN} + W_{Coul} + W_{xc}\,. \tag{A.10}$$

However, using T_s instead, this can be rewritten as

$$E_{tot} = T_s + V_{Ne} + V_{NN} + W_{Coul} + E_{xc} \tag{A.11}$$

which defines $E_{xc} = (T - T_s) + W_{xc}$.

The major goal is to find a good functional form for the exchange-correlation energy density per particle ε_{xc} where

$$E_{xc} = \int \rho(1)\,\varepsilon_{xc}(1)d1\,. \tag{A.12}$$

From these equations above and the variational principle, $\delta E/\delta\rho = 0$, the proof that $v_{xc} = \delta E_{xc}[\rho]/\delta\rho(r)$ is fairly straightforward. Defining $T_c = T - T_s$, a kinetic correlation energy density $v_{c,kin}$ is readily defined

$$T_c = \int \rho(1)\,v_{c,kin}d1\,. \tag{A.13}$$

Then the central equations follow

$$\varepsilon_{xc} = (1/2)v_{xc}^{hole} + v_{c,kin} \tag{A.14}$$

$$v_{xc} = v_{xc}^{hole} + v_{c,kin} + v_{resp}. \tag{A.15}$$

Time-dependent density functional theory (TDDFT) is the extension of density functional theory (DFT) to time-dependent problems.

Runge and Gross [9] were among those to provide a solid theoretical framework for TDDFT. They showed that DFT can be extended to problems where a time-dependent external perturbation is present, such as the oscillating electric field of a laser. The theory was originally applied in physics to simple systems, such as atoms or idealized metal surfaces. Initially the focus was on frequency-dependent polarizabilities and hyperpolarizabilities. TDDFT also allows the treatment of problems that fall outside the scope of standard perturbation theory, [10] such as high harmonic generation.

The following properties, previously not (easily) accessible within DFT, have become available: excitation energies and oscillator strengths [11,13], frequency-dependent polarizabilities [11,12], hyperpolarizabilities [14], circular dichroism spectra [15,16], optical rotatory strengths, optical rotatory dispersion [17], Raman intensities (determined at experimental laser frequency) [18], van der Waals dispersion coefficients [19], excited-state geometries, dipole moments and IR frequencies [20].

The basic quantity in TDDFT is the time-dependent electron density. Many important spectroscopic properties can be derived from it. As in ordinary (ground-state) DFT, the density is obtained from an auxiliary system of independent electrons which move in an effective potential, the time-dependent Kohn–Sham (KS) potential. With the exact KS potential $v_s[\rho](\boldsymbol{r}, t)$ the density of the noninteracting electron system will be equal to the true electron density. In practice, the KS potential contains the exchange-correlation (xc) potential, $v_{xc}(\boldsymbol{r}, t)$, for which approximations are needed.

The exact time-dependent density $\rho(\boldsymbol{r}, t)$ can be obtained from the time-dependent KS equations:

$$i\frac{\partial}{\partial t}\phi_j(\boldsymbol{r}, t) = \left[-\frac{\nabla^2}{2} + v_s[\rho](\boldsymbol{r}, t)\right]\phi_j(\boldsymbol{r}, t) \tag{A.16}$$

at the sum of the squares of the noninteracting KS orbitals:

$$\rho(\boldsymbol{r}, t) = \sum_{j=1}^{N} |\phi_j(\boldsymbol{r}, t)|^2.$$

(A.17)

The potential $v_s[\rho](\boldsymbol{r}, t)$ is called the time-dependent KS potential and written as:

$$v_s[\rho](\boldsymbol{r}, t) = v(\boldsymbol{r}, t) + \int d\boldsymbol{r}' \frac{\rho(\boldsymbol{r}', t)}{|\boldsymbol{r} - \boldsymbol{r}'|} + v_{xc}(\boldsymbol{r}, t).$$

(A.18)

Here, $v(\boldsymbol{r}, t)$ is the external field, which may include a time-dependent component, such as an oscillating electric field associated to a laser beam, and $v_{xc}(\boldsymbol{r}, t)$ is the time-dependent xc potential, the unknown part of $v_s(\boldsymbol{r}, t)$, which has to be approximated for practical applications.

In general theory, the first-order time-dependent density can be calculated from the exact linear response function χ acting on an external perturbing time-dependent potential $v_1(\boldsymbol{r}', t')$:

$$\rho_1(\boldsymbol{r}, t) = \int d\boldsymbol{r}' \int d\boldsymbol{r}' \chi(\boldsymbol{r}, t; \boldsymbol{r}', t') v_1(\boldsymbol{r}', t').$$

(A.19)

Similarly, for the KS system of noninteracting electrons, one finds the first-order change in the density from [2] where χ_s is the noninteracting linear density-density response function, and $v_{s,1}(\boldsymbol{r}, t)$ is the KS potential in first order of the external field, which differs forms $v_1(\boldsymbol{r}, t)$ in two terms which depend on ρ_1:

$$v_{s,1}(\boldsymbol{r}, t) = v_1(\boldsymbol{r}, t) + \int d\boldsymbol{r}' \frac{\rho_1(\boldsymbol{r}', t)}{|\boldsymbol{r} - \boldsymbol{r}'|} + \int d\boldsymbol{r}' \int dt' f_{xc}[\rho_0](\boldsymbol{r}, t; \boldsymbol{r}', t') \rho_1(\boldsymbol{r}', t')$$

(A.20)

Here the xc kernel f_{xc} has been introduced. It is the functional derivative of time-dependent xc potential $v_{xc}(\boldsymbol{r}, t)$ with respect to time-dependent density $\rho(\boldsymbol{r}, t)$:

Here the xc kernel f_{xc} has been introduced. It is the functional derivate of the time-dependent xc potential $v_{xc}(\boldsymbol{r}, t)$ with respect to time-dependent density $\rho(\boldsymbol{r}, t)$:

$$f_{xc}(\boldsymbol{r}, t; \boldsymbol{r}', t) = \frac{\delta v_{xc}(\boldsymbol{r}, t)}{\delta \rho(\boldsymbol{r}', t')}.$$

(A.21)

These equations are usually Fourier transformed from the time domain to the frequency domain. In the frequency representation, the KS response function is written in terms of the unperturbed KS orbitals $\varphi_j(\boldsymbol{r})$, their occupation number ε_j, and their orbital energies φ_j as:

$$\chi_s(\boldsymbol{r}, \boldsymbol{r}'; \omega) = \sum_{jk} (\eta_k - \eta_j) \frac{\phi_j(\boldsymbol{r})\phi_k^*(\boldsymbol{r})\phi_j^*(\boldsymbol{r}')\phi_k(\boldsymbol{r}')}{\omega - (\varepsilon_j - \varepsilon_k) + i\delta}. \tag{A.22}$$

where δ is a positive infinitesimal.

The first-order change in the electron density determines the change in the dipole moment under the influence of an external perturbation. In the most common case of an electric perturbation, the corresponding property is the frequency-dependent polarizability, which is directly related to (vertical) excitation energies ω_i, oscillator strengths f_i, and transition dipole moments μ_i [36]

$$\alpha_{av}(-\omega; \omega) = \sum_i \frac{f_i}{\omega_i^2 - \omega^2} = \frac{2}{3}\sum_i \frac{\omega_i \mu_i^2}{\omega_i^2 - \omega^2} \tag{A.23}$$

where α_{av} is the average polarizability, equal to the average of the α_{xx}, α_{yy}, and α_{zz}, components and i labels the excitations.

From this equation it is clear that the poles of the polarizability tensor are directly related to the exact excitation energies. Although only the dipole-allowed and spin allowed transitions have a nonzero contribution in this summation, the TDDFT approach also allows the determination of triplet excitation energies, as well as excitation energies with zero oscillator strength.

A.2 Electron Energy Loss Spectroscopy (EELS)

Electron energy loss spectroscopy (EELS) is a technique based on the analysis of electron energy losses undergone by primary electrons by means of the interaction with a sample. The study of the inelastic scattering of electrons offers information about the nature of the elementary excitations of the crystal, in a spatial region close to the surface. Energy losses are due mainly to three processes:

i) excitation of lattice vibrations of atoms on a clean surface (surface optical phonons, surface acoustical phonons) and/or vibrations of adsorbate atomic and molecular species;

ii) excitations of transitions involving the valence band (interband and intraband single-particle electronic excitations, surface states, and volume, surface and interface plasmons);

iii) core-level excitations.

The above mentioned possible excitations cover a wide spectral range which extends from few tenths of meV of loss energy for phonons or adsorbate vibrations up to several hundreds of eV necessary to ionize core electrons.

The treatment of the interaction electron-excitation in a solid, both in the semiclassical and quantum mechanical framework, is based on the fact that the electron interacts with the long-range Coulombic field induced by the charge-density fluctuations caused by the electric field it carries. Such charge-density fluctuations are correlated with the dielectric response, which is a function of both frequency and wavevector of the external perturbation.

The response of the medium to external fields can be described by the dielectric theory when it can be considered continuous and homogeneous. Due to inelastic scattering, an electron in the solid can gain energy $\hbar\omega$ and impulse $\hbar q$, while the incident electron undergoes a corresponding loss ΔE. The probability of adsorption of such energy $\Delta E = \hbar\omega$ and impulse $\hbar q$ for unit length is:

$$P(\boldsymbol{q},\omega) = \frac{W(\boldsymbol{q},\omega)}{\hbar\omega} \tag{A.24}$$

where $W(\boldsymbol{q},\omega)$ is the energy absorbed for unit volume in q-space, for unit frequency and unit path of the incident electron. Such probability can be related to the dielectric function of the investigated solid. If the incident electron is described as a charge distribution of the kind:

$$\rho(\boldsymbol{r},t) = -e\delta(\boldsymbol{r} - \boldsymbol{v}t) \tag{A.25}$$

one can write the Poisson equation for the potential generated by electron-solid interaction as follows:

$$\varepsilon(\boldsymbol{q}, \omega)\nabla^2\varphi(\boldsymbol{r}, t) = -4\pi\delta(\boldsymbol{r} - \boldsymbol{v}t) \tag{A.26}$$

and in Fourier space one obtains:

$$\psi(\boldsymbol{q}, \omega) = \frac{8\pi^2 e}{[q^2\varepsilon(\boldsymbol{q}, \omega)]} \tag{A.27}$$

where $\psi(\boldsymbol{q}, \omega)$ is the Fourier transform of $\varphi(\boldsymbol{r}, t)$.

The energy loss for unit path of the electron in the medium is:

$$-\frac{dW}{dx} = eE_{x|r=vt} \tag{A.28}$$

where E_x is the dielectric field component with respect to the x axis:

$$E(\boldsymbol{r}, t) = -\nabla\varphi(\boldsymbol{r}, t) = -i\int \boldsymbol{q}dq \int d\omega\varphi(\boldsymbol{q}, \omega)e^{(i\boldsymbol{q}\cdot\boldsymbol{r}-i\omega t)}. \tag{A.29}$$

By substituting Eq. (A.27) in Eq. (A.29) and considering that $\omega = \boldsymbol{q}\boldsymbol{v}$ one obtains for transition probability for unit path:

$$P(\boldsymbol{q}, \omega) = \frac{(e^2)}{q^2\pi^2\hbar\omega}\left\{-Im\left[\frac{1}{\varepsilon(\boldsymbol{q}, \omega)}\right]\right\} \tag{A.30}$$

where

$$-Im\left[\frac{1}{\varepsilon}\right] = -Im\left[\frac{1}{(\varepsilon_1 + i\varepsilon_2)}\right] = -Im\left[\frac{(\varepsilon_1 - i\varepsilon_2)}{(\varepsilon_1^2 + \varepsilon_2^2)}\right] = \frac{\varepsilon_2}{(\varepsilon_1^2 + \varepsilon_2^2)}. \tag{A.31}$$

The quantity $-Im[1/\varepsilon(\boldsymbol{q}, \omega)]$ is called volume loss function. It exhibits a strong maximum at $\varepsilon_1 = 0$ and $\varepsilon_2 \approx 0$ for a given value of ω and extra peaks corresponding to those of ε_2 shifted by the factor $1/|\varepsilon|^2$.

The volume loss function describes the volume loss for fast electrons, therefore in transmission experiments. Nevertheless, it is used with good results also in reflection EELS and with low primary beam energies. The trend of the loss function can be explained as follows. The charge-density fluctuations induced by the incident electrons cause Coulombic long-range forces between positive and negative charges, accompanied by excitations of collective oscillations such as plasmons for a free-electron gas. These oscillations are normal modes if the system is weakly damped.

On the other hand, if an oscillation is a normal mode it can self-sustain without an external field. Therefore it holds:

$$\boldsymbol{E}^{ext} - \boldsymbol{D} - \varepsilon \boldsymbol{E} = 0 \,. \tag{A.32}$$

Since $\boldsymbol{E}$, the field induced by the separation of positive and negative chares, must be different from zero, one must have:

$$\varepsilon(\omega) = \varepsilon_1 + i\varepsilon_2 = 0 \tag{A.33}$$

therefore the plasma is defined at $\varepsilon_1 = 0$ and $\varepsilon_2 \approx 0$, condition with corresponds to a maximum in the loss function.

The plasma oscillations can exist because for small transferred impulses the loss function does not always act a screening factor. The energy of a plasmon is in the range 10-20 eV, and it depends upon the density of the more weakly bound electrons, meaning the electrons for which $\hbar\omega_p$, where $\omega_p^2 = 4\pi n e^2 / m_e$ is the plasma frequency, is large with respect to the binding energy. In metals the electrons in the conduction band are involved in plasmon creation, while in semiconductors the ones in the valence band.

The dispersion law for such collective excitations is:

$$\omega_q = \omega_p \left(1 + \frac{3q^2 v_F^2}{10\omega_p^2} \right). \tag{A.34}$$

It is shown in Figure A.1 for a free-electron gas. If the transferred momentum q exceeds a critical value q_c (approximately ω_p / v_F, where v_F is the Fermi velocity), the incident electrons do not excite collective oscillations any longer, but transfer energy and impulse to single electrons according to the dispersion curve shown in Figure A.1 (shaded area).

Therefore for each q value Figure A.1 shows the region of possible single-particle excitations (shaded area) and the dispersion curve for collective excitations which crosses in $q = q_c$ the curve $\hbar\omega_{max}(\boldsymbol{q})$. If a plasmon with $q \geq q_c$ is excited, it decays in a single electron-hole pair.

The important result of this treatment is that the incident electrons can induced any elementary excitation in a crystal.
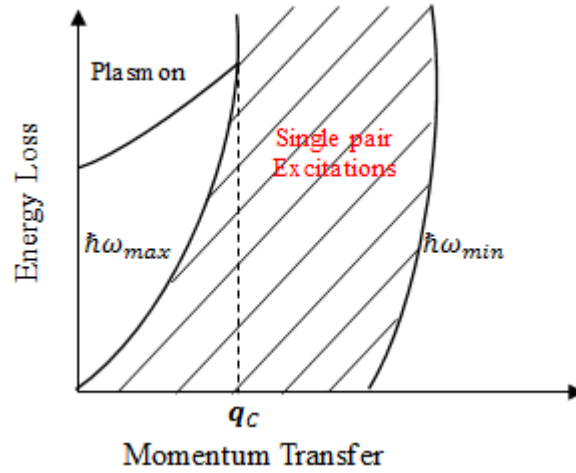
Figure A.1. Excitation spectrum of a free-electron gas.

These excitations can be of various nature: collective-plasmonic, single-particle interband and intraband, phononic, if the energy loss is small. These transitions occur with exchanged momenta different from zero, and therefore they are only partly similar to those induced by photon adsorption.

The loss function allows to derive the dielectric function $\varepsilon(\mathbf{q},\omega)$ by means of the Kramers-Kronig (KK) relations, making it possible the comparison with optical data obtained from reflectivity or adsorption measurement. In this respect, should stress that $\varepsilon(\mathbf{q},\omega)$ measured by EELS is the longitudinal dielectric function $(\mathbf{q},\omega)$ that coincides with the transverse dielectric function $\varepsilon^{T}(\mathbf{q},\omega)$, induced by electromagnetic fields, in limit of $\mathbf{q} \rightarrow 0$:

$$\varepsilon^{L}(\mathbf{q} \rightarrow 0, \omega) = \varepsilon^{T}(\mathbf{q} \rightarrow 0, \omega). \qquad (A.35)$$

$\varepsilon^{T}(\mathbf{q} \rightarrow 0, \omega)$ is the optical limit, since the momentum of the transferred photon $(q = \hbar\omega/c)$ is negligible with respect to the dimension of the Brillouin zone. The dielectric function which must be used for EELS spectroscopy is $\varepsilon^{L}(\mathbf{q}, \omega)$, which is therefore equal to the optical one only in the limit $\mathbf{q} \rightarrow 0$. In practice, the range of variability of $\mathbf{q}$ is fixed by the amount of the loss energy compared to the primary beam energy. The limit $\mathbf{q} \rightarrow 0$ is never verified in EELS measurements, since $\mathbf{q}_{min}$ is never negligible. However, it can be small if the loss energy is small with respect to the

primary energy. These processes take place at small scattering angles θ around the directions of Bragg-type elastic scattering. This condition is not always satisfied, but since the cross sections decrease rapidly as the transferred momentum is increased, and the agreement with experimental is usually good, the comparison between dielectric functions obtained from optical and EELS measurements is at least acceptable.

EELS, in the energy range 1-30 eV, provides a description of the structure in a solid. In what follow we will show how this electronic structure is related to the dielectric function, and compare EELS and optical data.

Classically the behavior of solids is described by the models of Drude and Lorentz. The Drude model considers the conduction electrons as a gas of free electrons not affected by the atomic potential. In this case, the dielectric function in the limit $\mathbf{q} \to 0$ is written:

$$\varepsilon(\omega) = \frac{1 - \omega_p^2}{(\omega^2 + i\omega/\tau)} \qquad (A.36)$$

where ω_p is the plasma frequency and τ is the relaxion time which takes into account the interaction undergone by the electrons.

Separated into a real and imaginary part $\varepsilon = \varepsilon_1 + i\varepsilon_2$:

$$\varepsilon_1(\omega) = \frac{1 - \omega_p^2}{(\omega^2 + 1/\tau^2)} \qquad (A.37)$$

$$\varepsilon_2(\omega) = \frac{\omega_p^2/\tau}{\omega(\omega^2 + 1/\tau^2)} \qquad (A.38)$$

In Figure A.2 the trends are shows of the real and the imaginary part of ε and of the loss function $-Im(1/\varepsilon)$. The ε_2 does not show any structure, the loss function shows a maximum of half-width $\Gamma = 1/\tau$ corresponding to ω_p, which indicates the existence of a volume plasmon.

If the dependence upon transferred $\mathbf{q}$ is explicitly introduced, single-particle transitions can take place, which for an electron gas can be only of intraband type.

In this case the dielectric function is described by Lindhard equation:

$$\varepsilon(\boldsymbol{q}, \omega) =$$

$$1 - lim_{\tau \to 0} \frac{4\pi e^2}{(q^2 V) \sum_k [f^0(E_k) - f^0(E_{k+q})]/(E_k - E_{k+q} + \Delta E - i\hbar/\tau)} \qquad (A.39)$$

where $f^0(E_k)$ is the Fermi-Dirac distribution, $4\pi e^2/q^2$ is the Fourier transform of the Coulomb potential and V is the volume of the system.

Its real and imaginary part give:

$$\varepsilon_1(\boldsymbol{q}, \omega) = 1 - 4\pi e^2 \Big/ (q^2 V) \sum_k [f^0(E_k) - f^0(E_{k+q})]/(E_k - E_{k+q} + \Delta E) \qquad (A.40)$$

$$\varepsilon_2(\boldsymbol{q}, \omega) = 1 - 4\pi e^2 \Big/ (q^2 V) \sum_k [f^0(E_k) - f^0(E_{k+q})]\delta(E_k - E_{k+q} + \Delta E) \qquad (A.41)$$
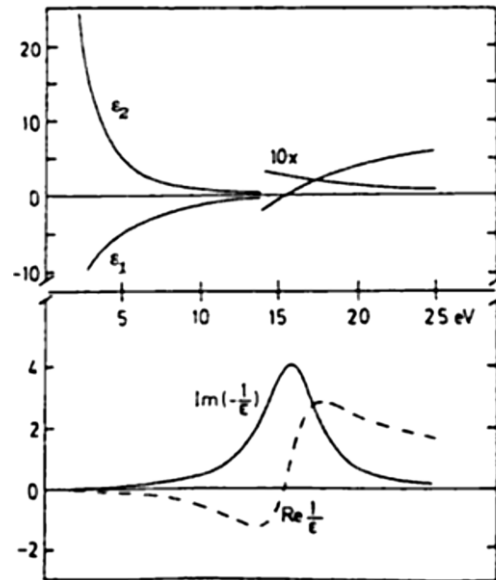
Figure A.2. Upper part: real and imaginary part of the dielectric function ε according to free-electron model. Lower part: loss function (solid line) and $Re(1/\varepsilon)$ (dashed line).

For $\boldsymbol{q}$ finite ε_1 has two zeroes, corresponding to the plasmonic excitation at high energy and the intraband one at low loss energy. This latter transition, due to the high value of ε_2 (large damping) appears only as a small structure at low energy loss. This model takes into account the electron-induced excitations in electron-gas-type metals (Al, K,Na etc.)

For all other metals, the presence of bounds electrons such as d electrons is better described by Lorentz oscillators with resonance frequency ω_0. In general, this is a good approximation also for semiconductors and insulators.

The dielectric function for only type of transition with energy $\hbar\omega_0$ is:

$$\varepsilon(\omega) = \frac{1 - \omega_p^2}{(\omega^2 - \omega_0^2 + i\omega/\tau)} \tag{A.42}$$

Separated into a real and imaginary part $\varepsilon = \varepsilon_1 + i\varepsilon_2$:

$$\varepsilon_1(\omega) = 1 - \omega_p^2 \frac{\omega^2 - \omega_0^2}{(\omega^2 - \omega_0^2)^2 + (\omega/\tau)^2} \tag{A.43}$$

$$\varepsilon_2(\omega) = \omega_p^2 \frac{\omega \, ^1/\tau}{(\omega^2 - \omega_0^2)^2 + (\omega/\tau)^2} \tag{A.44}$$

The related $\varepsilon_1, \varepsilon_2, -Im(1/\varepsilon)$ and $Re(1/\varepsilon)$ are shown in Figure A.3. It can be noticed that at the resonance frequency ω_0 the loss function does not show any structure, while ε_2 shows a maximum. For $\omega > \omega_0$ when $\varepsilon_1 \approx 0$ there is a plasmon-like structure.
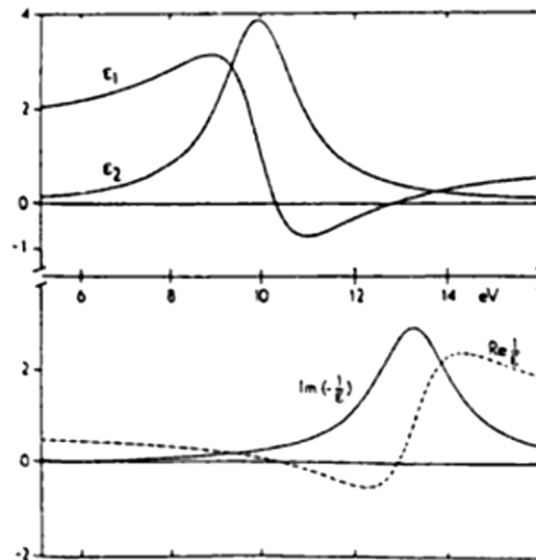
Figure A.3. Real and imaginary part of the dielectric function for a bound electron according to the Lorentz model. In the lower part the corresponding loss function (solid line) and $Re(1/\varepsilon)$ (dashed line).

This behavior is due to the fact that for excitation energies higher than binding energies electrons can be considered as free.

In general, the behavior of metals is described by a dielectric function given by the sum of intraband-type transitions (Drude) and interband-type transitions (Lorentz). The total dielectric function is given for each frequency by the sum of two terms, one corresponding to free electrons and another describing the bound electrons:

$$\varepsilon_1^{tot}(\omega) = \varepsilon_1^{free}(\omega) + \varepsilon_1^{bound}(\omega) \tag{A.45}$$

$$\varepsilon_2^{tot}(\omega) = \varepsilon_2^{free}(\omega) + \varepsilon_2^{bound}(\omega). \tag{A.46}$$

In reflection energy loss spectra features have been measured which are not at all described by Eq. (A.31). These losses are related to plasmonic excitations localized at the surface. This effect takes place mainly in reflection mode, since the mean free path is shorter than in transmission and electrons cross the surface twice before being detected. These losses can be treated on the ground of Mills theory, which describes the process of inelastic scattering at the surface of a semi-infinite medium due to charge-density fluctuations induced by the incident particle. The loss probability is proportional to $-Im[1/(\varepsilon + 1)]$, called surface loss function. The shape of this function can be explained with the following model. The interaction between the incident electron and the electron gas of the solid creates a polarization field time- and space-dependent, which in turn attenuates the electronic motion. This polarization field can be decomposed in plane waves by means of a Fourier expansion. These plane waves are attenuated in the medium in a way proportional to ε_2. In this way, the energy lost by the electron during its relaxation is given to the medium. Inside the solid, the amplitude of the electron field is screened by a factor $1/\varepsilon$. Since the process takes place at the surface, a factor $1/(\varepsilon + 1)$ should be considered which takes into account the screening due to the dielectric constants of the medium and the vacuum.

The related intensity will be screened by a factor $1/(\varepsilon + 1)^2$. In these conditions, the electron energy loss will be proportional to:

$$\frac{\varepsilon_2}{(\varepsilon + 1)^2} = -Im\left[\frac{1}{(\varepsilon + 1)}\right] \tag{A.47}$$

This loss function will have a maximum at a certain value of $\hbar\omega$ if $\varepsilon_1 = -1$ and $\varepsilon_2 \approx 0$, and other weaker maxima in correspondence with the maxima of ε_2 shifted by the screening factor $1/(\varepsilon + 1)$. This behavior can be explained on the ground of the same considerations reported for the volume loss function. Also in this case a plasma oscillation will occur (surface plasmon), this time at a frequency:

$$\hbar\omega = \frac{\hbar\omega_p}{\sqrt{2}} \tag{A.48}$$

The motion of such surface plasmons can be described by a crystal mode propagating along the surface and strongly attenuated exponentially perpendicularly to the surface. In general, a reflection EELS spectrum can be described by a linear combination of two probabilities of surface and volume loss, with proportionality factors which depend upon the experimental conditions of electron incidence and primary energy used.

The link between surface plasmon dispersion and the position of the centroid of the induced charge derived theoretically for half infinite free-electron (jellium model) already in the 1970's by different authors [21,22]. Great attention has been devoted to the study of dispersion of surface plasmon by Rocca et al. [23].

At variance with the relation for bulk plasmons reported in Eq. (A.34), the dispersion for surface plasmons is written as:

$$\omega_s(q_\parallel) = \omega_s \left[\frac{1 - d(\omega_s)q_\parallel}{2 + O(q_\parallel^2)} \right] \tag{A.49}$$

where ω_s is the surface-plasmon frequency and $d(\omega_s)$ is the distance of the position of the centroid of the induced charge from the jellium edge.

Energy-loss spectroscopy presents several analogies with optical spectroscopy. Both techniques provide information on the density of both filled and empty electronic states in a solid. The main advantage of EELS is the possibility of changing easily the energy of the incident electron, to acceed to wide energy range with the same equipment and without monochromators. Furthermore, the shallow penetration of electrons in a medium makes reflection energy loss more sensitive to the surface than optical spectroscopy.

Figure A.4 shows schematically the typical geometry of an inelastic scattering experiment on the ground of the Ewald sphere. The incident electron beam, after being reflected by the crystal, is divided in several Bragg-diffracted beams. Around each Bragg peak, in a cone of aperture θ, a certain number of electrons will be present which underwent inelastic scattering processes.
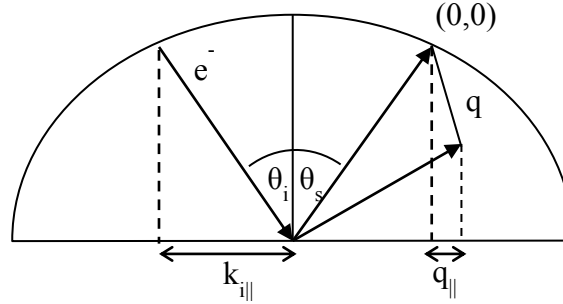
Figure A.4. Scattering geometry of the EELS experiment, on the basis of the Ewald sphere descriptions of the scattering process.

The energy conservation and $k_\parallel$ conservation laws are:

$$E_s = E_i - \Delta E$$
$$\boldsymbol{k}_{s\parallel} = \boldsymbol{k}_{i\parallel} + \boldsymbol{q}_\parallel \qquad (A.50)$$

where **g** is a two-dimensional surface reciprocal lattice vector, $\boldsymbol{q}_\parallel$ is the momentum transferred by the incident electron with wavevector $\boldsymbol{k}_i$. The scattered electron loses an energy ΔE and its momentum is $\boldsymbol{k}_s$. If the scattering geometry allows to determine the incident (i) and scattering (s) angles with good precision, one obtain:

$$\boldsymbol{q}_\parallel = \frac{1}{\hbar}\sqrt{2m}\left[\sqrt{E_i}sin\vartheta_i - \sqrt{E_i - \Delta E}sin\vartheta_s\right]. \qquad (A.51)$$

A.3 Scanning Transmission Electron Microscopy (STEM)

Scanning transmission electron microscopy (STEM) combines the principles of transmission electron microscopy and scanning electron microscopy and can be performed on either type of instrument.

Figure A.5 shows a schematic of the STEM optical configuration. A series of lenses focuses a beam to form a small spot, or probe, incident upon a thin, electron-transparent sample. Except for the final focusing lens, which is referred to as the objective, the other pre-sample lenses are referred to as condenser lenses. The aim of the lens system is to provide enough demagnification of the finite-sized electron source in order to form an atomic-scale probe at the sample. The objective lens provides the final, and largest, demagnification step. It is the aberrations of this lens that dominate the optical system. An objective aperture is used to restrict its numerical aperture to a size where the aberrations do not lead to significant blurring of the probe. The requirement of an objective aperture has two important consequences: (i) it imposes a diffraction limit to the smallest probe diameter that may be formed and (ii) electrons that do not pass through the aperture are lost, and therefore the aperture restricts the amount of beam current available.
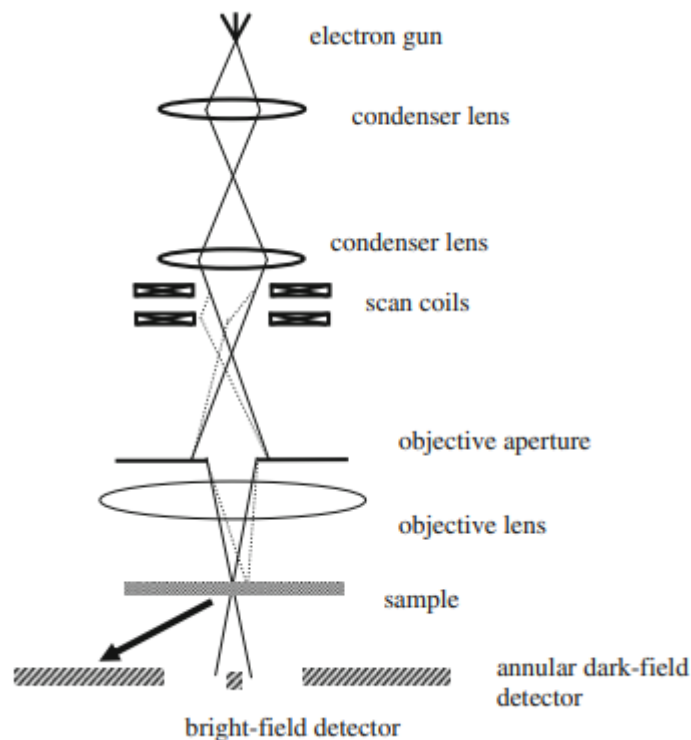
Figure A.5. A schematic diagram of a STEM instrument.

Scan coils are arranged to scan the probe over the sample in a raster, and a variety of scattered signals can be detected and plotted as a function of probe position to form a

magnified image. There is a wide range of possible signals available in the STEM, but the commonly collected ones are the following:

(i) Transmitted electrons that leave the sample at relatively low angles with respect to the optic axis (smaller than the incident beam convergence angle). This mode is referred to as bright field (BF).

(ii) Transmitted electrons that leave the sample at relatively high angles with respect to the optic axis (usually at an angle several times the incident beam convergence angle). This mode is referred to as annular dark field (ADF).

(iii) Transmitted electrons that have lost a measurable amount of energy as they pass through the sample. Forming a spectrum of these electrons as a function of the energy lost leads to electron energy loss spectroscopy (EELS).

(iv) X-rays generated from electron excitations in the sample (EDX).

The use of an annular dark-field detector gave rise to one of the first detection modes used by Crewe and co-workers during the initial development of the modern STEM. The detector consists of an annular sensitive region that detects electrons scattered over an angular range with an inner radius that may be a few tens of milliradians up to perhaps 100 mrad and an outer radius of several hundred milliradians. It was later proposed that high scattering angles ($\sim$100 mrad) would enhance the compositional and that the coherent effects of elastic scattering could be neglected because the scattering was almost entirely thermally diffuse. This idea led to the use of the high-angle annular dark-field detector (HAADF).

HAADF produces an annular dark field image formed by very high angle, incoherently scattered electrons (Rutherford scattered from the nucleus of the atoms) — as opposed to Bragg scattered electrons. This technique is highly sensitive to variations in the atomic number of atoms in the sample (Z-contrast images)[24].

For elements with a higher Z, more electrons are scattered at higher angles due to greater electrostatic interactions between the nucleus and electron beam. Because of this, the HAADF detector senses a greater signal from atoms with a higher Z, causing them to appear brighter in the resulting image [25,26].

This high dependence on Z (with contrast approximately proportional to Z^2) makes HAADF a useful way to easily identify small areas of an element with a high Z in a

matrix of material with a lower Z. A common application for HAADF is in catalysis research in which the determination of the size of metal particles and their distribution is extremely important.

STEM imaging can be combined with several material analysis techniques like EELS, Energy Filtered TEM (EFTEM) and Energy Dispersive X-ray (EDX).

EELS is a technique that provides elemental information on a nanometer scale when coupled with TEM. The energy of the incident electrons is altered as they pass through the sample. This Energy Loss can be characterised using EELS to provide elemental identification. Compared to EDX, EELS provides improved signal to noise, spatial resolution (down to 1 nm), energy resolution (<1 eV for EELS) and sensitivity to the lower atomic number elements.

A.4 Low-energy electron diffraction (LEED)

The diffraction of electrons, first observed by Davisson and Germer in 1927, provided the earliest proof of the wavelike properties of electrons. From this discovery, electron diffraction evolved into a powerful technique for the determination of bulk and surface structures. Electrons having energies less than several hundred eV have elastic mean free paths (average distance traveled before losing energy) measured in angstroms [Å], which means that low-energy electrons are particularly sensitive to surfaces, and this is the basis for low-energy electron diffraction (LEED).

LEED is the most common technique for determining surface structures and geometries [27,28]. It is a relatively fast and inexpensive technique, and the required instrumentation can be included conveniently in experimental systems designed to measure other surface properties. LEED is often used simply as a tool to check the surface order, and inspection of a LEED pattern provides some measure of the presence and degree of order, as well as information on the (lateral) surface unit cell. The determination of a surface geometry, including surface relaxation, stacking sequence, overlayer registry, and bond lengths, generally requires the measurement and analysis of

the LEED intensities. Because low-energy electrons incident on a surface tend to scatter multiple times before they emerge and are detected, it is generally not possible to determine a surface geometry by the direct or semidirect inversion methods that are used in X-ray diffraction. Therefore, the most common procedure is to assume a model structure and calculate the scattered intensities for comparison with the experimental intensities. LEED had been used to determine the surface geometries of almost all commonly studied single-crystal surfaces of metals and semiconductors. It had also been used to study many examples of atomic adsorbates and a few cases of simple molecules. On the other hand, it has been used to study relatively few insulator surfaces. The reason for this is mainly due to the charging that occurs on these surfaces when low energy electrons are incident upon them, rapidly leading to local electric fields that distort the electron trajectories. This charging can be due to a deficiency or an excess of electrons the deficiency arises from the large number of secondary electrons ejected from the surface. The same considerations for charging also can apply to insulating adsorbates. Although some progress has been made by using low-current electron guns coupled with image intensifiers or special detectors, or by using electron flood guns that flood the surface with low-energy electrons to balance the charge, there is still a relative dearth of LEED studies on insulating materials. The emphasis on surface structure determination over the past 10 years has been moving toward solving more complex structures, including crystals with large (or infinite) unit cells, large molecular adsorbates, oxide surfaces (most of which are insulating), and nanostructures at surfaces.

The basic principle of a standard LEED experiment is very simple: a collimated mono-energetic beam of electrons is directed towards a single crystal surface and the diffraction pattern of the elastically back-scattered electrons is recorded using a position-sensitive detector. For electrons, like for all wave-like objects, the angular intensity distribution due to the interference of partial waves back-scattered from a periodic array is described by Bragg's law or, more conveniently, by a set of Laue equations, one for each dimension of periodicity, which predict a regular pattern of diffraction spots.

Because of the short penetration depth of low-energy electrons the diffraction process is determined by a small number atomic layers at the crystal surface. The electrons do not

probe the full crystal periodicity perpendicular to the surface. Therefore, the array of relevant scatterers is only periodic in two dimensions. The surface lattice can be described by a pair of lattice vectors $\boldsymbol{a_1}$ and $\boldsymbol{a_2}$, which are parallel to the surface plane, and the surface unit cell. The surface consists of identical copies of the unit cell at every point

$$\boldsymbol{R} = m_1 \boldsymbol{a_1} + m_2 \boldsymbol{a_2} \tag{A.52}$$

with integer numbers m_1 and m_2. The left hand side of Figure A.6 illustrates common square, rectangular and hexagonal surfaces and the lattice vectors defining their unit cells.
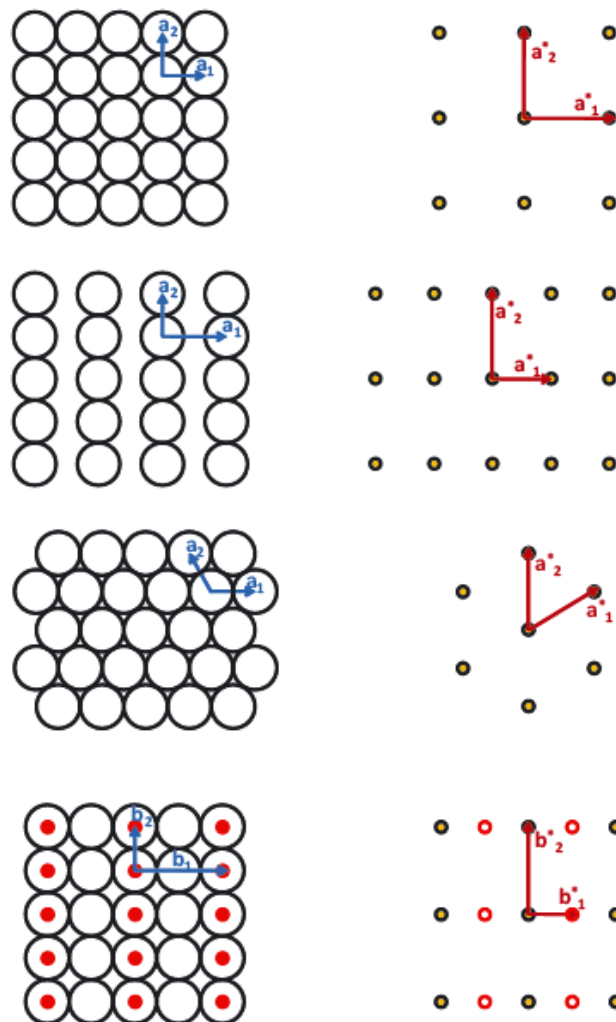
Figure A.6. (left from top to bottom) arrangement of atoms in the {100} (square) {110} (rectangular) and {111} (hexagonal) surfaces of a simple face centered cubic crystal lattice and a $p(2 \times 1)$ superstructure on a square surface; the diagrams include lattice vectors defining the surface unit cell and the corresponding reciprocal lattices (right).

The two-dimensional Laue equations are based reciprocal lattice vectors within the surface plane which are defined by the real space lattice vectors through a set of four simultaneous equations:

$$\boldsymbol{a_1} \cdot \boldsymbol{a_1^*} = 2\pi \qquad \boldsymbol{a_2} \cdot \boldsymbol{a_2^*} = 2\pi \qquad \text{(A.53 (a))}$$

$$\boldsymbol{a_1} \cdot \boldsymbol{a_2^*} = 0 \qquad \boldsymbol{a_2} \cdot \boldsymbol{a_1^*} = 0 \qquad \text{(A.53 (b))}$$

In order for the scalar products in Eq. (A.53 (a)) to be dimensionless, the reciprocal lattice vectors must have units of inverse length, nm[-1]. As a consequence of Eq. (A.53 (b)) $\boldsymbol{a_2^*}$ and $\boldsymbol{a_1^*}$ must be perpendicular to $\boldsymbol{a_1}$ and $\boldsymbol{a_2}$, respectively, which means that a rectangular real space lattice will also have a rectangular reciprocal lattice. For non-rectangular lattices the angles are different in real space and reciprocal space. The right-hand column of Figure A.7 shows the corresponding reciprocal lattices for each of the surfaces on the left. The reciprocal lattice vectors define the positions of the diffraction maxima through the Laue equation:

$$\boldsymbol{k}_{\parallel,out}(n_1, n_2) = \boldsymbol{k}_{\parallel,in} + n_1 \boldsymbol{a_1^*} + n_2 \boldsymbol{a_2^*} \qquad \text{(A.54)}$$

where $\boldsymbol{k}_{\parallel,out}$ is the component of the wave vector of the diffracted electrons, which is parallel to the surface plane (by convention, this is the xy-plane). $\boldsymbol{k}_{\parallel,in}$, is the parallel component of the wave vector of the incoming electron beam. Note that the Laue equation (A.54) defines a two-dimensional vector, hence it actually comprises two equations, one for each component. Each diffraction spot corresponds to the sum of integer multiples of $\boldsymbol{a_1^*}$ and $\boldsymbol{a_2^*}$. The integer numbers (n_1, n_2) are used as indices to label the spots.

Energy conservation demands that the length of the $\boldsymbol{k}$-vector is the same, $(2m_e E_{kin}/h^2)^{1/2}$, for both the incoming and the elastically scattered electron wave. This defines the vertical or z-component, $\boldsymbol{k}_{z,out}$ of the back-diffracted electrons in the (n_1, n_2) spot:

$$\boldsymbol{k}_{z,out}(n_1 n_2) = \left[2m_e E_{kin}/h^2 - \left|\boldsymbol{k}_{\parallel,out}(n_1 n_2)\right|^2\right]^{1/2}. \qquad \text{(A.55)}$$

Unlike for X-ray diffraction, there is no Laue-condition for the z-component of $\boldsymbol{k}_{z,out}$. The only condition for diffraction into a spot $(n_1 n_2)$ is that $\boldsymbol{k}_{z,out}$ has a real value. This

condition is synonymous with the obvious fact that the length of the parallel component of $\boldsymbol{k}$ cannot be greater than the length of the entire vector, but it also limits the number of observable LEED spots. The number of observable spots increases with increasing electron energy while the polar emission angle with respect to the specular spot (0,0) decreases for each spot.

Superstructures formed by adsorbates or rearrangements of the surface atoms can lead to a periodicity of the surface lattice greater than that of the bulk-truncated single crystal. In these cases, the lattice vectors for the superstructure, $\boldsymbol{b_1}$ and $\boldsymbol{b_2}$, can always be related to the lattice vectors of the bulk-truncated surface, $\boldsymbol{a_1}$ and $\boldsymbol{a_2}$, through

$$\begin{aligned}
\boldsymbol{b_1} &= m_{11}\boldsymbol{a_1} + m_{12}\boldsymbol{a_2} \\
\boldsymbol{b_2} &= m_{21}\boldsymbol{a_1} + m_{22}\boldsymbol{a_2}
\end{aligned}$$

(A.56)

the numbers m_{ij} are the coefficients of the *superstructure matrix* $M = [m_{11}\, m_{12}; m_{21}\, m_{22}]$, which is a straightforward way of characterizing any superstructure. Depending on whether all m_{ij} are integer numbers or not the superstructure is either called *commensurate* or *incommensurate*. Superstructures lead to additional spots in the LEED pattern, for which fractional indices are used. The reciprocal lattice vectors for these spots can be calculated directly from the coefficients of the superstructure matrix according to the following set of equations:

$$\begin{aligned}
\boldsymbol{b_1^*} &= (m_{11} \cdot m_{22} - m_{12} \cdot m_{12})^{-1} \cdot (m_{22}\boldsymbol{a_1^*} - m_{21}\boldsymbol{a_2^*}) \\
\boldsymbol{b_2^*} &= (m_{11} \cdot m_{22} - m_{12} \cdot m_{12})^{-1} \cdot (m_{12}\boldsymbol{a_1^*} - m_{11}\boldsymbol{a_2^*}).
\end{aligned}$$

(A.57)

Another, less general notation according to Wood specifies the lengths of the vectors $\boldsymbol{b_1}$ and $\boldsymbol{b_2}$ in units of $\boldsymbol{a_1}$ and $\boldsymbol{a_2}$, respectively, together with the rotation angle α between $\boldsymbol{b_1}$ and $\boldsymbol{a_1}$ (only specified if α is not zero):

$$p/c\, (|\boldsymbol{b_1}|/|\boldsymbol{a_1}| \times |\boldsymbol{b_2}|/|\boldsymbol{a_1}|)\, R\alpha$$

(A.58)

p indicates a "primitive" and c a "centred" surface unit cell.

Examples are "$p(2 \times 1)$", "$p(\sqrt{3} \times \sqrt{3})R30°$", and "$c(2 \times 2)$". This notation is not applicable to all superstructures but it is more frequently used than the matrix notation

because it is shorter. As an example, a $p(2 \times 1)$ superstructure on a square substrate surface is shown at the bottom of Figure A.7. The corresponding superstructure matrix is $[2\ 0; 0\ 1]$ and the reciprocal lattive vectors are $\boldsymbol{b_1^*} = {}^1\!/_2\ \boldsymbol{a_1^*}\ 1$ and $\boldsymbol{b_2^*} = \boldsymbol{a_2^*}$.

There is no Laue-condition for the z component of $\boldsymbol{k_{out}}$, i.e. diffraction spots are allowed for a wide range of kinetic energies. This does not mean, however, that the intensities of spots are constant with the energy. Although the electrons do not experience the full periodicity of the crystal perpendicular to the surface, there is still interference of electrons scattered from different atomic layers parallel to the surface. For infinite penetration depth this would impose a third Laue condition for $\boldsymbol{k_{z,out}}$ and therefore each $(n_1 n_2)$ spot would have sharp intensity maxima ("*Bragg peaks*") for certain values of E_{kin} and zero intensity for all other energies. Since the penetration depth is very small, the back-scattered electrons only interact with a few layers of atoms giving rise to broad maxima at the Bragg peak positions and non-zero intensities in the intermediate energy regimes of the intensity *vs* energy curve of each spot (also known as intensity *vs* voltage or *IV curve*). The combination of non-periodic layer distances near the surface, different atomic scattering potentials and multiple scattering events leads to shifts in the Bragg peaks and intensity maxima at other energies in the IV curves.

The standard modern LEED system is of the "rear view" type , which is schematically depicted in Figure A.7. The incident electron beam, accelerated by the potential V_0, is emitted from the electron gun behind a transparent hemispherical fluorescent screen and hits the sample through a hole in the screen. Typically, the electron beam has a current of around 1 μA and a diameter of 0.5 to 1 mm. The surface is in the centre of the hemisphere so that all back-diffracted electrons travel towards the LEED screen on radial trajectories. Before the electrons hit the screen they have to pass a retarding field energy analyzer (RFA). It consists of four (sometimes three) hemispherical grids concentric with the screen, each containing a central hole, through which the electron gun is inserted. The first grid (nearest to the sample) is connected to earth ground as is the sample, in order to provide a field-free region between the sample and this grid.
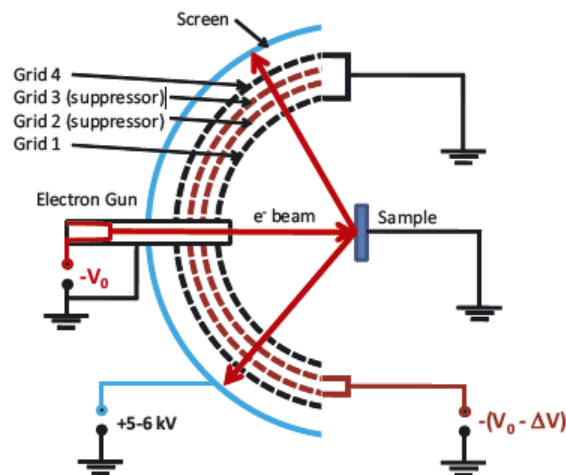
Figure A.7. Schematic diagram of a typical LEED instrument.

A negative potential $-(V_0 - \Delta V)$ is applied to the second and third grid, the so-called suppressor grids. These repel all electrons that have undergone non-elastic scattering processes and have lost more than $e\Delta V$ (typically around 5eV) of their original kinetic energy. Thus, only elastically scattered electrons and those with small energy losses can pass through to the fluorescent screen. The fourth grid is usually on ground potential in order to reduce field penetration of the screen voltage to the suppressor grids. The screen is at a potential of the order of 5-6 kV; it provides the electrons with enough energy to make the diffraction pattern visible on the fluorescent screen. The pattern can be observed through a view-port from behind the transparent screen. Only the electron gun assembly (diameter < 15 mm) limits the view slightly. The LEED pattern is recorded using a video camera with suitable image processing software. As with all methods that use electrons as probes, vacuum conditions are required because electrons cannot penetrate a gas atmosphere at normal pressures. In general, however, the vacuum conditions required to avoid contamination of clean surfaces are more rigorous (typically < 10^{-9} mbar) than those imposed by the use of electrons (typically < 10^{-6} mbar).

A.5 X-Ray Diffraction (XRD)

The discovery of X-rays by Wilhelm Conrad Roentgen in 1895 allowed important innovations in all scientific disciplines, making the development of new medical and

technical applications possible. In particular, the research on X-ray diffraction (XRD) by crystals initiated by Laue, Friedrich, and Knipping in 1912 opened new possibilities in the study of crystalline materials. The XRD methods are based on the ability of crystals to diffract X-rays in a characteristic manner allowing a precise study of the structure of crystalline phases. Recorded diffraction patterns contain additive contributions of several micro- and macrostructural features of a sample. With the peak position, lattice parameters, space group, chemical composition, macrostresses, or qualitative phase analysis can be investigated. Based on the peak intensity, information about crystal structure (atomic positions, temperature factor, or occupancy) as well as texture and quantitative phase analyses can be obtained. Moreover, the peak shape gives information about sample broadening contributions (microstrains and crystallite size). When X-ray photons reach matter, several types of interactions can take place leading to different absorption and scattering effects, which will not be treated here. An elastic (coherent) scattering, also called Rayleigh scattering, occurs between the photons and the electrons surrounding the atomic nuclei. In this case, the energy of the scattered wave is unchanged and it retains its phase relationship to the incident wave [29]. As a consequence, the X-ray photons impinging on all atoms of an irradiated volume are scattered in all directions [30]. However, due to the periodic nature of a crystalline structure, constructive or destructive scattered radiation will result, leading to characteristic diffraction phenomena which can be studied to investigate the crystal structure of materials. The principle of the methods is based on the diffraction of X-rays by periodic atomic planes and the angle or energy-resolved detection of the diffracted signal. The geometrical interpretation of the XRD phenomenon (constructive interferences) has been given by W.L. Bragg [31]. Figure A.8 gives the details about the geometrical condition for diffraction and the determination of Bragg's law given by the Eq. (A.59).

$$n\lambda = 2d_{hkl}sin\theta \qquad\qquad (A.59)$$

In Eq. (A.59), n is the order of diffraction, λ the wavelength of the incident beam in nm, d_{hkl} the lattice spacing in nm and θ the angle of the diffracted beam in degree.

In a polycrystalline, untextured material with fine grains, diffraction occurs for each lattice plane and direction that satisfies the Bragg's law in the case of constructive

interferences. This results in the occurrence of diffraction cones appearing in the form of so-called Debye rings or diffraction rings if detected by a plane detector (Figure A.9).
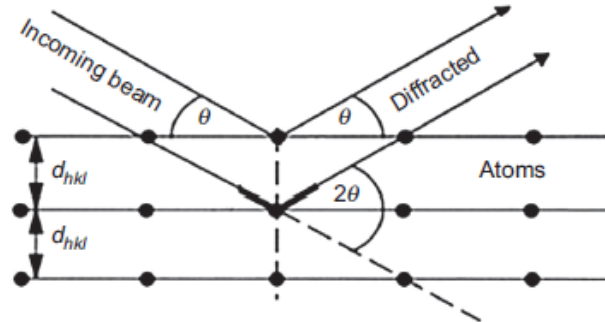
Figure A.8. Geometrical condition for diffraction from lattice planes.
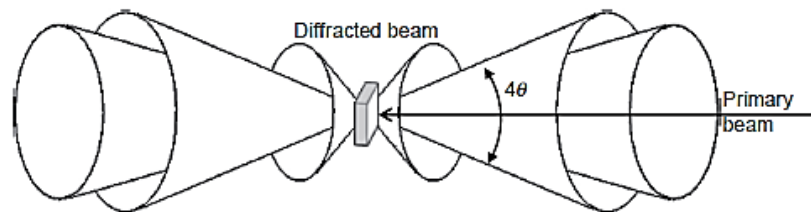
Figure A.9. Diffraction cones in transmission and reflection occurring for a polycrystalline material.

The total intensity diffracted by a considered unit cell is described by the summation of the intensity scattered from the individual atoms [30]. The diffracted intensities I_{hkl} are directly proportional to the square of the crystallographic structure factor $F_{(hkl)}$ which is a complex quantity (Eq. A.59)

$$F_{(hkl)} = \sum_{j=1}^{N} f_j \times exp\left(2\pi i(hx_j + ky_j + lz_j)\right)$$

(A.60)

with f_j the form factor or atomic scattering factor of atom j, hkl the Miller indices of the diffracting planes and xyz the relative atomic positions in the unit cell. The summation j runs over all atoms in one unit cell.

According to the crystal symmetry, different extinctions of interferences will occur, leading to different diffraction patterns. For example, in the case of body-centered

lattices, diffraction occurs if the condition $h + k + l = 2n$ is satisfied, while in face-centered lattices, the condition $h + k, k + l, h + l = 2n$ has to be satisfied.

The total diffracted intensity for a lattice plan family ($I_{(hkl)}$) depends on several factors. These terms are combined to obtain an expression describing the total intensity at any 2θ position (Eq. A.60):

$$I_{(hkl)} = K \times \left|F_{(hkl)}\right|^2 \times f_a e^{\frac{-B \sin^2 \theta}{\lambda^2}} \times A \times L(\theta) \times P(\theta) \times m \qquad \text{(A.61)}$$

with K, a constant independent of 2θ, $f_a e^{\frac{-B \sin^2 \theta}{\lambda^2}}$ the temperature factor describing the average displacement of atoms from their mean position due to temperature, A the absorption factor, $L(\theta)$ the Lorentz factor which is equal to $1/\sin 2\theta$, $P(\theta)$ the polarization factor which is equal to $(1 + \cos^2 2\theta)/2$ and m the multiplicity describing the number of equivalent planes that can diffract at a given Bragg angle [30].

As real materials always contain imperfections, the intensity distribution of the signal diffracted by considered family of *hkl* planes can be altered. The shape of the diffracted signal is influenced by different factors, and the resulting signal is then a convolution of the following contributions:

• The instrumental broadening which depends on the X-ray source, primary and secondary optics, detector, etc.;

• Composition heterogeneity within the analyzed crystallites (leading to a distribution of lattice constants and so to a possible broadening);

• The size of the coherently diffracting domains (also called crystallite size);

• Crystal defects like dislocations, stacking faults, twins, etc.;

• Inhomogeneous strains and microstrains.

In general, diffraction data are represented as intensity distribution as a function of the 2θ angle. The information content that can be extracted is represented in Figure A.10. After background subtraction, the maximum peak intensity Imax can be defined as well as the integrated intensity I_{int} (area under the peak). The peak position can be determined by several methods (center of gravity, fit of different mathematical function, etc.).
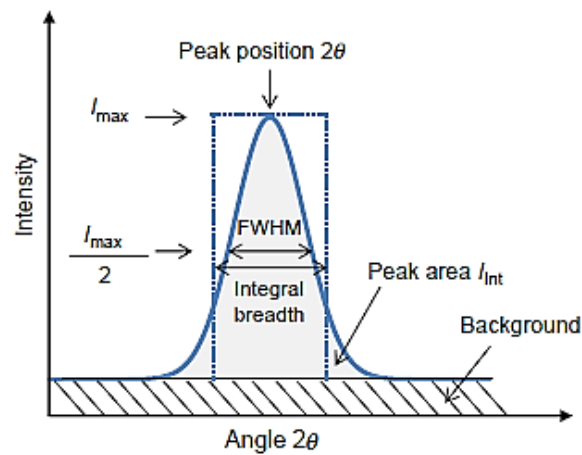
Figure A.10. Diffraction peak and information content that can be extracted.

The peak width can be generally characterized either by the full width at half maximum (FWHM) corresponding to the peak breadth at half of the maximum intensity, or by the integral breadth (IB), which corresponds to the width of a rectangle of the same maximal and integrated intensity as the considered peak. Depending on the purpose of the measurements, the different peak parameters are used.

As a consequence of absorption and scattering effects, X-rays are weakened along their path in the material. The intensity loss is exponential and follows the general law of Lambert-Beere. The transmitted intensity I can be calculated by Eq. (A.62) with I_0 being the initial beam intensity, x is the thickness of the absorbing layer, and μ is the mass absorption coefficient depending on the wavelength of the X-rays and on the material. The depth penetration of X-rays produced in laboratory equipment is typically in the range of a few micrometers to a maximum of several tens of micrometers for common wavelengths in metals.

$$I = I_0 \exp(-\mu x). \tag{A.62}$$

Modern lab diffractometers are computer-controlled and equipped with different hardware depending on their scope of action. The instruments are all composed of an X-ray source, primary and secondary optics, a goniometer, a sample holder, and a detector.

The goniometer, which is the central part of the diffractometer allowing to move the X-ray source, the sample and the detector relative to each other in a very precise manner. In general, Bragg-Brentano geometry is used, which means that the distance

between the sample and the detector is constant for all θ angles. For the investigation of powder or massive samples with laboratory equipment, the reflexion mode is generally used as the strong absorption of the X-ray beam by the material does not allow transmission measurements. Two major basic types of goniometer are widespread: θ/θ goniometers, where the sample is fixed [Figure A.11(a)], while the X-ray source as well as the detector moves, and $\theta/2\theta$ goniometers for which the X-ray source is at a fixed position while the sample and the detector are moving [Figure A.11(b)].
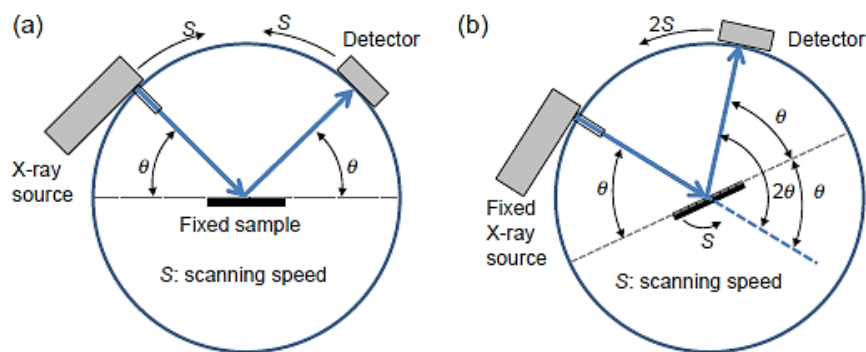
Fig A.11. Principle of (a) θ/θ goniometers and (b) of $\theta/2\theta$ goniometers.

For residual stress and texture measurements, additional rotation axes are generally required in order to position the sample as needed for these investigations. The in-plane rotation of a sample (azimuth angle φ) and the tilt-angle (also called pole angle χ) are commonly available (so-called four-circles goniometers). The χ -rotation can be either achieved by eulerian cradle, as shown in Figure A.12, by special tilting devices or by using a robot arm.

According to the sample geometry and the purpose of the measurement, specific sample holders (eg, to achieve automatic sample positioning, automatic sample changing, continuous sample rotation or translation, etc.), or even a controlled sample environment for in situ investigations can be used. In the case of powder samples, amorphous polymer or glass plates can be used to carry the powder. For solid samples, in particular for engineering applications, heavy samples and complex geometries are common. Therefore, adapted sample positioning devices have to be used.
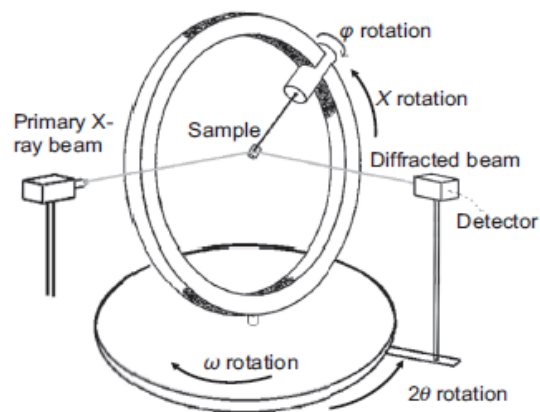
Figure A.12. Principle of a four-circles goniometer.

When a diffraction pattern has been measured, a qualitative phase analysis can be performed. In order to identify the present phases, a comparison of the present diffraction peaks with known data from a database has to be performed.

Once the present phases are known, quantitative phase content analysis can be performed. According to the investigated sample and the purpose of the analysis, different methods can be used:

• method with external standard: consists of comparing the intensity of the reflexion measured at a multiphase material with the intensity of a pure sample of the considered phase measured under the same experimental condition;

• method with internal standard: is based on the addition of a standard phase with defined volume or mass in the investigated compound. This is only possible for powder samples;

• method of intensity ratio: consists in calculating directly the intensity ratios of the reflexions of each present phase in a sample by correcting them with factors taking into account multiplicity and other parameters for each reflexion. This method is well indicated for solid samples for which the addition of an internal standard is not possible;

• Rietveld method: is a whole pattern method. This means that the evaluation is based on the simultaneous analysis of several peaks. Here, the whole measured pattern is refined with a calculated pattern taking into account several structural, microstructural, and experimental parameters.

A.6 X-ray Photoelettron Spectroscopy (XPS)

X-ray photoelectron spectroscopy (XPS), also known as electron spectroscopy for chemical analysis (ESCA), is a technique for analyzing the surface chemistry of a material. XPS can measure the elemental composition, chemical state and electronic state of the elements within a material. This spectroscopy is based on the photoelectron effect.

The energy of an incident photon (hv) is transferred to a bound electron. If the energy of the photon is greater than the binding energy of the electron and the electron has enough energy to overcome the work function (Φ) of the solid, it can leave the solid (Figure A.13).
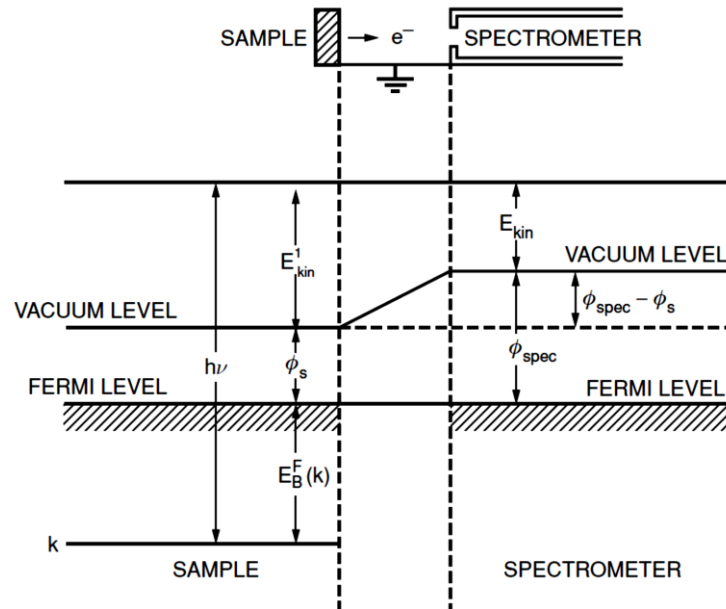
Figure A.13. Schematic representation of x-ray photoemission.

Due to the emission of the electron, the inner shell of the atom (A) is ionized. The energy conservation requires:

$$E(A) + hv = E(A^*) + E_{kin} + \Phi$$
$$E_{kin} = hv - [E(A^*) - E(A)] - \Phi = hv - E_B - \Phi \qquad (A.63)$$

where E_B is the binding energy relative to the Fermi level E_F and E_{kin} is the kinetic energy of the photoelectron (relative to the vacuum level E_V). The photoelectron

spectrum is given by the kinetic energy distribution of the photoelectron measured with an electron analyzer. For a known photon energy ($h\nu$) the binding energy can be determinate for all core electrons with $E_B < h\nu - \Phi$.

By collecting the emitted photoelectrons with an appropriate electron analyzer and studying the spectrum of the number of electrons versus its distribution of kinetic or binding energy, it is possible to recognize the material they come from. The analysis of a wide range of BEs will provide unique signatures of the elements as a function of their atomic number, thus providing elemental analysis.

To explain an XPS spectrum, a survey spectrum (Figure A.14) of elemental uranium excited by a 1486.6 eV Al $K\alpha$ monochromatic X-ray line is used. Primary peaks resulting from the photoelectron process (a) can be seen. Some of them are in groups of two peaks as a consequence of the spin-orbit splitting (degeneration) that takes place in all orbital levels except in the s one. The intensity ratio between the two peaks depends only on the angular momentum l of the orbital level, but the distance between them depends also on the atomic number Z. The width of every primary peak depends quadratically on three contributions, one related to the physical nature of the atoms, another one concerning the analyzer characteristics, and a final one produced by the excitation source. The physical contribution cannot be modified because it originates from Heisenberg's uncertainty principle, but the two others can be reduced by improving the technique methodology. The characteristic background (b) of the XPS spectrum is mainly due to the inelastically scattered electrons.
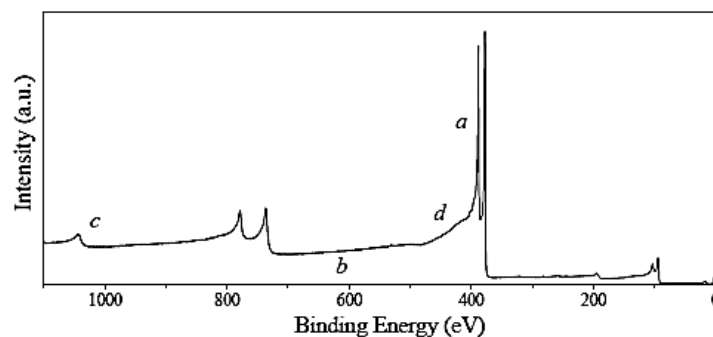
Figure A.14. XPS spectrum of elemental uranium.

The electrons excited by the X-ray source at a certain depth not too far from surface cannot leave the surface without losing kinetic energy by inelastic scattering with atoms

of the solid. This random energy loss appears in the spectrum as an increase of the background for binding energies greater than each primary peak. The Auger electrons (*c*) can also be detected in the spectrum. Some Auger transitions can be seen, but the energy position is not relevant because the transitions do not dependent on the irradiation energy. They appear as a broad band because they are the result of the different combinations of energy losses from electrons of two or three different orbital levels. Second order features of the XPS spectra (*d*) worth pointing out are: peaks due to the X-ray satellites of the excitation sources, shake-up and shake-off satellites, multiple splitting and asymmetric metal levels, and bulk and surface plasmons.

XPS can be considered as a quantitative technique, because the relative atomic concentration of the different constituents can be determined in elemental percentage. The number of electrons produced by photoelectric effect depends not only on the quantity of chemical elements present, but also on the ionization cross section of the orbital level (the probability that an ionization is produced) and other geometrical and analyzer parameters. The most common method used for quantification is the relative sensitivity factor (RSF) method, which supposes that

$$I = n \cdot F_S \tag{A.64}$$

where I is the intensity (or the area) of a photoelectric peak of a given element, n is the number of atoms per cm^3 of the element in the sample and F_S is a constant value called sensitivity factor which depens on the X-ray flux Thus, if all elements present at the surface are detected and one peak of each element with its well known Fs can be chosen, the following equation can be established

$$C_x = \frac{N_x}{\sum n_i} = \frac{I_x/F_s}{\sum I_i/F_i} \tag{A.65}$$

where C_x is the concentration of one element in percentage present at the surface.

In XPS measurements, a soft monochromatic X-ray source obtained by high-voltage excitation (10 to 15 kV) under UHV conditions is used as excitation source. Usually

Al K_α or Mg K_α lines, with energies of 1486.6 eV and 1256.6 eV respectively, are used because they have enough energy to excite orbital levels of all stable atoms and are thin enough to be used in HR measurements. To decrease the energy width that these sources introduce, the use of a monochromator is advisable, which also reduces satellites, Bremsstralhlung irradiation and other minor artefacts.

The spectrometer part of XPS equipments consists of electromagnetic lenses, an analyzer and a detector or electronic counting system (Figure A.15). The lenses usually operate in a mode called constant analysis energy (CAE), which retards the electrons to specific energies (called pass energies) and allows to have constant energy resolution along all the range of kinetic energies. The lenses also drive the electrons to the entrance of the concentric hemispherical analyzer (CHA). A CHA consists of two charged concentric metal hemispheres that create an electric field between them. The electrons going across it are captured by the outer or inner sphere depending on their kinetic energy. Only electrons in a narrow energy region (close to the pass energy) succeed in getting all the way round from the hemispheres to the detector. The detector is often a multichannel electronic device that can collect several groups of electrons with different kinetic energies. Spectrometers define the effective area of measurement, typically a circle of about 0.8 mm in diameter. A tricky feature of them is that the intensity is inversely proportional to the energy resolution of any mode of working.
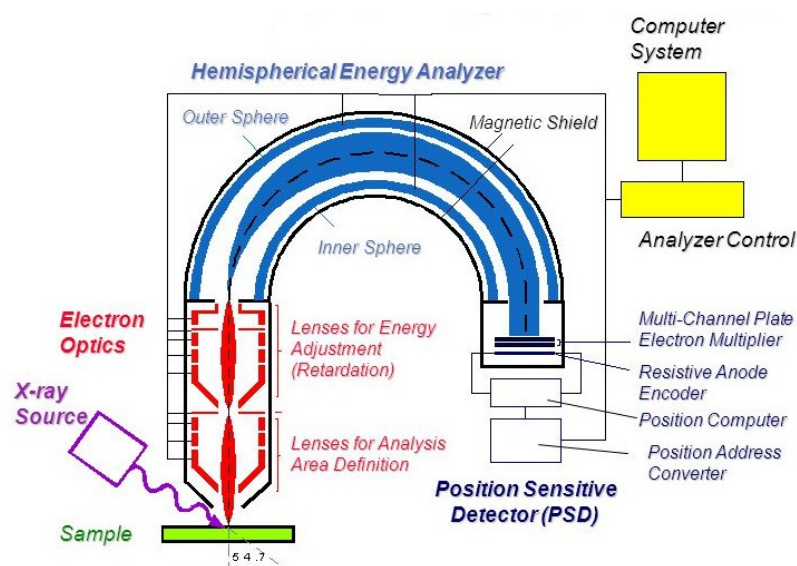
Figure A.15. Schematic representation of an XPS system.

References

[1]   T. Lovell, Himo F., W.G. Han, Density functional methods applied to metalloenzymes, L. Noodleman, Coord. Chem. Rev. **238**, 211 (2003).

[2]   P.E.M Siegbahn, and M.R.A Blomberg, Density functional theory of biologically relevant metal centers, Annu. Rev. Phys. Chem. **50**, 221 (1999).

[3]   M. Springborg, Density-functional methods in chemistry and material science New York: Wiley (1997).

[4]   E. I. Solomon, and K. O. Hodgson, Ed., ACS Symposium Series 692: Spectroscopic Methods in Bioinorganic Chemistry, American Chemical Society: Washington DC, **179** (1998).

[5]   C. Daul, E. J. Baerends, and P. Vernooijs, A density functional study of the mlct states of [ru (bpy) $_3$] $^{2+}$ in D_3 symmetry, Inorg. Chem. **33**, 3538 (1994).

[6]   D.M. Adams, L. Noodleman, and D.N. Hendrickson, Density Functional Study of the Valence-Tautomeric Interconversion Low-Spin [Co^{III}(SQ)(Cat)(phen)] $\rightleftharpoons$ High-Spin [Co^{II}(SQ)$_2$(phen)], Inorg. Chem. **36**, 3966 (1997).

[7]   L. Noodleman, and E.J.J. Baerends, Electronic structure, magnetic properties, ESR, and optical spectra for 2-iron ferredoxin models by LCAO-X. alpha. valence bond theory, Am. Chem. Soc. **106**, 2316 (1984).

[8]   S.J.A Van Gisbergen, J.A. Groeneveld, A. Rosa, J.G. Snijders, and E.J.J. Baerends, Excitation Energies for Transition Metal Compounds from Time-Dependent Density Functional Theory. Applications to MnO$_4^-$, Ni(CO)$_4$, and Mn$_2$(CO)$_{10}$, Phys. Chem. A **103**, 6835 (1999).

[9]   E. Runge, and E.K.U. Density-functional theory for time-dependent systems, Gross, Phys. Rev. Lett **52**, 997 (1984).

[10]   E.K.U., Gross, J.F. Dobson, and M. Petersilka, In Density Functional Theory, Springer Series, Topics in Current Chemistry; Nalewajski, R.F., Ed.; Springer: Heidelberg, Germany (1996).

[11]   M.E. Casida, In Recent Advances in Density-Functional Methods; D. P. Chong, Ed., World Scientific: Singapore (1995).

[12]   S J.A. van Gisbergen, J.G. Snijders, and E.J.J. Baerends, A density functional theory study of frequency-dependent polarizabilities and Van der Waals dispersion coefficients for polyatomic molecules, Chem. Phys. **103**, 9347 (1995).

[13]   R. Bauernschmitt, and R. Ahlrichs, Treatment of electronic excitations within the adiabatic approximation of time dependent density functional theory, Chem. Phys. Lett. 256, 454–464 (1996).

[14]   S.J.A van Gisbergen, J.G. Snijders, and E.J.J. Baerends, Calculating frequency-dependent hyperpolarizabilities using time-dependent density functional theory, Chem. Phys. **109**, 10644–10656 (1998).

[15]   F. Furche, R. Ahlrichs, C. Wachsmann, E. Weber, A. Sobanski, F. Vögtle, and S. Grimme, Circular dichroism of helicenes investigated by time-dependent density functional theory, J. Am. Chem. Soc. **122**, 1717 (2000).

[16]   J. Autschbach, T. Ziegler, S.J.A van Gisbergen, and E.J.J. Baerends, Calculating molecular electric and magnetic properties from time-dependent density functional response theory, Chem. Phys. **116**, 891 (2002).

[17]   S. Grimme, Chem. Phys. Lett., **339**, 380–388 (2001).

[18] S.J.A. van Gisbergen, J.G. Snijders, E.J. Baerends, Calculation of frequency dependent optical rotation using density functional response theory, Chem. Phys. Lett. **259**, 599 (1996).

[19] V. P Osinga, S. J. A. van Gisbergen, J. G. Snijders, E. J. J. Baerends, Chem. Phys. **106**, 5091 (1997).

[20] C. Van Caillie, R.D. Amos, Geometric derivatives of density functional theory excitation energies using gradient-corrected functionals, Chem. Phys. Lett. **317**, 159 (2000).

[21] A.J. Bennet, Influence of the electron charge distribution on surface-plasmon dispersion, Phys. Rev. B **1** , 203 (1970).

[22] H. F. Budd and J. Vannimenus, Surface Forces and the Jellium Mode, Phys. Rev. Lett. **31**, 1430 (1973).

[23] M. Rocca, Low-energy EELS investigation of surface electronic excitations on metals, Surface Science Reports **1**, 1 (1995).

[24] E.D. Jesson, J.S. Pennycook (1995), Incoherent Imaging of Crystals Using Thermally Scattered Electrons, Proc. Roy. Soc. A. 449, 273 (1936).

[25] P.D. Nellist, S.J. Pennycook, The principles and interpretation of annular dark-field Z-contrast imaging, Advances in Imaging and Electron Physics, Elsevier, pp. 147–203, (2000).

[26] Max T. Otten, High-Angle annular dark-field imaging on a tem/stem system, Journal of Electron Microscopy Technique **17**, 221 (1992).

[27] M.A. Van Hove, Atomic-scale structure: From surfaces to nanomaterials, Surface Science **10**, 1301 (2009).

[28] E.A Soares, M.C. Caio de Castilho, and E. Vagner de Carvalho, Advances on surface structural determination by LEED, Journal of Physics: Condensed Matters **30**, (2011).

[29] R.E Dinnebier, and S.J.L Billinge, Powder Diffraction: Theory and Practice. Royal Society of Chemistry (2008).

[30] I.C. Noyan and J.B. Cohen, Noyan, Residual Stress, Measurement by Diffraction and Interpretation, New York: Springer Verlag (1987).

[31] W. H. Bragg and W. L. Bragg, The reflection of X-rays by crystals, Proceeding of the Royal Society of London (1913).

Part II

3 Carbon nano-onions

3.1 Introduction

Since the discovery of the fullerene C_{60} [1], carbon nanomaterials have been attracted much attention due to their singular properties.

Carbon nano-onions (CNOs) comprise a new class of carbon allotropes with unique microstructural and electronic properties. CNOs in their spherical or polyhedral form, are made of concentric shells of graphitic carbon. Due to their high surface area [2–4], high electric conductivity (1–10 S/cm) [4-6], high thermal stability and appropriate mesoporous microstructure [2,3,7,8], CNOs are getting rapidly growing attention for various applications. Many potential applications of CNOs have been proposed, including gas storage [9], photovoltaic cells [3], optically transparent electrodes [10], catalysis [11], electrochemical energy storage devices [8,12–16], and biomedical applications [17]. CNOs' desirable electrical conductivity and higher surface area than carbon nanotubes (CNTs) make them potential candidates for the development of miniaturized fuel cells [3]. The tribological properties of CNOs impart them with adequate and even superior lubrication properties compared to conventional graphitic materials and other lubricants [18].

3.2 Stuctural properties

CNOs are spherical or polyhedral carbon nanoparticles (Fig 3.1), but unlike fullerenes [1,19] they consist not of just one but of several concentric stacks of graphene-like carbon shells.
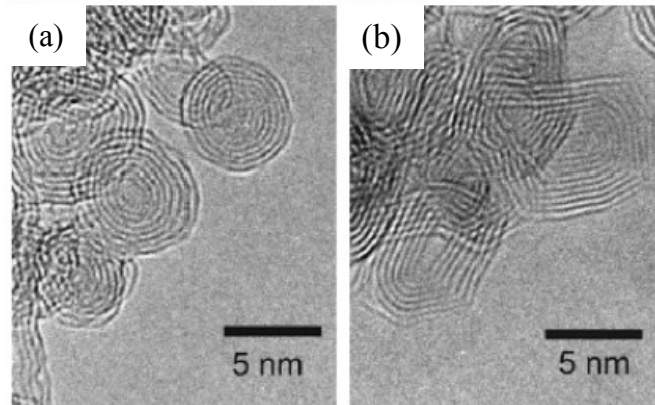
Figure 3.1. HRTEM images of (a) spherical carbon onions and (c) polyhedral carbon onions [20].

The structural properties of CNOs depend on the precursor, the synthesis conditions, and the post-synthesis treatment.

Nanodiamonds [21] are an interesting precursor for the gram-scale synthesis [22] of carbon onions with high level of control over the resulting structure and properties via thermal annealing [4].

The typical size of nanodiamonds used for CNOs synthesis is around 5 nm [21] with dangling bonds on the surface that are typically stabilized by functional groups, mostly carboxyls [21,23], and locally terminated by a thin layer of sp^2-hybridized carbon [24-26]. These two surface features contribute to the aggregation of individual nanodiamond particles forming clusters in the range of tens to hundreds of nanometer [27]: individual grains are engulfed by thin layers of graphitic carbon or covalently linked by bridging functional groups [21,27], leading to the formation of so-called tight agglomerates. In addition, a significant mass of each nanodiamond grain is not related to carbon but to nitrogen, oxygen, and hydrogen, and metal impurities such as iron, silver, or copper are often found [21].

Studies on the synthesis of carbon onions from nanodiamonds indicate that the sp^3-to-sp^2 transformation starts at around 600 °C by forming amorphous carbon [28]. At temperatures between 900 and 1100 °C, this amorphous layer progressively graphitizes and continuing sp^3-to-sp^2 transformation protrudes from the outside to the core of the particles [29]. TEM investigations have shown that smaller particles can be transformed to sp^2-hybridized carbon more readily resulting in a possible coexistence of small carbon onions with larger, partially transformed nanodiamonds [29,30,31]. In addition,

the presence of surface functional groups significantly influences the onset temperature of the nanodiamond-to-CNO conversion [32].

Conversion from nanodiamond to a fully graphitized CNOs was investigated using XRD analysis. The diffraction pattern of the nanodiamond powder compared to those of the carbon nano onions synthesized at various temperatures is shown in Figure 3.2 [33]. XRD of nanodiamond samples [Figure 3.2(a)] has prominent peaks at angles of 43.34°, 74.68°, 90.36° and 118.37° which correspond to the normal peaks for the [111], [220], [311] and [400] diamond planes, respectively. In addition, a small peak centered at 26° corresponding to the [002] peak of graphite was also observed, suggesting that there may be some contribution from surface sp^2 carbon fragments. Upon annealing at 1400 °C [Figure 3.2(b)] a significant narrowing of the diamond peaks followed by a significant increase in the intensity of the [002] graphitic peaks and the appearance of the [004] and [110] graphitic peaks was observed. Further annealing at 1700 °C results in an almost complete disappearance of the diamond [111] peak as well as a significant reduction of the second, third and fourth diamond peaks. This indicates that much of the sp^3 coordination has been effectively removed at higher temperatures [Figure 3.2(c)]. Further heating transforms the spectrum completely into a graphitic one, with well pronounced [002], [100], [004], [110] and [200] peaks [Figure 3.2(d)]. During the transformation, not only the carbon onion/diamond ratio increases, but also the degree of sp^2 carbon ordering. A high degree of sp^2 carbon ordering is desirable to enhance the electrical conductivity and can be accomplished by using high synthesis temperatures (above 1500 °C). With higher annealing temperature, carbon onions become more graphitic, leading to an increase of the density states of conductive electrons and furthermore to a higher intrinsic conductivity [111] For spherical carbon onions, consisting of small poorly connected domains of graphitic sp^2-hybridized carbon, dangling bonds due to structural defects were detected using electron spin resonance (ESR). The p-electrons localized in the small graphitic domains might not provide sufficient conductivity. Gan and Banhart showed that spherical carbon onions are highly stable up to temperatures of more than 1200 °C [34]. For comparison, in polyhedral carbon onions, which form at temperatures higher than 1800–1900 °C [4,35] dangling bonds were reduced and delocalization of p-electrons increased the intrinsic conductivity [35].
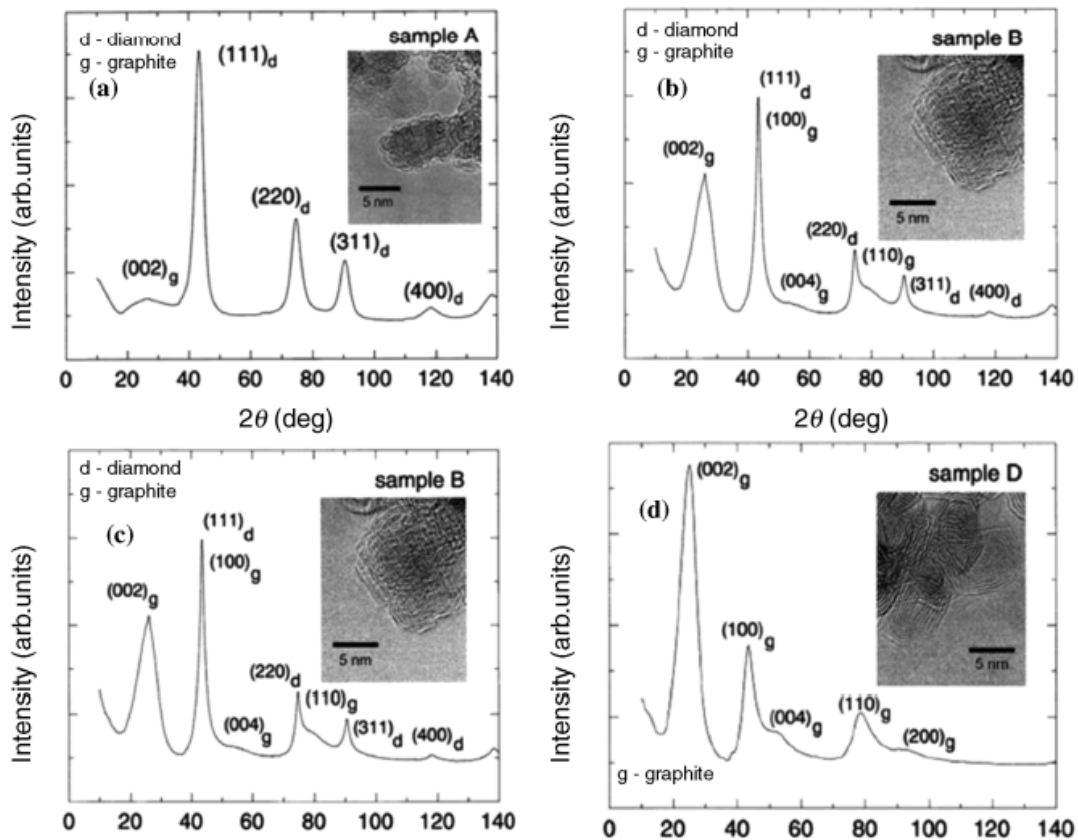
Figure 3.2. X-ray diffraction intensity of (a) nanodiamond (b) after heating at 1400 °C (c) after heating at 1700 °C (d) after heating at 2000 °C [33].

Raman spectroscopy is a powerful tool to characterize the structure of carbon onions [36-40]. The spectrum of a nanodiamond powder shows a relatively narrow single Raman band at 1323 cm^{-1} over a strong photoluminescence background. This band is a characteristic signal of the nanodiamonds. Due to crystal size effects, the position is shifted toward lower wavenumbers when compared with that of a single diamond crystal (1332 cm^{-1}) [38]. The Raman spectrum of the nanodiamonds annealed at temperatures around 900 °C show two wide Raman bands, the D band at 1350 cm^{-1} and the G band at 1600 cm^{-1}. As a consequence it has been proposed that the two bands arise from the carbon phase formed on the surface of a diamond particle to stabilize the sp^3 -bonds left dangling after the thermal desorption of the foreign impurities (Figure 3.3) [38]. At 1100 °C the weak peaks from the diamond core almost completely disappear and the D band corresponding to the defective carbon nano-onions being formed becomes even more pronounced. At temperatures around 1500 °C the Raman spectrum of this sample shows peaks of disordered carbon (D peak at 1350 cm^{-1} and G

peak at 1584 cm^{-1} with a distinctive side band at 1572 cm^{-1}). At temperatures between 1500–1800 °C onions form joint graphitic layers with their neighboring onions and the Raman spectra are similar to those of amorphous carbon. At the highest annealing temperatures nanodiamonds transform into a multi-shelled structure with the Raman bands becoming even more pronounced.
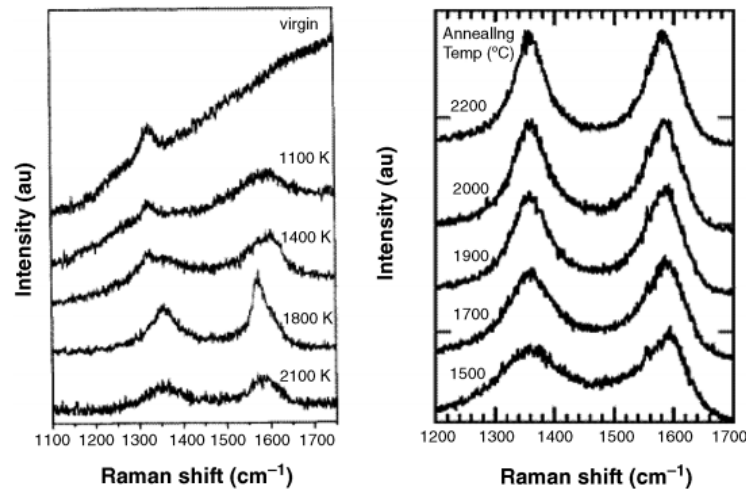
Figure 3.3. Evolution of the Raman spectra of the nanodiamonds with increasing temperature [35,38].

The Raman spectra of polyhedral carbon nano-onions (PCOs), obtained by underwater arc discharge of graphite electrodes, have been studied by Pujals et al. [41]. While the general Raman spectrum of PCO is very similar to those of other carbon nanostructures, including spherical nano-onions, the fine structure of the G and 2D bands gives valuable information that allows using Raman spectroscopy for differentiating the PCO from other carbon structures. In particular, the authors observed that in these materials the G band is composed of two or three peaks, which correspond to different contributions from the curved zones and from the plane zones of the polyhedron [Figure 3.4(a)]. The 2D band is basically composed of two or four peaks [Figure 3.4(b),(c)], with the former corresponding to PCOs with graphitic turbostratic walls, while the latter comes from particles with walls formed by ordered graphite. The existence of cases with more complex fine structure of the 2D band is also reported, as well as the presence of a very defined and sharp peak in the zone of (1400–1450) cm^{-1} , which is absent in the Raman spectra of the spherical nano-onions.
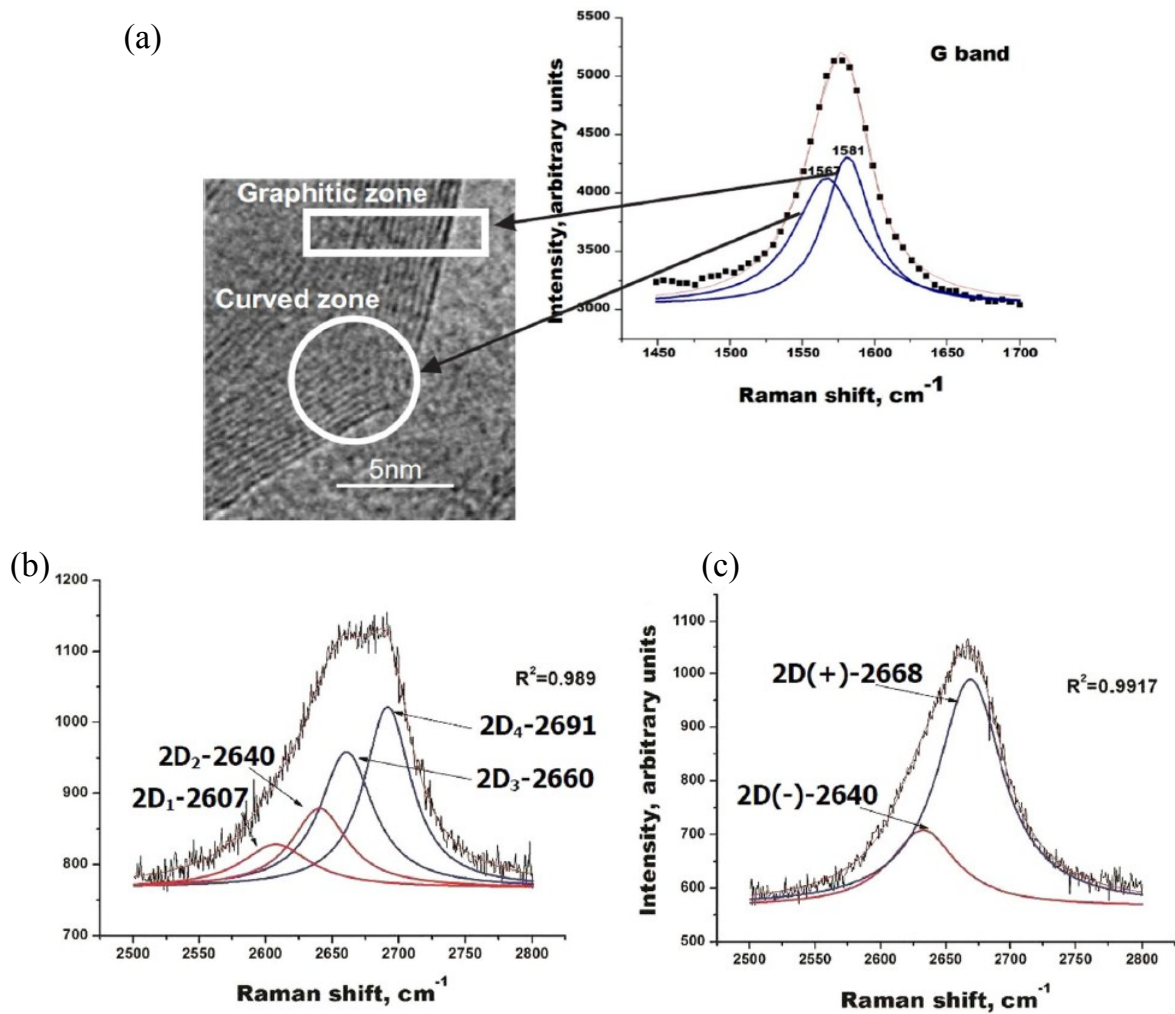
Figure 3.4. Raman spectra of PCOs [41]. (a) Deconvolution of the Raman G band in two Lorentzians and the association of each peak of the doublet with different zones of the PCO as seen in TEM image. (b), (c) Two examples of fitting of the 2D band in different samples. In (a) the fitting was obtained with four Lorentzians, while in (b) with only two of them.

3.3 Synthesis of CNOs

CNOs were observed for the first time in 1980 by Iijima [42]. In 1992, Ugarte [43], obtained CNOs by strong electron irradiation of carbon soot containing tubular carbon structures and amorphous carbon.

Among the different methods for the synthesis of CNOs, the more investigated in recent years are the annealing of detonation nanodiamonds, and the arc discharge between graphite electrodes in deionized water.

The Kuznetsov method [44] is based on annealing ND particles (average diameter of 5 nm) at high temperatures in an inert atmosphere under a high vacuum [44]. This method leads to the creation of spherical CNOs with a small diameter (6-8 graphitic shells and diameters of 5-6 nm) and high reactivity. As mentioned above, the production of this CNOs is a multistep process. The physico-chemical properties of nanodiamond-derived CNOs are described in Figure 3.5 as a function of synthesis temperature [30,36,45-49]. The graphitization process of NDs starts at 600 °C on the surface and progressively extends into the bulk of the particle. The transformation of sp^3 to sp^2 starts by amorphous carbon, which graphitizes at temperatures between 900 and 1100 °C. The complete transformation of the diamond core occurs at temperatures above 1600 °C. This annealing leads to the formation of small spherical carbon particles. Further thermal annealing of NDs leads to the formation of polyhedral nanostructures with simultaneous formation of tight agglomerates. The thermal annealing of NDs at temperatures ranging from 1100 to 1900 °C results in an increase in the ratio of the number of carbon atoms sp^3 to sp^2 from 0.39 to 1.

		700-800 °C	900-1100 °C	1300-1500 °C	>1700 °C
mass	100 %	95 %	91 %	90 %	88 %
oxygen content	5 %	4 %	4 %	3 %	1 %
ND content	>90 %	>90 %	>75 %	>40 %	0-5 %
density	3.3 g/cm³	2.9 g/cm³	2.5 g/cm³	2.5 g/cm³	1.9 g/cm³
surface area	280 m²/g	300 m²/g	350 m²/g	390 m²/g	400 m²/g
sp² carbon ordering	very low	low	low	medium	high
conductivity	~ 0 S/cm	0.25 S/cm	2 S/cm	2 S/cm	2-4 S/cm
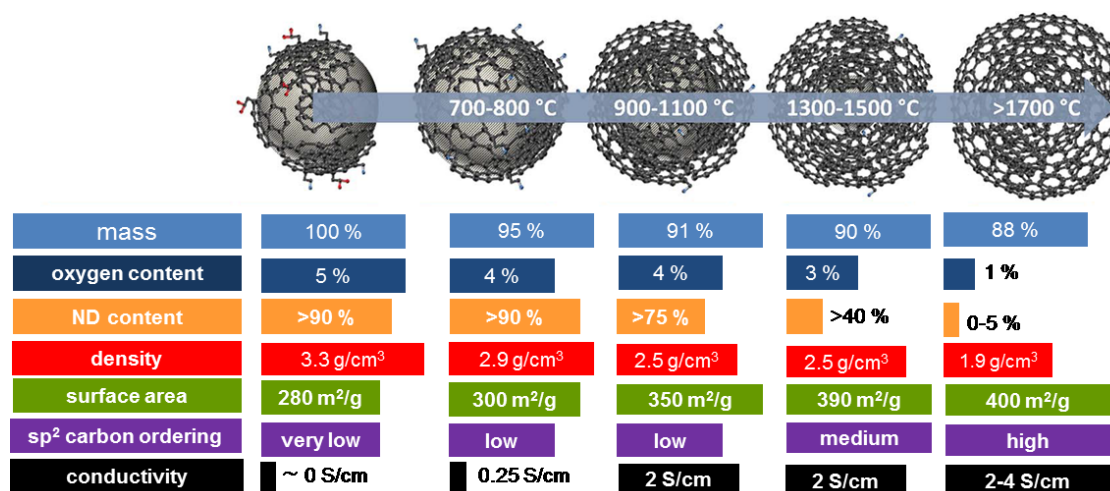
Figure 3.5. Properties of nanodiamond-derived carbon onions dependent on the synthesis temperature. [50].

Kuznetsov et al. proposed a mechanism for the formation of carbon nano onions using what has been described as a zipper type mechanism. It has been proposed that out of every three [111] diamond planes, the center plane migrates into the bulk of the diamond crystal. The atoms of the central diamond layer distribute equally in the formation of two graphitic sheets. This is the only way in which one can obtain the

same lengths for the two growing graphitic sheets. Figure 3.6 illustrates the process, in which each of the marked groups of atoms contributes to the formation of an additional row of graphite sixfold rings. The process probably proceeds via successive insertion of two carbon atoms per two sixfold ring of a growing sheet with the intermediate formation and subsequent reconstruction of eightfold rings [51].
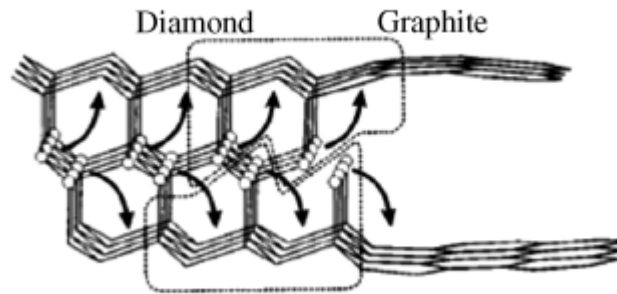
Figure 3.6. Proposed mechanism of transformation of nanodiamonds into carbon nano onions [51].

This process is also connected with a decrease in the density of CNOs from 3.3 to 1.9 g cm^{-3}, suggesting a change in the ND structure in the CNOs [40-44]. These values are close to the density of ND ($\sim$ 3.3 g cm^{-3}) and graphite carbon ($\sim$ 2.2 g cm^{-3}) [53]. At the same time, increasing the ND annealing temperature above 1700°C leads to an increase in the electrical conductivity from 0 to approximately 4 S cm^{-1} (Figure 3.5) [54]. The specific surface area (SSA) values determined by the nitrogen adsorption/desorption technique for CNOs were as high as ca. 560 m^2 g^{-1}, which varies from the ND of ca. 300 m^2 g^{-1} [7,45]. This value is mainly related to particle size. For NDs with diameters of 4-6 nm and 5-7 nm, the SSA was 370-556 m^{2}g^{-1} and 259-363 m^2 g^{-1}, respectively [45]. SSA is also connected with the size and chemical character of CNO agglomerates, which are usually covered by amorphous carbon or graphene-like layers [45].

In 2001 Sano and co-workers reported the arc discharge synthesis of carbon nano onions underwater [54]. In this method, two high purity graphite rods were electrically arced under water by applying a bias potential of 16–17 V between them and maintaining a constant current of 30 A. During the synthesis, CNOs with average diameter of 25–30 were obtained as a floating powder on the surface of the water while

other subproducts such as multi-walled carbon nanotubes precipitated to the bottom of the container.

In 2002, the same group proposed a formation mechanism of CNOs and carbon nanotubes (CNTs) in a water arc [9]. In such model, solidification of carbon vapor is supposed to happen in a bubble surrounding the plasma zone, and is attributed to the temperature gradient present in the bubble from the hotter region to the gas–water interface (Figure 3.7). Moreover, the main gaseous components in the bubble are supposed to be CO and H_2, and the mechanism of formation of CNOs and CNTs is related to the directionality of C ion currents in the bubble. Therefore, they supposed the synthesis of CNTs to be favored in the zone adjacent to the plasma, whereas CNOs were favored in the peripheral zone of the bubble, far from the hot plasma zone. In a successive investigation, the same group obtained CNOs by grinding the solid fragments found mostly at the bottom of the reactor [39]. They did not observe any deposits on the cathode, but they supposed some of the recovered fragments as due to the peeling of deposits formed similarly to what happens in arc discharge experiments in He [55]. In 2004, the Sano group compared the nanomaterials obtained by arc discharge between graphite electrodes in water and in liquid nitrogen [56]. In water, they collected samples containing only CNOs on the top of a thick powder floating, and they attributed this finding to a self-separation process leading to the aggregation of CNOs. Rettenbacher et al [57] found no differences in the percentage of CNOs between samples floating or recovered on the bottom of the reactor.

Borgohain et al. [58] optimized the production of CNOs by an automated apparatus, reporting also an efficient purification method based on the reactivity of CNOs with polyoxometalates. However, the authors did not mention any formation of cathodic deposits. Recently, Kim et al. [59] produced graphitic nanoparticles with different dimensionalities by varying the power in underwater arc discharge. However, the authors did not report the observation of any cathodic deposits, probably due to the particular experimental arrangement, in which the anode was moved so as to contact the cathode 2 times per second.
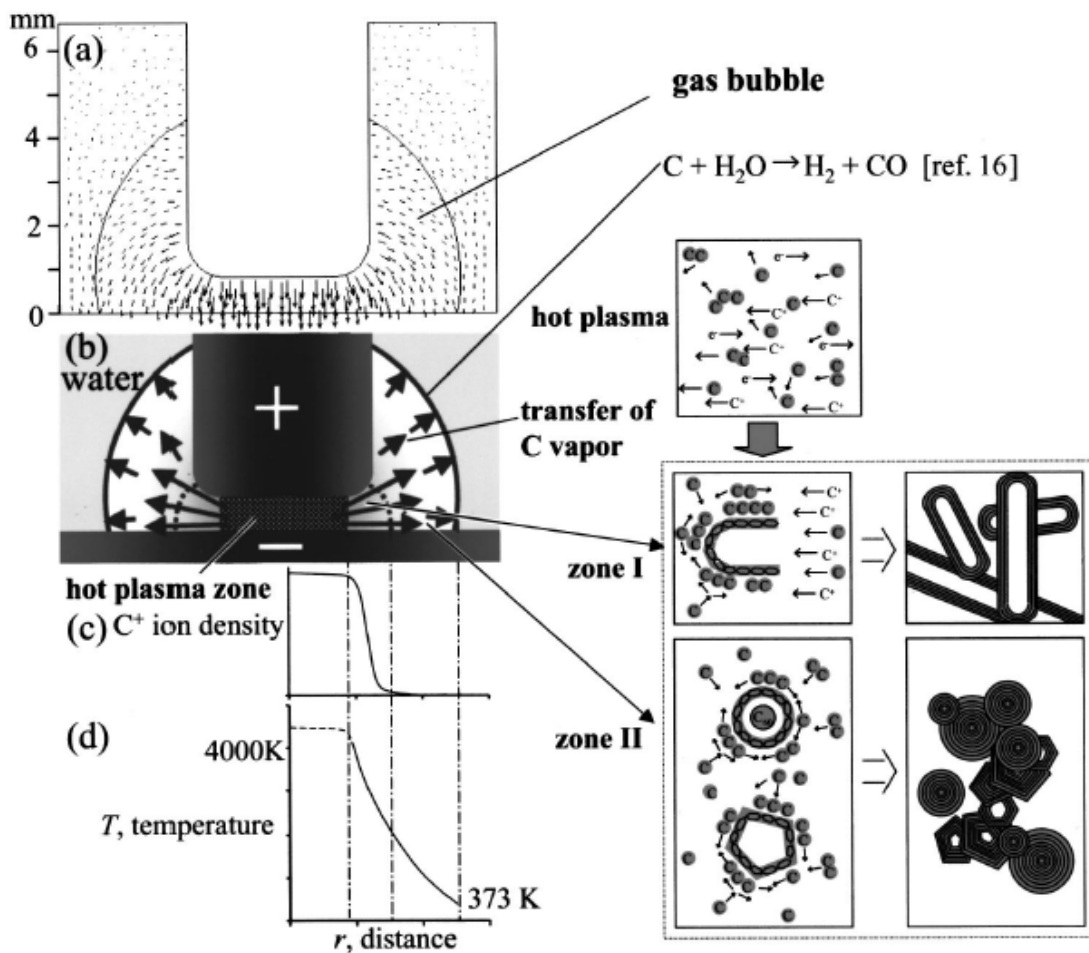
Figure 3.7. Production mechanism of carbon nano-onions in a water arc discharge [18].

CNOs prepared by arc discharge inevitably contain a large amount of carbonaceous impurities such as polyaromatic hydrocarbons, amorphous carbon, CNTs, CNT-like structures, graphitic debris and metallic impurities. Carbonaceous impurities originate from incomplete vaporization of graphitic particles dislodged from the rods and from the uncontrolled formation of other nanostructures in the plasma.

Thus, purification is essential to obtain high-purity CNOs suitable for fundamental research and targeted applications.

Since CNOs have similar behavior to CNTs, purification methods can be adapted from reported CNT purifications. Chemical methods utilized to purify CNTs are based on faster etching of amorphous carbon compared to ordered carbon nanoparticles [60]. Chemical oxidation can be conducted in the gas phase, the liquid phase (refluxing acidic solution) or to some extent via electrochemical oxidation [61]. In liquid-phase

oxidation, various oxidizing agents such as HNO_3, H_2O_2, Br_2 or $KMnO_4$, often a combination of strong acids, are commonly used to remove amorphous carbon and metal impurities from CNTs [62,63]. However, these harsh treatments usually produce unwanted defect sites in CNTs. Other types of purifications based upon the physical properties such as differences in size, aspect ratio, solubility, thermal stability and electronic or magnetic properties of constituents in the sample have led to the extensive study on methods such as chromatography [64], centrifugation, electrophoresis [65], field-flow fractionation (FFF) [66] and high-temperature annealing (graphitization) [67]. Most of these methods require high dispersion of materials, which is often difficult to achieve. Fullerenes can be easily removed by extraction with organic solvents. Trace metal impurities are usually removed by washing with mineral acids. Polyaromatic hydrocarbons and amorphous carbon can be eliminated by mild oxidation because of their high density of defects [61].

For CNOs purification, further challenges come from carbonaceous impurities such as CNTs, CNT-like structures and graphitic debris that have similar physical/chemical properties. These carbonaceous impurities have a small difference in thermal stability; so direct annealing at high temperature cannot remove them effectively. These factors make it difficult to develop highly efficient purification methods based on only physical or chemical properties of A-CNOs, so an efficient combination is required to purify them.

3.4 Potential applications

Biological sensing: In the study of Luszczyn et al. [68], CNOs were covalently functionalized with biomolecules and studied for the first time as biosensors by using avitin–biotin interactions. The CNO served as linking layers between the biomolecules and the gold surface of the sensor and led to an amplified signal of the biosensor, as determined by surface plasmon resonance spectroscopy. In addition, the biocompatibility of CNOs was investigated and found to be excellent.

Enviroment: An application of CNO in environmental remediation was studied by Li group [69], who revealed that surface-oxidized CNO in aqueous suspensions have a high sorption capacitance for heavy metal ions such as Pb^{2+}, Cu^{2+}, Cd^{2+}, Ni^{2+} and Zn^{2+}. The sorption capacitance of oxidized CNOs was found to be up to ten times higher than the one of fullerene C_{60}. These encouraging results could be a first step toward in situ remediation of heavy metal contaminants.

Lithium-Ion batteries: Carbon nanotubes are widely studied for a use in lithium ion batteries [70]. H. Y. Yang and co-workers reported lithium-ion batteries incorporating CNOs in combination with Co_3O_4 [64] and MnO_2 [71] as electrode material. In the earlier study, they observed an increase of the specific capacitance from 190 $mA \cdot h \cdot g^{-1}$ to 632 $mA \cdot h \cdot g^{-1}$ at a current density of 200 $mA \cdot g{-}1$ and also an increased rate capability [72]. In the latter, the specific capacitance increased from 260 $mA \cdot h \cdot g^{-1}$ to 630 $mA \cdot h \cdot g^{-1}$, at a current density of 50 $mA \cdot g^{-1}$.

Capacitors: Carbon materials are commonly used as electrode materials in capacitors, but the first study probing CNOs as electrode materials in electrical double-layer capacitors (EDLC) with an organic electrolyte was published only in 2007 [7]. Bushueva et al., found capacitance values of the investigated CNO material of 20–40 $F \cdot g^{-1}$ and 70–100 $F \cdot g^{-1}$ with acidic or basic electrolyte solutions, respectively [73]. In 2010, Pech et al. published the preparation and characterization of ultrahigh-power micrometer-sized supercapacitors based on CNOs [8]. In an extensive electrochemical study in different aqueous and organic electrolytes, McDonough et al. investigated the influence of the CNO structure on their electrochemical performance in supercapacitor electrodes [4]. Composite materials were studied for application in capacitors as well. The specific electrochemical capacitance of a CNO–PANI composite (206.64 $F \cdot g^{-1}$) was much larger than for pure oxidized CNOs (12.15 $F \cdot g^{-1}$) [15]. Another example for CNO composite-based capacitors was reported by the group of H. Y. Yang [74]. The composite was prepared from $KMnO_4$ and CNOs in different weight ratios in deionized water by heating in an autoclave. The formed CNO–MnO_2 composite was then implemented in an asymmetric pseudocapacitor with the CNO–MnO_2 composite as

working electrode and nickel foam as counter electrode. The capacitance of pure MnO_2 ($40 \ F \cdot g^{-1}$) could be increased by the incorporation of CNO up to $177.5 \ F \cdot g^{-1}$.

Catalysis: One of the most important catalytical reactions in industry is the oxidative dehydrogenation (ODH) of ethylbenzene to styrene. In 2002, Keller et al. published a study showing the potential of CNOs as catalyst for this reaction with conversion levels of up to 92% after an activation period of 2h and stable styrene yields of 62%, outperforming industrial K–Fe catalysts and other carbon materials [11].

Trybology: In tribology, CNOs are widely studied and have shown promising results as lubricants. In 2002, Cabioc'h et al. reported that CNOs incorporated in silver layers significantly reduced wear, while the friction coefficient is largely unaffected by their presence [75]. In the following years, several reports were published on the characterization of the tribological properties of CNO materials, produced through different methods [76-78]. Mechanisms by which CNOs can reduce friction and wear were investigated in greater detail in 2009 by Martin and collaborators in a combined experimental and computational study [79].

3.5   Results and discussion

3.5.1 Experimental apparatus

Two high purity graphite rods were approached in deionized water while applying a bias potential between them. The electrode diameters were 5 and 10 mm for the anode and the cathode respectively, and they were mounted on an apparatus submerged in a $1000 \ cm^3$ beaker. Figure 3.8 shows a schematic illustration of the experimental apparatus, which allowed to translate the anode and to rotate it around its axis. The roto-translation allowed to approach the anode to the fixed cathode, and to maintain a stable discharge on time intervals of the order of 5 min.

The best discharge conditions were obtained for a bias potential of 12 V and a current of 30 A, with a rotation speed of the anode of 20 rounds per minute.
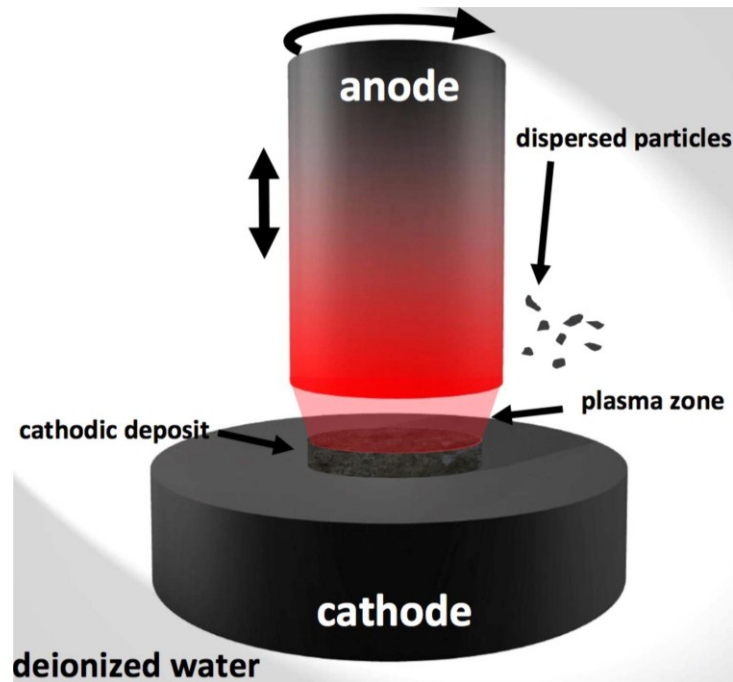
Figure 3.8. Schematic illustration of the experimental apparatus used for arc discharge experiments, in which the anode rotates as it moves towards the cathode.

In these conditions, a powder dispersed in water was formed, partially floating and partially at the bottom of the beaker. The floating material was collected by a microscope slide, while the bottom material was obtained by evaporating water at 80 °C. Moreover, a cylindrical-shaped black hard deposit of about 3 mm diameter was found, weakly bound to the surface of the cathode, and it was possible to remove it by applying a weak lateral force.

Scanning electron microscopy [Appendix B.5] was used to obtain images of the electrodes and of the cathodic deposits. The dispersed samples (floating and bottom) were ultrasonicated in ethanol for 30 min. To study the materials contained in the hard deposits it was necessary to grind them for four hours in a booling mill machine. The resulting dust was suspended in ethanol. All samples were heated in air at 400 °C to eliminate residual traces of amorphous carbon, and then studied by transmission electron microscopy and micro-Raman spectroscopy [Appendix B.3]. The nanostructures present in the deposit were also studied by high-resolution TEM [Appendix B.7]. The composition of the deposit samples was determined by energy-dispersive x-ray spectroscopy (EDX) [Appendix B.5] by using an electron microprobe analyzer. Thermogravimetric analysis [Appendix B.6] in air flux was performed on

dispersed and deposit samples without any pre-treatment. A 10% yield of CNOs was calculated in the deposits, as the ratio between the mass of each deposit after annealing at 400 °C, and the corresponding mass lost by the anode in the discharge.

3.5.2 CNOs produced by arc discharge in water

The arc discharge generates carbon nanostructures by crystallization of carbon atoms evaporated from the anode. The crystallization is driven by the temperature gradients present in the peripheral zones of the plasma. The presence of the cathodic deposit cannot be explained in terms of the model proposed by Sano et al [9], in which crystallization is driven by temperature gradients at the interface with surrounding water. A different mechanism for the formation of CNOs deposited on the cathode was proposed, in which crystallization is due to a temperature gradient on the cathode surface. The experimental arrangement used in the present investigation, which allows the rotation of the anode when approaching the cathode, is probably the key point to obtain stable discharges favouring the formation of cathodic deposits rich of CNOs. This is very likely due to the fact that rotation prevents the stabilization of strong local discontinuities in the arc. It has to be mentioned that a roto-translation movement of the anode has also been used by Lee et al. [80] in arc discharge experiments in He atmosphere aimed at the production of CNTs. However, in that case the rotation speed was 10.000 rounds per minute, and the purpose of the rotation was to avoid the formation of the deposit on the cathode surface. In this work, on the contrary, the rotation is aimed to optimize the conditions for the formation of the deposits. Figures 3.9(a) and (b) show SEM micrographs of the cathode surface before and after the arc discharge, respectively, from which it can be seen that the surface is not eroded in the process. The black line in (b) evidences some residual parts of the deposit still attached to the cathode, after having detached the deposit by applying a gentle lateral force. A front-view and a side-view of the anode after the discharge are shown in Figures 3.9(c) and (d) (the anode surface before the discharge appears very similar to the cathode surface and is not shown). The shape of the eroded anode shows the central area from which carbon atoms evaporated in the discharge.

SEM micrographs of a cathodic deposit are shown in Figure 3.10. The deposit exhibits a nearly cylindrical shape, with radius and height of about 2.5 and 5.0 mm, respectively (the height is in the direction perpendicular to the image plane). The surface of the deposit is made of submicron-sized particles, as shown in Figure 3.10(b).
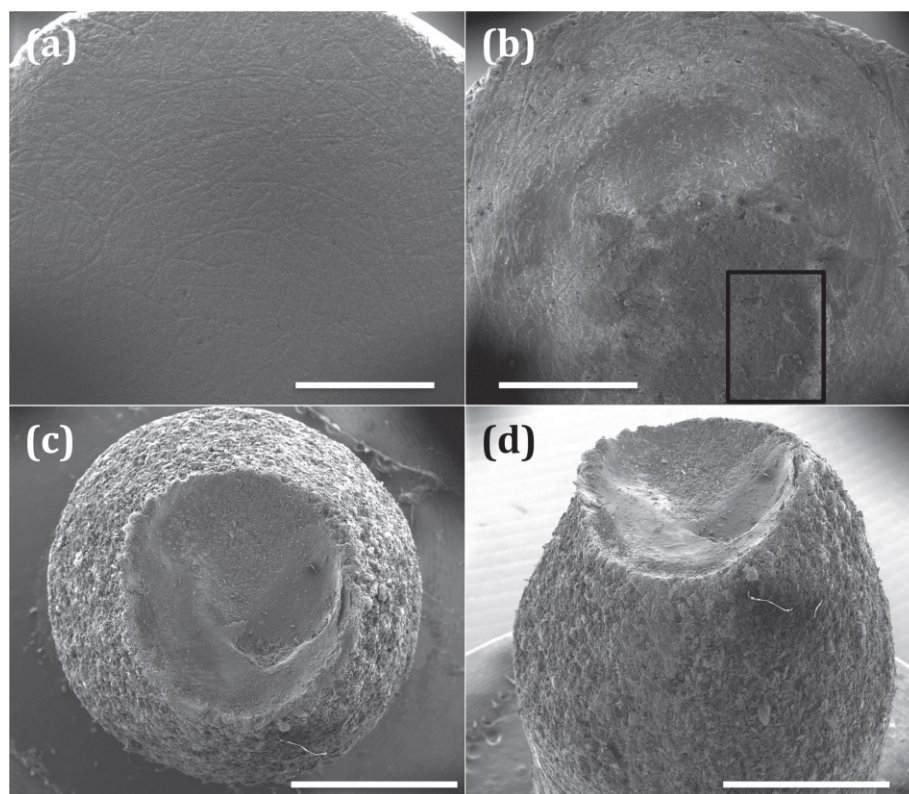
Figure 3.9 (a) and (b) SEM micrographs of the cathode surface before and after the discharge, (c) front-view and (d) side-view of the anode after the discharge (all bar lengths are 2 mm). The black line in (b) evidences some residuals of the deposit after his detachment from the cathode surface.

The composition of cathodic deposits has been investigated by EDX, averaging over a total area of about 100 μm^2 for each sample. Figure 3.11 shows a typical EDX spectrum, which refers to the portions of the deposit surface indicated by rectangles in the inset. The deposit results to be composed of 98.8% carbon and 1.2% oxygen, with oxygen possibly resulting from water adsorption in some sites of the air exposed sample. No traces of other contaminants have been observed in the different deposits examined.
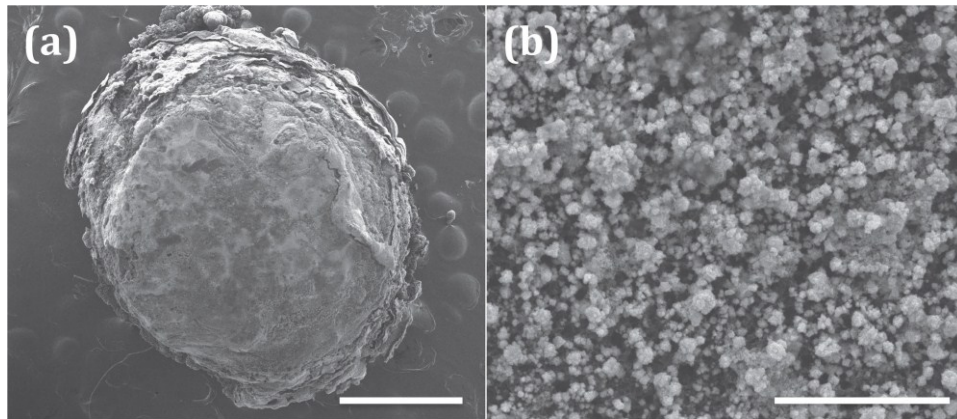
Figure 3.10. SEM micrographs of a cathodic deposit, showing in (a) a nearly cylindrical shape, and in (b) a surface structure made of particles with submicron size. Bar lengths are 1.0 mm in (a) and 5.0 μm in (b).

The materials floating and at the bottom of the beaker (DISP samples), and those obtained by grinding the deposit (DEP samples), were studied by TEM and Raman. Floating and bottom samples did not show remarkable differences. Figure 3.12 shows four TEM images representative of the DISP samples, in which are present CNOs and other nanoparticles, including CNTs, layered structures and ovoid particles with dimensions of the order of hundreds of nm. TEM images of DEP samples are shown in Figure 3.13, indicating a high level of homogeneity.
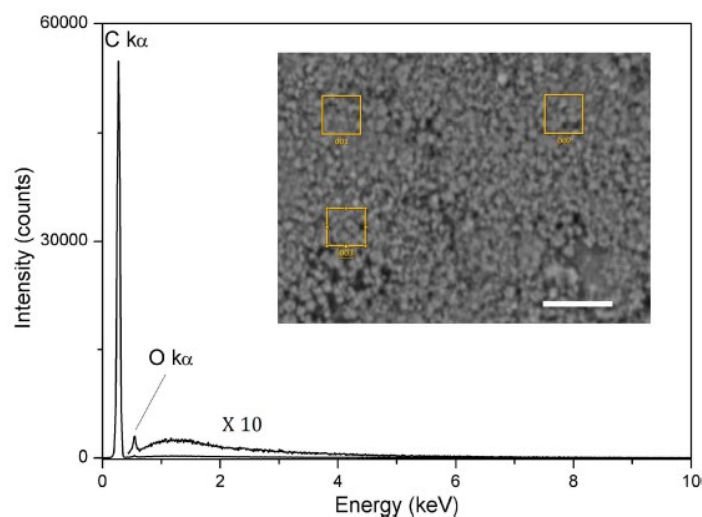
Figure 3.11. EDX spectrum obtained on a cathodic deposit by averaging over a total area of about 100 μm^2. The inset shows the surface of the deposit, where the areas investigated are indicated by rectangles (bar length is 10 μm).

Mainly 0D particles are present, having the aspect of polyhedral CNOs, although some of them appear elongated. Some cylindrical structures similar to nanotubes are also present.
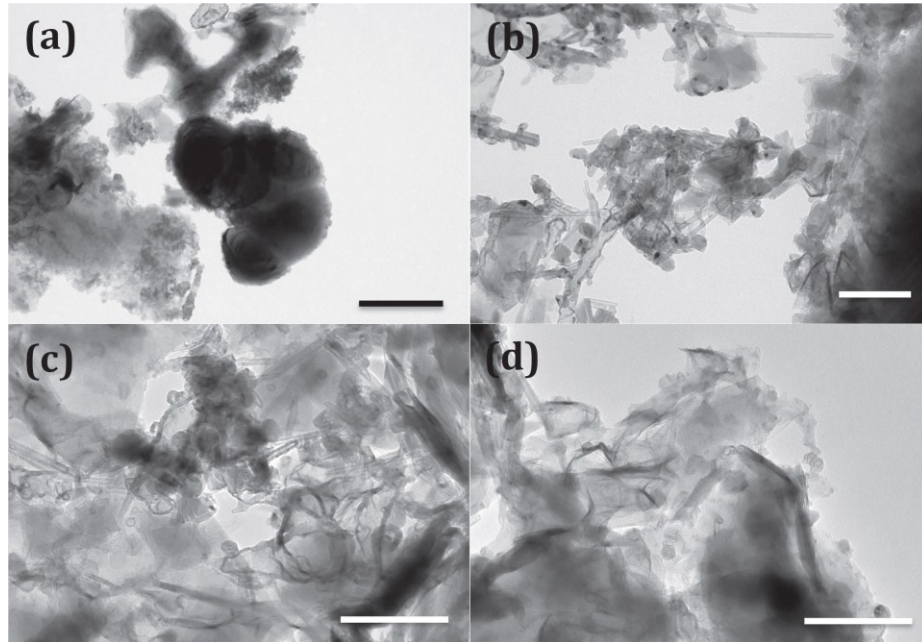
Figure 3.12. TEM images of the DISP samples. Bar lengths are 500 nm in (a), and 200 nm in (b)–(d).
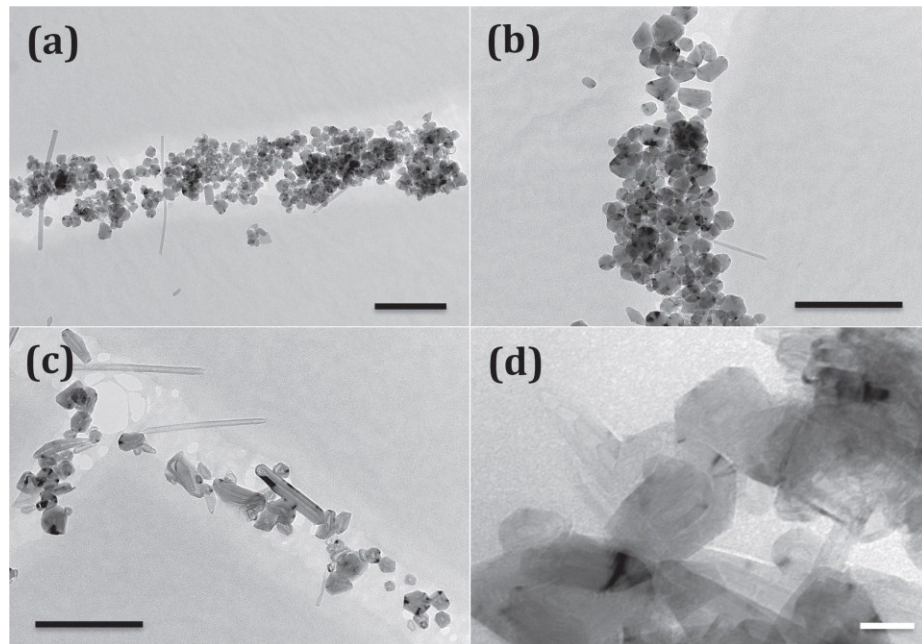
Figure 3.13. TEM images of the DEP samples. Bar lengths are 200 nm in (a)–(c), and 20 nm in (d).

The size distribution of CNOs has been obtained by graphical analysis of TEM images. Figure 3.14 shows the size distribution, from which an average and a standard deviation of 28 and 8 nm were calculated, respectively. To investigate deeper the nanostructure of DEP CNOs, they were studied by high resolution TEM (HRTEM) at 60 keV primary beam energy.
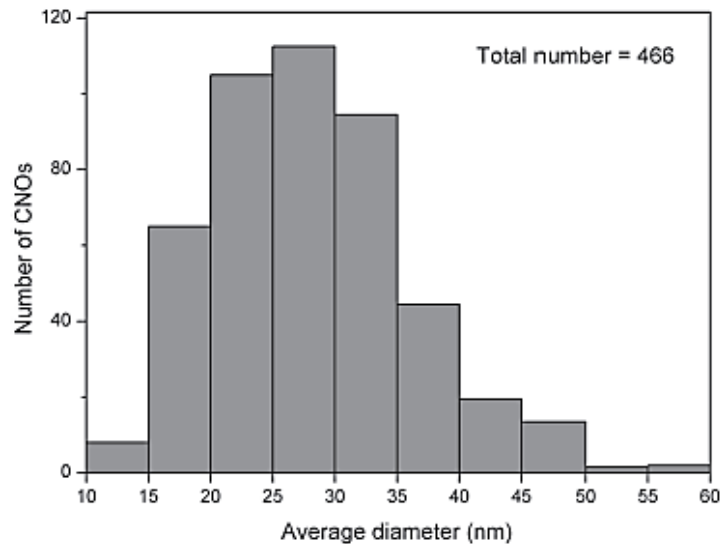
Figure 3.14. Size distribution of DEP CNOs obtained by analysis of TEM images.

Figure 3.15 shows atomic resolution high-angle annular dark-field images of some CNOs with different shapes and sizes. The polyhedral character of CNOs is confirmed, with planar zones dominating over curved zones. All the observed CNOs have a hollow core, the carbon shells are well defined, and the spacing between adjacent shells appears at a first look irregular. The average interlayer spacing between onion shells in two CNOs has been determined by measuring the intensity profiles along the dashed lines in Figures 3.15(b) and (d).

Figure 3.16 shows the two profiles, from which values of 0.352 and 0.371 nm were obtained, by averaging respectively over 25 and 31 interlayer spacings. For a typical CNO with average diameter of 28 nm, as the one shown in Figure 3.15(b), the number of shells is about 30.

DISP and DEP samples were studied by Raman spectroscopy. Figure 3.17(a) shows three spectra measured in different points of the DISP samples, in which different shapes and intensities of the peaks can be noted. On the contrary, spectra obtained in

different points of the DEP samples are very similar, and the spectrum in Figure 3.17(b) was obtained by averaging over four spectra measured in different points of the sample.
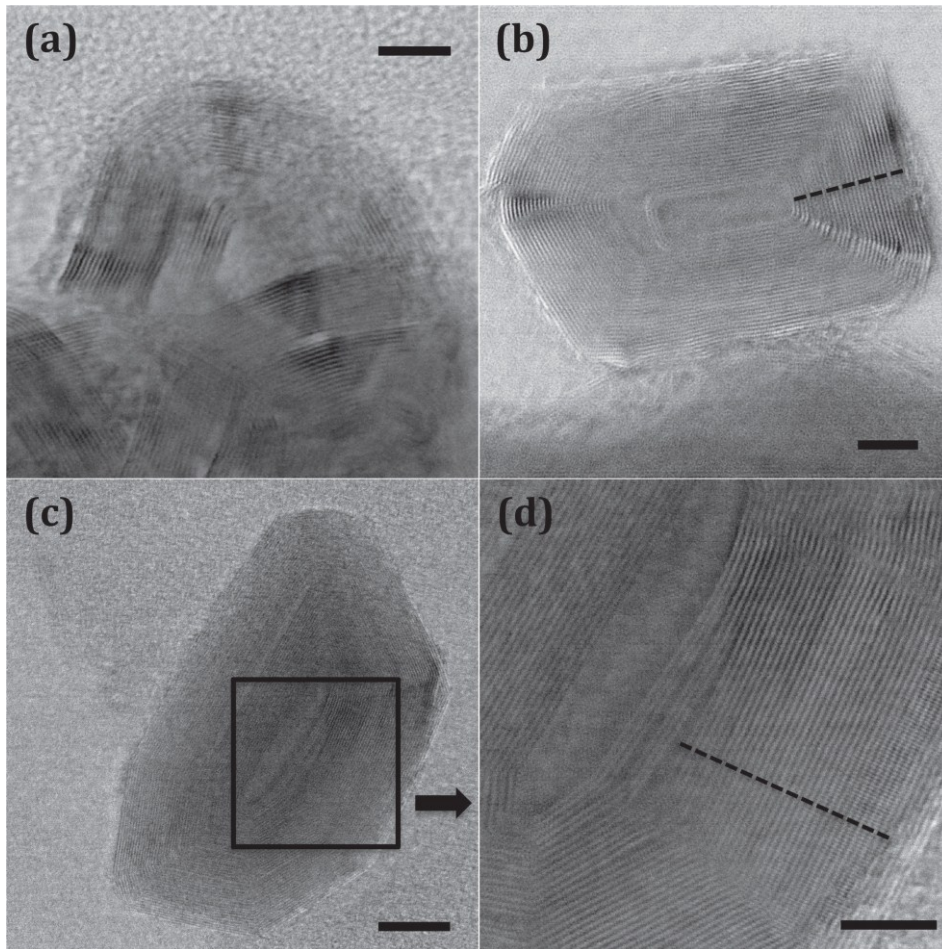
Figure 3.15. HRTEM images of DEP CNOs. Intensity profiles along the dashed lines in (b) and (d) are shown in figure 3.16. Bar lengths are 5 nm in (a), (b) and (d), and 10 nm in (c).
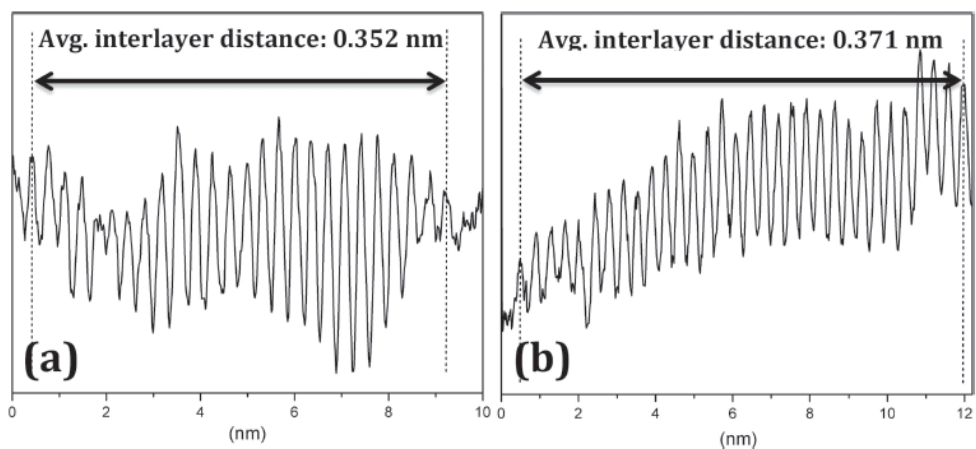
Figure 3.16. HRTEM intensity profiles (in arbitrary units) along the dashed lines in figures 3.15(b) and (d).

In graphitic materials, the G peak corresponds to the E_{2g} phonon, related to the stretching mode of sp_2 carbon pairs, and is located at about 1560 cm^{-1} [81]. The double-resonance D peak is activated by defects and is due to the breathing mode of carbon rings, related to TO phonons at the K point of the Brillouin zone. The D$'$ peak is also activated by defects, and is related to an intravalley process involving points of the same cone. The D and D$'$ peaks are located on the two sides of the G peak. The 2D band, located at about 2700 cm^{-1}, is the second order of the D peak, and does not need defects to be active, because the process satisfies momentum conservation. For single-layer graphene, the 2D peak exhibits a monomodal shape and has intensity much higher than the G peak. Its intensity strongly decreases in the case of bilayer graphene, and its shape is dependent on the number of graphene layers up to about 10 layers, when it assumes the typical bimodal shape of graphite. The 2D peak has a monomodal shape also for the so-called turbostratic graphite, in which individual graphene layers are arranged randomly with respect to rotation about the axis perpendicular to the planes [81]. Moreover, it has been shown that the D/D$'$ intensity ratio can be related to the type of defects present in the graphitic layers [82]. The ratio has a minimum value of about 3.5 for boundary-like defects, increases to a value of 7 for vacancy like defects, and reaches a maximum value of about 13 for sp^3 defects. Raman spectra in Figure 3.17(a) indicate that DISP samples are made of graphitic materials, with different degrees of structural order indicated by the different intensities of the D peaks in spectra taken in different points. The 2D peak shape also changes in the three spectra, very likely due to the contributions of different kinds of carbon nanoparticles. The Raman spectrum in Figure 3.17(b) looks very different from those shown in Figure 3.17(a). In fact, the 2D peak is monomodal and centered at 2697 cm^{-1}. The D and D$'$ peaks are located at 1348 and 1618 cm^{-1}, and the fit of the G, D and D$'$ by Lorentzian functions gives a value of 3.7 for the D/D$'$ intensity ratio. The value of 3.7 for the D/D$'$ ratio indicates that the defects are predominantly of the boundary type. These defects are inevitably observed on CNOs with graphenic planes having lateral dimensions of the order of tens of nanometers, considering that the area probed in the Raman spectrum is of the order of micrometers. It is interesting to compare these Raman results with those relative to CNOs obtained by purification of the materials dispersed in water in similar arc discharge experiments [41]. In that case, the 2D peak was fitted by two Lorentzian functions, which were

attributed to the contributions of planar and curved zones of concentric shells in turbostratic polyhedral CNOs.

The monomodal 2D shape indicates that the curved zones in the CNOs found in the cathodic deposit do not contribute significantly to the spectrum. As reported above, the monomodal 2D Raman peak can be attributed to stacking disorder between carbon shells in DEP CNOs. Angular disorder causes decoupling of the adjacent layers, resulting in an interlayer spacing higher than 0.342 nm, larger than the value in AB-stacked crystalline graphite (0.335 nm) [83].
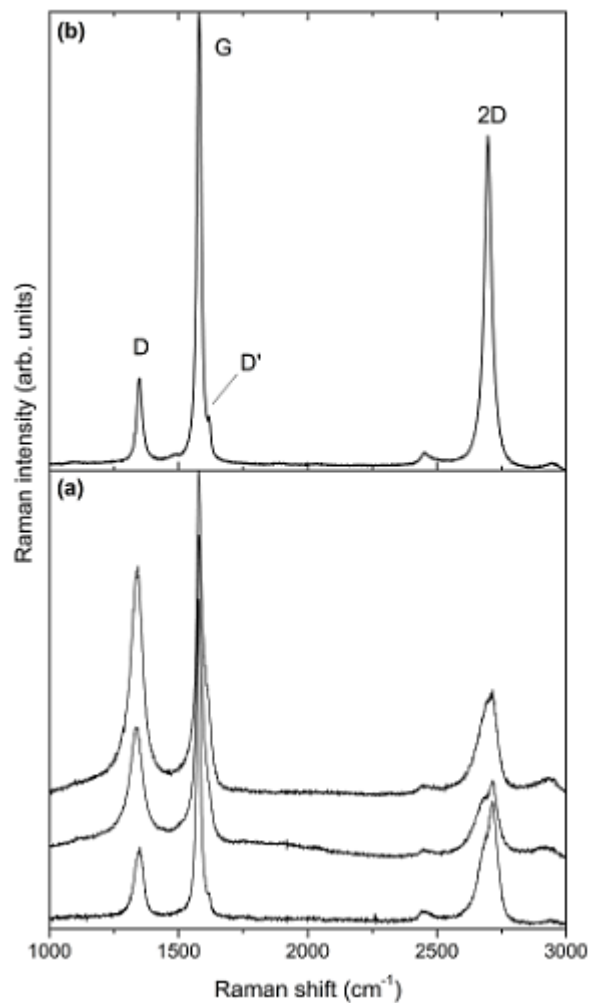
Figure 3.17. (a) Micro-Raman spectra measured in different positions on DISP samples. (b) Micro-Raman spectrum obtained by averaging 4 spectra measured on DEP samples.

Therefore, the average values of 0.352 and 0.371 nm measured on two different CNOs can be attributed to angular disorder, in agreement with the Raman findings. Moreover, the absence of the contribution in the 2D peak, due to curved zones in polyhedral

CNOs, agrees with HRTEM images, in which it appears that carbon shells are predominantly planar.

CNOs dispersed in water were not isolated from other nanomaterials, but TGA measurements allowed to get information about the difference between CNOs suspended in water and those found in the deposit.

Full line in Figure 3.18(a) is the TGA curve obtained on the DISP sample. The whole sample, including suspended CNOs, was burned at 850 °C, and the slope changes indicate the inhomogeneity already observed by TEM and Raman measurements. The dashed curve in Figure 3.18(a), obtained on the DEP sample, made almost exclusively of CNOs, indicates on the contrary a much higher stability, that allowed almost 30% of the initial mass to be still present at 850 °C. Moreover, the regular shape of the curve confirms the sample homogeneity. This measurements were compared with the results obtained by Palkar et al. [2] on suspended materials obtained in underwater arc discharge experiments. Figure 3.18(b) shows the TGA measurements for CNOs obtained by purification of the material collected either on the top or the bottom of the water vessel. Full-and dashed-line refer to pristine CNOs and to CNOs annealed at 210 K in He atmosphere, respectively. The comparison of the two dashed curves in Figure 3.18 shows that CNOs dispersed in water reach a thermal stability comparable to that of DEP CNOs only after thermal annealing in He, very likely due to a decrease of the density of defects in graphitic planes. The TGA findings can also be compared with the results shown in [58] for CNOs obtained by purification of nanomaterials, synthesized at different arc powers.

Whatever the power, the CNOs reported in [58] were completely burnt at 850 °C. These results show that in underwater arc discharge experiments, two kinds of CNOs are formed, found dispersed in water (DISP) and in the cathodic deposit (DEP).

As a consequence, it appears that some points of the model proposed by Sano et al. [54] have to be addressed. The model supposes a gas bubble to be present in the plasma zone, in which the main components are carbon monoxide and molecular hydrogen. This hypothesis is based on the analysis of the vapor collected above the discharge vessel, and also on similar results obtained by Richardson [84]. In fact, Lange et al. [85] have shown by plasma spectroscopy that in arc discharge in water between graphite

electrodes, the strongest bands are those coming from C_2 radicals, carbon atoms and ions, atomic hydrogen and oxygen.
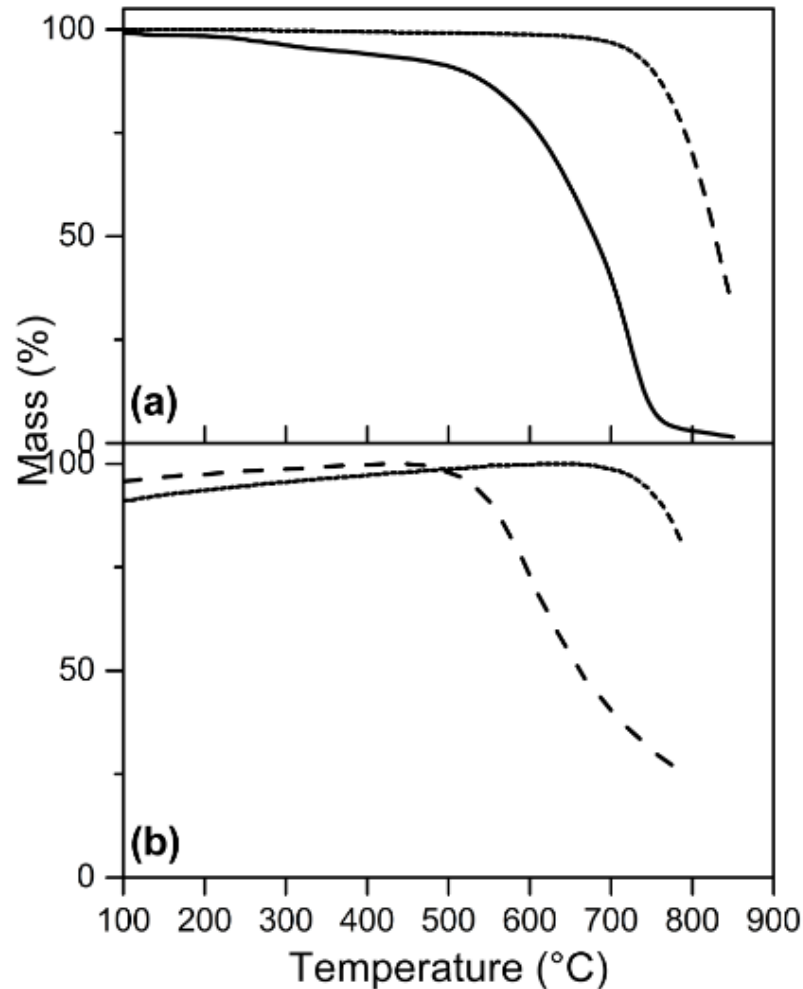
Figure 3.18. (a) TGA measurements obtained on the DISP sample (full curve) and on the DEP sample (dashed curve). (b) TGA results for CNOs obtained by purification of dispersed materials in arc discharge experiments, without thermal pre-treatment (full line) and with a thermal pre-treatment at 2300 K in He atmosphere [2].

The fact that molecular hydrogen and carbon monoxide are not detected in the plasma zone means that they are formed by interaction of species generated in the discharge with the surrounding water, not in the plasma zone. The Sano's model supposes that CNTs are formed in the zone very close to the plasma, but this hypothesis is in contrast with the existence of the cathodic deposit. In fact, the deposit is formed in the hottest zone of the discharge, and is composed mainly of CNOs. The crystallization of such CNOs cannot be ascribed to a temperature gradient due to the presence of surrounding

water. It is hard to measure the local temperature of the cathode surface, but clearly it is always lower with respect to the anode, due to the fact that the anode is bombarded by electrons, and also due to the size of the cathode. In fact, the cathode is not eroded during the discharge, and its surface remains unaltered after the removal of the deposit. Moreover, during and immediately after the discharge the cathode does not emit in the visible, while the anode still emits after time intervals of the order of tens of seconds. Taking in mind that the surface of the cathode is very close to the plasma zone, in which the temperature can be higher than 6000 K [85], a strong temperature gradient must exist in the space very close to the cathode surface. Carbon ions evaporated from the anode and coming onto the cathode, very likely crystallize due to this temperature gradient at the beginning of the process. Subsequently, the temperature gradient keeps causing the crystallization on the surface of the growing deposit. The nanoparticles dispersed in water, on the other hand, very likely crystallize in temperature gradients due to the presence of surrounding water. Such particles are formed in an environment with temperature much lower than the environment in which particles crystallize to form the deposit. This is probably the reason why the graphitic layers of the CNOs in the cathodic deposit have a higher structural order with respect to dispersed CNOs. The high temperature environment could also explain why the cathodic deposit contains mainly 0D nanoparticles. In fact, it has been shown that under intense electron beam irradiation, tubular carbon structures convert in quasi-spherical particles made of concentric graphitic shells [43]. The structural fluidity induced by electron irradiation can be considered similar to the fluidity due to a high temperature regime, as it happens in the zone where the cathodic deposit is formed. This causes probably the prevalence of CNOs with respect to CNTs in the deposit.

3.6   Conclusions

Using an experimental apparatus that allows the rotation of the anode, cathodic deposits were obtained in underwater arc discharge between graphite electrodes, composed mainly of CNOs with an average size of 28 nm, with high level of purity and structural order on the graphitic planes, that resulted in random stacking. The mechanical

fragmentation of the deposits allowed to obtain CNOs without any purification procedure. Obtained results indicate that these CNOs have different properties with respect to CNOs dispersed in water, mainly regarding the structural order in the graphitic planes. A model for the formation of the deposit was proposed, in which the crystallization is driven by an intense temperature gradient in the space very close to the cathode surface.

References

[1] H.W. Kroto, J.R. Heath, S.C. O'Brien, R.F. Curl, and R.E. Smalley, C60: buckminsterfullerene, Nature **318**, 162 (1985).

[2] A. Palkar, F. Melin, C.M. Cardona, B. Elliott, A.K. Naskar, D.D. Edie, a. Kumbhar, and L. Echegoyen, Reactivity differences between carbon nano onions (CNOs) prepared by different methods, Chem Asian J. **2,** 625 (2007).

[3] A.S. Rettenbacher, B. Elliott, J.S. Hudson, A. Amirkhanian, and L. Echegoyen, Preparation and functionalization of multilayer fullerenes (carbon nano-onions), Chem. Eur. J. **12**, 376 (2006).

[4] J. K. McDonough, A. I. Frolov, V. Presser, J. Niu, C.H. Miller, T. Ubieto, M.V. Fedorov, and Y. Gogotsi, Influence of the structure of carbon onions on their electrochemical performance in supercapacitor electrodes, Carbon **50**, 3298 (2012).

[5] V.L. Kuznetsov, Y.V. Butenko, A.L. Chuvilin, A.I. Romanenko, and A.V. Okotrub, Electrical resistivity of graphitized ultra-disperse diamond and onion-like carbon, Chem. Phys. Lett. **336**, 397 (2001).

[6] M.K. Sreeramoju, Preparation, characterization and applications of functionalized carbon nano-onions. Ph.D Thesis, University of Kentucky, Lexington, KY, (2013).

[7] C. Portet, G. Yushin, and Y. Gogotsi, Electrochemical performance of carbon onions, nanodiamonds, carbon black and multiwalled nanotubes in electrical double layer capacitors, Carbon **45**, 2511 (2007).

[8] D. Pech, M. Brunet, H. Durou, P. Huang, V. Mochalin, Y. Gogotsi, P-L. Taberna, and P. Simon, Ultrahigh-power micrometre-sized supercapacitors based on onion-like carbon, Nat. Nanotechnol. **5**, 651 (2010).

[9] N. Sano, H. Wang, I. Alexandrou, M. Chhowalla, K.B.K. Teo, and G.A.J Amaratunga, Properties of carbon onions produced by an arc discharge in water, J. Appl. Phys. **92**, 2783 (2002).

[10] E. Koudoumas, O. Kokkinaki, M. Konstantaki, S. Couris, S. Korovin, P. Detkov, V. Kutznetsov, S. Pimenov, and V. Pustovoi, Onion-like carbon and diamond nanoparticles for optical limiting, Chem. Phys. Lett. **357**, 366 (2002).

[11] N. Keller, N.I. Maksimova, V.V. Roddatis, M. Schur, and G. Mestl, Y.V Butenko, The catalytic use of onion-like carbon materials for styrene synthesis by oxidative dehydrogenation of ethylbenzene, Angew. Chem. Int. **41**, 1885 (2002).

[12] S. Park, K. Lian, and Y. Gogotsi, Pseudocapacitive behavior of carbon nanoparticles modified by phosphomolybdic acid, J. Electrochem Soc. **156**, A921 (2009).

[13] Y. Gao, Y.S. Zhou, M. Qian, X.N. He, J. Redepenning, P. Goodman, H. M. Li, L. Jiang, and Y.F. Lu, Chemical activation of carbon nano-onions for high rate supercapacitor electrodes, Carbon **51**, 52 (2013).

[14] Y. Wang, S.F. Yu, C.Y. Sun, T.J. Zhu, and H. Y. Yang, MnO_2/onion-like carbon nanocomposites for pseudocapacitors, J. Mater. Chem. **22**, 1784 (2012).

[15] M.E. Plonska-Brzezinska, J. Mazurczyk, B. Palys, J. Breczko, A. Lapinski, A. T. Dubis, and L. Echegoyen, Preparation and characterization of composites that contain small carbon nano-onions and conducting polyaniline, Chem. Eur.

J. **18**, 2600 (2012).

[16]   R. Borgohain, J. Li, J.P. Selegue, and Y.T Cheng, Electrochemical study of functionalized carbon nano-onions for high-performance supercapacitor electrodes, J. Phys. Chem. C **116**, 15068 (2012).

[17]   X. H. Chen, F. M. Deng, J.X. Wang, H.S. Yang, G.T. Wu, X.B Zhang, J.C. Peng, and W.Z. Li, New method of carbon onion growth by radiofrequency plasma-enhanced chemical vapor deposition, Chem. Phys. Lett. **336**, 201 (2001).

[18]   A. Hirata, M. Igarashi, and T. Kaito, Study on solid lubricant properties of carbon onions produced by heat treatment of diamond clusters or particles, Tribol. Int. **37**, 899 (2004).

[19]   I. Suarez-Martinez, N. Grobert, and C.P. Ewels, Nomenclature of sp_2 carbon nanoforms, Carbon **50**, 741 (2012).

[20]   J. Beilstein and S. Giordani, J. Nanotechnol. **5**, 1980 (2014).

[21]   V. N. Mochalin, O. Shenderova, D. Ho, and Y. Gogotsi, The properties and applications of nanodiamonds, Nat. Nanotechnol. **7**, 11 (2021).

[22]   Y. Gogotsi, and V. Presser, Carbon nanomaterials, 2nd edition. CRC Press (2014).

[23]   A. Barnard, S. Russo, and I. Snook, Structural relaxation and relative stability of nanodiamond morphologies, Diam. Relat. Mater. **12**, 1867 (2003).

[24]   X. Fang, J. Mao, E Levin, and K. Schmidt-Rohr, Nonaromatic core-shell structure of nanodiamond from solid-state NMR spectroscopy, J. Am. Chem. Soc. **131**, 1426 (2009).

[25]   A. Panich, A. Shames, H-M Vieth, E.Ōsawa, M. Takahashi, and A.Y. Vul, Nuclear magnetic resonance study of ultra nanocrystalline diamonds, Eur. Phys. J. B **52**, 397 (2006).

[26]   M. Dubois, K. Guérin, E. Petit, N. Batisse, A. Hamwi, N. Komatsu, J. Giraudet, P. Pirotte, and F. Masin, Solid-state NMR study of nanodiamonds produced by the detonation technique, J. Phys. Chem. C **113**, 10371 (2009).

[27]   A. Krüger, F. Kataoka, M. Ozawa, T. Fujino, Y. Suzuki, A. Aleksenskii, A. Ya.Vul', and E.Ōsawa, Unusually tight aggregation in detonation nanodiamond: identification and disintegration, Carbon **43**, 1722 (2005).

[28]   Q. Zou, M.Z. Wang, Y.G. Li, B. Lv, and Y.C. Zhao, HRTEM and Raman characterisation of the onion-like carbon synthesised by annealing detonation nanodiamond at lower temperature and vacuum, J. Exp. Nanosci. **5**, 473 (2010).

[29]   Q. Zou, M. Wang, Y. Li, Y. Zhao, and L. Zou, Fabrication of onion-like carbon from nanodiamond by annealing, Sci. China Ser. E Technol. Sci. **52**, 3683 (2009).

[30]   Y.V. Butenko, V.L. Kuznetsov, A.L. Chuvilin, V.N Kolomiichuk, S.V. Stankus, R. A. Khairulin, and B.Segall Kinetics of the graphitization of dispersed diamonds at ''low'' temperatures, J. Appl. Phys. **88**, 4380 (2000).

[31]   P. Ganesh, P. Kent, and V. Mochalin, Formation, characterization, and dynamics of onion-like carbon structures for electrical energy storage from nanodiamonds using reactive force fields, J. Appl. Phys. **110**, 073506 (2011).

[32]   Y.V. Butenko, V.L. Kuznetsov, E.A. Paukshtis, A.I. Stadnichenko, I.N. Mazov, S.I Moseenkov, A. Boronin and S.V. Kosheev, The thermal stability of nanodiamond surface groups and onset of nanodiamond graphitization, Fullerenes Nanotubes Carbon Nanostruct. **14**, 557 (2006).

[33] S. Tomita, A. Burian, J.C. Dore, D. LeBolloch, M. Fujii and S. Hayashi, Diamond nanoparticles to carbon onions transformation: X-ray diffraction studies, Carbon, **40**, 1469 (2002).

[34] Y. Gan and F. Banhart, The mobility of carbon atoms in graphitic nanoparticles studied by the relaxation of strain in carbon onions, Adv. Mater. **20**, 4751 (2008).

[35] S. Tomita, T. Sakurai, H. Ohta, M. Fujii and S. Hayashi, Structure and electronic properties of carbon onions, J. Chem. Phys. **114**, 7477 (2001).

[36] K. Bogdanov, A. Fedorov, V. Osipov, T. Enoki, K. Takai, T. Hayashi, V. Ermakov, S. Moshkalev, and A.Baranov, Annealing-induced structural changes of carbon onions: high-resolution transmission electron microscopy and Raman studies, Carbon **73**, 78 (2014).

[37] J. Cebik, J. K. McDonough, F. Peerally, R. Medrano, I. Neitzel, Y. Gogotsi, and S. Osswald, Raman spectroscopy study of the nanodiamond-to-carbon onion transformation, Nanotechnology **24**, 205703 (2013).

[38] E.D. Obraztsova, M. Fujii, S. Hayashi, V. L. Kuznetsov, Y.V. Butenko and A. L. Chuvilin, Raman identification of onion-like carbon, Carbon **36**, 821 (1998).

[39] D. Roy, M. Chhowalla, H. Wang, N. Sano, I. Alexandrou, T. W. Clyne, and G.A.J Amaratunga, Characterisation of carbon nanoonions using Raman spectroscopy, Chem. Phys. Lett. **373**, 52 (2003).

[40] S.N. Bokova-Sirosh, A.V. Pershina, V.L. Kuznetsov, A.V. Ishchenko, S.I. Moseenkov, A.S. Orekhov, and A.S. Obraztsova, Raman Spectra for Characterization of Onion-Like Carbon, J. Nanoelectron. Optoelectron. **8**, 106 (2013).

[41] C. D. Puja, O. Arias de Fuentes, L.F. Desdín García, E. Cazzanelli, and L.S.Caputi, Appl. Phys. A **120**, 1339 (2015).

[42] S. Iijima, Direct observation of the tetrahedral bonding in graphitized carbon black by high resolution electron microscopy, J. Cryst. Growth **50**, 675 (1980).

[43] D. Ugarte, Curling and closure of graphitic networks under electron-beam irradiation, Nature **359**, 707 (1992).

[44] V.L. Kuznetsov, A.L. Chuvilin, Y.V. Butenko, L.Y. Mal'kov, V.M. Titov, Onion-like carbon from ultra-disperse diamond, Chem. Phys. Lett. **222**343 (1994).

[45] M. Zeiger, N. Jäckel, M. Aslan, D. Weingarth and V. Presser, Understanding structure and porosity of nanodiamond derived carbon onions, Carbon **84**, 584 (2015).

[46] M. Zeiger, N. Jäckel, D. Weingarth and V. Presser, Vacuum Or fowing argon: What is the best synthesis atmosphere for nanodiamond-derived carbon onions for supercapacitor electrodes?, Carbon **94**, 507 (2015).

[47] A. Ferrari, A. Libassi, B. Tanner, V. Stolojan, J. Yuan, L. Brown, S.E. Rodil B. Kleinsorge, and J. Robertson, Density, sp^3 fraction, and cross-sectional structure of amorphous carbon films determined by X-ray reflectivity and electron energy-loss spectroscopy, Phys. Rev. B: Condens. Matter Mater. Phys. **62**, 11089 (2000).

[48] D. Weingarth, M. Zeiger, N. Jäckel, M. Aslan, G. Feng and V. Presser, Graphitization as a universal tool to tailor the potential-dependent capacitance of carbon supercapacitors, Adv. Energy Mater. 4,1400316 (2014).

[49] M. Ishigami, J. Cumings, A. Zettl, and S. Chen, A simple method for the

continuous production of carbon nanotubes, Chem. Phys. Lett., **319**, 457 (2000).

[50] M. Zeiger, N. Jäckel, V. N. Mochalin, and V. Presser, J. Mater. Chem. A **4**, 3172 (2016).

[51] V.L. Kuznetsov, I.L. Zilberberg, Y.V. Butenko, A.L. Chuvilin and B. Segall, Theoretical study of the formation of closed curved graphite-like structures during annealing of diamond surface, J. Appl. Phys. **86**, 863 (1999).

[52] V. L. Kuznetsov and Y. V. Butenko, in Synth. Prop. Appl. Ultrananocrystalline Diam. (Eds.: D.M. Gruen, O.A. Shenderova, A.Y. Vul'), Springer-Verlag, Berlin/Heidelberg, pp. 199–216 (2005).

[53] K. D. Sattler, Ed., Carbon Nanomaterials Sourcebook. Graphene, Fullerenes, Nanotubes, and Nanodiamonds, Taylor & Francis Group, Boca Raton (2016).

[54] N. Sano, H. Wang, M. Chhowalla, I. Alexandrou and G.A.J. Amaratunga, Synthesis of carbon 'onions' in water, Nature **414**, 506 (2001).

[55] E. G. Gamaly and Ebbesen T. W., Mechanism of carbon nanotube formation in the arc discharge, Phys. Rev. B **52** 2083 (1995).

[56] I. Alexandrou, H. Wang, N. Sano and G.A.J. Amaratunga, Structure of carbon onions and nanotubes formed by arc in liquids, J. Chem. Phys. **120**,1055 (2004).

[57] A. S. Rettenbacher, B. Elliott, J. S. Hudson, A. Amirkhanian and L. Echegoyen, Preparation and functionalization of multilayer fullerenes (carbon nano-onions), Chem. Eur. J. **11**, 1 (2005).

[58] R. Borgohain, J. Yang, J. P. Selegue and D. Y. Kim, Controlled synthesis, efficient purification, and electrochemical characterization of arc-discharge carbon nano-onions, Carbon **66**, 272 (2014).

[59] S. Kim, Y. Song, and M. J. Heller, Seamless aqueous arc discharge process for producing graphitic carbon nanostructures, Carbon **120**, 83 (2017).

[60] K. Morishita, and T Takarada, Scanning electron microscope observation of the purification behaviour of carbon nanotubes, J. Mater. Sci. **34**, 1169 (1999).

[61] P.-X. Hou, C. Liu, and H.-M. Cheng, Purification of carbon nanotubes, Carbon **46**, 2003 (2008).

[62] J. Zhang, H. Zou, Q. Qing, Y. Yang, Q. Li, Z. Liu, X. Guo, and Z. Du, Effect of chemical oxidation on the structure of single-walled carbon nanotubes, J. Phys. Chem. B **8**, 3712 (2003).

[63] P.X. Hou, S. Bai, Q.H. Yang, C. Liu, and H.M. Cheng, Multi-step purification of carbon nanotubes, Carbon **40**, 81 (2002).

[64] B.J. Bauer, M.L. Becker, V. Bajpai, J.A. Fagan, E.K. Hobbie, K. Migler, c.M. Guttman, and W.R. Blair, Measurement of single-wall nanotube dispersion by size exclusion chromatography, J. Phys. Chem. C **111**, 17914 (2007).

[65] S.K. Doorn, M.S. Strano, M.J. O'Connell, E.H. Haroz, K.L. Rialon, R.H. Hauge, and R. E. Smalley, Capillary electrophoresis separations of bundled and individual carbon nanotubes, J. Phys. Chem. B **107**, 6063 (2003).

[66] J. Chun, J.A. Fagan, E.K. Hobbie, and B.J. Bauer, Size separation of single-wall carbon nanotubes by flow-field flow fractionation, Anal. Chem. **80**, 2514 (2008).

[67] R. Andrews, D. Jacques, D. Qian, and E.C. Dickey, Purification and structural annealing of multiwalled carbon nanotubes at graphitization temperatures, Carbon **39**, 1681 (2001).

[68] J. Luszczyn, M.E. Plonska-Brzezinska, A. Palkar, A.T. Dubis, A. Simionescu, D.T. Simionescu, B. Kalska-Szostko, K. Winkler, and L. Echegoyen, Small

noncytotoxic carbon nano-onions: first covalent functionalization with biomolecules, Chem.– Eur. J. **16**, 4870 (2010).

[69] M. B. Seymour, C. Su, Y. Gao, Y. Lu, and Y. Li, Characterization of carbon nano-onions for heavy metal ion remediation, J. Nanopart. Res. **14**, 1087 (2012).

[70] B. J. Landi, M. J. Ganter, C. D. Cress, R. A. DiLeo, and R. P. Raffaelle, Energy Environ. Sci. **2**, 638 (2009).

[71] Y. Wang, F. Yan, S.W. Liu, A.Y.S. Tan, H. Song, X.W. Sun, H.Y. Yang, Carbon nanotubes for lithium ion batteries, J. Mater. Chem. A **1**, 5212 (2013).

[72] Y. Wang, Z.J. Han, S. F. Yu, R. R. Song, H.H. Song, K. Ostrikov, and H.Y. Yang, Core-leaf onion-like carbon/MnO$_2$ hybrid nano-urchins for rechargeable lithium-ion batteries, Carbon **64**, 230 (2013).

[73] E.G. Bushueva, P.S. Galkin, A.V. Okotrub, L.G. Bulusheva, N.N Gavrilov, V. L. Kuznetsov, and S.I. Moiseekov, Double layer supercapacitor properties of onion-like carbon materials, Phys. Status Solidi B **245**, 2296 (2008).

[74] Y. Wang, S.F. Yu, C.Y. Sun, T.J. Zhu, and H.Y. Yang, MnO$_2$/onion-like carbon nanocomposites for pseudocapacitors, J. Mater. Chem. **22**, 17584 (2012).

[75] T. Cabioc'h, E. Thune, J.P. Rivière, S. Camelio, J.C. Girard, P. Guérin, M. Jaouen, L. Henrard, and P. Lambin, Structure and properties of carbon onion layers deposited onto various substrates, J. Appl. Phys. **91**, 1560 (2002).

[76] N. Matsumoto, L. Joly-Pottuz, H. Kinoshita, and N. Ohmae, Application of onion-like carbon to micro and nanotribology, Diamond Relat. Mater. **16**, 1227 (2007).

[77] L. Joly-Pottuz, B. Vacher, N. Ohmae, J. M. Martin, T. Epicier, Anti-wear and friction reducing mechanisms of carbon nano-onions as lubricant additives, Tribol. Lett. **30**, 69 (2008).

[78] L. Joly-Pottuz, N. Matsumoto, H. Kinoshita, B. Vacher, M. Belin, G. Montagnac, J. M. Martin, and N. Ohmae, Diamond-derived carbon onions as lubricant additives, Tribol. Int. **41**, 69 (2008).

[79] L. Joly-Pottuz, E.W. Bucholz, N. Matsumoto, S.R. Phillpot, S.B. Sinnott, N. Ohmae, and J. M. Martin, Friction properties of carbon nano-onions from experiment and computer simulations, Tribol. Lett. **37**, 75 (2010).

[80] S.J Lee, H.K. Baik, J. Yoo and J. H. Han, Large scale synthesis of carbon nanotubes by plasma rotating arc discharge technique, Diam. Relat. Mater. **11**, 914 (2002).

[81] A. Jorio, R. Saito, G. Dresselhaus and M. S. Dresselhaus, Raman Spectroscopy Graphene Related Systems, Berlin:Wiley (2011).

[82] A. Eckmann, A. Felten, A. Mishchenko, L. Britnell, R. Krupke, K.S. Novoselov and C. Casiraghi, Probing the nature of defects in graphene by Raman spectroscopy Nano Lett. **12**, 3925 (2012).

[83] M.A. Pimenta, G. Dresselhaus, M. S. Dresselhaus, L.G. Cançado, A. Jorio and R. Saito, Studying disorder in graphitebased systems by Raman spectroscopy Phys. Chem. Chem. Phys. **9**, 1276 (2007).

[84] W.H. Richardson Jr,. Electric power generation without harmful emissions, Infinite Energy **9**, 45 (1996).

[85] H. Lange, M. Sioda, A. Huczko, Y.Q. Zhu, H.W. Kroto and D. R. M. Walton, Nanocarbon production by arcdischarge in water Carbon **41**, 1617 (2010).

4 Electrochemical performance of activated carbon in aqueous electrolytes

4.1 Introduction

Depletion of fossil-fuel energy resources creates a demand for sustainable energy technologies and therefore necessitates the development of sustainable energy storage devices with sustainable materials, eco-efficient synthetic methods, and robust cycle life. Supercapacitors are potential candidates for sustainable energy storage devices thanks to their high power density, a key missing feature of fuel cells and electrical batteries. They are based on the formation of an electrical double layer on the extensive surface of porous carbon materials, which is profited to store energy that can be delivered in few seconds. This energy storage mechanism is often complemented with pseudocapacitive processes produced by fast redox reactions occurring in electroactive surface functional groups. The development of electrode materials with large surface area, electroactive functional groups and high electrochemical stability is crucial for the improvement of the energy density and durability of supercapacitors devices [1].

Activated carbons (ACs) have attracted intense interests as electrode materials for supercapacitors, because of their high surface area, electrical conductivity, high electrochemical stability and low cost [2]. Also, their surface chemistry can be modified to introduce surface functionalities that could improve the performance of these materials by an increase of electrochemical stability, conductivity, wettability or pseudocapacitance [3]. For instance, oxygen groups in aqueous electrolytes can increase the wettability of the surface, improving the electrolyte-electrode interaction and rendering a larger amount of the surface accessible for the formation of the electrical double layer, and can also participate in reversible faradaic reactions that contribute to the energy storage through pseudocapacitance [4].

4.2   Activated carbons

Porous carbon materials are solids with a high content of carbon atoms that exhibit large apparent surface areas and pore volumes [5,6,7]. Most of these solids have a wide pore size distribution (PSD), and can be obtained by different techniques and with different morphologies, such as powder, pellets, granules, fibers, monoliths, etc.

Porosity in carbon materials is responsible for their adsorption properties. The pore width is the most relevant porosity parameter and it determines the adsorption mechanism. According to the International Union of Pure and Applied Chemistry (IUPAC), pores are classified into three categories: micropores (less than 2 nm), mesopores (between 2 and 50 nm), and macropores (larger than 50 nm).

Activated carbons, also called activated charcoal, are used in a wide variety of applications, mainly due to their high specific surface-area, porous structure and presence of different functional groups on their surface. This material is composed primarily of aromatic configurations of carbon atoms joined by random cross-linkages. AC differs from another form of carbon — graphite — in that activated carbon has sheets or groups of atoms that are stacked unevenly in a disorganized manner. The degree of order varies based on the starting raw material and thermal history. Randomized bonding creates a highly porous structure with numerous cracks, crevices and voids between the carbon layers. Activated carbon's molecular size porosity and the resulting enormous internal surface area make this material extremely effective for adsorbing a wide range of impurities from liquids and gases. It can also be used as a catalyst support for solid-gas reactions, if the temperature and pressure of the gas phase are such that the carbon support is stable under gaseous reactants of the catalytic process [8-10]. In electrochemistry, ACs are mainly used as electrodes in different energy storing devices including batteries, capacitors and supercapacitors [11-14].

Activated carbons are normally produced using activation methods that can be classified as physical or chemical, according to the activation agents used. They can be made from a number of precursors such as coconut shell [15,16], phenol resin [17,18], and petroleum-/coal-based coke [19,20].

The pore characteristics of activated carbon are determined by the precursors, carbonization process, and activation process conditions used.

In physical activation a carbon rich precursor is submitted to a controlled gasification at high temperatures (700–1000 °C) mainly with carbon dioxide and steam, although other gases that can produce controlled carbon gasification can be used [6,21]. This method can be employed for the production of microporous ACs with surface areas over 1500 m^2g^{-1}.

On the other hand, chemical activation can be directly conducted over lignocellulosic precursors [22-25] and coal [21,24,26]. In this procedure, the carbon precursor is mixed with the chemical agent, carbonized at temperatures and times usually lower than those employed in physical activation, and thoroughly washed in order to recover the chemical agent (phosphoric acid, zinc chloride, alkaline hydroxides, etc.) and release the porosity of the resulting AC. Thus, ACs with surfaces over 3000 m^2g^{-1} and tunable pore size distributions that can contain micropores, mesopores or both of them, can be prepared [21, 27-29].

4.2.1 Surface chemistry

The presence of heteroatoms (such as O, N, H, S, etc., originating from the precursor used, the activation method, or introduced after treatment) bound to the edges of the graphene layers originates a variety of surface functional groups that have steric, tautomeric and intramolecular hydrogen bond effects since they are close to other different functionalities.

Oxygen functionalities are the most important due to their surface properties, and since they can be formed spontaneously by exposure of the carbon material to the atmosphere. The unsaturated carbon atoms at the edges of the crystallite basal planes are associated to high concentrations of unpaired electrons, which play a very important role in chemisorption. As activated carbons have a disordered structure, the area of the edges of basal planes is high, resulting in an affinity for oxygen chemisorption.

Moreover, the basal planes of microcrystallites can have several imperfections, dislocations and discontinuities, which are also active for oxygen chemisorption [30,31], leading to the formation of oxygen functional groups with variable thermal stability. Oxygen functional groups are not formed exclusively by reaction with oxygen, as they can also result from the reaction with other oxidant gases (such as O_3, N_2O, CO_2, etc.) and with oxidising solutions (nitric acid, hydrogen peroxide, etc.). There are extensive studies in the literature on the identification and quantification of the oxygen functional groups [32-44]. Figure 4.1 illustrates the rich variety of surface oxygen groups that can be found in carbon materials.
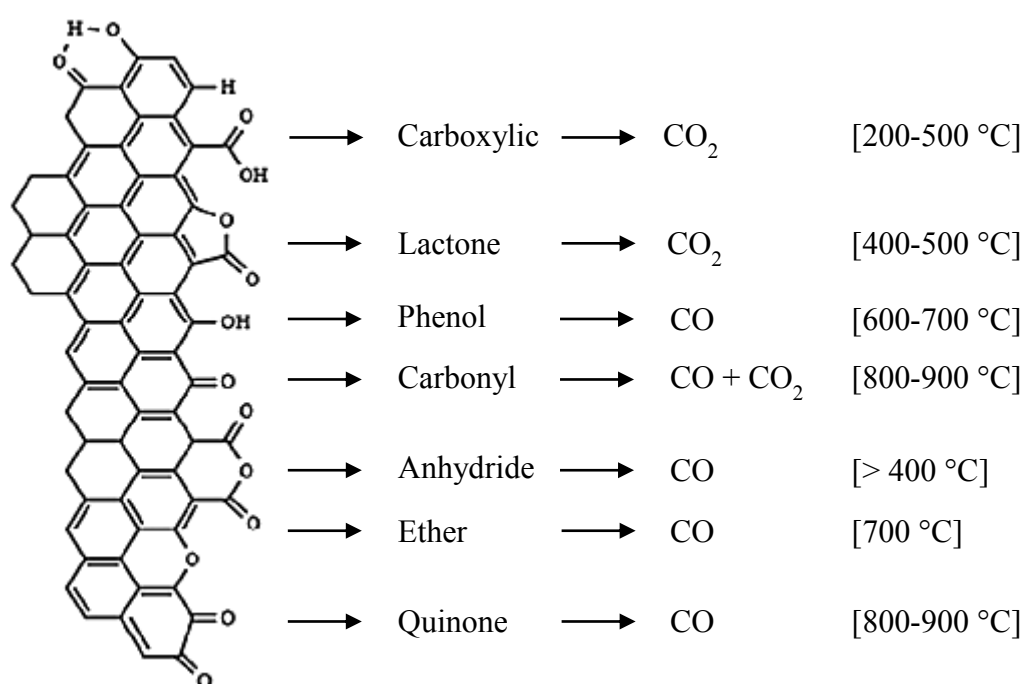
Figure 4.1. Surface oxygen groups of carbon and their decomposition temperatures.

There exist well established techniques that can be employed for their classification and quantification. Temperature programmed desorption (TPD) is one of the most powerful techniques available for this purpose. In this technique, the carbon material is submitted to a thermal treatment in inert atmosphere at a constant heating rate. As the temperature increases, the functional groups on the surface of carbon materials are thermally decomposed, releasing certain gases at different temperatures, which depend on the kind of functional group. The presence of these functionalities is responsible for activated carbons acid-base character. Furthermore, the surface oxygen groups are distinguished

by their decomposition temperature [45-48]. Thus, carboxylic acids decompose as CO_2 at low temperatures (200–400 ºC). Anhydrides and lactones decompose as CO_2 at medium temperatures (400–500 ºC). Decomposition of anhydrides also releases an additional CO molecule. Phenols evolve as CO at higher temperatures (600–700 ºC), while carbonyl, ether and quinones are reported to be more stable, decomposing at temperatures over 700 ºC.

4.3 General properties of electrochemical capacitors

4.3.1 Electrochemical capacitors

Electrochemical capacitors (ECs) are a special kind of capacitors based on charging and discharging at the electrode–electrolyte interface of high surface area materials, such as porous carbons or some metal oxides [49]. They are also often referred to by a number of alternative names including double-layer capacitors, supercapacitors, ultracapacitors, power capacitors, gold capacitors, pseudocapacitors, and power cache, each supposedly used to indicate different types of capacitors that display high capacitance [50].

In Figure 4.2 is shown the scheme of a supercapacitor. The main components are:

(i) the electrodes, which are usually composed of porous carbon particles and a small amount of additives, such as conductivity promoters (usually a carbon black,) and a binder, mostly polytetrafluoroethylene, PTFE, and polyvinylidene difluoride, PVDF [51], although other polymeric matrixes can be employed for this purpose [52,53], and even binderless electrodes of improved conductivity can be used [54,55];

(ii) the electrolyte

(iii) the separator, a porous non-conductive membrane that isolates both electrodes.

Supercapacitors are governed by the same basic principles as conventional capacitors and are ideally suited to the rapid storage and release of energy. However, they incorporate electrodes with much higher effective surface areas (SA) and thinner dielectrics (which are defined by the thickness of the double layer), leading to an increase in both capacitance and energy by a factor of 10 000 or so than those

achievable by regular capacitors. Therefore, while conventional capacitors are often rated in the micro- and milli-farad ranges, ECs can be rated as high as tens, hundreds, and even thousands of farads per device. They still store electric charge in a highly reversible way, as does a regular capacitor, and by maintaining a low equivalent series resistance (ESR), can be operated at high specific power (kW kg^{-1}); substantially higher than most batteries. While ECs can also be regarded as functioning like rechargeable batteries in storing or delivering electric charge, their mechanism of charge storage differs from those typically operating in batteries (i.e., electrostatic/*non-faradic* vs chemical/*faradic*).
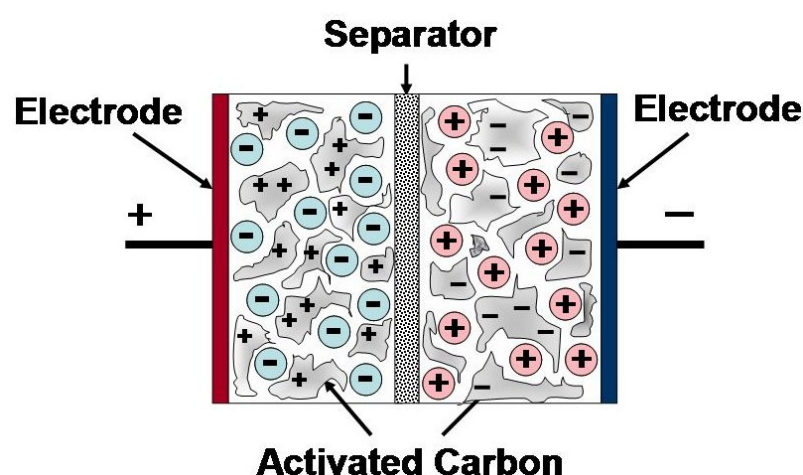
Figure 4.2. Scheme of a supercapacitor based on activated carbon.

Therefore, ECs should not be considered as battery replacements but rather as complementary energy storage devices occupying a niche position, in terms of specific power and energy. Through appropriate cell design, both the specific energy and specific power ranges for ECs can cover several orders of magnitude, which makes them extremely versatile as a stand-alone energy supply for certain applications, or in combination with batteries as a hybrid system. This unique combination of high power capability, coupled with good specific energy, allows ECs to occupy a functional position between batteries and conventional capacitors (Figure 4.3). They can offer very fast charge and discharge rates relative to batteries of a comparable volume, but their specific energy is less than that of batteries. The highly reversible and rapid charge acceptance/delivery of ECs arises largely due to the fact that no slow chemical processes or phase changes take place between charge and discharge as they do in most

battery-type energy storage devices. In addition to their high power density, ECs have several advantages over electrochemical batteries including very short charge times, longer cycle life (millions vs thousands for batteries), long shelf life, high efficiency (charge in ≈ charge out) and can be fully charged or discharged without affecting performance or lifetime [49,55].
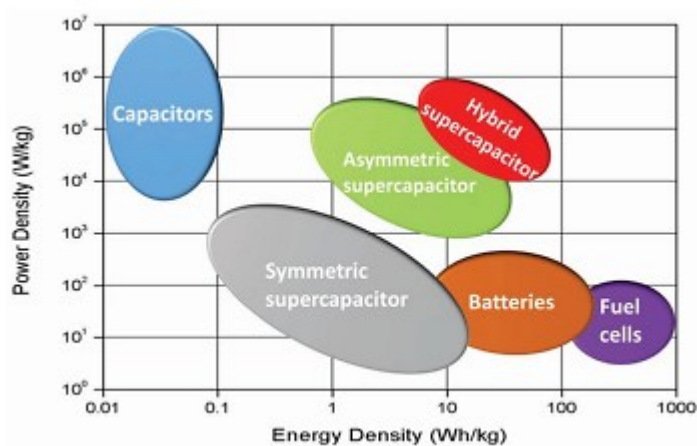
Figure 4.3. Specific energy and power capabilities of electrochemical energy storage/ conversion devices.

An important difference between a capacitor and a battery is that there is always an intrinsic increase in voltage on charge (or decrease on discharge) for a capacitor as a result of the increase (or decrease) in charge stored on the capacitor electrodes. Current research into ECs can be divided into three main areas, based primarily on their mode of energy storage and construction: (i) the electric double-layer capacitor (EDLC*)*, (ii) the *redox* EC (also referred to as *pseudocapacitor*), and (iii) hybrid systems incorporating combinations of double layer and *pseudocapacitance.*

Despite the wide array of possible materials and device architectures, the EDLC version is currently the most developed form of EC and dominates the market. Carbon, in its various forms, is currently the most extensively examined and widely utilized electrode material in commercial EDLCs.

In an EDLC, a physical mechanism generates the electric double layer that performs the function of a dielectric (Figure 4.4). The charge-discharge cycle is created through an ion absorption layer at the surface of the positive and negative activated carbon electrodes. EDLCs use ion migration inside a thin membrane of activated carbon to

store electrical charges. Applying a voltage across the capacitor's two electrodes causes the ions in the electrolyte to migrate in an attempt to reverse the charge on the electrodes (the charging part of the cycle). Positively charged ions move to the negative electrode and negatively charged ions move the positive electrode, forming two charged layers inside the electrolyte: one positive and one negative. Removing the voltage causes the ions to move in the opposite direction, creating the discharge half of the cycle.
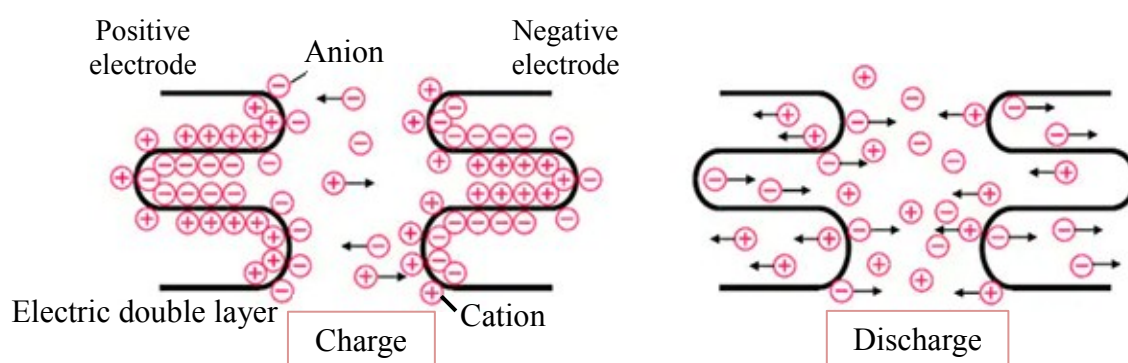
Figure 4.4. EDLCs typically store electrical charges in activated carbon electrodes.

4.3.2 The electrical double-layer

The concept of a double layer corresponds to a model consisting of two array layers of opposite charges, separated by a small distance having atomic dimensions, and facing each other, as on the plates of a two-plate hardware capacitor. This model was adopted by von Helmholts [56] to describe his perception of the distribution of opposite charges, quasi-2-dimensionally, first at the interface of colloidal particles. It is illustrated in Figure 4.5(a), which shows its compact structure, and is referred to as the Helmholtz double-layer model [56].

In the original model for colloidal interfaces, the charges on the surface side of the double layer arise either from acid-base ionization, as with proteins or polyelectrolytes, or on account of the adsorption of ions, as at lyophobic colloids.
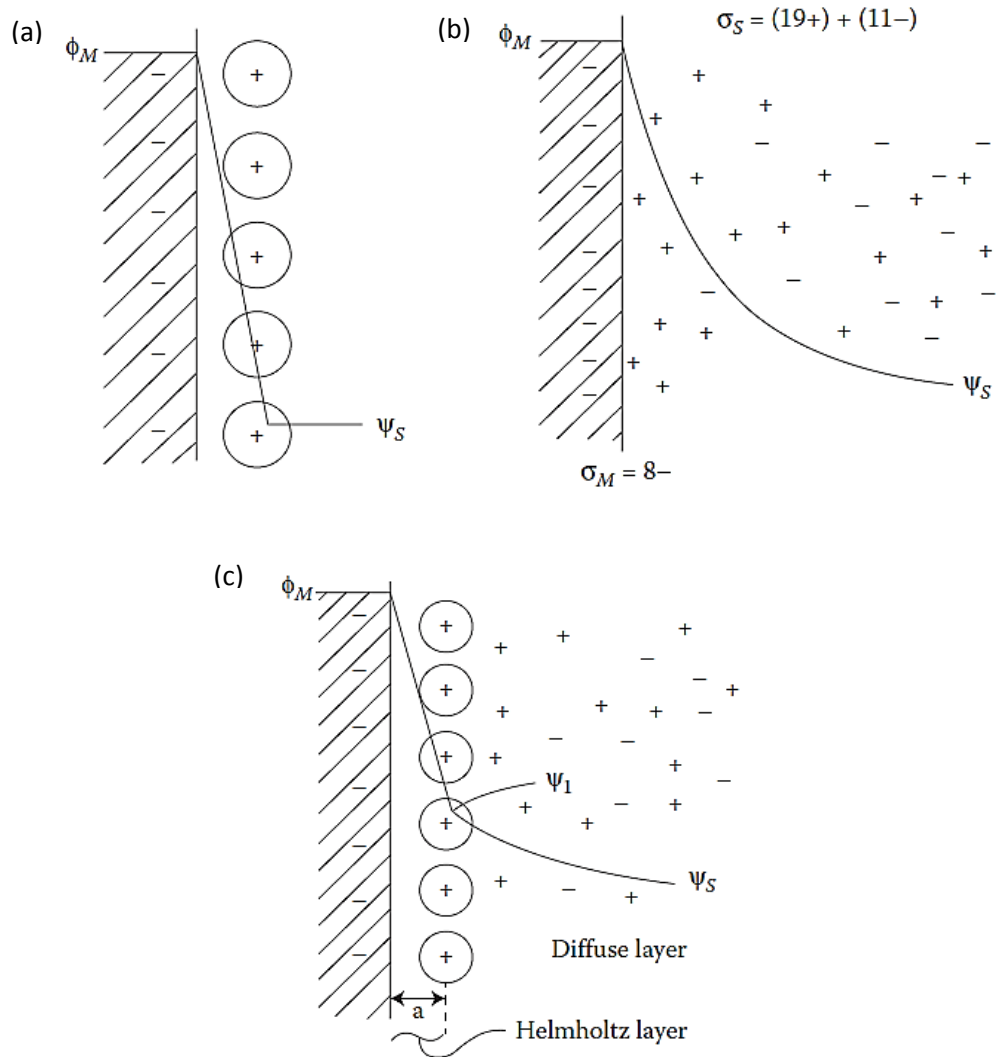
Figure 4.5. Double layer models: (a) Helmholtz model, (b) Gouy-Chapman model, and (c) Stern model [49].

On the solution side of the double layer, counterions of opposite sign of charge accumulate to balance the charge on the colloid, forming a double-layer array of positive and negative charges. The Helmholtz model was later adapted to the case of electrode interfaces where, on the metal side, a controllable surface density of excess negative or positive charge can arise that corresponds to an excess or deficiency of electron charges of the delocalized electron plasma of the metal. Owing to the high free electron density in the metal, any net charge density of electrons at the surface is strongly screened, so the gradient of electron density at a charged metal interface is highly localized over distance of only 0.05 to 0.2 nm, the so-called Thomas-Fermi screening distance. Because the wave function amplitudes of the conduction-band

electrons retain significant but diminishing magnitudes outside the formal electrode surface plane, there is significant spillover of electron density into the double layer on the solution side of the interface [57,58] and the effect is potential dependent.

In the case of p- or n-semiconductors, the charge-carrier (hole or electron) densities are, however, very much smaller than in metals but a factor varying from about 10^{-4} to 10^{-5}. As consequence, there is a distributions of the charge carriers away from the interface but extending into the bulk of the semiconductor over a relatively large distance that is inversely related to the charge-carrier density. The distribution of charge carriers within semiconductors, near their interfaces, follows mathematically exactly the same form as for ion distribution in the diffuse layer on the solution side.

Some time after von Helmholtz's model was proposed, it became realized that ions on the solution side of the double layer would not remain static in a compact array as in Figure4.4(a) but would be subject to the effects of the thermal fluctuations [59] according to the Boltzmann principle. This latter effect would depend on the extent to which the electrostatic energy U_e (together with any chemisorption energy U_c) of the ions' interactions with the charged metal surface exceeded, or were exceeded by, the average thermal energy, kT, at temperature, T, K, i.e. the ratio $(U_e + U_c)/kT$.

Gouy [59] introduced this thermal fluctuation factor into a modified representation of the double layer in which the counterions conjugate to the metal surface's electron charge were envisaged as a 3-dimensional diffusely distributed population of cations and anions [Figure 4.4(b)] of the electrolyte having a net charge density equal and opposite to the virtually 2-dimensional electron excess or deficit charge on the metal surface. In this model, the ions were assumed to be point charges. Historically, this was an important restriction since it led to a failure of Gouy's model on account of (1) an incorrect potential profile and local field near the electrode surface and (2) consequently a too-large capacitance being predicted, that quantity being defined as the rate of change of net ionic charge on the solution side with the change of metal-solution potential difference across the interphase. The interphasial capacitance associated with this model is commonly referred to as the "diffuse" double-layer capacitance.

A full mathematical treatment of the Gouy diffuse-layer model was given in some detail by Chapman in 1913 [60], based on the combined application of Boltzmann's energy distributions equation and Poisson's equations for the relation between ionic space

charge density in the interphasial region to the second derivate of electric potential, ψ, with respect to distance from the electrode surface. It is interesting to note that the mathematics and principles used by Chapman anticipated the approch taken by Debye and Hückel in 1923 [61] in determining ion distribution in three dimensions around a given ion in their treatment of activity coeffcients and conductance of electrolytes. Later it was used by Onsager, in an improved treatment of the conductivity of electrolytes.

In both Chapman's and Debye and Huckel's treatments of ionic charge distributions, the key equations resulting from the combination of Boltzmann's energy distribution function and Poisson's electrostatic equation has been referred to as the Poisson-Boltzmann equation. It is also utilized in the treatment of band profiles and space charge effercts in semiconductors.

The serious problem with the Gouy-Chapman treatment, overestimation of the double-layer capacitance, was overcome by Stern in 1924 [62] in the next stage of development of the theory of double layers. In his model and calculations it was recognized that the inner region of the ion distribution could be treated in terms of an adsorpion process according to Langmuir's adsorption isotherm, and the region beyond this inner layer, into the solution, could be validly treated in terms of a diffuse region of distributed ionic charge [Figure4.5(b)] as treated by Gouy [59] and by Chapman [60]. In addition, if the ions were recognized as having finite size, including the annular thickness of their hydration shells, it was easy to define a geometrical limit to the compact region of adsorption of ions at the electrode surface [Fig 4.5(c)]. This is taken to correspond to a Helmholtz type of compact double layer having a capacitance C_H, while the remaining ionic charge density beyond this compact ion array is referred to as the diffusive region of the double layer, having a capacitance C_{diff}. C_{diff} and C_H are conjugate components of the overall double-layer capacitance, C_{dl}, related by the equation

$$\frac{1}{C_{dl}} + \frac{1}{C_H} + \frac{1}{C_{diff}} \tag{4.1}$$

Parsons, in an important article in 1954 [63], presented a treatment in which the limit for a distinction between the Helmholtz compact layer and the diffuse layer beyond it

can be understood in terms of the distance of closest approach of counter anions or counter cations to the metal electrode surface.

By introducing a distance of closest approach of finite-sized ions and thus geometrically defining a compact Helmholtz inner region of the double layer, the problem of a far too high capacitance that arises in the Gouy-Chapman treatment is automatically avoided. This difficulty arises since the capacitance of two separated arrays of charges increases inversely as their separation distance, so very large capacitance values would arise in the limit of infinitesimally small (point charge) ions very closely approaching the electrode surface.

The Stern theory of the double layer remained a good basis for general interpretations of electrode interface phenomena, including double-layer effects in electrode kinetics until the detailed work of Grahame in the 1940s on the double layer capacitance at the mercury electrode in aqueous electrolyte solutions.

Grahame's work emphasized the great significance of the specificity of double-layer capacitance behavior at Hg to the nature of the cations and anions of the electrolyte, partuculary the size, polarizability, and electron-pair donor properties of the anions of the electrolyte.

This led Grahame to make an important distinction between an inner and outer Helmholtz layer in the interphase which correspond to the different distances of closest approach that can arise for anions vis a vis cations at the elctrod surface. This difference of distances of closest approach is mainly caused by the fact that most common cations are smaller than common anions and retain solvation shells due to strong ion-solvent dipole interaction. Thus, the Grahame model (Figure4.6) consists of three distinguishable regions: the inner Helmhotz layer, the outer Helmoholtz layer, and always a diffuse ion distribution region.

At extremes of polarization, one or the other of the Helmholtz layer regions dominates, with population of anions or cations, corresponding to such polarizations. Because anion distances of closest approach are usually smaller than hydrated cation distances of closest approach, the inner layer capacitance at positively charged electrode surfeces is usually about twice that at a corresponding negatively charged surface, though this depends on the metal and the ions of the electrolyte, and the solvent. These aspects of

double-layer capacitance behavior are of the great significance for understanding the properties of double-layer supercapacitors and the magnitude of capacitance that can be achived per square centimeter over various ranges of potential and various electrode materials.
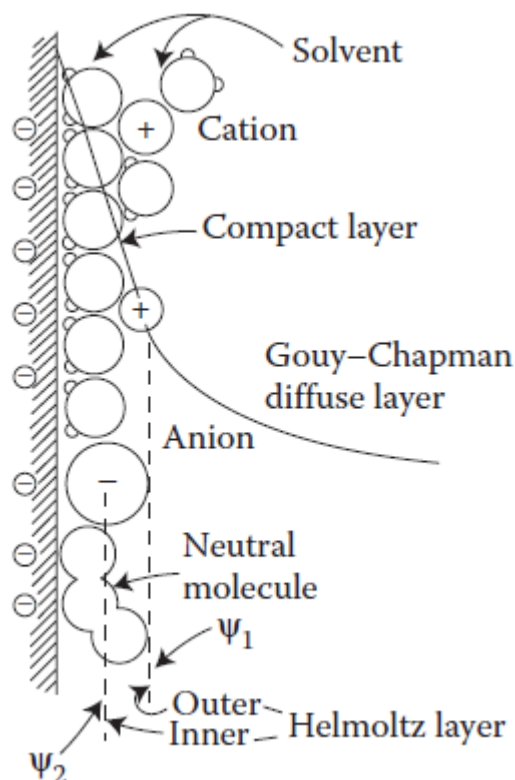
Figure 4.6. General representation of the structure of the double layer showing different regions for adsorption of hydrated cations and less hydrated anions (Grahame model[64]), together with solvent molecules and an adsorbed neutral molecule.

4.3.3 Supercapacitors parameters

- Energy and Power

Two primary attributes of a capacitor are its energy and power density, both of which can be expressed as a quantity per unit weight (specific energy or power) or per unit volume.

When a voltage, V, is applied to the capacitor for a short time, a small amount of work, dW, is done to move a small quantity of charge, dQ, to be accumulated at the electrode/electrolyte interface

$$dW = VdQ . \qquad (4.2)$$

Assuming an insignificant heat loss, dW is equivalent to the amount of energy stored in the capacitor, and considering that the voltage of a capacitor is proportional to the amount of charge accumulated in the capacitor, through the equation 4.2,

$$C = \frac{Q}{V} \qquad (4.3)$$

where C is the capacitance (proportional to the ratio of the area of the electrode/dielectric interface and the separation distance between the two electrode plate), it will be possible to integrate equation 4.1 as follows:

$$W = E = \int_0^Q VdQ = \int_0^Q \frac{Q}{C} \, dQ = \frac{1}{2}CV^2 . \qquad (4.4)$$

Therefore, the energy storage in a capacitor depends on the capacitance and applied voltage. This parameters are mostly governed by the two main components of supercapacitors: the electrolyte and the electrode material.

The power output, P, from a capacitor can be in principle derived from dividing W by t, the time needed to fully discharge the capacitor,

$$P = \frac{W}{t} . \qquad (4.5)$$

The maximum power output is determined by the shortest discharging time.

It is a fact that any electric power source has an internal resistance known as the equivalent series resistance, or simply ESR. Therefore, the resistance of the internal components of the capacitor needs to be taken into account in order to determine maximum power output. The ESR, by introducing a voltage drop, determines the maximum voltage of the capacitor during discharge and therefore limits the maximum energy and power of a capacitor. The maximum power P_{max}. for capacitors is given by the following equation

$$P_{max.} = \frac{V^2}{4ESR}.$$ (4.6)

A very high internal resistance limits the power of a supercapacitor and consequently its applications. Three main factors that determine the energy and power are the equivalent series resistance, the voltage and the capacitance.

- Equivalent series resistance (ESR)

The equivalent series resistance (ESR) of a capacitor includes the intrinsic electronic resistance of the electrode material, the interfacial resistance between the active electrode material and current collector, the ionic (diffusion) resistance of ions moving in small pores, the ionic resistance of ions moving through the separator and the electrolyte ionic resistance.

To reduce the ESR existing in the carbon-based electrochemical capacitor, activated carbon are usually prepared using a binder that can maintains the structural integrity of the active particles or powders and help electrode materials to adhere uniformly onto the current collector. To date, fluorinated polymeric binders, such as poly(vinylidene fluoride) (PVDF) and polytetrafluoroethylene (PTFE), have been extensively used for ECs. The nature and the amount of the binders can also greatly influence the performance of the electrodes and the assembled ECs [65,66]. For instance, Tsay et al. [66] found that for Na_2SO_4 electrolyte-based ECs using carbon BP2000 electrodes, the maximum value of the specific capacitance was obtained when the PTFE binder content was 5 wt%. Decreasing or further increasing the content of PTFE the specific capacitance decreases. Since PTFE is hydrophobic, too large an amount of PTFE could inhibit the penetration of aqueous electrolyte ions into pores in the carbon electrode materials, resulting in a lower specific capacitance [66]. For this reasons, the electrode preparation include the use of carbon black as conductive additive although the use of carbon nanotubes has also been proposed [67].

Novel strategies to minimize the electrode resistance are:

(i) the use of advanced materials with high conductivity, such as carbon nanotubes [68];

139

(ii) the use of porous materials with low-tortuosity, such as ordered porous carbon materials [68,69];

(iii) the preparation of carbon electrodes directly on the current collector to improve the contact between the electrode and the current collector [70];

(iv) the preparation of carbon monoliths with a continuous structure that significantly increases the interparticle contact with respect to activated carbon powder, making the use of binders and conductivity promoters unnecessary.

- Voltage

In supercapacitors, the operating voltage is strongly depending on the stability window of the electrolyte. In water medium, although the thermodynamic value is 1.23 V, practically it ranges from 0.7 to 1 V. In organic electrolyte, the operating voltage can reach 2.7–2.8 V. Recent studies have shown that ionic liquids can anable operative voltage up 5 V. Hence, due to the square dependence of energy with voltage, the electrical energy accumulated in EC can be significantly enhanced by the selection of an organic medium or ionic liquid. Unfortunately due to the low conductivity of these solutions (20 mS/cm against 1 S/cm for water medium) this profit can be quite doubtful in the case of the high specific power demanded. Additionally for practical applications, the use of these electrolytes can meet certain technological, economical and safety barriers. However, the possibility of reaching 3V or more, is still very attractive and a lot of research is performed especially for applications with a low specific power.

- Capacitance

The capacitance of electric double-layer supercapacitors is, in principle, independent of voltage and depends mainly on the specific available area, which is determined as the part of the total specific area corresponding to the porosity accessible to the electrolyte. The capacitance of pseudocapacitive capacitors, on the other hand, depends on the concentration of electroactive surface species and the potential window where their capacitance is maximized. The determination of the capacitance of a valid electrode material for use in a supercapacitor is therefore of great importance. The most

commonly used electrochemical techniques for its determination are cyclic voltammetry [Appendix B.2] and galvanostatic charge and discharge cycles (chronopotentiometry [Appendix B.1]), which can be performed in a two- or three-electrode electrochemical cell. The former is used to characterize the electrode material, whereas the latter is used to get information on the behavior of the supercapacitor in conditions closer to its real use. As mentioned above, the most common electrochemical cell configuration for the electrochemical characterization of the electrode material is that of the three-electrode cell (Figure 4.7).

The cell is filled with the electrolyte and is composed of a working electrode, which consists of the current collector with the electrode material to characterize attached to it, an inert counter electrode immersed in the same electrolyte to close the circuit, and a reference electrode, which is sometimes placed away from the working electrodes, and a counter electrode using a Luggin capillary. The two-electrode cells consist of two electrodes separated by a sandwich membrane. To carry out the characterization of the material, it is necessary to consider several aspects. The active phase mass and electrode thickness must be known. It is recommended to use a sufficient mass to increase the characterization precision. The thickness of the electrode must be similar to that of the application for which the material will be destined, since thickness is one of the determining factors of the ESR. The current collector must be stable and inert in the selected electrolyte and in the potential window to be analyzed. In cyclic voltammetry, the potential of the electrode (three-electrode cell) is varied over time at a constant scanning speed between two potential limits, V_0 and V_x, registering the current between counter electrode and working electrode. If the capacitor is characterized in a two-electrode cell, what varies is the cell voltage, that is, the difference between positive electrode (anode) and negative electrode (cathode). The current is directly related to the capacitance through the scanning speed, if the variation in the capacitance over time is neglected:

$$\frac{Q}{t} = i = C\frac{\partial V}{\partial t} + V\frac{\partial C}{\partial t} = C\frac{\partial C}{\partial t} \tag{4.7}$$

$$C = \frac{i}{\partial V/\partial t} = \frac{i}{v}. \tag{4.8}$$

This expression allows the capacitance to be estimated from the average current in the selected potential range.

Working electrode

Counter electrode
Platinum wire

Reference electrode
Ag/AgCl (3M KCl)
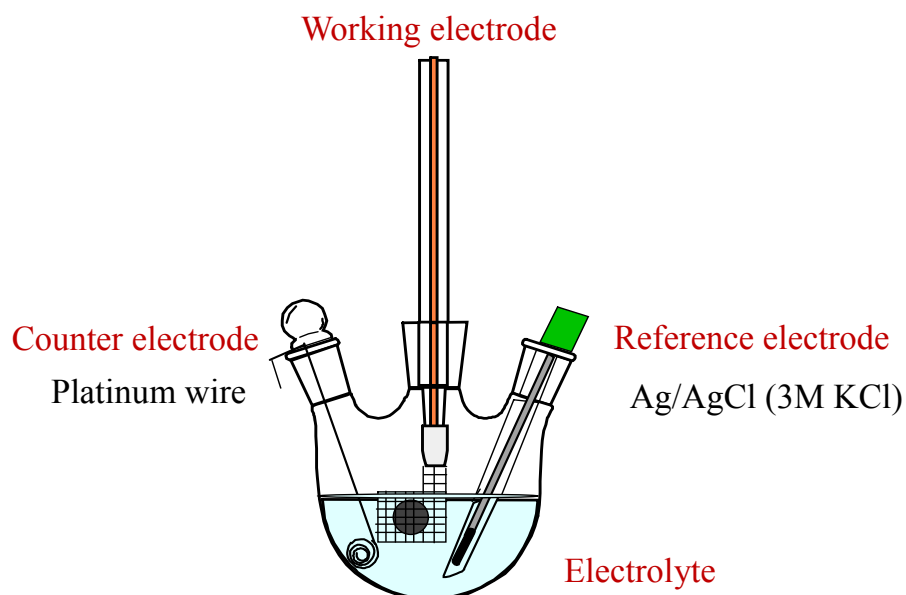
Electrolyte

Figure 4.7. Three-electrode cell configuration.

In addition to the material capacitance, the possible redox processes that occur in the electrode and the stability window of the electrolyte and electrode can also be detected. Figure 4.8 shows two typical voltammograms for an electrode (three-electrode cell): one, whose mechanism is electric double-layer, and the other one that has pseudo-capacitive, respectively. The former presents a rectangular shape, since in these materials the capacitance is constant with the potential. The latter shows redox processes, V_R, of species or superficial functional groups.

(a) i

V   V V

(b) i

V

V   V V
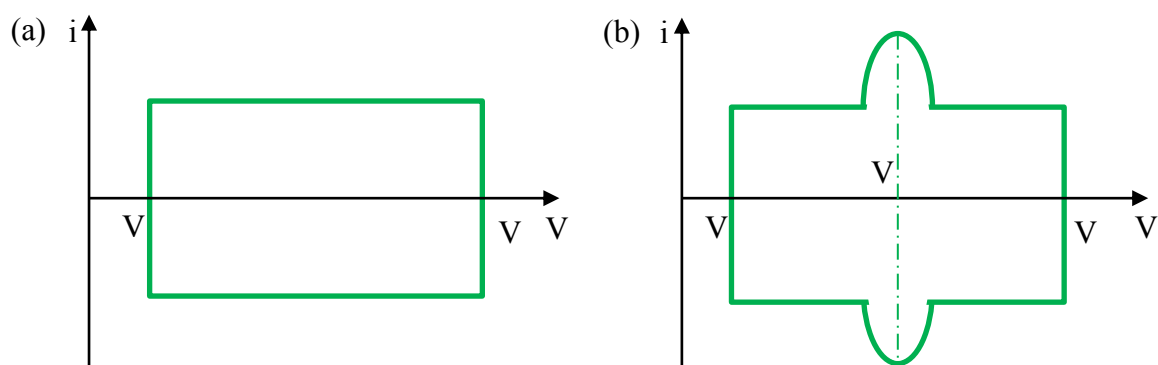
Figure 4.8. Typical voltammograms of an electrode with (a) capacitive and (b) pseudocapacitive behaviour.

Another suitable technique for estimating the capacitance of electrode material and supercapacitor is the chronopotentiometry, also called galvanic static discharge. As an example, Figure 4.9 shows a charge/discharge cycle of a two-electrode cell supercapacitor. In this experiment, a constant current is applied between both electrodes, producing a variation of the voltage over time starting from a zero voltage. At a certain potential value, the polarity of the current is reversed. The process where the potential of the device is increased is called charge, while the inverse is the discharge, both constituting a cycle. From the chronopotentiometry experiments, the ohmic drop corresponding to the resistance of the material or the capacitor (ESR) can be determined at different currents. This ohmic drop must be discounted when the material capacitance is calculated, which can be estimated from the following expression:

$$C = \frac{Q}{\Delta V} = \frac{i\Delta t}{\Delta V - iR\Omega} \qquad (4.9)$$

It is worth remembering that, when working in a three-electrode cell, the capacitance measured in the galvanostatic discharge experiments is referred to a single electrode (working electrode), being four times greater than that obtained in a two electrode cell, since in this type of symmetric capacitor arrangement there are two capacitors in series (corresponding to each electrode) and, therefore, the experimentally obtained capacitance corresponds to half of each electrode. The total capacitor capacitance (C) formed by two electrodes can be calculated with the following equation:

$$\frac{1}{(m_+ + m_-)C} = \frac{1}{m_- C_-} + \frac{1}{m_+ C_+} \qquad (4.10)$$

where: m_+ and m_- correspond to the mass of the positive electrode and the mass of the negative electrode, respectively; C_+ and C_- to the capacitance of the positive electrode and the capacitance of the negative electrode respectively.

Therefore, the capacitance when working with electrodes of different material or mass will always be determined by that of the electrode of lower capacitance. In addition to the techniques mentioned so far, it is possible to use another series of electrochemical techniques to, for example, study the kinetics of formation of the double layer

(impedance or potentiometric jumps) or the stability of the electrodes (potentiostatic experiments and also thermostatized cell at high or low temperatures).
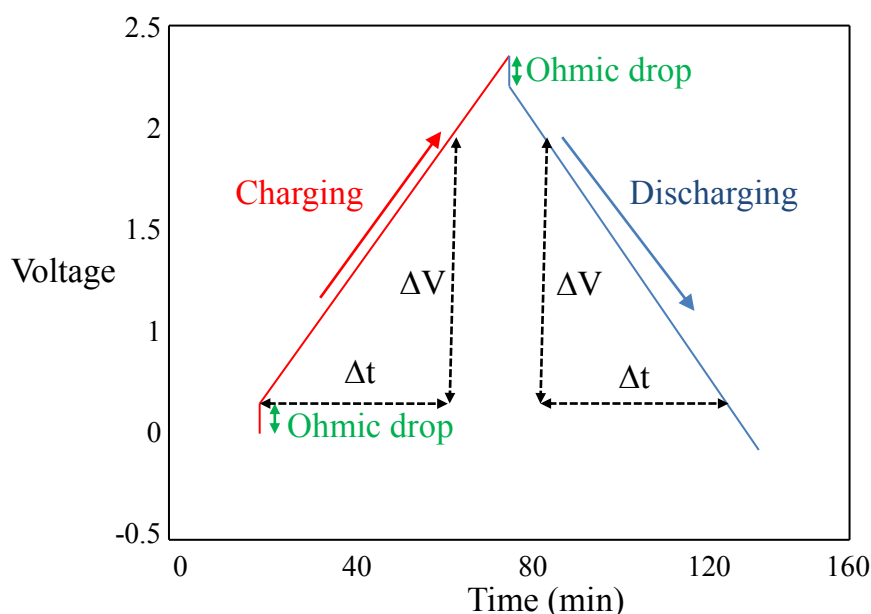
Figure 4.9. Galvanostatic charge-discharge curve.

In the potentiostatic experiments, the condenser is subjected to a high potential for a long period to then determine the specific capacitance drop, which allows simulating the condenser aging process during its lifetime, being one of the most appropriate techniques to establish the durability of the electrodes.

4.3.4 Supercapacitors configurations

- Symmetric capacitors

The symmetrical configuration is the simplest and most common for electrochemical capacitors. It consists of two electrodes of the same material with the same mass. It is the most frequent and easiest configuration used in the industry. However, in this configuration it is not possible to fully exploit the performance of electrodes and electrolytes to maximize the charge storage.

- Asymmetric supercapacitors

Materials used as electrodes in capacitors may not show the same capacitance in the range of potentials in which each electrode works. In these cases, the capacitance depends on the applied potential. In the case of capacitors based on carbonaceous materials, this effect can occur when electrolytes with different cation and anion sizes are used, and the effective pore size for electro-absorption is similar to that of one of the ions [71]. In these cases, the adsorption of one of the ions will be higher than that of the other, and will have a higher capacitance in the range of potential in which its adsorption is favorable. In these cases, the mass of the electrodes can be optimized to maximize the energy stored in the capacitor. The optimal mass ratio was proposed by Snook et al. [72]

$$\frac{m_+}{m_-} = \sqrt{\frac{c_-}{c_+}} \tag{4.11}$$

where m_+ and m_- are the masses of the positive and negative electrodes, respectively, C_+ and C_- are the capacities of the positive and negative electrodes, respectively. Another cause of wasting the maximum energy of a capacitor is that the materials are stable in different windows of stability potentials. In this case, the optimum mass ratio can be determined by knowing the stability window and the capacitance of the electrodes in those windows, establishing an equal ratio of charges between the positive and negative electrode [73]:

$$Q = Q_+ = Q_- \tag{4.12}$$

$$m_+ C_+ \Delta E_+ = m_- C_- \Delta E_- \tag{4.13}$$

$$\frac{m_+}{m_-} = \frac{C_- \Delta E_-}{C_+ \Delta E_+} \tag{4.14}$$

where Q is the electrochemical capacitor charge, Q_+ is the positive electrode charge, Q is the negative electrode charge, ΔE_+ and ΔE_- are the windows of positive and negative electrode stability potentials, respectively.

4.3.5   Aqueous electrolytes

Liquid electrolytes are classified as: aqueous, organic and ionic liquids. The main properties to consider when selecting an electrolyte are its window of stability potentials and its ionic conductivity.

Aqueous electrolytes have several advantages for use in supercapacitors. Compared to organic electrolytes and ionic liquids, they have higher conductivity (~ 1 S/cm) and provide higher values of specific capacitance. In addition, they have a lower cost, are less harmful to the environment and facilitate theconstruction of the device, since they do not require the use of inert atmosphere chambers. However, the thermodynamic potential for water decomposition (1.23 V) limits the voltages of these supercapacitors to approximately 1 V. Therefore, electrochemical capacitors based on aqueous electrolytes provide lower energy values than those related to organic medium and ionic liquid [2,51,74]. Aqueous electrolytes can be classified as: acidic, basic and neutral. The most representative of each type of these groups are: H_2SO_4, KOH and Na_2SO_4. In acidic medium, the voltage is usually limited to 1-1.3 V [51].

In the case of neutral electrolytes, the specific capacitance and ionic conductivity is lower than that of H_2SO_4 and KOH, so the devices have a higher ESR. However, these electrolytes are less corrosive and have a greater stability window, so that they reach higher voltages. In Na_2SO_4, voltages of even 2.2 V have been obtained through asymmetric configurations [54].

4.3.6   Carbon materials as electrode in supercapacitors

- Influence of porous texture

The porous texture of carbonaceous materials (defined by specific surface area, pore volume and pore size distribution) is a key parameter in their behavior as supercapacitor electrodes [2,75]. In general, the specific capacitance of carbonaceous materials is directly proportional to the specific surface at low values, but reaches a constant value

at specific surfaces greater than 1200-1500 m^2/g [76]. A plausible explanation for this effect is the decrease in the average thickness of the pore walls in highly activated coals. On the other hand, it has been observed that the average pore size increases with the specific surface when the degree of activation increases. However, the cargo storage mechanism cannot be exclusively related to surface effects.

Bleda-Martínez et al. [75] demonstrated the importance of the arrangement of microporosity on the external surface of the material. In carbon fibers, the microporosity is mainly arranged perpendicularly to the fiber axis, so it has a relatively low tortuosity. Differently, in the case of activated carbons, they are characterized by a very disorderly porous network, which leads to a high degree of tortuosity. Consequently, activated carbon showed a complete loss of capacitance under high frequency (high power) measurement conditions at 0.5 M Na$_2$SO$_4$, while carbon fiber retained 25% of capacitance. This is due to the higher tortuosity in the diffusional path of the electrolyte in activated carbon.

- Influence of surface chemistry

As described in the introduction, surface chemistry is a characteristic parameter of carbonaceous materials that has a great influence on several applications.

The surface chemistry of carbonaceous materials affects various physicochemical and electrochemical properties of materials, such as: wettability, electrical conductivity, electrochemical stability and contribution to capacitance through pseudocapacitive processes. However, the effect of functional groups should be analyzed.

In the case of oxygenated functional groups, a positive correlation has been found between the capacitance and the number of groups that desorb as CO [4]. This is mainly due to the contribution to the pseudocapacitance of the quinone groups [4,77,78] and the hydrophilic nature of the hydroxyls, which increase the wettability of the electrode. The effect of pseudocapacitance depends on the pH of the electrolyte, because it involves

the exchange of protons. On a basic basis, the faradic contribution of CO groups is significantly smaller, although some contribution has been detected [79].

On the other hand, the groups that desorbed as CO_2 are harmful to carbonaceous materials, due to their electron-acceptor character, which results in a less delocalization of the charge and, thus, a decrease in electrical conductivity [31,78]. Finally, it has been observed that oxygenated functional groups decrease the electrochemical stability of carbonaceous materials in aqueous [80] and organic electrolytes [81].

4.4   Results and discussion

4.4.1   Porous texture and surface chemistry

A highly microporous activated carbon (named KUA), synthesized by chemical activation of a Spanish anthracite with KOH [26], was used to prepare the supercapacitor electrodes.

The nitrogen adsorption-desorption isotherm [Appendix B.3] of the activated carbon (Figure 4.10) shows a type I isotherm, characteristic of a microporous material with some amount of mesopores favourable for ions transportation.
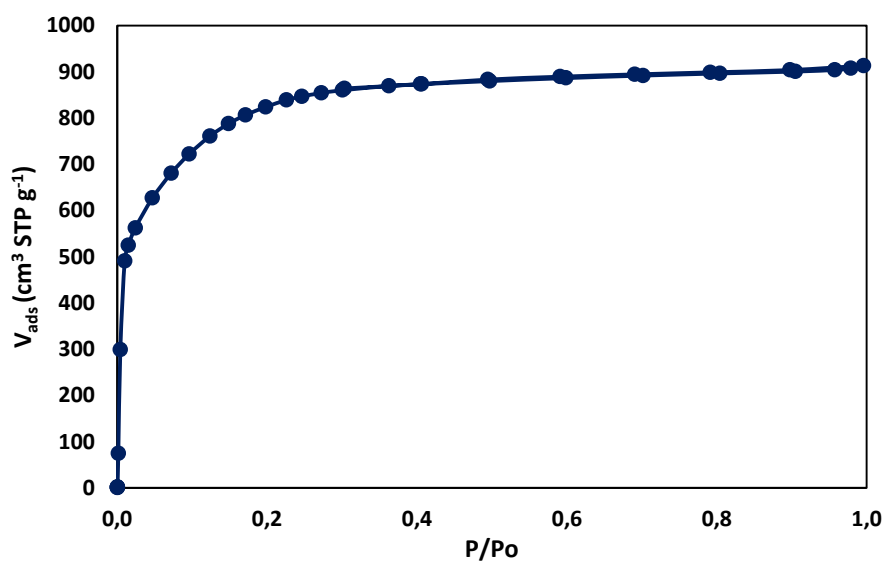
Figure 4.10. N_2 adsorption isotherm.

Nitrogen adsorption results were used to determine BET surface area [Appendix B.3] value and Dubinin-Radushkevich (DR) micropore volumes as well as the average pore size (Table 4.1). The activated carbon KUA exhibits large apparent surface area with well-developed microporosity. The micropore volume determined by N_2 adsorption corresponds to the whole microporosimetry ($< 2nm$), whereas the obtained CO_2 adsorption corresponds to the volume of the narrowest micropores which is the appropriate pore size for a rapid diffusion of electrolyte ions, especially under fast polarization conditions.

S_{BET} (m^2g^{-1})	$V_{DR}^{N_2}$ (cm^3/g)	$V_{DR}^{CO_2}$ (cm^3/g)
3077	1.17	0.54

Table 4.1. Specific surface area and pore volume data of activated carbon.

Temperature programmed desorption (TPD) is one of the most powerful techniques available to evaluate the amount and types of oxygen-containing surface groups in carbon materials.

As reported in literature [82], KUA is composed mainly by carbon and a relatively high amount of oxygen generating during the activation process. The desorbed CO results from the decomposition of carbonyls, quinones (CO at temperatures over 700 °C), and phenols (CO at 600-700 °C) [40].

4.4.2 Electrochemical characterization

- Characterization of the carbon

Carbon electrodes for electrochemical characterization were prepared by mixing the activated carbon with acetylene black and polytetrafluoroethylene (PTFE) as binder in a ratio of 90:5:5 (w/w). The weight of the electrodes was between 5-6 mg (dry basis). For shaping the electrodes, a sample sheet was cut into a circular shape with an area of 0.79 cm^2 and pressed onto a titanium mesh used as current collector for 1 min at 1.5 ton

to guarantee a homogeneous thickness. The electrodes were impregnated into the electrolytes (1MH_2SO_4 and 0.5M Na_2SO_4) previously to electrochemical measurements.

The electrochemical characterization of the electrodes was performed by cyclic voltammetry (CV) in a Biologic VSP multichannel potentiostat and using a standard three-electron configuration. As reference electrode, Ag/AgCl (3M KCl) was used and a spiral of platinum wire was used as a counter electrode. The electrolytes employed in this thesis were 1M H_2SO_4 and 0.5M Na_2SO_4. CV capacitance was calculated from the area of the voltammogram. The results are expressed in F/g, taking into account the weight of the active material of the working electrode.

Activated carbon has been characterized by cyclic voltammetry using scan rates between 1 and 100 mVs^{-1}. KUA sample in 1M H_2SO_4 exhibits a quasi-rectangular shape, characteristic of a pure capacitive electrode, over a wide range of scan rates [Figure 4.11(a)]. On the other hand, KUA in 0.5 Na_2SO_4 solution shows a capacitive behavior only up to 20 mVs^{-1}. At higher scan rates the cyclic voltammograms curves appear distorted with a smaller integrate area due to the electrolyte mass-transfer resistance [Figure 4.11(b)].

These observations are in agreement with the gravimetric capacitance values reported in Table 4.2.

A low scan rate provides enough time for ion diffusion into the pore network, so all the surface wetted by the electrolyte will be available for the formation of the double layer.

The differences observed in CVs behaviors of activated carbon in different electrolytes come from different physical properties of the ions from these different electrolytes. The main factors that determine the performance of a supercapacitor when using different electrolytes are the mobility and conductivity of the ions.

H^+ ion has the highest molar conductivity with a value of 349.6 cm^2 Ω^{-1} mol^{-1}, while Na^+ ions have a value of 50.1 cm^2 Ω^{-1} mol^{-1}. Consequently, H^+ ions being characterized by the highest mobility can easily migrate into the electrode/electrolyte surface during charging and into the electrolyte bulk during discharging.
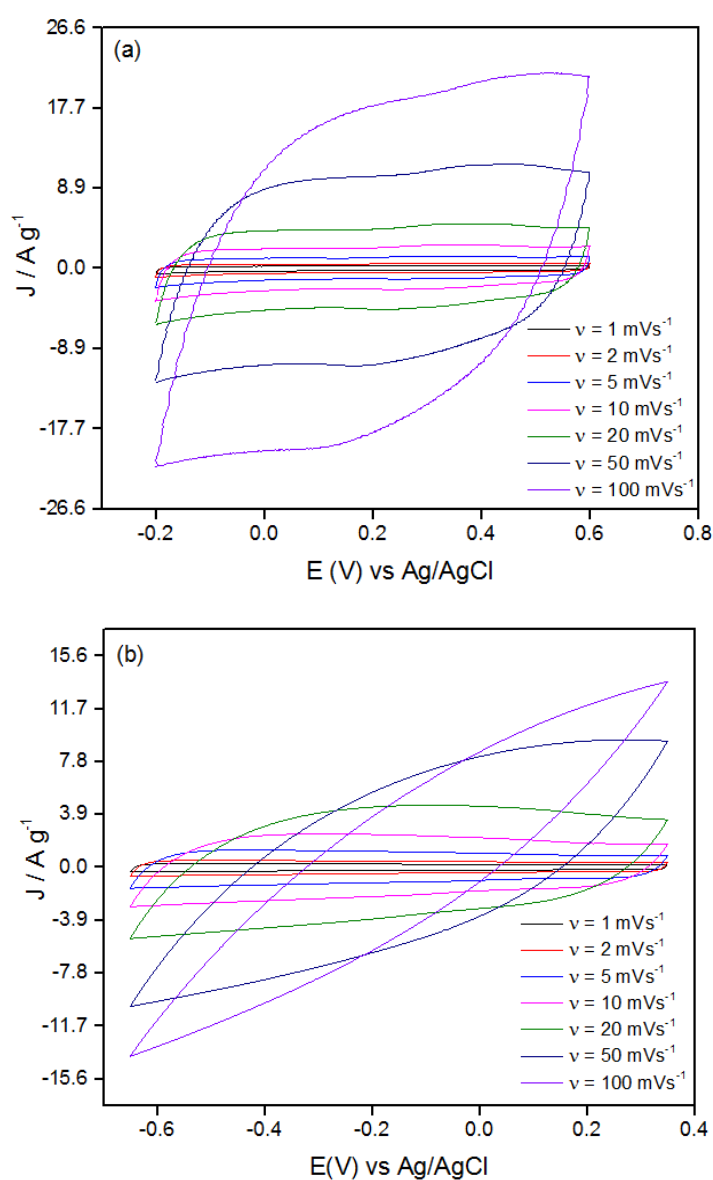
Figure 4.11. Cyclic voltammograms for KUA in (a)1M H_2SO_4 and (b) 0.5 M Na_2SO_4.

v (mV/s)	C_g [H_2SO_4] (Fg^{-1})	C_g [Na_2SO_4] (Fg^{-1})
1	292	248
2	261	241
5	257	228
10	241	210
20	223	175
50	190	95
100	152	38

Table 4.2. Gravimetric capacitances (C_g) determined for KUA using H_2SO_4 and Na_2SO_4 electrolytes.

Figure 4.12(a) shows the cyclic voltammograms for KUA sample in H_2SO_4 from a fixed upper potential value toward less positive ones. It is observed that voltammogram between 0.4 and -0.2 V exhibits a quasi-rectangular shape related to the formation of the electric double layer. If the lower potential limit decreases, this shape changes and a reduction peak appears at -0.3V related to the hydrogen evolution reaction [83]. During the positive-going scan, it happens an increase in the oxidation current, which becomes larger when the lower potential limit is less positive. Electrochemical behavior for the same sample to positive potential values is shown in Figure 4.12(b). The voltammograms also show a rectangular shape. If the upper potential limit increases, the oxidation of the carbon material is observed at 0.8 V. It is possible to observe in the reverse scan a cathodic current at 0.4 V which can be associated with the reduction of electroactive surface groups generated in the positive scan. The redox processes observed in this case are related to electroactive functional groups that correspond with the pseudocapacitive contribution of the quinone/hydroquinone

The cyclic voltammograms obtained for KUA in Na_2SO_4 are presented in Figure 4.13. The CVs exhibit a rectangular shape characteristic of a pure capacitive behavior. At negative sweep, a reduction peak at potential close to -0.9 V is observed and its corresponding oxidation peak appears during the positive sweep at 0.7 V.
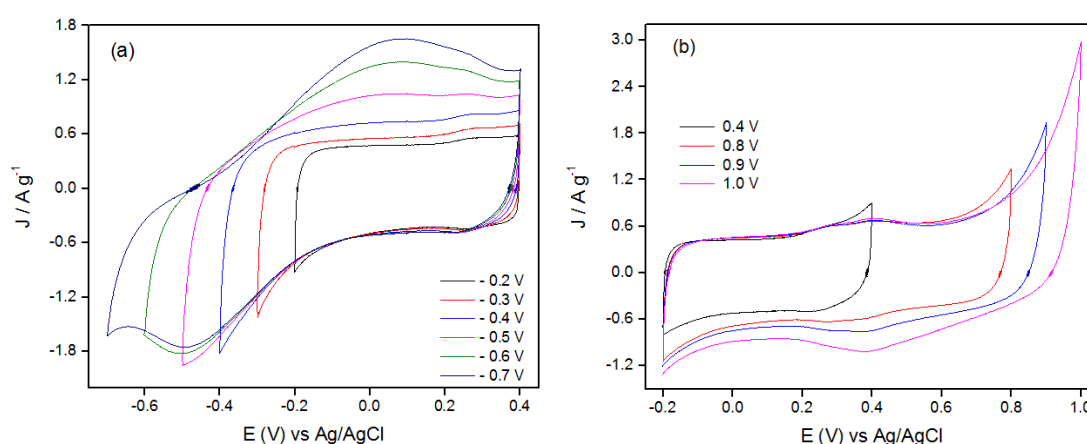
Figure 4.12. Cyclic voltammograms for KUA electrode in the potential range (a) -0.7-0.4 V and (b) -0.2-1.0 V. 1M H_2SO_4. $\nu = 2$ mV/s.
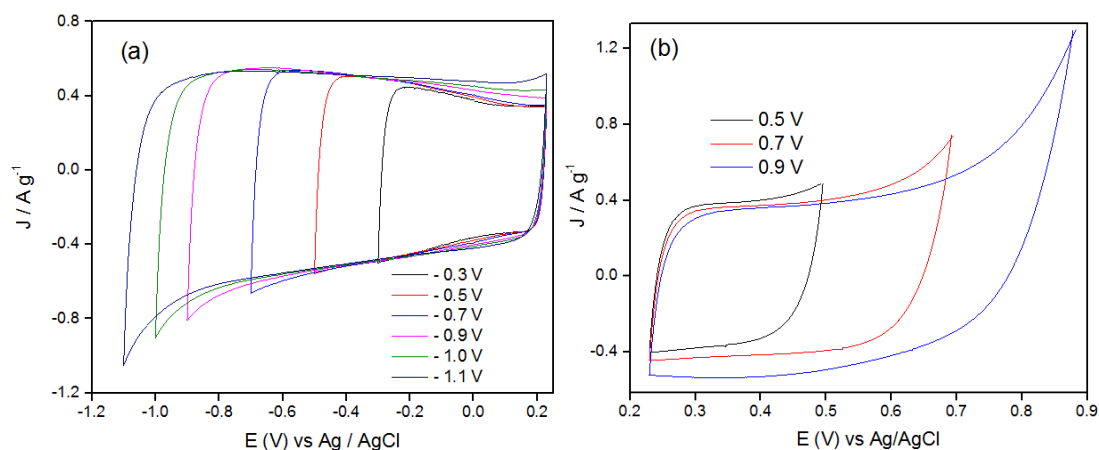
Figure 4.13. CV voltammograms of KUA sample toward (a) negative potentials and (b) positive potentials. 0.5M Na_2SO_4. υ=2 mVs^{-1}.

KUA in H_2SO_4 shows pseudocapacitive contributes delivering a higher capacitance than the KUA sample in Na_2SO_4 (Table 4.2). This result must be a consequence of the presence of electroactive surface oxygen functionalities. Hence, the pseudocapacitance observed in acid medium is a consequence of functionalities that are not electroactive in neutral medium.

The reason why the oxygen groups make a positive contribution to the capacitance can either be due to the improved wettability of the carbon material by the electrolyte, thus favoring the ions to reach the microporosity, or to a faradic process involving the oxygen groups that contribute to a pseudocapacitance. These advantages are related to CO desorbing groups, while the presence of CO_2-desorbing groups is unfavorable because of their electron-withdrawing properties that diminish the delocalization of the charge (and thereby the electrical conductivity).

- <u>Optimization of asymmetric capacitor</u>

Once the activated carbon samples have been characterized in a three-electrode cell, their maximum voltage window can be determined. In symmetric supercapacitors the positive electrode has generally a narrower potential window than the negative electrode. Therefore, the positive electrode is usually charged to its positive potential

limit before the negative electrode reaches its negative potential limit. In this way, the maximum voltage window for a symmetric supercapacitor will be always lower than that potential window obtained in a three-electrode cell for the same carbon material [73]. Hence, a suitable optimization of the mass ratio can be useful to increase the cell voltage.

As described in the 4.3.4 section, this method consists in determining the working potential windows (ΔV_+ and ΔV_-) of electrochemical stability for the positive and negative electrodes from the open circuit potential (E_{OCP}), in determining the capacitances values (Cg_+ and Cg_-) in the potential windows, and, finally, in determining the optimum weight ratio (w_+/w_-) of the electrodes by the equation:

$$w_+/w_- = C_{g-}\,|\Delta V_-|/\left(C_{g+}\Delta V_+\right).$$

Figure 4.14 shows the steady voltammograms for KUA sample in NA$_2$SO$_4$ between E_{OCP} (0.23 V vs. Ag/AgCl) to positive or negative potential values.

It can be seen that suitable potential windows would be between 0.23 V and 0.70 V in the case of the positive electrode, while the negative potential window would be from 0.23 V to -0.90 V. Then, the voltage that can be reached with this capacitor could be 1.6 V.
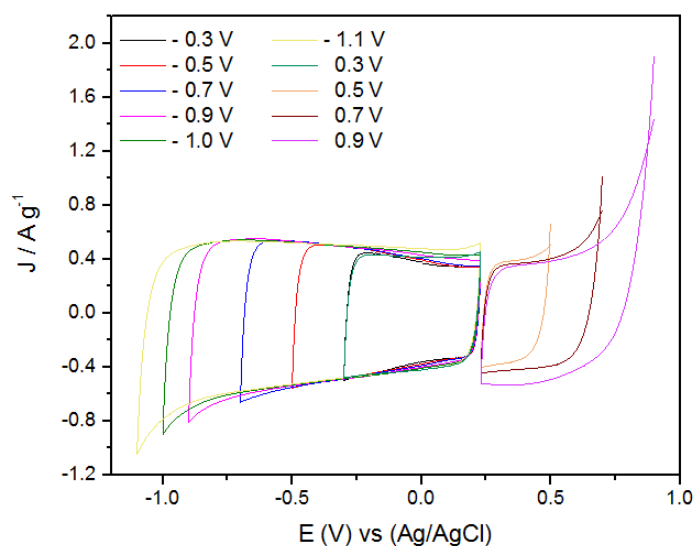
Figure 4.14. Steady voltammograms for KUA from E_{OCP} to positive and negative potential values. 0.5 M Na$_2$SO$_4$. υ=2 mVs^{-1}.
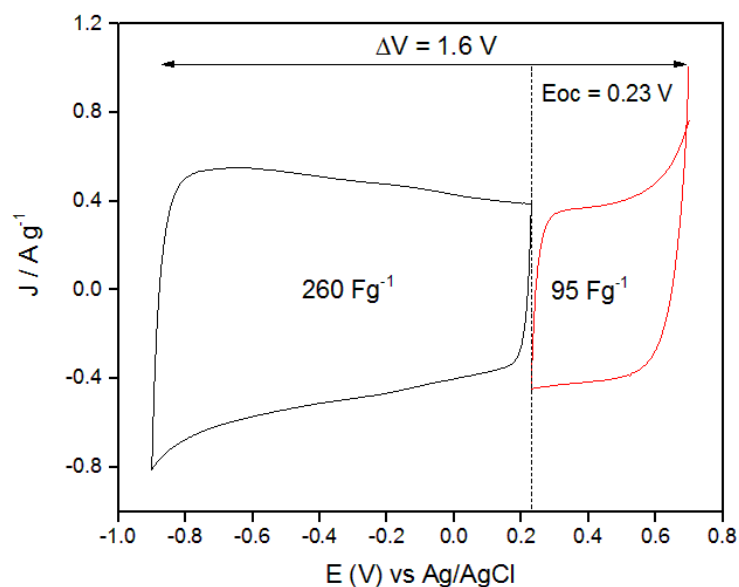
Figure 4.15. Steady voltammograms for KUA sample. 0.5 M Na_2SO_4. $\upsilon = 2mVs^{-1}$.

Once the interval of voltage was selected for each electrode, the capacitance for both electrodes was calculated from voltammograms shown in the Figure 4.15. Specific capacitance value is 95 F/g for the positive potential range and 260 F/g for the negative potential one. The mass ratio used in the construction of this cell was calculated to be 3.3.

Following the same procedure the mass ratio for the asymmetric supercapacitor based H_2SO_4 electrolyte was calculated to be 1.30.

Table 4.3 shows the capacitances, the potential window values, the weight of the electrodes and the open circuit potential employed for the construction of each supercapacitor.

	C_{g+} (Fg^{-1})	C_{g-} (Fg^{-1})	ΔV_+ (V)	ΔV_- (V)	w_+ (mg)	w_- (mg)	E_{OCP} (V)
KUA [H_2SO_4]	361	369	0.8	0.6	1.2	1.6	0.40
KUA [Na_2SO_4]	260	95	0.7	0.5	1.6	5.2	0.35

Table 4.3. Parameters employed for the design of asymmetric capacitors, and open circuit potential.

155

- <u>Characterization of symmetric and asymmetric supercapacitors</u>

Symmetric and asymmetric capacitors were assembled for the carbon material. For symmetric capacitors, two electrodes (surface area: 0.196 cm^2) were prepared with a weight of ~1.5 mg (active phase) each.

As showed before, in case of asymmetric configuration, the mass of the electrodes was determined following the procedures detailed by Peng. Their values are reported in Table 4.3. The electrodes were attached to a stainless steel collector by using a conducting adhesive. Supercapacitors were constructed by pressing both electrodes against each other and separating them by a nylon membrane filter (pore size: 450 nm) [Figure 4.16]. These devices were characterized by CV at different scan rates and galvanostatic charge-discharge (GCD) cycles at current densities from 0.1 to 50 A/g and in 1M H_2SO_4 and 0.5 M Na_2SO_4 solutions.
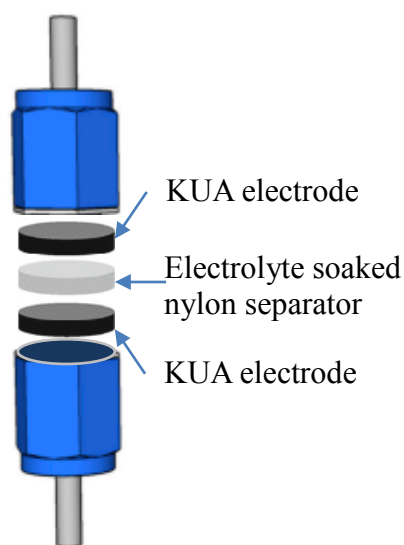
Figure 4.16. Two electrode cell configuration.

Current density and specific capacitance are defined based on the total active weight of the carbon material included in both electrodes.

The energy density and power density of symmetric and asymmetric supercapacitors were calculated in order to obtain all relevant information about their performance. Energy density was obtained during the discharge cycle by the Eq. (4.4) and power density (P) was calculated according to Eq. (4.5).

Symmetric supercapacitors

The resistance of the carbon material plays a major role in its behavior as electrodes for supercapacitors, since the performance of supercapacitors at high power density depends on the rate of charge and discharge, which is faster when the overall resistance is lower. This explains the best performance observed for KUA in H_2SO_4 in the Ragone plot (measured using CGD experiments at 1.4 V under different specific currents) shown in Figure 4.17. This supercapacitor keeps larger energy density at high power density due to its lower resistance, and provides a maximum power density of 0.5 kW/kg (Table 4.4 and 4.5). On the other hand, KUA in Na_2SO_4 based capacitor evidences lower capacitance and energy density.

This can be noticed in the shape of the galvanostatic charge-discharge profiles shown in the Figure 4.19. The profile of KUA in H_2SO_4 shows a shape which is closer to the ideal triangular shape, whereas a ohmic drop produced during the transition of charge to discharge in the GCD profile is observed in the case of KUA in Na_2SO_4. Also, the energy efficiency values (i.e. the ratio between the energy employed in charging the cell and the energy recovered upon discharge of the cell), have further confirmed the best performance of KUA in H_2SO_4.

Coulombic efficiency is 100% in all cases. This fact demonstrates the absence of irreversible faradic reactions that can occur on the surface of carbonaceous materials, connected to the malfunctioning of aqueous capacitor cells.
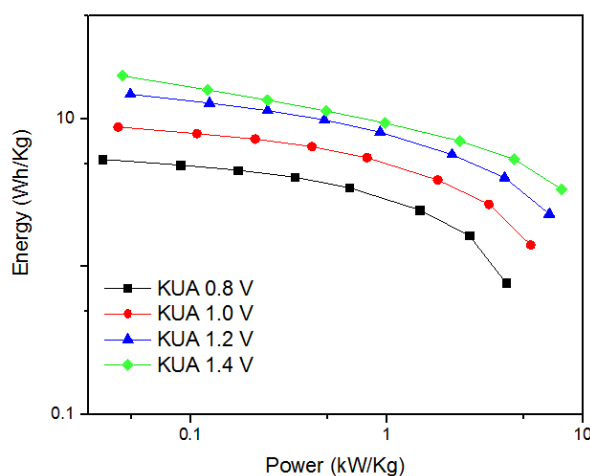
Figure 4.17. Ragone plot at 0.8, 1.0, 1.2 and 1.4 V for the KUA symmetric supercapacitor. 1 M H_2SO_4. j=1 A/g.

Voltage [H$_2$SO$_4$] (V)	C$_g$ [H$_2$SO$_4$] (F/g)	E [H$_2$SO$_4$] (Wh/kg)	P [H$_2$SO$_4$] (kW/kg)	Coulombic efficiency [H$_2$SO$_4$] (%)	Energy Efficiency [H$_2$SO$_4$] (%)
0.8	58	4.0	0.3	100%	79%
1.0	59	6.5	0.4	100%	76%
1.2	63	9.9	0.5	100%	70%
1.4	68	11.4	0.5	100%	61%

Table 4.4. Gravimetric capacitance (Cg), energy density (E), power density (P) and energy efficiency determined for KUA symmetric supercapacitor at voltages 0.8, 1.0, 1.2 and 1.4 V by galvanostatic charge-discharge cycles. 1 M H$_2$SO$_4$. j =1 A/g.
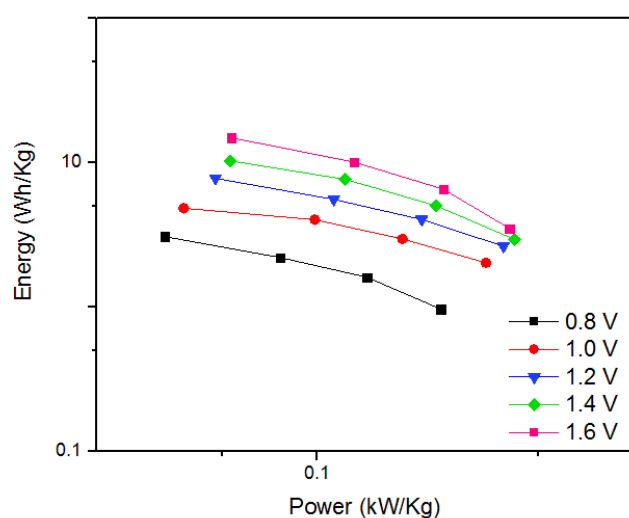
Figure 4.18. Ragone plot at 0.8, 1.0, 1.2 ,1.4 and 1.6 V for the KUA symmetric supercapacitor. 0.5 M Na$_2$SO$_4$. j=1 A/g.

Voltage [Na$_2$SO$_4$] (V)	C$_g$ [Na$_2$SO$_4$] (F/g)	E [Na$_2$SO$_4$] (Wh/kg)	P [Na$_2$SO$_4$] (kW/kg)	Coulombic efficiency [Na$_2$SO$_4$] (%)	Energy Efficiency [Na$_2$SO$_4$] (%)
0.8	26	1.0	0.3	100%	51%
1.0	29	2.1	0.3	100%	52%
1.2	33	2.6	0.4	100%	49%
1.4	35	2.9	0.4	100%	48%
1.6	38	3.0	0.4	100%	45%

Table 4.5. Gravimetric capacitance (Cg), energy density (E), power density (P) and energy efficiency determined for KUA symmetric supercapacitor at voltages 0.8, 1.0, 1.2, 1.4 and 1.6 V by galvanostatic charge-discharge cycles. 0.5 M Na$_2$SO$_4$. j =1 A/g.
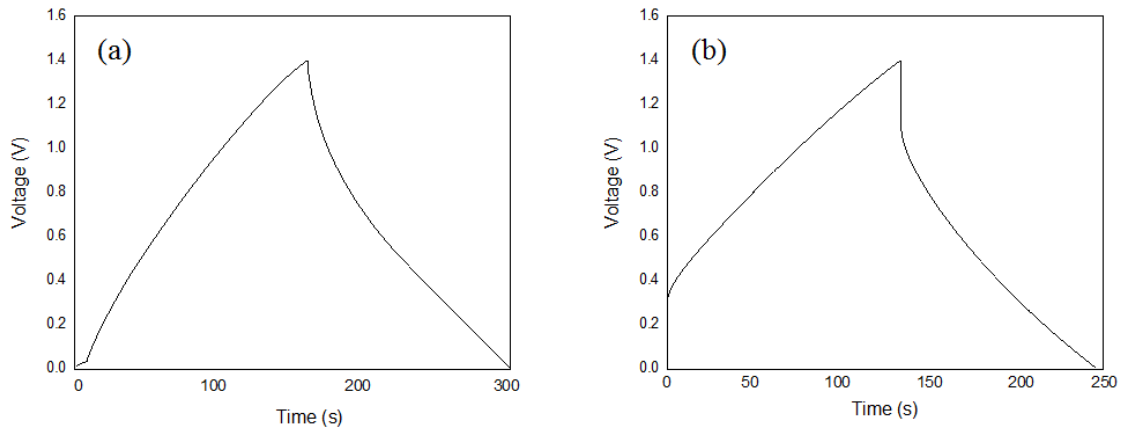
Figure 4.19. Galvanostatic charge-discharge for KUA in (a) H_2SO_4 and (b) Na_2SO_4. j =1 A/g.

Asymmetric supercapacitors

Figures 4.20 and 4.21 show the Ragone plots obtained for all asymmetric supercapacitors working at various range of potential. As in the case of symmetric device, KUA in H_2SO_4 based capacitor evidences shows higher values of capacitance and energy density than KUA in Na_2SO_4 (Tables 4.6 and 4.7).
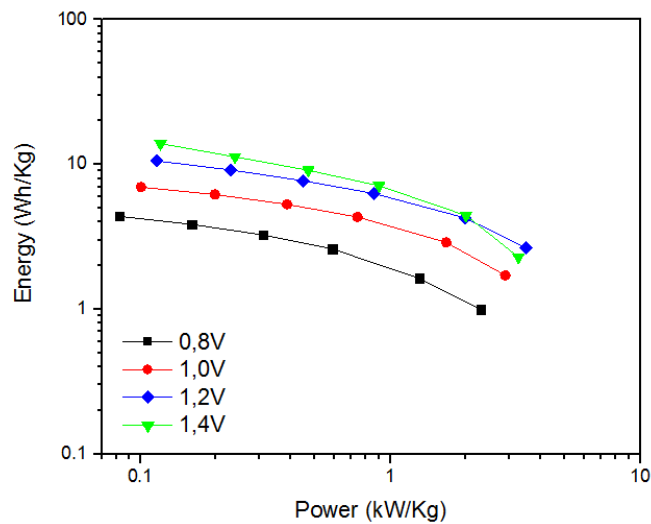
Figure 4.20. Ragone plot at 0.8, 1.0, 1.2 and 1.4 V for the KUA symmetrics supercapacitor. 1 M H_2SO_4. j=1 A/g.

Voltage [H$_2$SO$_4$] (V)	C$_g$ [H$_2$SO$_4$] (F/g)	E [H$_2$SO$_4$] (Wh/kg)	P [H$_2$SO$_4$] (kW/kg)	Coulombic efficiency [H$_2$SO$_4$] (%)	Energy Efficiency [H$_2$SO$_4$] (%)
0.8	51	3.3	0.3	100%	71%
1.0	55	5.3	0.4	100%	70%
1.2	60	7.7	0.5	100%	66%
1.4	65	9.1	0.5	100%	58%

Table 4.6. Gravimetric capacitance (Cg), energy density (E), power density (P) and energy efficiency determined for KUA asymmetric supercapacitor at voltages 0.8, 1.0, 1.2 and 1.4 V by galvanostatic charge-discharge cycles. 1 M H$_2$SO$_4$. j =1 A/g.
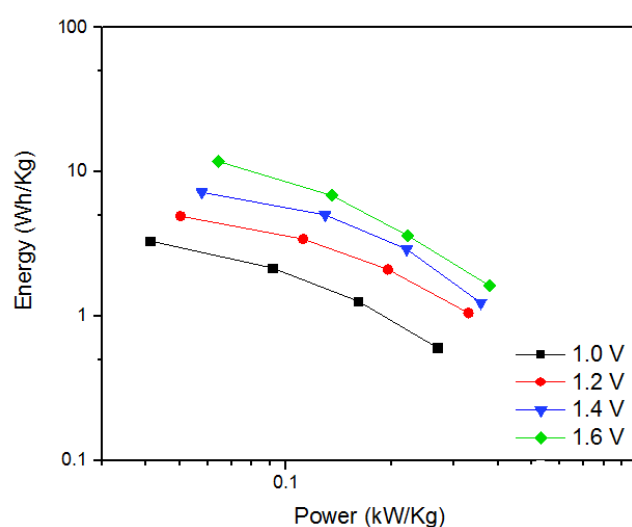
Figure 4.21. Ragone plot at 0.8, 1.0, 1.2 ,1.4, and 1.6 V for the KUA asymmetric supercapacitor. 0.5 M Na$_2$SO$_4$. j=1 A/g.

Voltage [Na$_2$SO$_4$] (V)	C$_g$ [Na$_2$SO$_4$] (F/g)	E [Na$_2$SO$_4$] (Wh/kg)	P [Na$_2$SO$_4$] (kW/kg)	Coulombic efficiency [Na$_2$SO$_4$] (%)	Energy Efficiency [Na$_2$SO$_4$] (%)
1.0	15	0.6	0.3	100%	38%
1.2	20	1.1	0.3	100%	39%
1.4	23	1.3	0.3	100%	37%
1.6	25	1.5	0.4	100%	31%

Table 4.7. Gravimetric capacitance (Cg), energy density (E), power density (P) and energy efficiency determined for KUA symmetric asupercapacitor at voltages 0.8, 1.0, 1.2, 1.4 and 1.6 V by galvanostatic charge-discharge cycles. 0.5 M Na$_2$SO$_4$. j =1 A/g.

4.5 Conclusions

Activated carbon, synthesized by chemical activation of a Spanish anthracite, was electrochemically characterized in two different aqueous media, with the same anion but different cation, to understand the different parameters affecting the electrode-electrolyte interface.

AC has been characterized by cyclic voltammetry using different scan rates in H_2SO_4 and Na_2SO_4 solutions.

At low scan rates (1-20 mV/s), the formation of the electrical double layer is manifested in both samples, evidenced by the rectangular shape of their voltammograms, characteristic of a pure capacitive electrode. At faster scan rates (50 and 100 mV/s), AC in neutral medium showed a resistive behavior due to the electrolyte mass-transfer resistance. Carbon activated in acid medium exhibited redox processes related to electroactive functional groups that can often be beneficial for the electrochemical performance of carbon materials since they can provide pseudocapacitance. Therefore, higher values of gravimetric capacitance were observed for AC in acid medium.

The electrochemical behavior of activated carbon was studied as electrode for supercapacitors in acid and neutral media. The best performance was observed for the capacitors based on acid electrolyte. In this case, symmetric and asymmetric capacitors generated higher energy densities than the values obtained using neutral medium.

References

[1]   K. S.Novoselov, A.K. Geim, S.V. Morozov, D. Jiang,Y. Zhang, S. V. Dubonos, I. V. Grigorieva, and A. A. Firsov, Electric field effect in atomically thin carbon films, Science **306**, 666 (2004).

[1]   P. Simon, and Y. Gogotsi. Materials for electrochemical capacitors, Nat. Mater. **7**, 845 (2008).

[2]   F. Béguin, E. Frackowiak, editors. Carbons for Electrochemical Energy Storage and Conversion Systems. 1st ed. CRC Press; (2009).

[3]   T.J. Bandosz, and C.O. Ania. Surface chemistry of activated carbons and its characterization. In: T.J. Bandosz, editor. Act. Carbon surfaces Environ. Remediat. 1st ed., Elsevier; (2006).

[4]   M.J. Bleda-Martínez, J.A. Maciá-Agulló, D. Lozano-Castelló, E. Morallón, D. Cazorla-Amorós, A. Linares-Solano. Role of surface chemistry on electric double layer capacitance of carbon materials, Carbon **43**, 2677 (2005).

[5]   R.C. Bansal, Donnet J.B. and F. Stoeckli, Active Carbon. Marcel Dekker, New York, USA (1998).

[6]   H. Marsh, and F.R. Reinoso, Activated Carbon, Elsevier Science, Oxford, UK (2006).

[7]   D. Lozano-Castelló, F. Suárez-García, D. Cazorla-Amorós and A. Linares-Solano, Porous texture of carbons. pp. 115–162. *In*: F. Béguin, and E. Frackowiak (eds.). Carbons for Electrochemical Energy Storage and Conversion Systems. CRC Press, Taylor & Francis group, New York, USA.

[8]   B. Cuil, J. Zhang, S. Liu, X. Liu, W. Xiang, L.Liu, H. Xin, M.J. Lefler, and S. Licht, Electrochemical synthesis of ammonia directly from N2 and water over iron-based catalysts supported on activated carbon, Green Chemistry **19**, 298 (2017).

[9]   G. Zhang, Z. Li, H. Zheng, T. Fu, Y. Ju, Y. Wang, Influence of the surface oxygenated groups of activated carbon on preparation of a nano Cu/AC catalyst and heterogeneous catalyst in the oxidative carbonylation of methanol, Appliaed Catalysis B: Enviromental 179, 95 (2015).

[10]   H. Watanable, S. Asano, S. Fujita, H. Yoshida, and M. Arai, Nitrogen-doped, metal-free activated carbon catalysts for aerobic oxidation of alcohols, Acs Catalysis 5 (5), 28886 (2015).

[11]   X. Han, H. Jiang, Y. Zhou, E. Hong, Y. Zhou, P. Gao, R. Ding, and E. Liu, A high performance nitrogen-doped porous activated carbon for supercapacitor derived from pueraria, Journal of Alloy and Compounds **744**, 544 (2018).

[12]   M. Tian, J. Wu, R. Li, Y. Chen, and D. Long, Fabricating a high-energy-density supercapacitor with asymmetric aqueous redox additive electrolytes and fee-standing activated carbon-felt electrodes, chemical Engineering Journal **363**, 183 (2019).

[13]   L. Yu, L. Hu, B. Anasori, Y.-T. Liu, Q. Zhu, P. Zhang, Y. Gogotsi, and B. Xu, MXene-bonded activated carbon as a flexible electrode for high-performance supercapaciors, ACS Energy Letters **3**, 1597 (2018).

[14]   Q. Li, Y. Zhu, P. Zhao, C. Yuan, M. Chen, and C. Wang, Commercial activated carbon as a novel precursor of the amorphous carbon for high-performance sodium-ion batteries anode, Carbon **129**, 85 (2018).

[15] J. Mi, X. R. Wang, R.-J. Fan, W.-H. Qu, and W-C. Li, Coconut-shell-based porous carbons with a tunable micro/mesopore ratio for high-performance supercapacitors, Energy & Fuels **25**, 5312 (2012).

[16] A. Jain and S.K. Tripathi, Fabrication and characterization of energy storing supercapacitor devices using coconut shell based activated charcoal electrode, Materials Science and Engineering: B **183**, 54 (2014).

[17] R.-L. Tseng, F.-C. Wu, and R-S. Juang, Adsorption of CO_2 at atmospheric pressure on activated carbons prepared from melamine-modified phenol-formaldehyde resins, Separation and Purification Technology **140**, 53 (2015).

[18] C-G. Lee, J-W. Jeon, M.-J Hwang, K.-H. Ahn, C. Park, J.W. Chol, and S.-H Lee, Lead and copper removal from aqueous solutions using carbon foam derived from phenol resin, Chemosphere **130**, 59 (2015).

[19] T. Mochizuki, M. Kubota, H. Matsuda, and L. F. D'Elia Camacho, Adsorption behaviors of ammonia and hydrogen sulfide on activated carbon prepared from petroleum coke by KOH chemical activation, Fuel processing technology **144**, 164 (2016).

[20] Y. Zhang, Y. Zhang, J. Huang, D. Du, W. Xing, and Z. Yan, Enhanced capacitive performance of N-doped activated carbon from petroleum coke by combining ammoxidation with KOH activation, Nanoscale Research Letters **11**, 245 (2016).

[21] A. Ahmadpour, and D.D. Do, The preparation of active carbons from coal by chemical and physical activation, Carbon **34**, 471 (1996).

[22] E. Gonzalez-Serrano, T. Cordero, J. Rodriguez-Mirasol and J.J. Rodriguez, Development of porosity upon chemical activation of kraft lignin with $ZnCl_2$. Ind. Eng. Chem. Res. **36**, 4832 (1997).

[23] M. Jagtoyen, and F.Derbyshire, Activated carbons from yellow poplar and white oak by H_3PO_4 activation. Carbon **36**, 1085 (1998)

[24] A. Linares-Solano, D. Lozano-Castelló, M.A. Lillo-Ródenas and D. Cazorla-Amorós, Carbon activation by alkaline hydroxides preparation and reactions, porosity and performance. pp. 1–62. *In*: L.R. Radovic, (ed.). Chemistry and Physics of Carbon: Volume 30. CRC Press, Taylor & Francis group, New York, USA (2008).

[25] J.M. Rosas, J. Bedia, J. Rodríguez-Mirasol and T. Cordero, HEMP-derived activated carbon fibers by chemical activation with phosphoric acid, Fuel **88**, 19 (2009)

[26] D. Lozano-Castelló, M.A. Lillo-Ródenas, D. Cazorla-Amorós and A. Linares-Solano, Preparation of activated carbons from Spanish anthracite: I. Activation by KOH, Carbon **39**, 741 (2008).

[27] F. Rodríguez-Reinoso, and M. Molina-Sabio, Activated carbons from lignocellulosic materials by chemical and/orphysical activation: an overview, Carbon **30**, 1111 (1992).

[28] M.A. Lillo-Ródenas, D. Cazorla-Amorós and A. Linares-Solano, Understanding chemical reactions between carbons and NaOH and KOH: An insight into the chemical activation mechanism, Carbon **41**, 267 (2003).

[29] M.A. Lillo-Ródenas, J. Juan-Juan, D. Cazorla-Amorós and A. Linares-Solano. About reactions occurring during chemical activation with hydroxides. Carbon **42**, 1371 (2004).

[30] HP. Boehm, Some aspects of the surface chemistry of carbon blacks and other

carbons, Carbon **32**, 759 (1994).

[31] C. Leon y Leon, and L. Radovic, Chemistry and Physics of Carbon, Thrower, PA, editor, Vol. 24, Dekker, M, publisher; New York (1994).

[32] J. L. Figueiredo, M.F.R. Pereira, M.M.A Freitas, and J.J:M. Órfão, Characterization of active sites on carbon catalysts, Ind. Eng. Chem. Res, **46**, 4110 (2007).

[33] P. Serp, and J.L. Figueiredo, editors, Carbon Materials for Catalysis. Hoboken, New Jersey, John Wiley and Sons, Inc. (2009).

[34] M. Belhachemi, R. Rios, F. Addoun, J. Silvestre-Albero, A. Sepulveda-Escribano, F. Rodriguez-Reinoso, Preparation of activated carbon from date pits: Effect of the activation agent and liquid phase oxidation, J. Anal. Appl. Pyrol. **86**, 168 (2009).

[35] I. Gniot, P. Kirszensztejn, M. Kozlowski, Oxidative dehydrogenation of isobutene using modified activated carbons as catalysts, Appl. Catal. A: Gen. **362**, 67 (2009).

[36] H.P. Boehm, Some aspects of the surface chemistry of carbon blacks and other carbons, Carbon **32**, 759 (1994).

[37] C. Moreno-Castilla, M.A. Ferro-García, J.P. Joly, I. Bautista-Toledo, F. Carrasco-Marín, and J. Rivera-Utrilla, Activated carbon surface modifications by nitric acid, hydrogen peroxide and ammonium peroxydisulfate treatments, Langmuir **11**, 4386 (1995).

[38] L. Radovic, and F. Rodríguez-Reinoso, Chemistry and Physics of Carbon. Thrower, PA, editor, Vol. 25, Dekker, M, publisher; New York (1997).

[39] G. de la Puente, J.J Pis, J.A. Menendez, and P. Grange, Thermal stability of oxygenated functions in activated carbons, J. Anal. Appl. Pyrol. **43**, 125 (1997).

[40] C. Moreno-Castilla, M.V. Lopez-Ramon, and F. Carrasco-Marín, Changes in surface chemistry of activated carbons by wet oxidation, Carbon **38**, 1995 (2000).

[41] I.I. Salame, and T.J. Bandosz, Surface chemistry of activated carbons: Combining the results of temperature-programmed desorption, Boehm, and potentiometric titrations, J. Colloid Interf. Sci. **204**, 252 (2001).

[42] S.B. Wang, and Z.H. Zhu, Effects of acidic treatment of activated carbons on dye adsorption, Dyes Pigments **75**, 306 (2007).

[43] H.F.Gorgulho, J.P. Mesquita, F. Gonçalves, M.F.R. Pereira, and J.L. Figueiredo, Characterization of the surface chemistry of carbon materials by potentiometric titrations and temperature-programmed desorption, Carbon **46**, 1544 (2008).

[44] S. Kohl, A. Drochner, and H.Vogel, Quantification of oxygen surface groups on carbon materials via diffuse reflectance FT-IR spectroscopy and temperature programmed desorption, Catal. Today **150**, 67 (2010).

[45] H.P. Boehm, Surface oxides on carbon and their analysis: a critical assessment, Carbon **40**, 145 (2002).

[46] J.L. Figueiredo, M.F.R. Pereira, M.M.A. Freitas and J.J.M. Órfão, Modification of the surface chemistry of activated carbons, Carbon **37**, 1379 (1999).

[47] Y. Otake, and R.G. Jenkins, Characterization of oxygen-containing surface complexes created on a microporous carbon by air and nitric acid treatment., Carbon **31**, 109 (1993).

[48] M.C. Román-Martínez, D. Cazorla-Amorós, A. Linares-Solano and C.S.-M. de Lecea, Tpd and TPR characterization of carbonaceous supports and Pt/C

catalysts, Carbon **31**, 895 (1993).

[49] B.E. Conway, Electrochemical Supercapacitors. Scientific Fundamentals and Technological Applications, Kluwer Academics/Plenum Publishers, New York (1999).

[50] D. Petreus, D. Moga, R. Galatus, and R.A. Munteanu, Modeling and sizing of supercapacitors, Adv. Electr. Comput. Eng. **8**, 15 (2008).

[51] C. Zhong, Y. Deng, W. Hu, J. Qiao, L. Zhang and J. Zhang, A review of electrolyte materials and compositions for electrochemical supercapacitors, Chem. Soc. Rev. **44**, 7484 (2015).

[52] N. Böckenfeld, S.S. Jeong, M. Winter, S. Passerini and A. Balducci, Natural, cheap and environmentally friendly binder for supercapacitors, J. Power Sources **221**, 14 (2013)

[53] M. Aslan, D. Weingarth, N. Jäckel, J.S. Atchison, I. Grobelsek and V. Presser. Polyvinylpyrrolidone as binder for castable supercapacitor electrodes with high electrochemical performance in organic electrolytes, J. Power Sources **266**, 374 (2014).

[54] R. Berenguer, F.J. García-Mateos, R. Ruiz-Rosas, D. Cazorla-Amorós, E. Morallón, J. Rodríguez-Mirasol, and T. Cordero. Biomassderived binderless fibrous carbon electrodes for ultrafast energy storage, Green Chem **18**, 1506 (2016).

[55] J. Miller, and A.F Burke, Electrochemical capacitors: challenges and opportunities for real-world applications, Electrochem. Soc. Interface, **17** (Spring), 31 (2008).

[56] H. von Helmholtz, Ueber einige Gesetze der Vertheilung elektrischer Ströme in körperlichen Leitern, mit Anwendung auf die thierisch-elektrischen Versuche (Schluss.), Ann. Phys. (Leipzig) **89**, 211 (1853).

[57] N. D. Lang and W. Kohn, Theory of metal surfaces: work function, Phys. Rev. B **1**, 4555 (1970); B 3, 1215 (1971).

[58] S. Amokrane and J.P. Badiali, in Modern Aspects of Electrochemistry, J. O'M. Bockris, B.E. Conway, and R. White, eds, vol. 22, Chapter I, Plenum, New York (1992).

[59] G. Gouy, Ann. Phys., Paris, **7**, 129 (1917).

[60] D.L. Chapman, A contribution to the theory of electrocapillarity, Phil. Mag., **25**, 475 (1913).

[61] P. Debye and E. Huckel, Phys Zeit., **24**, 185, (1923).

[62] O. Stern, Zur theorie der elektrolytischen doppelschichtZeit. Elektrochem. **30**, 508 (1924).

[63] R. Parsons, Chapter 4 in Modern Aspects of Electrochemistry, J. O'M. Bockris, B.E. Conway, and R. White, eds, vol. 1, Chapter 4, Butterworths, London (1954).

[64] D.C. Grahme, The electrical double layer and the theory of electrocapillarity, Chem. Rev. **41**, 441 (1947).

[65] Y. C. Hsieh, K. T. Lee, Y. P. Lin, N. L. Wu, and S. W. Donne, Investigation on capacity fading of aqueous $MnO_2 \cdot nH_2O$ electrochemical capacitor, Journal of Power Sources **177**, 660 (2008).

[66] K. C. Tsay, L. Zhang, and J. J. Zhang, Effects of electrode layer composition/thickness and electrolyte concentration on both specific capacitance and energy density of supercapacitor, Electrochimica Acta **60**, 428 (2012).

[67] Z. Q. Niu, P. S. Luan, Q. Shao, H. Dong, J. Li, J. Chen, D. Zhao, L. Cai, W. Zhou, X. Chen, and S. Xie, A "skeleton/skin" strategy for preparing ultrathin free-standing single-walled carbon nanotube/polyaniline films for high performance supercapacitor electrodes, Energy Environmental Science **5**, 8726 (2012).

[68] Q.-L. Chen, K.-H. Xue, W. Shen, F.-F. Tao, S.-Y. Yin, and W. Xu, Fabrication and electrochemical properties of carbon nanotube array electrode for supercapacitors, Electrochim. Acta **49**, 4157 (2004).

[69] H. Jiang, P.S. Lee, and C. Li, 3D carbon based nanostructures for advanced supercapacitors, Energy Environ. Sci. **6**, 41 (2013).

[70] A. Berenguer-murcia, R. Ruiz-Rosas, J. Garcia-Aguilar, K. Nueangnoraj, H. Nishihara, E. Morallon, D. Cazorla-Amoros, and T. Kyotani, Binderless thin films of zeolite-templated carbon electrodes useful for electrochemical microcapacitors with ultrahigh rate performance, Phys. Chem. Chem. Ph. **15**, 1033 (2013).

[71] G. Salitra, A. Soffer, L. Eliad, Y. Cohen, and D. Aurbach, Carbon Electrodes for Double-Layer Capacitors I. Relations Between Ion and Pore Dimensions, J. Electrochem. Soc. **147**, 2486 (2000).

[72] G.A. Snook, G.J. Wilson, and A.G. Pandolfo, Mathematical functions for optimization of conducting polymer/activated carbon asymmetric supercapacitors, J. Power Sources **186,** 216–223 (2009).

[73] C. Peng, S. Zhang, X. Zhou, and G.Z. Chen, Unequalisation of electrode capacitances for enhanced energy capacity in asymmetrical supercapacitors, Energy Environ. Sci. **3**, 1499 (2010).

[74] F. Béguin, V. Presser, A. Balducci, E. Frackowiak, Carbons and electrolytes for advanced supercapacitors, Adv. Mater. **26** (2014).

[75] M.J. Bleda-Martínez, D. Lozano-Castelló, D. Cazorla-Amorós, and E. Morallón, Kinetics of Double-Layer Formation: Influence of Porous Structure and Pore Size Distribution, Energy & Fuels **24**, 3378 (2010).

[76] O. Barbieri, M. Hahn, A. Herzog, and R. Kötz, Capacitance limits of high surface area activated carbons for double layer capacitors, Carbon **43**, 1303 (2005).

[77] H. Nishihara, and T. Kyotani, Zeolite-templated carbons - threedimensional microporous graphene frameworks, Chem. Commun. **54**, 5648 (2018).

[78] M.J. Bleda-Martínez, D. Lozano-Castelló, E. Morallón, D. Cazorla-Amorós, and A. Linares-Solano, Chemical and electrochemical characterization of porous carbon materials, Carbon **44**, 2642 (2006).

[79] H.A. Andreas, and B.E. Conway, Examination of the double-layer capacitance of an high specific-area C-cloth electrode as titrated from acidic to alkaline pHs, Electrochim. Acta **51**, 6510 (2006).

[80] S. Leyva-García, K. Nueangnoraj, D. Lozano-Castelló, H. Nishihara, T. Kyotani, E. Morallón, and D. Cazorla-Amorós, Characterization of a zeolite-templated carbon by electrochemical quartz crystal microbalance and in situ Raman spectroscopy, Carbon **89**, 63 (2015).

[81] D. Cazorla-Amorós, D. Lozano-Castelló, E. Morallón, M.J. Bleda- Martínez, A. Linares-Solano, and S. Shiraishi, Measuring cycle efficiency and capacitance of chemically activated carbons in propylene carbonate, Carbon **48**, 1451 (2010).

[82] M. J. Mostazo-López, R. Ruiz-Rosas, E. Morallón and, D. Cazorla-Amorós,

Nitrogen doped superporous carbon prepared by a mild method. Enhancement of supercapacitor performance, International Journal of hydrogen **41**, 19691 (2016).

[83] M.J. Bleda-Martínez, J.M. Pérez, A. Linares-Solano, E. Morallón, and D. Cazorla- Amorós, Effect of surface chemistry on electrochemical storage of hydrogen in porous carbon materials, Carbon N.Y. **46**, 1053 (2008).

Appendix B

B.1 Chronopotentiometry (CP)

Chronopotentiometry (CP) is the study of the variation of the potential of a working electrode with time upon imposition of a controlled current.

Redox-active species diffuse to the working electrode surface to balance the applied current, until the diffusion-limited concentration of redox species reaches zero at the electrode surface, at which time potential changes to the redox potential of the next species, if present, in solution (which could be solvent). CP is commonly used during battery charge and discharge experiments which allow to determine characteristic parameters of supercapacitors, such as: specific capacitance, reversibility, durability, ohmic drop, energy, power, etc.

The specific capacitance of an electrode or capacitor is given by the following equation

$$C = \frac{i\Delta t}{m\Delta E} \tag{B.1}$$

where i is the applied electric current intensity (A), Δt is the discharge time (s), ΔE is the potential window (V) and m is the electrode mass or of both electrodes in the case of a supercapacitor.

The galvanostatic charge-discharge cycles allow to determine the Ohmic drop, which is related to the resistance of the material and the device. The value of the ohmic drop is subtracted from the voltage or potential applied when the capacitance is determined.

The most importante characteristics of electrochemical capacitors can be determined using charge-discharge cycles under different conditions. The main studies that are used to characterize these devices are:

(i) cycles at different current densities (A/g), to determine energy as a function of power (Ragone plot);

(ii) several charge-discharge cycles at a given current and voltage density, to evaluate the durability of the device [28].

B.2 Cyclic Voltammetry (CV)

Cyclic voltammetry is a type of potentiodynamic electrochemical measurement. In a cyclic voltammetry experiment, a voltage is applied to a working electrode in solution and current flowing at the working electrode is plotted versus the applied voltage to give the cyclic voltammogram. This method can be used to study the electrochemical properties of species in solution as well as at the electrode/electrolyte interface.

In a cyclic voltammetry experiment, as in other controlled potential experiments, a potential is applied to the system, and the faradaic current response is measured (a faradaic current is the current due to a redox reaction). The current response over a range of potentials (a potential window) is measured, starting at an initial value and varying the potential in a linear manner up to a pre-defined limiting value. At this potential (often referred to as a switching potential), the direction of the potential scan is reversed, and the same potential window is scanned in the opposite direction (hence the term cyclic). This means that, for example, species formed by oxidation on the first (forward) scan can be reduced on the second (reverse) scan. This technique is commonly used, since it provides a fast and simple method for initial characterization of a redox-active system. In addition to providing an estimate of the redox potential, it can also provide information about the rate of electron transfer between the electrode and the analyte, and the stability of the analyte in the electrolyzed oxidation states (e.g., whether or not they undergo any chemical reactions).

For the majority of experiments the electroactive species is in the form of a solution. The three-electrode method is the most widely used because the electrical potential of reference does not change easily during the measurement.

The method uses a reference electrode, working electrode, and counter electrode (also called the secondary or auxiliary electrode). Electrolyte is usually added to the test solution to ensure sufficient conductivity. The combination of the solvent, electrolyte and specific working electrode material determines the range of the potential.

In cyclic voltammetry, the electrode potential follows a linearly ramping potential vs. time as shown. The potential is measured between the reference electrode and the working electrode and the current is measured between the working electrode and the counterelectrode. This data is then plotted as current (i) vs. potential (E). As the

waveform shows, the forward scan produces a current peak for any analytes that can be reduced through the range of the potential scan. The current will increase as the potential reaches the reduction potential of the analyte, but then falls off as the concentration of the analyte is depleted close to the electrode surface. As the applied potential is reversed, it will reach a potential that will reoxidize the product formed in the first reduction reaction, and produce a current of reverse polarity from the forward scan. As a result, information about the redox potential and electrochemical reaction rates of the compounds are obtained.

In the voltammetric techniques we have consider to this point, we scan the potential in one direction, either to more positive potentials or to more negative potentials. In cyclic voltammetry we complete a scan in both directions. Figure B.1 shows a typical potential-excitation signal. In this example, we first scan the potential to more positive values, resulting in the following oxidation reaction for the species R

$$R \leftrightarrows O + ne^-.$$
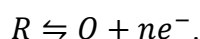
When the potential reaches a predetermined switching potential, we reverse the direction of the scan toward more negative potentials. Because we generated the species O on the forward scan, during the reverse scan it is reduced back to R

$$O + ne^- \leftrightarrows R .$$
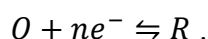
Because we carry out cyclic voltammetry in an unstirred solution, the resulting cyclic voltammogram, as shown in Figure B.1(b), has peak currents instead of limiting currents. The voltammogram has separate peaks for the oxidation reaction and the reduction reaction, each characterized by a peak potential and a peak current.

The peak current in cyclic voltammetry is given by the Randles-Sevcik equation

$$i_p = (2.69 \times 10^5)n^{3/2}AD^{1/2}v^{1/2}C = KC \qquad\qquad (B.2)$$

where n is the number of electrons in the redox reaction, A is the area of the working electrode, D is the diffusion coefficient for the electroactive species, v is the scan rate, and C is the concentration of the electroactive species at the electrode. For a well-behaved system, the anodic and cathodic peak currents are equal, and the ratio $i_{p,a}/i_{p,c}$ is

1.00. The half-wave potential, $E_{1/2}$, is midway between the anodic and cathodic peak potentials

$$E_{1/2} = \frac{E_{p,a} + E_{p,c}}{2}.$$ (B.3)
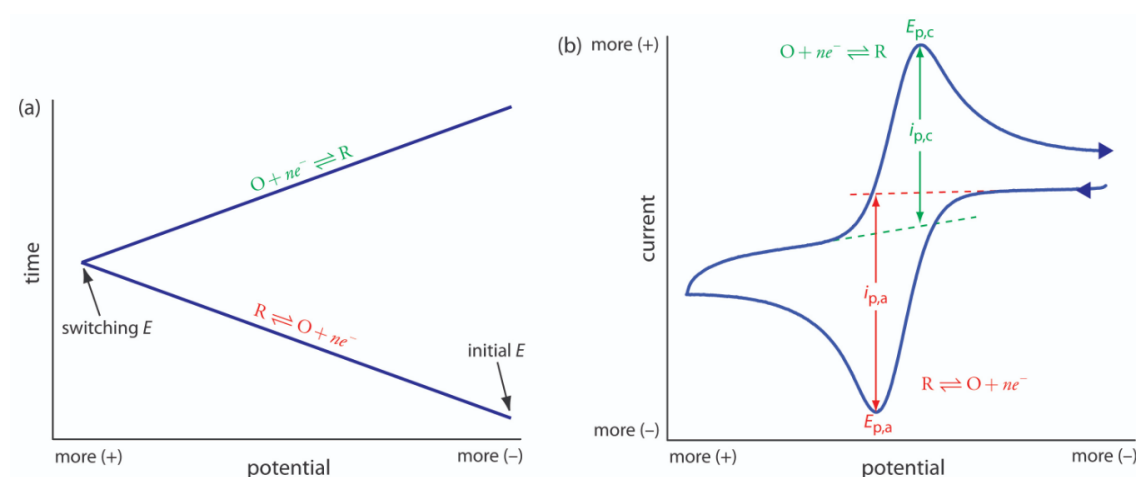
Figure B.1. (a) One cycle of the triangular potential-excitation signal showing the initial potential and the switching potential. (b) The resulting cyclic voltammogram showing the measurement of the peak currents and peak potentials.

Scanning the potential in both directions provides us with the opportunity to explore the electrochemical behavior of species generated at the electrode. This is a distinct advantage of cyclic voltammetry over other voltammetric techniques. Figure B.2 shows the cyclic voltammogram for the same redox couple at both a faster and a slower scan rate. At the faster scan rate we see two peaks. At the slower scan rate in Figure B.2(b), however, the peak on the reverse scan disappears. One explanation for this is that the products from the reduction of R on the forward scan have sufficient time to participate in a chemical reaction whose products are not electroactive.

The cyclic voltammetry allows to determine the capacitance by the following equation:

$$C = \frac{q}{E} = \frac{\int i dt}{E}.$$ (B.4)

In the case of carbon mater*ials* in which the fundamental electrochemical response is due to electrical double-layer processes, the corresponding cyclic voltagram has an ideally rectangular shape [Figure B.3(a)]. If the voltagram is recorded in a range of

potentials in which the material is not stable, faradic currents corresponding to the oxidation of the material and the electrolyte are observed. In the second case [Figure B.3(b)], carbon materials present a pseudocapacitive behavior in addition to the contribution of the electrical double-layer, as a result of the presence of electroactive functional groups, under the conditions of study, on its surface (for example, quinones).
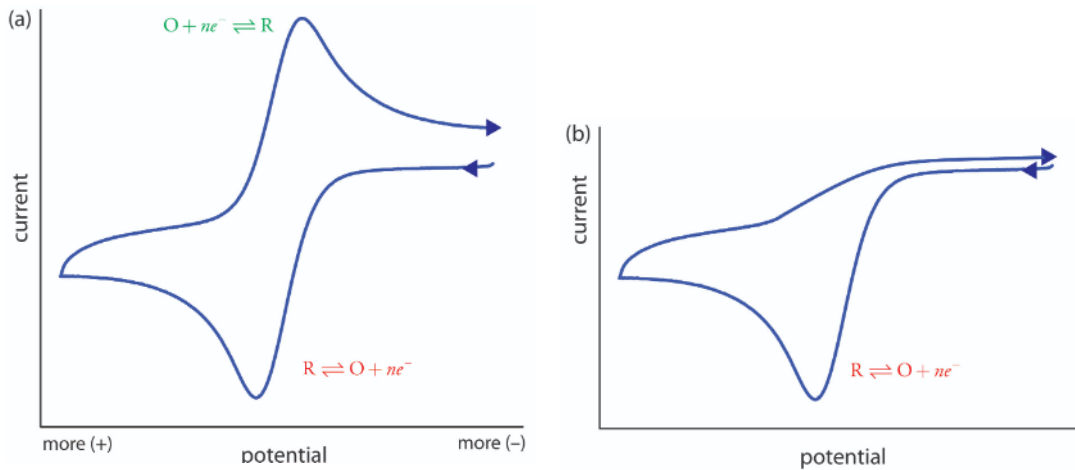
Figure B.2. Cyclic voltammograms for R obtained at (a) a faster scan rate and (b) a slower scan rate.
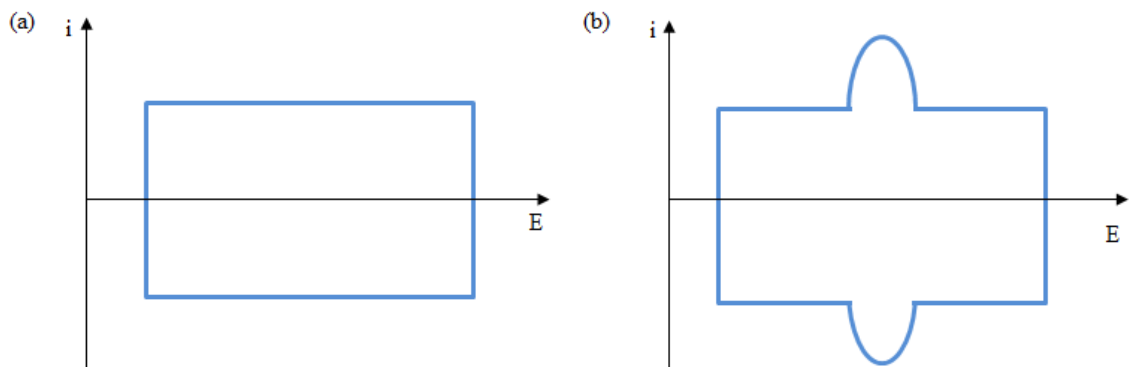
Figure B.3. (a) Ideal double-layer capacitive and (b) pseudocapacitive behaviors.

B.3 Gas adsorption and Brunauer-Emmett-Teller (BET) method

Gas adsorption is a well-established tool for the characterization of the texture of porous solids and fine powders [1]. Over the past 30 years major advances have been made in the development of nanoporous materials with uniform, tailor-made pore structures (e.g., mesoporous molecular sieves, carbon nanotubes and materials with hierarchical pore structures). Their characterization has required the development of high resolution experimental protocols for the adsorption of various subcritical fluids (e.g., nitrogen at T=77 K, argon at 87 K, carbon dioxide at 273 K) and also organic vapours and supercritical gases. Furthermore, novel procedures based on density functional theory and molecular simulation have been developed to allow a more accurate and comprehensive pore structural analysis to be obtained from high resolution physisorption data.

In general, *adsorption* is defined as the enrichment of molecules, atoms or ions in the vicinity of an interface. In the case of gas/solid systems, adsorption takes place in the vicinity of the solid surface and outside the solid structure. The material in the adsorbed state is known as the *adsorbate*, while the *adsorptive* is the same component in the fluid phase. The *adsorption space* is the space occupied by the adsorbate. Adsorption can be physical (physisorption) or chemical (chemisorption). *Physisorption* is a general phenomenon: it occurs whenever an adsorbable gas (the adsorptive) is brought into contact with the surface of a solid (the *adsorbent*). The intermolecular forces involved are of the same kind as those responsible for the imperfection of real gases and the condensation of vapours. In addition to the attractive dispersion forces and the short range repulsive forces, specific molecular interactions usually occur as a result of particular geometric and electronic properties of the adsorbent and adsorptive. In *chemisorption,* which is not dealt with in this document, the intermolecular forces involved lead to the formation of chemical bonds.

In the case of porous adsorbents, the surface can be subdivided into an external surface and an internal surface, but with two different meanings: (i) in the general case, the external surface is defined as the surface outside the pores, while the internal surface is then the surface of all pore walls; and (ii) in the presence of microporosity it has become customary to define the external surface as the non-microporous surface. Because the accessibility of pores is dependent on the size and shape of the probe

molecules, the recorded values of internal area and pore volume may depend on the dimensions of the adsorptive molecules (packing and molecular sieve effects). The roughness of a solid surface may be characterised by a roughness factor, i.e., the ratio of the external surface to the chosen geometric surface. Pore morphology describes the geometrical shape and structure of the pores, including pore width and volume as well as the roughness of the pore walls. Porosity is defined as the ratio of the total pore volume to the volume of the particle or agglomerate.

In the context of physisorption, it is expedient to classify pores according to their size (IUPAC recommendation) [2]:

(i) pores with widths exceeding about 50 nm are called *macropores*;

(ii) pores of widths between 2 nm and 50 nm are called *mesopores*;

(iii) pores with widths not exceeding about 2 nm are called *micropores*.

The quantity of gas adsorbed is measured in any convenient units, but for the presentation of the data, it is recommended that the amount adsorbed should be expressed in moles per gram of outgassed adsorbent. If possible, the composition of the adsorbent should be specified and its surface characterized. To facilitate the comparison of adsorption data, it is recommended that adsorption isotherms are displayed in graphical form with the amount adsorbed plotted against the equilibrium relative pressure (p/p_0), where p_0 is the saturation pressure of the pure adsorptive at the operational temperature, or against *p,* when the temperature is above the critical temperature of the adsorptive. If the adsorption measurements are made under conditions where the gas phase deviates appreciably from ideality (e.g., at high pressure), it is desirable that the isotherms should be presented in terms of gas fugacity rather than pressure.

The physisorption isotherms were grouped into six types and the classification is shown in Figure B.4.

Reversible Type I isotherms are given by microporous solids having relatively small external surfaces (e.g., some activated carbons, molecular sieve zeolites and certain porous oxides). A Type I isotherm is concave to the p/p_0 axis and the amount adsorbed approaches a limiting value. This limiting uptake is governed by the accessible micropore volume rather than by the internal surface area. A steep uptake at very low

p/p_0 is due to enhanced adsorbent-adsorptive interactions in narrow micropores (micropores of molecular dimensions), resulting in micropore filling at very low p/p_0. Reversible Type II isotherms are given by the physisorption of most gases on nonporous or macroporous adsorbents. The shape is the result of unrestricted monolayer-multilayer adsorption up to high p/p_0. If the knee is sharp, Point B -the beginning of the middle almost linear section- usually corresponds to the completion of monolayer coverage. A more gradual curvature (i.e., a less distinctive Point B) is an indication of a significant amount of overlap of monolayer coverage and the onset of multilayer adsorption. In the case of a Type III isotherm, there is no Point B and therefore no identifiable monolayer formation; the adsorbent-adsorbate interactions are now relatively weak and the adsorbed molecules are clustered around the most favorable sites on the surface of a nonporous or macroporous solid. In contrast to a Type II isotherm, the amount adsorbed remains finite at the saturation.
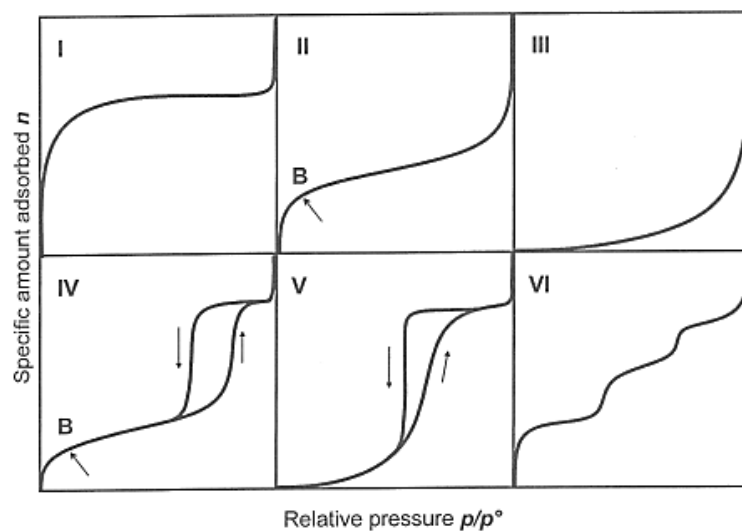
Figure B.4. IUPAC classification of adsorption isotherms.

Type IV isotherms are given by mesoporous adsorbents (e.g., many oxide gels, industrial adsorbents and mesoporous molecular sieves). The adsorption behaviour in mesopores is determined by the adsorbent-adsorptive interactions and also by the interactions between the molecules in the condensed state. In this case, the initial monolayer-multilayer adsorption on the mesopore walls, which takes the same path as the corresponding part of a Type II isotherm, is followed by pore condensation (the

phenomenon whereby a gas condenses to a liquid-like phase in a pore at a pressure p less than the saturation pressure p_0 of the bulk liquid [3,4]). A typical feature of Type IV isotherms is a final saturation plateau, of variable length (sometimes reduced to a mere inflexion point). In the low p/p_0 range, the Type V isotherm can be attributed to relatively weak adsorbent‑adsorbate interactions. At higher p/p_0, molecular clustering is followed by pore filling. For instance, Type V isotherms are observed for water adsorption on hydrophobic microporous and mesoporous adsorbents. The reversible stepwise Type VI isotherm is representative of layer-by-layer adsorption on a highly uniform nonporous surface. The step-height now represents the capacitance for each adsorbed layer, while the sharpness of the step is dependent on the system and the temperature. Amongst the best examples of Type VI isotherms are those obtained with argon or krypton at low temperature on graphitised carbon blacks.

The Brunauer‑Emmett‑Teller method [5,6] continues to be the most widely used procedure for evaluating the surface area of porous and finely-divided materials, in spite of the weakness of its theoretical foundations. Indeed, under certain carefully controlled conditions, the *BET-area* of a nonporous, macroporous or a mesoporous solid can be regarded as the 'probe accessible area' (i.e., the effective area available for the adsorption of the specified adsorptive).

Two stages are involved in the application of the BET method. First, it is necessary to transform a physisorption isotherm into the 'BET plot' and from it derive a value of the BET monolayer capacitance, n_m. In the second stage, the BET-area, *a*(BET), is calculated from n_m by adopting an appropriate value of the molecular cross-sectional area, σ.

It is customary to apply the BET equation in the linear form

$$\frac{p/p^0}{n(1 - p/p^0)} = \frac{1}{n_m C} + \frac{C - 1}{n_m C}(p/p^0) \qquad\qquad \text{(B.5)}$$

where *n* is the specific amount adsorbed at the relative pressure p/p^0 and n_m is the specific monolayer capacitance.

According to the BET theory, the parameter C is exponentially related to the energy of monolayer adsorption. It is now generally agreed that the value of C rather gives a useful indication of the shape of the isotherm in the BET range. Thus, if the value of C is at least ~80 the knee of the isotherm is sharp and Point B is fairly well defined (Figure B.4). It was this characteristic point which was first identified by Brunauer and Emmett as the stage of monolayer completion and the beginning of multilayer adsorption. If C is low (< ~50) Point B cannot be identified as a single point on the isotherm. There is then an appreciable overlap of monolayer and multilayer adsorption and the precise interpretation of n_m is questionable. When C < 2, the isotherm is either Type III or Type V and the BET method is not applicable. A high value of C (> ~150) is generally associated with either adsorption on high-energy surface sites or the filling of narrow micropores.

A convenient way to derive n_m from the BET equation is to make use of the linear relation between $(p/p^0/n)(1 - p/p^0)$ and p/p^0. The range of linearity of the BET plot is always restricted to a limited part of the isotherm, often within the p/p^0 range of ~ 0.05‑0.30 for Type II and Type IV isotherms. The linear BET range is shifted to lower relative pressures when the adsorption energy is high, especially if the surface is energetically homogeneous or crystalline. The first procedure which allows one to determine the linear BET range is particularly useful if micropores are present, when the linear BET range is also located at lower relative pressures. The second stage in the application of the BET method is the calculation of the BET-area from the monolayer capacitance. This requires a knowledge of the average area, σ_m *(molecular cross-sectional area),* occupied by the adsorbate molecule in the complete monolayer. Thus, the BET specific area of the adsorbent a_s (BET) per unit of mass is given by the following equation

$$a_S(BET) = n_m \cdot N_a \sigma_m / m \qquad (B.6)$$

where N_a is the Avogadro costant and σ_m the area effectively occupied by an adsorbed molecule in the complete monolayer.

B.4 Raman Spectroscopy

The first experimental evidence for the inelastic scattering of light by molecules such as liquids was observed by Raman and Krishnan in 1928 [7].

The Raman spectroscopy measures the vibrational motions of a molecule like the infrared spectroscopy. The origins of these two molecular spectroscopic methods are, however, quite different. Infrared spectroscopy involves the absorption of electromagnetic (IR) radiation, while Raman spectroscopy is based on the scattering of electromagnetic radiation, usually in the visible region. When a monochromatic beam of light from a laser is focused on to a vibrating molecule, the majority of the incident radiation is scattered elastically, i.e., with the same frequency as the incident radiation. This process is referred to as Rayleigh scattering. The remainder of the incident laser radiation is scattered inelastically, with frequencies either more or less than the frequency of the incident radiation. A useful diagram illustrating both Rayleigh and Raman scattering for a typical heteronuclear diatomic molecule, such as HCl, is shown in Figure B.5.
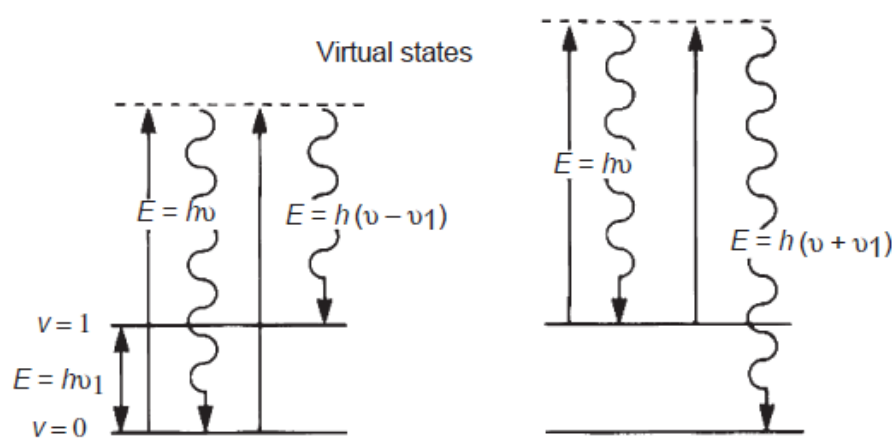
Figure B.5. Qualititative picture of Rayleigh and Raman scattering for a simple heteronuclear diatomic molecule [8].

Since electromagnetic radiation is quantized, the energy of the fundamental transition $(v = 0 \rightarrow v = 1)$ of HCl is given by $h\nu_1$. In the IR, this would be the energy absorbed by the vibrating HCl molecule. Exactly the same vibrational information is obtained from the Raman effect, but by a totally different process. In Figure B.5, the elastic Rayleigh scattering can originate from both the $v = 0$ and $v = 1$ levels. The inelastic

Raman scattering processes that are illustrated, however, result in either an energy loss $[E = h(\nu_0 - \nu_1)]$ or an energy gain $[E = h(\nu_0 + \nu_1)]$. The signals appearing at lower energies than does the central Rayleigh line are referred to as Stokes lines, while the signals appearing at higher energies are known as anti-Stokes lines. Rayleigh scattering is a much more favorable process than is Raman scattering by a factor of about 10^4. Moreover, because of the Boltzmann distribution, most molecules are in the $v = 0$ state at room temperature, so that the Stokes signals are usually more intense than are the anti-Stokes signals. Consequently, a Raman spectrum is normally scanned towards lower energies (decreasing wavenumber, cm^{-1}) from that of the incident laser line.

In the classical description of vibrational Raman scattering, when a molecule is in an electric field $\mathbf{E}$, the electron cloud and nuclei become polarized resulting in an induced dipole moment $\mathbf{P}$. The size of the dipole moment induced by a field of magnitude $\mathbf{E}$ is given by the polarizability α of the molecule:

$$\mathbf{P} = \alpha \mathbf{E}. \tag{B.7}$$

Light consists of oscillating electric and magnetic fields. For light of frequency $v = 0$, the magnitude of electric field may be written:

$$\mathbf{E} = \mathbf{E}_0 \cos(2\pi \nu_0 t). \tag{B.8}$$

Thus, the induced dipole moment oscillates in phase with the applied field:

$$\mathbf{P} = \alpha \mathbf{E} \cos(2\pi \nu_0 t). \tag{B.9}$$

The polarizability will depend upon the geometry of the molecule: as the molecule vibrates, the polarizability will change. If we write the polarizability as a Taylor series expansion in a nuclear coordinate r about its equilibrium position (r_0)

$$\alpha = \alpha_0 + \left(\frac{\partial \alpha}{\partial r}\right)_{r_0} (r - r_0) + \; ... \tag{B.10}$$

Alternatively, it is possible to expand α in terms of q_i, the vibrational coordinate of the ith normal mode. The classical normal mode vibration is

$$q_i = q_i^0 \cos(2\pi\nu_i t) \tag{B.11}$$

where ν_i is the frequency of normal mode i in the classical picture, thus we find that

$$\boldsymbol{P} = \alpha_0 \boldsymbol{E}_0 cos(2\pi\nu_0 t) + \left(\frac{\partial\alpha}{\partial q_i}\right)_0 \boldsymbol{E}_0 cos(2\pi\nu_0 t) q_i^0 \cos(2\pi\nu_i t)$$

$$= \alpha_0 \boldsymbol{E}_0 cos(2\pi\nu_0 t) + \frac{1}{2}\left(\frac{\partial\alpha}{\partial q_i}\right)_0 \boldsymbol{E}_0 q_i^0 [cos(2\pi(\nu_0 - \nu_i)t) + cos(2\pi(\nu_0 + \nu_i)t)]. \tag{B.12}$$

The intensity of the incident light I_0 is proportional to $\boldsymbol{E}_0^2$, while the scattered power is proportional to $|\boldsymbol{P}|^2$. The first term in Eq. (B.12) represents the Rayleigh scattering. The last two terms oscillate at the sum and difference frequencies, and represent the anti-Stokes and Stokes scattering, respectively.

The intensity of the Raman scattering is seen to be proportional to the derivative of the polarizability (squared):

$$I_{scatt} \propto |\boldsymbol{P} \cdot \boldsymbol{E}_0|^2 = |(\partial\alpha/\partial q_i)_0|^2 I_0^2 . \tag{B.13}$$

Therefore, the polarizability must change linearly with vibrational motion for vibrational Raman scattering to occur. The greater the change, the more intense the Raman scattering. If α is unchanged or at a minimum/maximum, there is no Raman scattering. This is the so-called double harmonic approximation, where we have made two assumptions:

- harmonic motion of the nuclei (normal mode or mechanical harmonic approximation);

- first term in the Taylor series expansion of α (electrical harmonic approximation).

Note also that the Raman intensity depends on the square of the incident intensity I_0 in Eq. (B.12). Raman spectroscopy is an example of a nonlinear optical method, i.e. one that depends nonlinearly on intensity.

The correct treatment of Raman Spectroscopy requires the use of quantum electrodynamics. However, one can use the semi-classical approach to arrive at selection rules.

The interaction Hamiltonian is given by:

$$H'(t) = \frac{1}{2}\alpha E^2 \approx \frac{1}{2}\alpha E^2 + \sum_j \frac{1}{2}E^2 \left(\frac{\partial\alpha}{\partial q_j}\right)_0 q_j + \dots \tag{B.14}$$

when we expand α in a Taylor series, and look at matrix elements coupling initial and final states $|v_i\rangle$ and $|v_f\rangle$ for normal mode j:

$$\langle v_f|H'|v_i\rangle = \frac{1}{2}E^2\left(\frac{\partial\alpha}{\partial q_j}\right)_0 \langle v_f|q_j|v_i\rangle \qquad (\text{B.15})$$

the matrix element of q_j leads to the vibrational Raman (harmonic oscillator) selection rule

$$\Delta v = \pm 1\,. \qquad (\text{B.16})$$

B.5 Scanning Electron Microscopy (SEM) and Energy Dispersive X-Ray Spectroscopy (EDX)

Scanning electron microscope (SEM) is one of the most versatile instruments available for the examination and analysis of the microstructural characteristics of solid objects. The primary reason for the SEM's usefulness is the high resolution that can be obtained: values of the order of 2 to 5nm are now usually quoted for commercial instruments.

Another important feature of the SEM is the three-dimensional appearance of the specimen image, a direct result of the large depth of field, as well as to the shadow-relief effect of the secondary and backscattered electron constrast.

The basic elements of the SEM are the lens system, electron gun, visual and recording cathode ray tubes, and the electronics associated with them.

The electron column (Figure B.6) consists of an electron gun and two or more lenses, operating in vacuum. The electron gun produces a source of electrons, and accelerates these electrons to an energy in the range 1-40 keV. The beam diameter produced directly by the conventional electron gun is too large to generate a sharp image at high magnification. Electron lenses are used to reduce the diameter of this source of electrons and place a small, focused electron beam on the specimen.

Most SEM can generate an electron beam at the specimen surface with a spot size less than 10 nm while still carrying sufficient current to form an acceptable image [9-14].
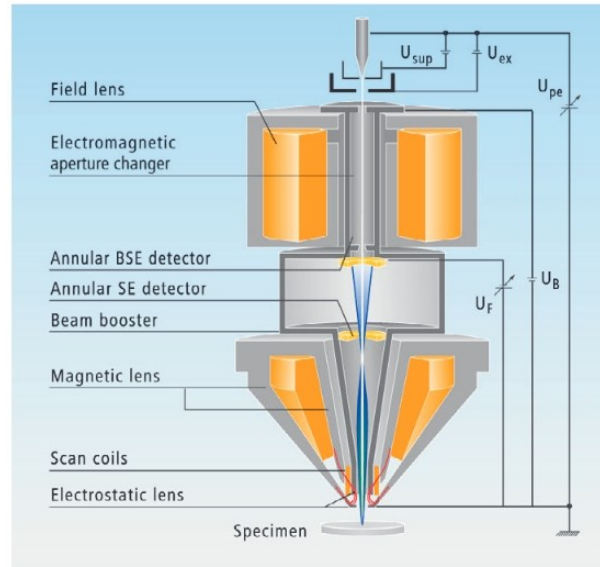
Figure B.6. Schematic drawing showing the electron column, the deflection system and the electron detectors.

In order to produce contrast in an image, the signal intensity from the beam-specimen interaction must be measured from point to point across the specimen surface.

The function of the deflection system is to scan the beam along the a line and then displace the line position for the next scan so that a rectangular raster is generated on the specimen.

Two pairs of electromagnetic deflection coils (scan coils) are used to control the raster of the beam. The magnification M of the specimen image is the ratio of the linear size of the viewing screen, known as the cathode ray tube (CRT), to the linear size of the raster on the specimen.

The interaction of the electron beam with the specimen causes the generation of many signals, which may be used to modulate the intensity of the viewing CRT and produce an image.

Indeed, the versatility of the SEM is derived in large measure from the rich variety of interactions that the beam electrons undergo in a specimen. These interaction can reveal information on many specimen's properties. The electron-specimen interactions can be divided in two classes: elastic and inelastic scattering.

Elastic scattering results from the deflection of the incident electron by the specimen atomic nucleus or by outer shell electrons of similar energy. This kind of interaction is

characterized by negligible energy loss during the collision and by a wide-angle directional change of the scattered electron. Incident electrons that are elastically scattered through an angle of more than 90° are called backscattered electrons (BSE), and yield a useful signal for imaging the sample.

Inelastic scattering occurs through a variety of interactions between the incident electrons and the electrons and atoms of the sample, and results in the primary beam electron transferring substantial energy to that atom. The amount of energy loss depends on whether the specimen electrons are excited singly or collectively and on the binding energy of the electron to the atom. As a result, the excitation of the specimen electrons during the ionization of specimen atoms leads to the generation of secondary electrons (SE), which are conventionally defined as possessing energies of less than 50 eV and can be used to image or analyze the sample. In addition to those signals that are utilized to form an image, a number of other signals are produced when an electron beam strikes a sample, including the emission of characteristic x-rays, Auger electrons, and cathodoluminescence. Figure B.7 shows the regions from which different signals are detected.
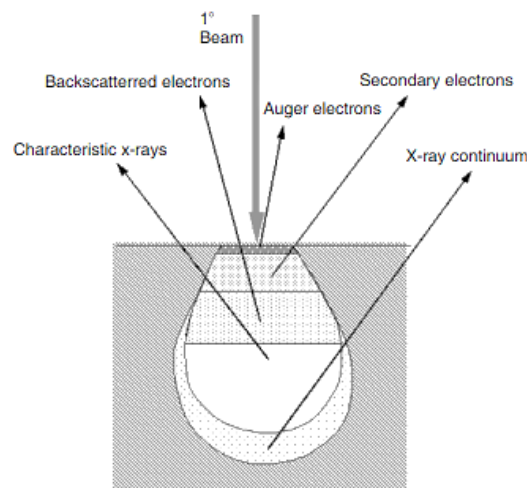
Figure B.7. Illustration of several signals generated by the electron beam–specimen interaction in the scanning electron microscope and the regions from which the signals can be detected [15].

In most cases when incident electron strikes the specimen surface, instead of being bounced off immediately, the energetic electrons penetrate into the sample for some distance before they encounter and collide with a specimen atom. In doing so, the

primary electron beam produces what is known as a region of primary excitation, from which a variety of signals are produced. The size and shape of this zone is largely dependent upon the beam electron energy and the atomic number, and hence the density, of the specimen. Figure B.8 illustrates the variation of interaction volume with respect to different accelerating voltage and atomic number. At certain accelerating voltage, the shape of interaction volume is "tear drop" for low atomic number specimen and hemisphere for specimens of high atomic number. The volume and depth of penetration increase with an increase of the beam energy and fall with the increasing specimen atomic number because specimens with higher atomic number have more particles to stop electron penetration.
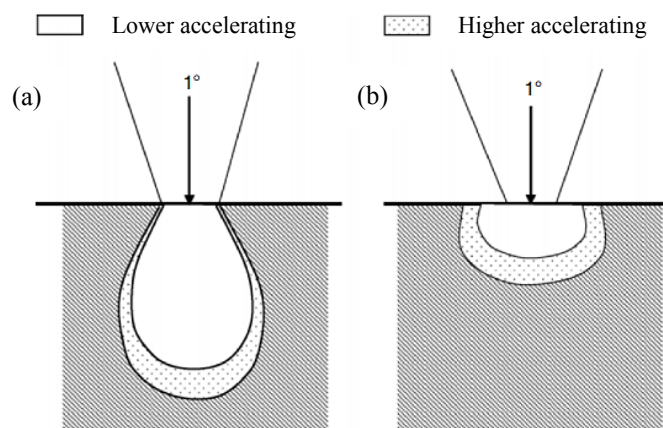
Figure B.8. Influence of accelerating voltage and specimen atomic number on the primary excitation volume: (a) low atomic number and (b) high atomic number[15].

Secondary electrons

The most widely used signal produced by the interaction of the primary electron beam with the specimen is the secondary electron emission signal.

When the primary beam strikes the sample surface causing the ionization of specimen atoms loosely bound electrons may be emitted and these are referred to as secondary electrons. As they have low energy, typically an average of around 3–5 eV, they can only escape from a region within a few nanometers of the material surface. So secondary electrons accurately mark the position of the beam and give topographic information with good resolution. Secondary electrons are used principally for topographic contrast in the SEM, i.e., for the visualization of surface texture and roughness. Due to their low energy, secondary electrons are readily attracted to a

detector carrying some applied bias. The Everhart– Thornley (ET) detector, which is the standard collector for secondary electrons in most SEMs therefore applies both a bias (+10 kV) to the scintillator and a lower bias (+300 V) to the Faraday cage, which screens the detector. In order to detect the secondary electrons a scintillator converts the energy of the electrons into photons (visible light). The photons then produced travel down a Plexiglas or polished quartz light pipe and move out through the specimen chamber wall, and into a photomultiplier tube (PMT) which converts the quantum energy of the photons back into electrons. The output voltage from the PMT is further amplified before being output as brightness modulation on the display screen of the SEM. Secondary electrons are used principally for topographic contrast in the SEM, i.e., for the visualization of surface texture and roughness. The topographical image is dependent on how many of the secondary electrons actually reach the detector. A secondary electron signal can resolve surface structures down to the order of 10 nm or better. Although an equivalent number of secondary electrons might be produced as a result of the specimen primary beam interaction, only those that can reach the detector will contribute to the ultimate image. Secondary electrons that are prevented from reaching the detector will generate shadows or be darker in contrast than those regions that have an unobstructed electron path to the detector. It is apparent in the diagram that topography also affects the zone of secondary electron emission. When the specimen surface is perpendicular to the beam, the zone from which secondary electrons are emitted is smaller than found when the surface is tilted.

Low voltage incident electrons will generate secondary electrons from the very surface region, which will reveal more detailed structure information on the sample surface.

Backscattered electrons

Another valuable method of producing an image in SEM is by the detection of BSEs, which provide both compositional and topographic information in the SEM. A BSE is defined as one which has undergone a single or multiple scattering events and which escapes from the surface with an energy greater than 50 eV. The elastic collision between an electron and the specimen atomic nucleus causes the electron to bounce back with wide-angle directional change. Roughly 10–50% of the beam electrons are backscattered toward their source, and on an average these electrons retain 60–80% of

their initial energy. Elements with higher atomic numbers have more positive charges on the nucleus, and as a result, more electrons are backscattered, causing the resulting backscattered signal to be higher. Thus, the backscattered yield, defined as the percentage of incident electrons that are reemitted by the sample, is dependent upon the atomic number of the sample, providing atomic number contrast in the SEM images. Due to the fact that BSEs have a large energy, which prevents them from being absorbed by the sample, the region of the specimen from which BSEs are produced is considerably larger than it is for secondary electrons. For this reason the lateral resolution of a BSE image is considerably worse (1.0 μm) than it is for a secondary electron image (10 nm). But with a fairly large width of escape depth, BSEs carry information about features that are deep beneath the surface. In examining relatively flat samples, BSEs can be used to produce a topographical image that differs from that produced by secondary electrons, because some BSEs are blocked by regions of the specimen that secondary electrons might be drawn around. The detector for BSEs differs from that used for secondary electrons in which a biased Faraday cage is not employed to attract the electrons. In fact the Faraday cage is often biased negatively to repel any secondary electrons from reaching the detector.

Auger electrons, cathodoliminescence and transmitted electrons

- Auger electrons are produced following the ionization of an atom by the incident electron beam and the falling back of an outer shell electron to fill an inner shell vacancy. The excess energy released by this process may be carried away by an Auger electron. This electron has a characteristic energy and can therefore be used to provide chemical information. Due to their low energies, Auger electrons are emitted only from near the surface. They have escape depths of only a few nanometers and are principally used in surface analysis.

- Cathodoluminescence is another mechanism for energy stabilization following beam specimen interaction. Certain materials will release excess energy in the form of photons with infrared, visible, or ultraviolet wavelengths when electrons recombine to fill holes made by the collision of the primary beam with the specimen. These photons can be detected and counted by using a light pipe and photomultiplier similar to the ones utilized by the secondary electron detector.

The best possible image resolution using this approach is estimated at about 50 nm.

- Transmitted electrons is another method that can be used in the SEM to create an image if the specimen is thin enough for primary beam electrons to pass through (usually less than 1 μ). As with the secondary and BSE detectors, the transmitted electron detector is comprised of scintillator, light pipe (or guide), and a photomultiplier, but it is positioned facing the underside of the specimen (perpendicular to the optical axis of the microscope). This technique allows SEM to examine the internal ultrastructure of thin specimens. Coupled with x-ray microanalysis, transmitted electrons can be used to acquisition of elemental information and distribution.

Qualitative and quantitative chemical analysis information is also obtained using an energy dispersive x-ray spectrometer (EDS o EDX) with the SEM. The EDX technique detects x-rays emitted from the sample during bombardment by an electron beam to characterize the elemental composition of the analyzed volume. Features or phases as small as 1 μm or less can be analyzed. When the sample is bombarded by the SEM's electron beam, electrons are ejected from the atoms comprising the sample's surface. The resulting electron vacancies are filled by electrons from a higher state, and an x-ray is emitted to balance the energy difference between the two electrons' states. The x-ray energy is characteristic of the element from which it was emitted. The EDX x-ray detector measures the relative abundance of emitted x-rays versus their energy. The detector is typically a lithium-drifted silicon, solid-state device. When an incident x-ray strikes the detector, it creates a charge pulse that is proportional to the energy of the x-ray. The charge pulse is converted to a voltage pulse (which remains proportional to the x-ray energy) by a charge-sensitive preamplifier. The signal is then sent to a multichannel analyzer where the pulses are sorted by voltage. The energy, as determined from the voltage measurement, for each incident x-ray is sent to a computer for display and further data evaluation. The spectrum of x-ray energy versus counts is evaluated to determine the elemental composition of the sampled volume.

B.6 Thermogravimetric Analysis (TGA)

Thermogravimetric analysis (TGA), or simply thermogravimetry (TG), is a technique for measuring changes in the sample mass that occur while the sample temperature is varied in accord with a controlled temperature program, T (t). The program can be either isothermal, T(t) = const, or nonisothermal. The most common nonisothermal program is the one in which the temperature changes linearly with time so that the heating rate

$$\beta = \frac{dT}{dt} \tag{B.17}$$

is constant. The measuring device is called a thermobalance, which is a combination of a sensitive analytical balance with an electronically programmed furnace. A typical temperature range of the instruments is from ambient to 1000–1600 °C. Although the heating rates can be set up in the range from a fraction to hundreds °C/min, the most commonly used range is 1–20 °C/min.

A TGA run can include a single temperature program, for example, heating from 25 to 600 °C at 10 °C/min, or a combination of several programs, for example, heating from 25 to 100 °C at 100 °C/min, followed by an isothermal hold at 100 °C for 60 min, then heating from 100 to 600 °C at 10 °C/min. The runs are conducted in controlled gaseous atmosphere that can be either static or dynamic. The dynamic atmosphere is accomplished by running a gas around the sample at a certain flow rate (50–100 ml/min). The gas can be either inert (nitrogen, or more rarely, argon or helium) or reactive (oxygen, hydrogen, carbon dioxide, etc). The most commonly used controlled static atmosphere is a gas at reduced pressure that can be as low as 10^3 to 10^4 Pa.

The samples studied by TGA are either solids or low volatility liquids. The sample size is normally within the range 1–100 mg, although the instruments for handling gram size samples are also available. The sensitivity of TGA is limited by the sensitivity of the balance, which can be as high as 0.1 mg. While heated or cooled, materials can undergo various changes accompanied by a loss or a gain of mass. Examples of mass loss processes include: degradation and/or decomposition, vaporization of bulk liquids or liquids adsorbed by solids, sublimation, reduction of metal oxides to metals, desorption

of gases. A mass gain can be observed in adsorption of gases as well as in reactions of solids with reactive gases such as oxygen, chlorine, and carbon monoxide. The result of TGA measurements is a thermogravimetric curve that can be presented in either integral or differential form. In the integral form (TG curve), mass (absolute in gram or relative in % of initial mass) is plotted against time or temperature. The resolution of TGA usually improves when decreasing the heating rate, which, however, results in significantly longer experiments. The resolution can be improved without a significant increase in experimental time when employing nonlinear temperature programs. Such programs are realized in the techniques known as sample controlled thermal analysis [16]. High resolution is accomplished in shorter time by varying the heating rate in inverse proportion to the process rate. That is, the heating rate is fast as long as there are no mass changes. Once a mass change is detected, the heating rate starts to slow down, reaching its minimum when the process rate is the fastest.

The shape and position of the TG curve is determined by the mechanism and kinetics of the process associated with the mass change. The kinetics of thermally stimulated processes can be parameterized in terms of three major variables: the temperature, T; the extent of conversion, α; the pressure, P as follows:

$$\frac{d\alpha}{dt} = k(T)f(\alpha)h(P) \qquad (B.18)$$

Assuming the pressure has no significant effect on the kinetics, the process rate can be presented as a function of only two variables, T and α:

$$\frac{d\alpha}{dt} = k(T)f(\alpha) \qquad (B.19)$$

The temperature dependence of the rate is represented by the rate constant, $k(T)$, whereas the conversion dependence by the reaction model, $f(\alpha)$. The extent of conversion is determined experimentally as a fraction of the total mass loss in the process so that for any current mass, m:

$$\alpha = \frac{m_i - m}{m_i - m_f} \qquad (B.20)$$

where m_i and m_f are the initial and final mass, respectively (Figure B.9). As the process proceeds from initiation to completion, α increases from 0 to 1. Generally, the value of α reflects the progress of the overall transformation of a material to products. The overall transformation can involve multiple steps each of which has it specific extent of conversion.

The temperature dependence of the process rate is typically parameterized through the Arrhenius equation

$$k(T) = A exp\left(\frac{-E}{RT}\right) \tag{B.21}$$

where A and E are kinetic parameters, the preexponential factor and the activation energy, respectively, and R is the universal gas constant. The temperature is controlled by TGA instruments in accord with a program set up by an operator.
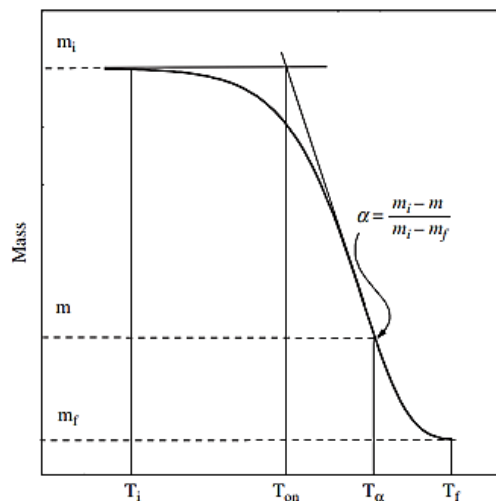
Figure B.9. Evaluation of characteristic temperatures of a TG curve [17].

Substitution of Eq. (B.16) into Eq. (B.14) followed by integration for isothermal program leads to an equation that describes an isothermal TG curve:

$$g(\alpha) \equiv \int_0^\alpha \frac{d\alpha}{f(\alpha)} = A exp\left(\frac{-E}{RT}\right) t \tag{B.22}$$

where $g(\alpha)$ is the integral form of the reaction model. Since only a changes under isothermal conditions, the a versus t curve shape is defined by the reaction model. Although there is a significant number of reaction models [18], they all can be reduced to three major types: accelerating, decelerating, and sigmoidal. Accelerating models

represent processes whose mass loss rate increases continuously throughout the process whose mass loss rate increases continuously throughout the process. An example here is a power-law model:

$$g(\alpha) = \alpha^{\frac{1}{n}} \tag{B.23}$$

where n is a constant. Models of the decelerating type represent processes whose mass loss rate decreases continuously. The most common example is a reaction-order model:

$$g(\alpha) = \frac{1 - (1 - \alpha)^{1-n}}{1 - n} \tag{B.24}$$

where n is the reaction order $\neq 1$. Sigmoidal models represent processes whose rate reaches maximum at some intermediate values of the extent of conversion. The Avrami–Erofeev models

$$g(\alpha) = [-ln(1 - \alpha)]^{\frac{1}{n}} \tag{B.25}$$

provide a typical example of the sigmoidal kinetics.

Substitution of Eq. (B.22) into Eq. (B.20) followed by integration for a linear heating program yields an equation that describes a nonisothermal TG curve:

$$g(\alpha) = \frac{A}{\beta} \int_0^T exp\left(\frac{-E}{RT}\right) dT \tag{B.26}$$

Because under nonisothermal conditions both T and a vary simultaneously, the shape of a nonisothermal TG curve cannot be readily linked to the reactionmodel type. As a matter of fact, all constant heating runs give rise to sigmoidal α versus T curves.

B.7 Transmission Electron Microscopy (TEM)

Early in the 20th century, physicists discovered that material particles such as electrons possess a wavelike character. By analogy with Einstein's photon description of electromagnetic radiation, Louis de Broglie proposed that the electron wavelength is given by

$$\lambda = \frac{h}{p} = \frac{h}{mv} \qquad\qquad (B.27)$$

where h = 6.626 × 10^{-34} Js is the Planck constant; p, m, and v represent the momentum, mass, and speed of the electron. For electrons emitted into vacuum from a heated filament and accelerated through a potential difference of 50 V, v ≈ 4.2 × 106 m/s and λ ≈ 0.17 nm. Since this wavelength is close to atomic dimensions, such "slow" electrons are strongly diffracted from the regular array of atoms present at the surface of a crystal, as first observed by Davisson and Germer (1927). Raising the accelerating potential to 50 kV, the electron wavelength shrinks to about 5 pm (0.005 nm) and such higher-energy electrons can penetrate distances of several microns (μm) into a solid. If this solid is crystalline, the electrons are diffracted by planes of atoms inside the material, as happens for x-rays. It is therefore possible to form a transmission electron diffraction pattern from electrons that have passed through a thin specimen, as first demonstrated by Thomson (1927). Later it was realized that if these transmitted electrons could be focused, their very short wavelength would allow the specimen to be imaged with a spatial resolution far superior to that of the light-optical microscope. The focusing of electrons relies on the fact that, in addition to their wavelike character, they behave as negatively charged particles and are therefore deflected by electric or magnetic fields. This principle was utilized in early cathode-ray tubes, television display tubes, and computer screens. In fact, the first electron microscopes made use of the technology developed for radar applications of cathode-ray tubes. In a transmission electron microscope (TEM), electrons penetrate a thin specimen and are then imaged by the appropriate lenses, in broad analogy with the light microscope.

Figure B.10 shows the key components of a TEM microscope, which comprises the electron gun, electrostatic lenses to focus the electrons before and after the specimen, and a transmitted electron detection system.

The electron gun in a TEM typically accelerates electrons through 80 e 300 kV accelerating voltage to give them sufficient energy to pass through up to 1 mm of material [18]. 200 e 300 keV electrons are typically used for routine imaging, with lower energy instrumentation may be fitted with a monochromator, which filters the electrons by energy to generate a beam of almost single energy [19]. A reduction in

energy spread of the electron beam is required for improved analysis of energy loss mechanisms inside materials [20].

TEM microscopes have many more electromagnetic lenses than SEM, arranged sequentially along the electron beam direction as an electron column. Condenser lenses before the specimen focus the electrons into a beam of controlled diameter and convergence. The objective lens focuses the transmitted electrons to form the diffraction pattern and first image. Projector lenses then magnify the image/diffraction pattern onto the detection system.
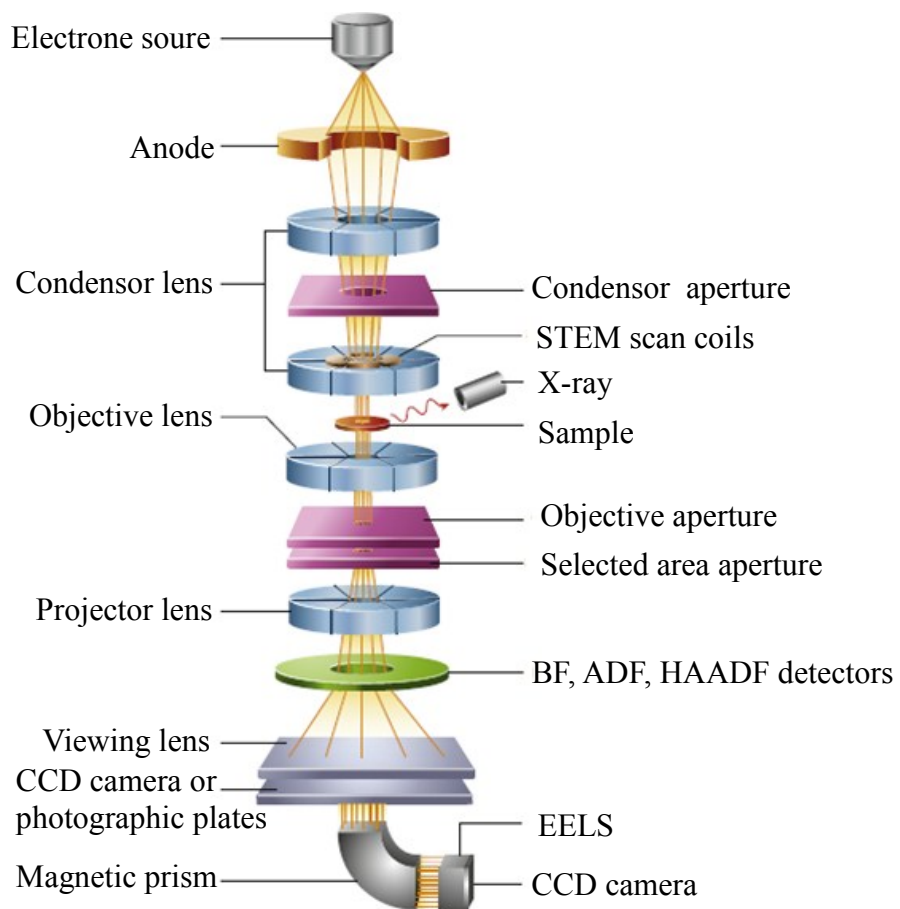
Figure B.10 Schematic components of a TEM microscope.

The contrast in TEM images is determined by the geometry of the electron illumination, the electron scattering within the specimen, and the path of the transmitted electrons through the postspecimen lenses, apertures, and detection system [18,21]. There are a great number of different TEM imaging modes developed to obtain the maximum amount of information from the specimen, and the most common are summarized here.

Bright-field (BF) imaging: Electrons which are scattered as they pass through the sample, either elastically (no energy loss) or inelastically (energy loss), move at an angle to the axis of the electron beam. Scattered electrons can be blocked by using an aperture (objective aperture) positioned in the back focal plane of the objective lens. Then, a BF image is formed from only unscattered electrons. In a BF image, areas of the specimen which are actively scattering have fewer electrons, and therefore darker contrast. There are many microstructural features which locally increase the electron scattering, particularly inelastic scattering, and so can be located as darker contrast in a BF image [22]. These include regions of increased thickness, increased mass (high Z-number/density), grain boundaries, and dislocations. Areas with strong elastic Bragg scattering will also appear dark in a BF TEM image, which can be used to detect changes in crystal orientation such as grain boundaries. The objective aperture can also be placed in the back focal plane to block unscattered electrons and choose a selection of scattered electrons to form a dark-field (DF) image. DF images are used to map regions of sample that generate specific electron scattering, which appear bright in the DF image.

Electron diffraction: Elastically scattered electrons can change direction but do not change their wavelength. Constructive and destructive interference of coherent elastically scattered electrons can generate strong beams of transmitted electrons at specific angles to the incoming electrons determined by the crystal structure and orientation of the material. This phenomenon, called electron diffraction or Bragg scattering, is analogous to X-ray diffraction [23]. When the orientation of a crystal is in a favorable orientation with respect to the incoming electron beam, elastically scattered electrons can be focused by the postspecimen lenses to form an electron diffraction pattern. Electron diffraction is one of the most frequently used analysis modes of TEM . The diffraction pattern is formed in the back focal plane of the objective lens and magnified by the projector lenses onto the recording device. Detailed analysis of diffraction patterns can determine the crystallography of the sample volume generating the diffraction pattern including lattice type, point group, lattice parameters, local crystal orientation, existence of different phases, and phase orientation relationships. The structural analysis by electron diffraction can be directly correlated with in situ BF imaging of the specimen, and potentially with chemical information from EDX or

electron energy loss spectroscopy (EELS) analyses. The nanoscale spatial resolution of electron diffraction is an advantage over X-ray diffraction; however, it can only be applied to electron transparent specimens.

High-resolution TEM (HRTEM): If specimens are ultrathin, of the order of 100 nm thickness or less, the elastic scattering dominates over inelastic scattering. The electron waves interacting with the crystal lattice diffract and form complex interference patterns visible at magnifications of 400 k or more [23]. Under some imaging conditions, the patterns correspond to atom positions, and this is called high-resolution TEM imaging.

Scanning TEM (STEM): Some TEM instruments are fitted with scan coils, which can scan a focused electron beam across the specimen [24]. This STEM mode is extremely useful for carrying out sequential chemical analysis across areas of the specimen. Advanced instruments, especially those fitted with extra lenses to correct spherical aberration in the electron beam (STEM probe correction), can obtain focused spots of less than 0.1 nm diameter [24]. This coupled with ultrastable scan electronics means that the electron beam spot can be sequentially positioned with accuracy down to different atom columns.

High angle annular dark field (HAADF): In STEM mode, unscattered electrons are collected to form BF images, and scattered electrons are collected to form ADF images. Electrons incoherently scattered through very high angles can be collected using a high angle annular dark field (HAADF) detector [24]. HAADF images show very strong contrast changes due to local changes in atomic number of the specimen (Z-contrast), and can be used to analyze chemistry at the atomic scale.

References

[1]   D. Lozano-Castelló, F. Suárez-García, D. Cazorla-Amorós, and Á. Linares-Solano, Porous Texture of Carbons, in: F. Béguin, E. Frackowiak (Eds.), Carbons Electrochem. Energy Storage Convers. Syst., 1st ed., CRC Press, pp. 115–162, (2010)

[2]   K. S. W. Sing, D. H. Everett, R. A. W. Haul, L. Moscou, R. A. Pieroti, J. Rouquerol, and T. Siemieniewska, Reporting physisorption data for gas/solid systems, with special reference to the determination of surface area and porosity (recommendations 1984), Pure Appl. Chem. **57**, (1985).

[3]   M. Thommes, andd. A. Cychosz, Physical adsorption characterization of nanoporous materials: progress and challenges, Adsorption **20**, 233 (2014).

[4]   P. A. Monson, Understanding adsorption/desorption hysteresis for fluids in mesoporous materials using simple molecular models and classical density functional theory, Microporous Mesoporous Mater. **160**, 47 (2012).

[5]   J. Rouquerol, F. Rouquerol, K. S. W. Sing, P. Llewellyn, G. Maurin. Adsorption by Powders and Porous Solids: Principles, Methodology and Applications, Academic Press (2014).

[6]   S. Lowell, J. Shields, M. A. Thomas, M. Thommes, Characterization of Porous Solids and Powders: Surface Area. Porosity and Density, Springer, (2004).

[7]   C.V. Raman, and K.S. Krishnan, A New Type of Secondary Radiation, Nature, **121**, 501 (1928).

[8]   C. L. Hill, In Comprehensive Coordination Chemistry-II: From Biology to Nanotechnology; A.G. Wedd, Ed.; Elsevier Ltd.: Oxford, UK, Vol. 4, pp 679-759 (2004).

[9]   L. Reimer, Scanning Electron Microscopy, second ed. Springer, Heidelberg, (1998).

[10]   J. Goldstein, D.E. Newbury, D.C. Joy, C.E. Lyman, P. Echlin, E. Lifshin, et al., Scanning Electron Microscopy and X-ray Microanalysis, third ed. Springer, (2007).

[11]   D. Stokes, Principles and Practice of Variable Pressure: Environmental Scanning Electron Microscopy, Wiley-Blackwell, (2008).

[12]   R. F. Egerton, Physical Principles of Electron Microscopy: An Introduction to TEM, SEM, and AEM, second ed. Springer, (2011).

[13]   J. Kuo, Electron Microscopy: Methods and Protocols (Methods in Molecular Biology), third ed. Humana Press. (2014).

[14]   J. Pawley, and H. Schatten, Biological Low-voltage Scanning Electron Microscopy, Springer, (2014)

[15]   G. Hüebschen, I. Altpeter, R. Tschuncky, and H.-G. Herrmann, Materials Characterization Using Nondestructive Evaluation (NDE) Methods 1st Edition (2016).

[16]   O. T. Sorensen, and J. Rouquerol, Sample Controlled Thermal Analysis: Origin, Goals, Multiple Forms, Applications and Future, Springer, Berlin, (2003).

[17]   S. Vyazovkin, Thermogravimetric Analysis, Characterization of Materials, Wiley online library, pp. 1-12 (2012).

[18]   L. Reimer, and H. Kohl, Transmission Electron Microscopy: Physics of Image Formation, fifth ed. Springer, (2008).

[19] R. Brydson, Aberration-corrected Analytical Electron Microscopy, Wiley, (2011).

[20] R. Brydson, Electron Energy Loss Spectroscopy, CRC Press, Oxford, (2001).

[21] J.C.H. Spence, High-resolution Electron Microscopy, fourth ed. Oxford University Press., (2013).

[22] D.B. Williams, and C.B. Carter, Transmission Electron Microscopy, Springer, (2009).

[23] J. Spence, and J.M. Zuo, Electron Microdiffraction, Springer, (1992).

[24] S. J. Pennycook, and P.D. Nellist, Scanning Transmission Electron Microscopy: Imaging and Analysis, Springer, (2011).

Conclusions

In this PhD Thesis, low-dimensional materials were investigated in order to understand their physico-chemical properties crucial for applications in many different fields: plasmonics, nanoelectronics, spintronics, catalysis and supercapacitors. This work was focused on the synthesis and characterization of the following materials: silicene, $PtTe_2$, carbon nano-onions and activated carbon.

Two reconstructions of silicene on Ag(111), due the phase $(2\sqrt{3} \times 2\sqrt{3})R30°$ and a mixture of the (4×4), $(2\sqrt{3} \times 2\sqrt{3})R30°$ and $(\sqrt{13} \times \sqrt{13})R13.9°$ superstructures were studied by electron energy loss spectroscopy.

The measurements, consistent with time dependent density functional theory calculations of the EL function of freestanding silicene, showed a well-resolved loss peak at 1.75 eV for a momentum transfer of the order of 10^{-2} Å^{-1}. The obtained results indicated that π or π^* character of the lowest-lying energy bands in silicene grown on Ag(111) may be maintained under specific geometric conditions. On the other hand, the absence of the π –like mode in eache the sigle pure phase of the above mentioned type, confirmed that the semimetallic character of freestanding silicene is lost in favor of the hybridized band structure.

Therefore, the weakened interaction of multiphase silicene with the substrate may provide a unique platform with the potential to develop different applications based on two-dimensional silicon systems.

The broadband excitation spectrum of bulk $PtTe_2$ was explored using electron energy-loss spectroscopy and density-functional theory. In addition to infrared modes related to intraband three-dimensional (3D) Dirac plasmon and interband transitions between the 3D Dirac bands, modes at 3.9, 7.5, and 19.0 eV were observed in the ultraviolet region. The comparison of the excitation spectrum with the calculated orbital-resolved density of states allowed to ascribe spectral features to transitions between specific electronic states. Additionally, the thickness dependence of the high-energy-loss peak were

studied in the PtTe$_2$ thin films. Unlike graphene, it has been observed that, the high-energy EELS peak in PtTe$_2$ thin film gets redshifted by ~ 2.5 eV with increasing thickness.

Arc discharge in water between graphite electrodes was used with the aim to optimize the production of CNOs, by an innovative experimental arrangement. The discharges generated dispersed nanomaterials and a black hard cathodic deposit, which were studied by TEM, SEM, Raman, TGA and EDX. A simple mechanical grinding of the deposits, has made it possible to obtain turbostratic polyhedral CNOs that exhibited higher stability towards burning in air, compared to CNOs found in water. A mechanism for the formation of the CNOs present in the deposit was proposed. In this model, the crystallization is driven by a strong temperature gradient existing close to the cathode surface at the beginning of the process, and subsequently close to the deposit surface whenever it is growing.

Activated carbon, obtained by chemical activation of a Spanish anthracite, was electrochemically characterized in aqueous solutions.
The study was carried out by cyclic voltammetry and galvanostatic charge/discharge experiments.
For high scan rate values, AC in 1 M H$_2$SO$_4$ showed larger capacitance values than those obtained with Na$_2$SO$_4$ due to the mass-transfer resistance that attain higher values in a neutral medium. In addition, redox processes related to the presence of electroactive oxygen groups were observed for AC in acid solution.
The electrochemical performance of this carbon material were analyzed by studying its performance as electrodes of symmetric and asymmetric supercapacitors in acid and neutral media. In both cases the best performance was observed for AC in H$_2$SO$_4$.